Author:
Collins, Ben W B

Title:
Euler's disk and the rocking can

a study of three-dimensional problems in rotational dynamics

Euler's disk and the Rocking Can

A study of three-dimensional problems in rotational dynamics

By

BEN COLLINS

Department of Engineering Mathematics
UNIVERSITY OF BRISTOL

A dissertation submitted to the University of Bristol in accordance with the requirements of the degree of DOCTOR OF PHILOSOPHY in the Faculty of Engineering.

FEBRUARY 2022

Word count: thirty six thousand five hundred and two

Abstract

When tilted and released, a can falls towards a flat, upright state. Instead of falling flat, the can experiences a bouncing motion before rising up and falling over. During the bounce, the can rotates through $\pm\Delta\psi$, an angle greater than π and observable in experiments [87]. This asymmetric behaviour is known as the rocking can phenomenon. A special case of Euler's disk, the equations of motion describing the rocking can contain two conserved quantities, for which we provide a physical justification of their existence. The dynamics are reduced to a singularly perturbed, second order ODE, with a small parameter corresponding to a combination of angular momenta. Using matched asymptotics, we split the dynamics into an outer region, which describes the initial rocking motion, and an inner region, which describes the bounce. The solution to the inner problem yields the same angle of turn found by Srinivasan and Ruina [87]. We gain new information about the sign of the angle of turn, with good agreement to the full non-linear equations. We find that large angles of turn require prohibitively large coefficients of friction.

The related problem of Euler's disk arises when dissipation is introduced to the system. When spun on a hard, smooth surface, Euler's disk rolls with a whirring noise that increases in frequency until an abrupt halt. This halting behaviour is investigated in two experiments. In the first experiment, we spin the disk on base-plates of different materials. We find that the energy closely follows the well-known power law [68], but that the energy exponent n, commonly used to characterise the motion, varies with the material characteristics of the base-plate. In the second experiment, we spin the disk and film it from two angles, tracking both its angle of inclination and the rotation of a strip drawn on the disk. We show that the disk continues to rotate after falling flat. The duration of the continued rotation can be increased by lubricating the surface and decreased by spinning the disk on a concave base-plate. It is suggested that the disk loses contact with the plane and is briefly supported by a layer of fluid between the disk and the base-plate.

To analyse Euler's disk, we derive the equations of motion subject to Coulomb friction and another unspecified dissipation mechanism. We check for Painlevé paradoxes, a mechanism for loss of contact, and find them to be impossible. In a relaxation of the rigid body assumption, we find equivalent definitions of classical rolling friction and contour friction. Taking contour friction, we numerically solve the equations of motion with initial conditions informed by experiments. We find that the disk undergoes alternating periods of slipping and rolling motion, ending with slipping motion. Furthermore, the disk encounters the discontinuity set of contour friction, providing a mechanism for the continued rotation observed in experiments. Finally, we analyse the post-falling flat motion, consisting of a lubrication theory-informed, contact-less phase followed by a Coulomb-governed slip to a halt. The predicted duration of the post-falling flat motion is in agreement with experiments. We posit that, on the concave base-plate, contour friction is the dominant dissipation mechanism. However, on flat, hard base-plates, we conjecture the presence of an air resistance based mechanism.

Dedication and acknowledgements

First and foremost, I would like to thank my supervisor, John, for his patience, insight and attention, both during my PhD and my Master's project. Since my first lecture at the University of Bristol in Engineering Mathematics 1, John has inspired creative and independent mathematical thought. I'm extremely grateful for all of John's guidance, both academic and professional. I would also like to thank Robert Szalai for agreeing to be my other supervisor. Although our meetings were infrequent, Robert's advice and suggestions were very much appreciated.

Kristian Kristiansen and Cameron Hall are both owed the greatest of thanks for their help and collaboration. Without both of their inputs, the rocking can might never have stopped rocking. Kristian deserves further thanks for his patience in explaining GSPT techniques to a confused first year PhD student. All academic discussions were valued highly. Thanks to Peter Varkonyi, Tamas Baranyai, Gabor Stepan, Panagiotis Kaklamanos and Oscar Benjamin, all of whom were kind enough to listen to me prattle on about spinning disks.

Inside the Department of Engineering Mathematics, I was lucky enough to be placed in the Buncaer, atop Queen's building. Here I met too many colleagues and friends to name. The first Thursdays (and Wednesdays), 'ten and two' coffees, cold winter swims, Buncaer runs and all the other events made the work a little easier and a lot more enjoyable. In no particular order, thanks to Sophie, Shree, Natasha, Rob, Ben, Chanelle, Mark, Zohar, Aaron, Tom, Fanqi, Fahad and many others.

Two others are due extra special thanks. Stanisław for innumerable codewords, plant watering, swims, runs, mathematical questions and many more. Noah, my academic brother, for his mathematical help and encouragement when the equations looked most deserted of meaning. Of course, the summer schools, conferences, sushi, and many hours of GeoGuessr should not go unmentioned. The pub trips will be sorely missed.

Support does not need to come in the form of academic help. Without 33 Abbotsford Road, I would be a very different person. Thank you to James, Kirsty, Mar, Mohit, Shania and Fabio for all your friendship and memories. Vlad, Finlay, Grace and Louis also receive special mentions for their friendship over these past four years.

No work is done in a vacuum, and this thesis is no exception. In particular, my sister Gemma deserves many, many thanks for her shrewd comments and suggestions on the manuscript. Any misplaced commas are entirely my own fault. The rest of my family are also owed thanks. Their enthusiastic encouragement and patience with my mathematical talk is deeply appreciated.

Finally, this thesis is dedicated to Amy, your love and encouragement means the world to me. I am eternally grateful for your understanding and patience during these past four years. Without you, this thesis could never have been written.

AUTHOR'S DECLARATION

I declare that the work in this dissertation was carried out in accordance with the requirements of the University's Regulations and Code of Practice for Research Degree Programmes and that it has not been submitted for any other academic award. Except where indicated by specific reference in the text, the work is the candidate's own work. Work done in collaboration with, or with the assistance of, others, is indicated as such. Any views expressed in the dissertation are those of the author.

SIGNED: B. COLLINS DATE: FEBRUARY 8, 2023

TABLE OF CONTENTS

List of Tables

Table **Page**

List of Figures

Figure **Page**

CHAPTER 1

INTRODUCTION

A good desk toy exhibits a physical principle in miniature. The archetypal example is Newton's cradle, which exemplifies the conservation of momentum through its click-clacking pendulums. Chaos is found in the desktop double pendulum. Each mesmerising swing is unique due to the sensitive dependence on initial conditions. A common childhood toy, spinning tops are important to cultures around the world: Judaism has the dreidel, China has da tuoluo and Malaysia has gasing pangkah, to name a few diverse examples. Clearly, rotational motion is a universally captivating phenomenon and some of its most counter-intuitive properties are typified in desk toys. Despite their simplicity, rattlebacks, tippe tops and even eggs show surprising behaviour for which explanations are non-trivial. In this thesis, we study two desktop phenomena that have thus far evaded satisfactory explanation: the rocking can and Euler's disk.

Figure 1.1: Examples of spinning tops. The dreidel [2], da tuoluo [1] and gasing pangkah [4].

The rocking can phenomenon is easily replicated at home. Take an empty food can, a cylindrical shell capped at both ends. When placed on a horizontal plane and tilted, the phenomenon is observed by giving the can a small push, as in fig. 1.2. The can tilts, falling towards the flat

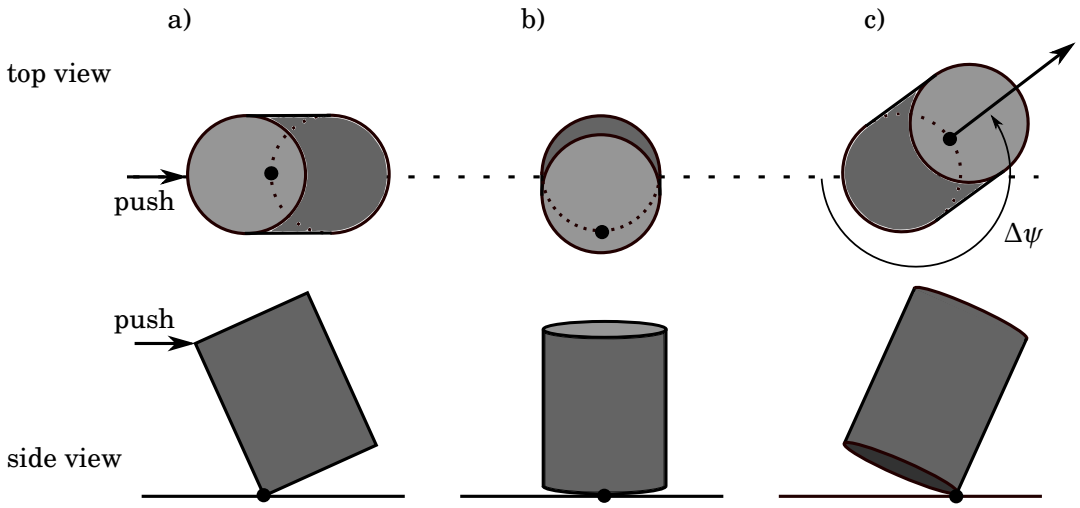

Figure 1.2: The angle of turn phenomenon. a) The can begins tilted about a point on the rim given by the black circle. On release, the can falls down. b) As the can approaches the flat state the contact point rapidly races around the rim of the can. c) The can rises up again, pivoting about the contact point. The contact point has moved through an angle $\Delta\psi$ around the rim of the can.

upright state. Just before impact with the plane the can pivots, avoiding the impact, and the contact point races around the rim. The can then rocks back up and falls over. Surprisingly, the final state is not diametrically opposed to the initial state. The can has rotated through an angle greater than π. Srinivasan and Ruina [87] compute this angle of turn using formal assumptions on the motion and obtain agreement with experiments. In Chapter 2, we derive and analyse the equations of motion for the rocking can. We reduce the system to a single, second order, singularly perturbed, ordinary differential equation (ODE) by means of a Frobenius series. A matched asymptotic approach splits the motion into two phases: one close to impact when the can is almost flush with the plane, and one far away where the can is tilted over. We confirm and extend the findings of Srinivasan and Ruina [87], determining the feasibility and direction of the angle of turn along with the motion of the contact locus.

The remainder of this thesis examines a problem closely related to the rocking can: Euler's disk, a desk toy comprising of a heavy, spinning disk. Contrary to its name, Euler's disk was invented by Joseph Bendik [14] in 1987. A commercial version, machined out of steel, has been developed with accompanying mirrored, concave base-plate and magnetic decorations. An example is shown in fig. 1.3. The mirrored surface and holographic decorations are purely aesthetic, an important consideration for a desk toy. On spinning the disk on the base-plate, the motion continues for around two minutes. Beginning upright and spinning purely about the vertical axis, the disk quickly falls into a more horizontal attitude. As the disk falls further, it appears to spin faster, producing a whirring noise that increases in frequency. The noise carries on for far longer than one might expect, with the disk oscillating only millimetres above the

surface. Suddenly, the disk falls flat with a bang. A fair imitation of the phenomenon may be achieved by spinning a coin or, better yet, a saucepan lid. A rigorous explanation for the motion has not yet been found despite considerable academic interest.

Figure 1.3: The commercial Euler's disk [3].

We study Euler's disk experimentally in Chapter 3. In the first of two experiments, we film the disk spinning on base-plates of different materials. Key dynamical variables are extracted from the footage and we compute the energy of the disk. We find differences in the behaviour of the disk on different base-plates. In the second experiment, we place a strip on top of the disk to track its rotation. Appropriate placement of a mirror enables a second, synchronised view of the disk. Analysis of the footage suggests that the disk continues to rotate for a short time after falling flat. In both experiments, differences in behaviour are observed between the flat and concave base-plates.

In Chapter 4 we derive the non-smooth equations of motion for Euler's disk subject to an unspecified dissipation mechanism. We discuss a number of candidate mechanisms that could explain the motion of the disk, before analysing the most likely candidate: contour friction. Numerical solutions of the equations of motion show behaviour qualitatively consistent with experiments, but an augmented variant of contour friction gives the closest quantitative agreement. The continued rotation of the disk can be explained by the presence of a discontinuity in the contour friction formulation. We propose that the disk loses contact and continues to rotate, supported by a thin layer of air. After making contact with the base-plate, Coulomb friction quickly brings the disk to a halt.

In the remainder of this introduction we discuss the existing literature surrounding the rocking can phenomenon and Euler's disk, before giving an outline of the thesis in Section 1.5.

1.1 Rotating bodies

It may be argued that rotating bodies have been studied informally since the invention of the wheel in 4000 BCE. However, rotational dynamics rarely make for easy problems. For example, consider the most basic three-dimensional rotational problem: spinning tops. These are not integrable in general, but special cases have been analysed by the mathematical giants Euler, Lagrange and Kovalevskaya [43, 63, 65]. The problem of rolling motion was seriously considered towards the end of the 19^{th} century in mathematical studies undertaken by Chapylgin [25], Vierkandt [95], Appell [10] and others.

Figure 1.4: A rattleback [5]. When spun the rattleback wobbles to a halt before reversing direction.

Figure 1.5: The tippe top.

More than two hundred years after Chaplygin [25], rolling bodies are still the subject of academic study. Many of the simplest rotating systems including the rattleback, the tippe top and the mysterious spinning cylinder have only recently been afforded a mathematical explanation. A rattleback, pictured in fig. 1.4, exhibits 'spin reversal' where, upon spinning, the rattleback will slow, stop and then start spinning in the opposite direction [24]. Often such motion is chiral, occurring in only one direction, though bidirectional rattlebacks do exist. The behaviour is attributed to a 'misalignment between the mass distribution and the ellipsoidal shape of the bottom of the rattleback' [24]. Borisov and Mamaev [18] discovered that the rattleback exhibits chaotic dynamics.

The aptly named tippe top in fig. 1.5 consists of a truncated sphere connected to a stem. When spun briskly, the tippe top wobbles and tips over until the stem makes contact with the ground. The tippe top then flips upside-down, balancing about the stem rather than the spherical base. Cohen's [29] entertaining paper studies the dynamics of the tippe top and suggests it is friction that causes the inversion, a claim upheld by Or [75]. A similar problem, the tippedisk is studied by Sailer and Leine [85] and shown in fig. 1.6. With the hole placed upwards, the spinning motion

is unstable and quickly switches to a configuration with the hole oriented downwards. This is reminiscent of the spinning egg phenomenon where, upon spinning, a hard-boiled egg rises up about its narrow end.

A final example involves even simpler geometry, a cylinder. Jackson et al. [57] analysed the so-called 'mysterious spinning cylinder' with two marks at either end (shown in Figure 1.7). When spun, only one of these marks is visible. The other is repeated periodically around the circle traced out by the cylinder. The occurrence is due to a line of zero velocity points from the point of contact through the centre of mass to the tip of the rod. The mark 'X' can only be seen when directly above the contact point, far from the zero velocity line. It is therefore moving too quickly to be visible. Meanwhile, the mark 'O' can only be seen when facing upwards, very close to the zero velocity line. By contrast, it moves slowly and is visible. Six copies of 'O' appear due to the 1:6 ratio of the cylinder's diameter to length. Such rotational toy problems are celebrated in the article by Featonby [39] entitled 'Dare we teach tops?', the sentiments of which are echoed in this thesis.

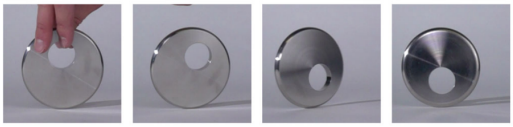

Figure 1.6: A tippedisk, figure reproduced from [85].

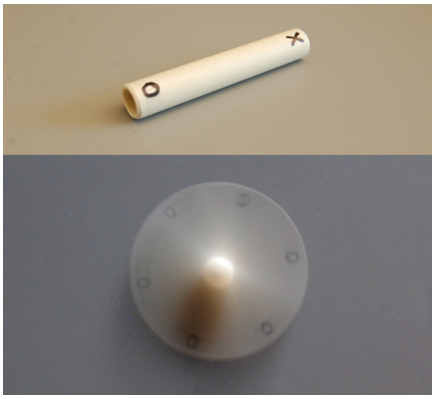

Figure 1.7: The mysterious spinning cylinder, reproduced from [57]. When the cylinder is spun with a downwards snapping motion at 'X' only one of the symbols is visible.

1.2 The rocking can

Chapter 2 of this thesis tackles the rocking can phenomenon which is intimately connected to the mysterious spinning cylinder. Srinivasan and Ruina performed a comprehensive analysis of the phenomenon in their 2008 paper [87]. It was found experimentally that the angle of turn $\Delta\psi \approx 217°$. They also note that the can may rotate clockwise or anticlockwise exhibiting a sensitive dependence on the initial conditions. In addition to experiments, Srinivasan and Ruina [87] derived the equations of motion for the can rolling without slip on the horizontal plane. Numerical simulation of the equations exposed a formal relationship between two dynamical variables, also employed by Vassiliou et al. [94] in their study of cylindrical structures during

earthquakes. In this thesis we rigorously derive this relationship and give physical justification for its existence. In their formal analysis, Srinivasan and Ruina [87] gave the following expression for the angle of turn

$$\Delta\psi = \pi\sqrt{\frac{A + mR^2 + mH^2}{A + mH^2}}, \tag{1.1}$$

where A is the moment of inertia of the can around the non-symmetry axes and H and R are the height and radius of the can respectively. The cylinder characteristics A, R and H can be varied to predict a wide range of $\Delta\psi$. For a homogeneous disk $\Delta\psi = \pi\sqrt{5}$, or 402° more than a full rotation. A tall cylinder has the minimum angle of turn $\Delta\psi \approx \pi$ and simply rocks back and forth in the manner of the rocking block analysed by Housner [52]. Later work by Srinivasan et al. [86] examined the dynamics of the rocking can with a slight asymmetry in the mass distribution and found chaotic motion.

Cushman and Duistermaat [33] studied the rolling behaviour of the thin disk with $H = 0$. They found the same angle of turn and gained information about its direction. Batista [13] explored the colliding motions of the thick disk with the plane using a similar method to Chapter 2: reduction and subsequent integration of the equations of motion. The collisions were analysed assuming elastic impacts, but Batista [13] did not discuss the angle of turn phenomenon nor its dynamics.

1.3 Euler's disk

Euler's disk has received popular interest, appearing in the television series 'The Big Bang Theory' [1] as well as many informative YouTube videos most notably by 'stand-up mathematician' Matt Parker [2]. At the time of writing, some videos have received upwards of 5 million views, a testament to the striking nature of the motion. We first review the dissipation-free case.

1.3.1 The dissipation-free disk

A large body of work exists studying the behaviour of rolling disks in a conservative setting [20, 76, 79, 88, 92]. There are two classes of dissipation-free motion, given by zero and sufficient Coulomb friction. In the absence of friction the disk slips without loss of energy. For sufficiently rough surfaces, the disk rolls without slip and no energy is dissipated. O'Reilly [76] studied a thin, upright, rolling disk with both zero and sufficient friction and identified pitchfork bifurcations in the motion. Rolling a penny on a horizontal surface in a straight line is stable at high angular velocities, but as the speed decreases the rolling motion becomes unstable and the penny topples to the left or right. It is observed that the critical angular velocity is larger in the absence of friction and similar bifurcations are found for the vertically spinning disk. In addition, O'Reilly

[1] Season 10, episode 16.

[2] `https://www.youtube.com/watch?v=8pSLffliCk0`

[76] identified so-called 'steady motions' where the angle of inclination remains constant. Colliding motions where the disk impacts on the horizontal plane with a 'slap' are analysed.

Paris and Zhang [79] also studied the thin, rolling disk and computed its steady motions. They calculated the amplitude and frequency of the oscillations when the disk is perturbed from the steady motions. Stanislavsky and Weron [88] also computed these oscillations and paid particular attention to the nonlinear oscillations that occur far from the steady motions. The amplitude and frequency of the oscillations are linked to both the whirring noise emitted by the disk and the dissipation mechanism.

In experiments, Takano et al. [92] placed the disk on a vibrating plate and achieved sustained motion. Numerical simulations suggested that a rolling disk still stops despite the vibrating plate, but if the disk slips then sustained motion is possible. However, in the absence of an energy input Euler's disk always comes to a halt. The manner and cause of this halt has been at the centre of the debate concerning Euler's disk since the turn of the millennium.

1.3.2 Energy loss in Euler's disk

In the past two decades there has been a great deal of discussion concerning the abrupt stop of Euler's disk. No agreement has been reached on exactly what happens in the final stages of the motion nor the cause of the halt. The energy profile of the disk has been estimated from experimental data and shows a clear power-law form [23, 68, 71]

$$E(t) = A_e(t_0 - t)^n, \tag{1.2}$$

where A_e is a multiplicative constant, t_0 is the time of the stop and n is the energy exponent. Experimental estimates for n lie in the range $[0,1]$ resulting in a sharp decrease to zero energy, accounting for the abrupt nature of the halt. The precession and contact point velocity of the disk approach a finite-time singularity as $t \to t_0$ producing the characteristic whirring noise [36]. However, Moffatt [74] noted that 'nature abhors a singularity and some physical effect must intervene to prevent its occurrence'.

A number of experiments have been performed that track the state variables of the disk to estimate the energy exponent [23, 68, 71]. Ma et al. [71] measured the variables using a pair of synchronised high-speed cameras and found that $n \approx 2/3$. Experiments by Caps et al. [23] employed a laser to measure the inclination of the disk for an estimate of $n \approx 2/3$. Finally, Leine [68] used a single high-speed camera to film the disk's motion and found $n \approx 2/3$ for times $t \ll t_0$ and $n \approx 1/2$ as $t \to t_0$.

Despite these experiments, the energy dissipation mechanism that brings the disk to a halt is not fully understood. Authors typically take a candidate dissipation mechanism and then compute the energy exponent n. Although many mechanisms may remove energy from Euler's disk, the mechanism with the smallest n is *dominant* as $t \to t_0$. Moffat [74] proposed that viscous dissipation in the layer of air between the disk and the base-plate is the dominant dissipation

mechanism. Energy considerations in addition to a suite of assumptions gave a power law of the form eq. (1.2) with $n = 1/3$. This estimate is rather too low when compared with experimental data. Subsequent analysis by Bildsten [15] revised this estimate upwards to $n = 4/9$.

Borisov et al. [17] performed experiments examining the retrograde motion of rolling disks and rings. Three experiments were performed: the ring was spun without modifications, with the hole sealed, and in a vacuum. No major differences in behaviour were observed between experiments. Similar experiments by van den Engh et al. [93] span a magnetic Dutch 2.5 guilder coin in a vacuum noting no *qualitative* difference in behaviour. Note that this does not exclude *quantitative* differences in behaviour during the final stages of the disk's motion that could be attributed to air resistance.

Caps et al. [23] and Petrie et al. [80] suggested that sliding friction may be the major source of energy dissipation. In most mechanical problems this is a safe assumption, but analysis by Leine [68] showed that Coulomb friction is unable to bring the disk to a halt, let alone be the dominant mechanism. Caps et al. [23] noted that different materials give slightly different values of n. This is also seen in the experiments by Ma et al. [71]. In Chapter 3 we investigate the material dependence of n.

It is frequently argued that a form of rolling friction brings the disk to a halt. However, in three-dimensions a body has three independent angular velocities which give rise to many possible variants and combinations of rolling frictions. Ma et al. [70, 71] propose a viscous friction model proportional to the square of an angular velocity, and obtain good agreement with experiments for the whole motion. Three stages of motion are identified for Euler's disk: 1) A fast sliding stage where sliding friction dominates; 2) A slow creeping stage where both sliding and rolling friction dominate; 3) A purely rolling stage where rolling friction dominates. However, sliding motion is difficult to observe experimentally because the disk is almost stationary in the final stages of the disk's motion.

Cross [31, 32] also asserted that rolling friction is responsible, stating that 'the sudden stop appears to be due to a rapid increase in the coefficient of rolling friction'. Cross [32] suggested that asperities in the surface may cause the increase. As the disk falls closer to the plane it comes into contact with asperities over a wider contact region. Kwang-Hua [28] suggested that Cross should consider deformations instead of asperities. In Chapter 4, we do so by relaxing the rigid body assumption and derive new rolling frictions in a contact region approach.

Le Saux et al. [67] numerically analysed the disk subject to a number of rolling frictions and noted that viscous and dry contour friction, as well as dry classical rolling friction, resulted in a finite-time halt of the disk. Viscous classical rolling friction and dry Contensou friction [30] gave an asymptotic decrease in energy, such that the disk does not stop in finite time. Subsequently, Leine [68] reviewed and collated different dissipation mechanisms for the disk. Dry and viscous contour friction gave promising estimates for n: 2/3 and 1/2 respectively. It is tentatively suggested by Leine [68] that a dry contour friction followed by a viscous contour friction may explain the

motion of Euler's disk.

Mechanisms that are not based on a variant of friction have been proposed. Villaneuva [96] suggested that vibrations in the disk may cause loss of contact just before the halt. Kessler and O'Reilly [60] agreed, and proposed that excitation of the modes of vibration in the disk account for the whirring sound and the eventual loss of contact with the plane. However, it is not clear that energy loss due to the vibration is a significant factor.

Baranyai and Varkonyi [11] discussed a dissipation mechanism based on imperfections of the disk. Supposing a polygonal disk, Baranyai and Varkonyi [11] discretised the disk's motion from one impact to the next. At each impact a proportion of the energy is dissipated via a coefficient of restitution. Eventually, the disk may have more than one point of contact or even lose contact with the base-plate entirely. Self-similar motion, whereby an impact at one vertex is followed by the next vertex along the contour of the polygonal disk, is shown to have an energy power-law exponent of $n = 2$. Thus it falls outside the range of experimental estimates. Baranyai and Varkonyi [11] noted that 'imperfections may affect energy dissipation during the last few tenths of a second', which could be the cause of the rattling noise that some authors have noticed.

Finally, loss of contact is predicted by Borisov et al. [19] in a pleasing experiment. Current is passed through the disk and base-plate and when contact is lost, the circuit is broken. With this method, an interval of no-contact lasting around 10-40 ms was observed at the halt. Prior to the halt, many 'micro-losses' of contact are detected, each lasting for no more than 5 ms. We give an explanation for the final loss of contact in Chapter 4.

1.4 Applications

Stefanou et al. [89] examined the dynamics of tall frustra rolling on a horizontal plane, with applications to ancient classical columns excited by earthquakes. Two types of motion were identified: 'in-plane' rocking and 'out-of-plane' wobbling. It was shown that collision with the plane takes place under certain specific initial conditions. Otherwise, in the absence of dissipation the cylinder periodically rocks between a maximum and minimum angle. Burger et al. [22] also investigated tall cylindrical structures, subject to a ground forcing designed to mimic an earthquake. Similarly, Aik et al. [61] and Vassiliou et al. [94] studied tall cylindrical structures as extensions of Housner's planar rocking block [52], paying particular attention to the overturning conditions, an important engineering consideration. The analysis of the rocking can in Chapter 2 could be used to inform future work in cylindrical structures.

Clearly, rolling contact and rolling friction is an area of great engineering concern: wheels, rollers and bearings are ubiquitous. The unknown dissipation mechanism causing the halt of Euler's disk may have implications for rolling friction. Rolling friction is an empirical area of research and new analytic models may shed light on other previously unknown features. For example, the rolling behaviour of tyres is commonly described by the empirical 'magic formula

tyre model' [77].

Dynamical models of phenomena, such as wheel shimmy [44, 91], are dependent on the nature of the rolling contact as noted by Le Saux et al. [67]. Often, friction models are non-smooth and in three-dimensions may result in codimension two and even codimension three discontinuity sets [8, 9, 27]. In these cases the form of rolling friction may be particularly important.

1.5 Outline

Chapter 2 discusses the rocking can phenomenon introduced by Srinivasan and Ruina [87]. We reduce the equations of motion to a single, second order, nonlinear ODE describing the inclination of the can. A rigorous matched asymptotic description of the motion is given. The outer solution describes the inverted pendulum behaviour of the can as it rocks down. The inner solution contains the angle of turn phenomenon where the can undergoes the impact-like bouncing motion. This description yields expressions for the dynamical variables during the bounce, enabling an exploration of the characteristics of the rocking can phenomenon. These include the direction of the angle of turn, the contact point dynamics and the feasibility of the motion.

In Chapter 3, we present two sets of experiments concerning Euler's disk. In the first experiment, we spin the disk on a number of different materials and extract the data from the footage. We estimate the parameters of the power law, eq. (1.2), from the data and uncover material dependence of the energy exponent. In the second set of experiments, we film the disk from above and the side and discover that the disk continues to rotate *after* falling flat. The experiments are repeated on the concave base-plate. We discuss both experiments and their consequences for the dominant dissipation mechanism.

In Chapter 4 we work towards an explanation for the disk's motion that agrees with the experimental results from Chapter 3 and the literature. We derive the equations of motion subject to both Coulomb friction and unspecified dissipative moments. A review of the commonly used dissipation mechanisms is given and we derive new mechanisms based on a relaxation of the rigid body assumption. Numerical analysis suggests that a variant of contour friction can explain the motion of Euler's disk observed in experiments. However, we do not discount air resistance as a dominant mechanism for flat base-plates. For the concave base-plate, it appears that contour friction is sufficient. We explain the disk's continued rotation after falling flat by a loss of contact and a supportive layer of air. After making contact with the base-plate, Coulomb friction brings the disk to a halt. Analysis of both post-falling flat stages are in agreement with the experimental results for the flat and concave base-plates in Chapter 3.

Finally, concluding remarks are given in Chapter 5.

CHAPTER 2

THE ROCKING CAN

2.1 Introduction

Consider an empty food can, placed on a horizontal, hard surface and balanced about a point on its rim. When the can is released, perhaps with a small push along the centre line (fig. 2.1a), it rocks downwards in the manner of an inverted compound pendulum, pivoting about the contact point. The rocking motion continues until the can is almost flush with the surface, at which point the can appears to bounce and rock back up again. During the bounce the contact point moves rapidly around the rim of the can (fig. 2.1b). However, the can does not rock back up diametrically opposed to the starting direction (fig. 2.1c). In fact the can rises up pointing in one of two directions. Experiments by Srinivasan and Ruina [87] determined that the can rotates either clockwise or anticlockwise, moving through an angle $\Delta\psi$ dubbed the 'angle of turn'. For the specific can studied by Srinivasan and Ruina [87], the experimental angle of turn was found to be approximately $\pm 217°$. These hand-performed experiments produced repeatable estimates for the angle of turn, suggesting that it depends not on the initial conditions imparted by the push, but the physical characteristics of the can. However, the sign of angle of turn *is* determined by the initial conditions and there exists a trajectory separating the clockwise and anticlockwise motions. This singular trajectory ends in an impact where all points on the can's rim contact the plane simultaneously. Differences in initial conditions and small disturbances mean such an impact is not seen in experiments and the can falls either to one side or the other.

In addition to their experiments, Srinivasan and Ruina [87] studied the rocking can problem analytically. Employing small angle approximations and formal assumptions on the dynamics, they computed the angle of turn for a rotationally symmetric rigid body with a circular base. As a precursor to the rocking can problem, Cushman and Duistermaat [33] studied the nearly flat

falling motions of a thin disk and uncovered the bouncing behaviour, along with the angle of turn and its sign. Batista [13] explored the colliding motions of a partially linearised thick disk. Upon integration, collisions with the plane are shown to be dependent upon two constants of integration. Conditions for loss of contact were also determined. However, physical definitions of the integration constant are not given, nor is an analysis of the rocking can phenomenon. Further work by Srinivasan [86] showed that breaking the symmetry of the can with a small off-centre point mass results in chaotic motion.

In this chapter we use asymptotics to study the same rocking can problem introduced by Srinivasan and Ruina [87]. We consider a rotationally symmetric can rolling and spinning on a horizontal plane with coefficient of friction μ. Particular attention is paid to the motion with small angular momenta that give rise to the rocking can phenomenon.

In Section 2.2 we rederive and non-dimensionalise the equations of motion for the can. The subsequent section studies the equations of motion and determines the static equilibria and steady motions along with their stability properties. Section 2.4 details the reduction of the equations of motion from a system of six, first order ODEs to one, singularly perturbed, planar ODE, eq. (2.63).

In Section 2.5 we carry out asymptotic analysis for the reduced equation of motion. Matched asymptotics applied to the singularly perturbed differential equation yields approximate solutions to the rocking can problem. Considering the regular perturbation problem gives the outer solution. The inner solution is found in the region where the outer solution breaks down. In the case of the can, we find that the outer solution describes the slow, pendulum-like motion as the can rocks down. Close to the flat configuration, the inner solution captures the fast bouncing motion. The two solutions evolve on different time-scales that are visible in tabletop experiments. The initial downward pivoting is slow relative to the fast bounce as the can falls almost flat. Such differences in the time scales indicate a slow-fast system, but the equation of motion is in non-standard form [97]. Therefore, traditional techniques from multiple time scale dynamics will struggle, as they require the use of Geometric Singular Perturbation Theory (GSPT) and blowup [64]. By studying the problem with a matched asymptotic approach we gain a uniformly valid approximation for the dynamics and make rigorous the formal assumptions of Srinivasan and Ruina [87].

Section 2.6 contains analysis of some properties of the rocking can phenomenon. We compute the angle of turn and obtain the same expression as Srinivasan and Ruina [87]. Furthermore, we compute the condition for the can to fall clockwise or anticlockwise, extending the work of Cushman and Duistermaat [33] from the thin disk to the can. Numerical simulations with a variety of initial conditions corroborate the condition. Cushman and Duistermaat [33] also explore the shapes traced out by the contact locus as a disk rolls. For the rocking can problem, we find that the contact locus moves in a circle at a variable speed, spending more time in some positions than others. For other initial conditions, a range of behaviours are visible including cusp-like and petaloid patterns.

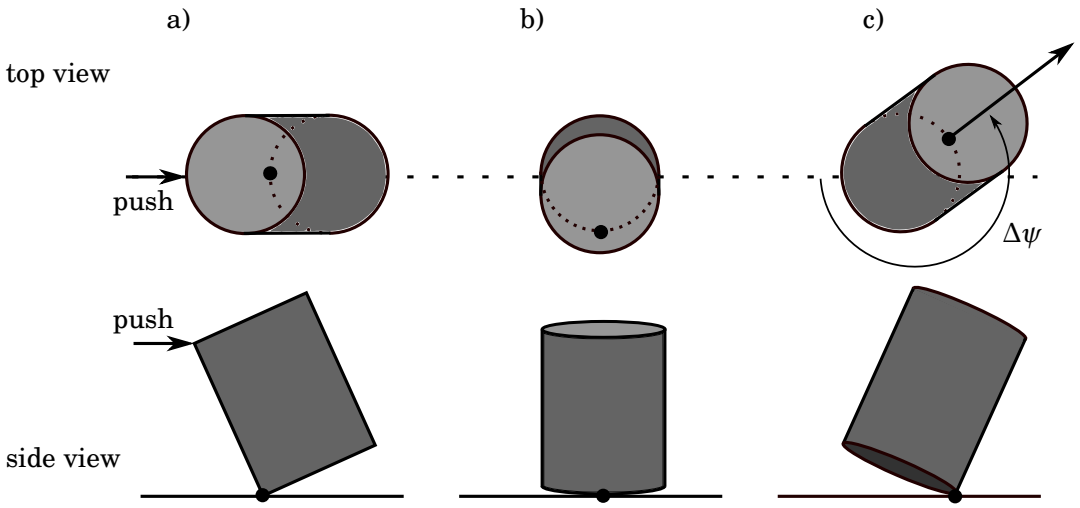

Figure 2.1: The angle of turn phenomenon, repeated from fig. 1.2. a) The can begins tilted about a point on the rim given by the black circle. On release, the can falls down. b) As the can approaches the flat state the contact point rapidly races around the rim of the can. c) The can rises up again, pivoting about the contact point. The contact point has moved through an angle $\Delta\psi$ around the rim of the can.

Finally, we test the feasibility of the angle of turn phenomenon by computing a lower bound for the coefficient of friction. This bound depends only upon the physical characteristics of the can and not the initial conditions. The large angles of turn mentioned by Srinivasan and Ruina [87] require very large coefficients of friction which renders them infeasible. The new analytic results are confirmed with numerical simulations, performed in MATLAB.

2.2 Derivation of the equations of motion

The dynamics of a disk rolling on a horizontal plane have been studied since Appell [10], Korteweg [62] and Vierkandt [95] and perhaps even earlier. More recently, the equations of motion for a can rolling on a rough horizontal plane have been derived by Srinivasan and Ruina [87], Leine [68], Ma et al. [71] and Borisov et al. [17]. Here we establish our notation and rederive equations in the manner of Srinivasan and Ruina [87].

The can, shown in fig. 2.2, is a rigid, rotationally symmetric cylinder with height $2H$, radius R and moment of inertia tensor $\mathrm{I} = \mathrm{diag}(A, A, C)$, where C is the moment of inertia about the symmetry axis and A is the moment of inertia about the non-symmetry axes. The can moves on a rough horizontal plane with a coefficient of Coulomb friction μ, that is assumed large enough to ensure rolling motion (an assumption investigated in Section 2.6). A normal reaction force, $\underline{N}$, and friction force, $\underline{F}$, act at the contact point, $\underline{P}$.

To describe the orientation of the cylinder, we require three reference frames: the global

frame $\mathcal{G}$, the body frame $\mathcal{B}$ and an intermediary frame $\mathcal{I}$. The frames are defined by Euler angles specifying successive rotations. In the global frame, the axes are aligned with the horizontal plane. Rotation by ψ, the *precession* angle, around the $z^{\mathcal{G}}$ axis gives the intermediary frame $\mathcal{I}$. Next, rotation by ϕ, the *nutation* angle, about the $y^{\mathcal{I}}$ axis brings the can into the body frame $\mathcal{B}$. A final rotation θ, the *rotation* angle, about the $z^{\mathcal{B}}$ axis is aligned with the symmetry axis of the cylinder. The rotations are shown in fig. 2.2 and the 3×3 rotation matrices converting frame i to frame j are given by R_{ij}

$$\mathrm{R}_{\mathcal{G}\mathcal{I}} = \begin{pmatrix} \cos\psi & \sin\psi & 0 \\ -\sin\psi & \cos\psi & 0 \\ 0 & 0 & 1 \end{pmatrix}, \quad \mathrm{R}_{\mathcal{I}\mathcal{B}} = \begin{pmatrix} \cos\phi & 0 & \sin\phi \\ 0 & 1 & 0 \\ -\sin\phi & 0 & \cos\phi \end{pmatrix}. \tag{2.1}$$

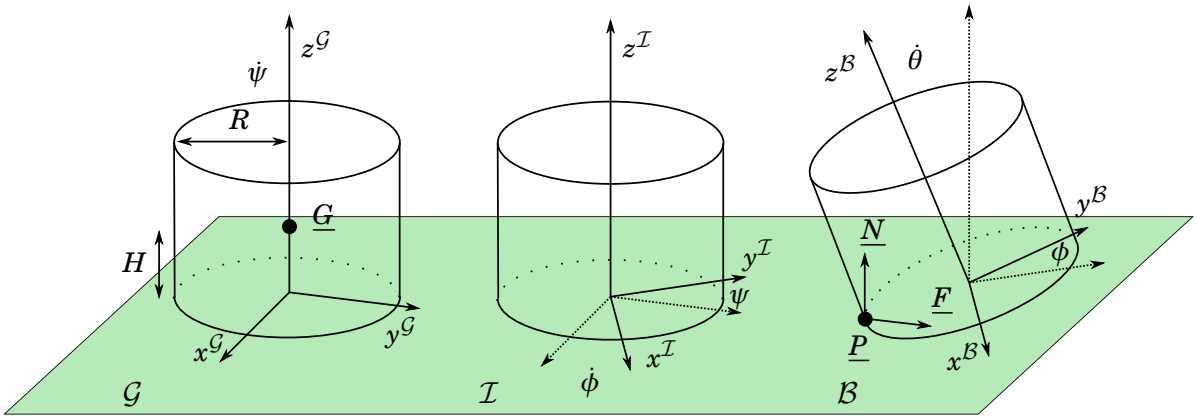

Figure 2.2: Rocking can setup. The three reference frames: the global $\mathcal{G}$, intermediate $\mathcal{I}$ and body frame $\mathcal{B}$, are given by the successive rotations ψ and ϕ.

Applying Newton's second law to the can linearly and rotationally gives the equations of motion

$$m\underline{a}_G^{\mathcal{G}} = -mg\underline{\hat{z}}^{\mathcal{G}} + \underline{N}^{\mathcal{G}} + \underline{F}^{\mathcal{G}}, \tag{2.2}$$

$$\mathrm{I}\dot{\underline{\Omega}}^{\mathcal{B}} + \underline{\omega}^{\mathcal{B}} \times \mathrm{I}\underline{\Omega}^{\mathcal{B}} = \underline{GP}^{\mathcal{B}} \times \mathrm{R}_{\mathcal{G}\mathcal{B}}\left(\underline{N}^{\mathcal{G}} + \underline{F}^{\mathcal{G}}\right), \tag{2.3}$$

where the superscripts indicate the reference frame of the vector. The vector $\underline{\hat{z}}^{\mathcal{G}}$ denotes a unit vector in the $z^{\mathcal{G}}$ axis. Other unit vectors are defined analogously. The vector from the centre of mass, $\underline{G}$, to the contact point, $\underline{P}$, is given by $\underline{GP}^{\mathcal{B}} = (-R, 0, -H)^\intercal$. The acceleration of the centre of mass is $\underline{a}_G = (\ddot{X}_G, \ddot{Y}_G, \ddot{Z}_G)^\intercal$. The angular velocity vector in the body frame is $\underline{\Omega}^{\mathcal{B}} = (\dot{\psi}\sin\phi, -\dot{\phi}, \dot{\psi}\cos\phi + \dot{\theta})^\intercal$ and $\underline{\omega}^{\mathcal{B}} = (\dot{\psi}\sin\phi, -\dot{\phi}, \dot{\psi}\cos\phi)^\intercal$ is the angular velocity of the body frame about the global frame. The linear force balance, eq. (2.2), is expressed in the global frame. The moment balance, eq. (2.3), is expressed in the body frame, because the moment of inertia tensor, I, is aligned with the can's axes.

The rolling without slip constraint provides the necessary information to determine the contact forces $\underline{N}$ and $\underline{F}$. Rolling motion is defined by zero velocity at the contact point, hence

$$\underline{V}_P^{\mathcal{G}} = \underline{V}_G^{\mathcal{G}} + \mathrm{R}_{\mathcal{B}\mathcal{G}}\left(\underline{\Omega}^{\mathcal{B}} \times \underline{GP}^{\mathcal{B}}\right) = \underline{0}, \tag{2.4}$$

where $\underline{V}_P$ and $\underline{V}_G$ are the velocities of the contact point and centre of mass respectively. We compute the components of the velocity of the centre of mass by expanding eq. (2.4)

$$\begin{pmatrix} \dot{X}_G \\ \dot{Y}_G \\ \dot{Z}_G \end{pmatrix}^{\mathcal{G}} = \begin{pmatrix} -\cos\psi(\dot{\phi}(R\sin\phi + H\cos\phi) - \sin\psi(\dot{\psi}(R\cos\phi - H\sin\phi) + R\dot{\theta}) \\ \cos\psi(\dot{\psi}(R\cos\phi - H\sin\phi) + R\dot{\theta}) - \sin(\psi)(\dot{\phi}(R\sin\phi + H\cos\phi)) \\ \dot{\phi}(R\cos\phi - H\sin\phi) \end{pmatrix}. \tag{2.5}$$

Differentiating the velocities in eq. (2.5) yields the equations of motion for the position of the centre of mass

$$\begin{aligned} \ddot{X}_G =& \left(-(R\sin\phi + H\cos\phi)\ddot{\phi} - (R\cos\phi - H\sin\phi)\left(\dot{\psi}^2 + \dot{\phi}^2\right) - R\dot{\theta}\dot{\psi}\right)\cos\psi \\ &+ \left(-(R\cos\phi - H\sin\phi)\ddot{\psi} - R\ddot{\theta} + 2(R\sin\phi + H\cos\phi)\dot{\phi}\dot{\psi}\right)\sin\psi, \end{aligned} \tag{2.6a}$$

$$\begin{aligned} \ddot{Y}_G =& \left((R\cos\phi - H\sin\phi)\ddot{\psi} + R\ddot{\theta} - 2(R\sin\phi + H\cos\phi)\dot{\phi}\dot{\psi}\right)\cos\psi \\ &+ \left(-(R\sin\phi + H\cos\phi)\ddot{\phi} - (R\cos\phi - H\sin\phi)\left(\dot{\psi}^2 + \dot{\phi}^2\right) - R\dot{\psi}\dot{\theta}\right)\sin\psi, \end{aligned} \tag{2.6b}$$

$$\ddot{Z}_G = \ddot{\phi}(R\cos\phi - H\sin\phi) - \dot{\phi}^2(R\sin\phi + H\cos\phi). \tag{2.6c}$$

Substituting the accelerations into the force balance, eq. (2.2), determines the normal and friction forces

$$\begin{aligned} F_x =& m\left(-(R\sin\phi + H\cos\phi)\ddot{\phi} - (R\cos\phi - H\sin\phi)\left(\dot{\psi}^2 + \dot{\phi}^2\right) - R\dot{\theta}\dot{\psi}\right)\cos\psi \\ &+ m\left(-(R\cos\phi - H\sin\phi)\ddot{\psi} - R\ddot{\theta} + 2(R\sin\phi + H\cos\phi)\dot{\phi}\dot{\psi}\right)\sin\psi, \end{aligned} \tag{2.7a}$$

$$\begin{aligned} F_y =& m\left((R\cos\phi - H\sin\phi)\ddot{\psi} + R\ddot{\theta} - 2(R\sin\phi + H\cos\phi)\dot{\phi}\dot{\psi}\right)\cos\psi \\ &+ m\left(-(R\sin\phi + H\cos\phi)\ddot{\phi} - (R\cos\phi - H\sin\phi)\left(\dot{\psi}^2 + \dot{\phi}^2\right) - R\dot{\psi}\dot{\theta}\right)\sin\psi, \end{aligned} \tag{2.7b}$$

$$N = mg + m\ddot{\phi}(R\cos\phi - H\sin\phi) - m\dot{\phi}^2(R\sin\phi + H\cos\phi), \tag{2.7c}$$

where F_x and F_y are the components of the friction force $\underline{F}$ in the $x^{\mathcal{G}}$ and $y^{\mathcal{G}}$ axes. The scalar normal force, N, is given by $\underline{N} = N\hat{\underline{z}}^{\mathcal{G}}$. Substituting the contact forces into the moment balance, eq. (2.3), determines the unknown torques $\underline{GP}^{\mathcal{B}} \times \mathrm{R}_{\mathcal{G}\mathcal{B}}\left(\underline{N}^{\mathcal{G}} + \underline{F}^{\mathcal{G}}\right)$, and hence the equations of motion for the orientation of the disk [87]

$$\begin{aligned} \left((A + mH^2)\sin\phi - mHR\cos\phi\right)\ddot{\psi} - mHR\ddot{\theta} =& (C - 2A - 2mH^2)\dot{\psi}\dot{\phi}\cos\phi \\ &+ C\dot{\phi}\dot{\theta} - 2mHR\dot{\psi}\dot{\phi}\sin\phi, \end{aligned} \tag{2.8a}$$

$$\begin{aligned} \left(mR^2 + mH^2 + A\right)\ddot{\phi} =& \left((A + mH^2 - C - mR^2)\sin\phi\cos\phi - mRH\cos(2\phi)\right)\dot{\psi}^2 \\ &- mg(R\cos\phi - H\sin\phi) - \left((C + mR^2)\sin\phi + mRH\cos\phi\right)\dot{\theta}\dot{\psi}, \end{aligned} \tag{2.8b}$$

$$\left((C + mR^2)\cos\phi - mRH\sin\phi\right)\ddot{\psi} + (C + mR^2)\ddot{\theta} = C\dot{\psi}\dot{\phi}\sin\phi + 2mR\dot{\psi}\dot{\phi}(R\sin\phi + H\cos\phi). \tag{2.8c}$$

Together, the linear and rotational equations of motion, eqs. (2.6) and (2.8), determine the state of the disk. We rescale the lengths by R and the moments of inertia by mR^2, introducing

$$h = \frac{H}{R}, \quad x = \frac{X_G}{R}, \quad y = \frac{Y_G}{R}, \quad z = \frac{Z_G}{R}, \quad a = \frac{A}{mR^2}, \quad c = \frac{C}{mR^2}. \tag{2.9}$$

The choice of R to non-dimensionalise lengths is made to avoid large quantities when considering thin disks where $0 < H \ll R$. We also scale t by $\sqrt{R/g}$ and overload the notation so that the dot notation means differentiation with respect to the scaled time. We write $\Phi = \dot{\phi}$, $\Psi = \dot{\psi}$ and $\Theta = \dot{\theta}$. Then, the dimensional equations of motion for the centre of mass, eq. (2.6), may be written in non-dimensionalised form

$$\begin{aligned}\ddot{x} =& \big(-(\sin\phi + h\cos\phi)\dot{\Phi} - (\cos\phi - h\sin\phi)\Psi^2 - \Theta\Psi - (\cos\phi - h\sin\phi)\Phi^2\big)\cos\psi \\ &+ \big(-\dot{\Psi}(\cos\phi - h\sin\phi) - \dot{\Theta} + 2(\sin\phi + h\cos\phi)\Phi\Psi\big)\sin\psi,\end{aligned} \tag{2.10a}$$

$$\begin{aligned}\ddot{y} =& \big((\cos\phi - h\sin\phi)\dot{\Psi} + \dot{\Theta} - 2(\sin\phi + h\cos\phi)\Phi\Psi\big)\cos\psi \\ &+ \big(-(\sin\phi + h\cos\phi)\dot{\Phi} - (\cos\phi - h\sin\phi)\dot{\Psi} - \Psi\Theta - (\cos\phi - h\sin\phi)\Phi^2\big)\sin\psi,\end{aligned} \tag{2.10b}$$

$$\ddot{z} = \dot{\Phi}(\cos\phi - h\sin\phi) - \Phi^2(\sin\phi + h\cos\phi). \tag{2.10c}$$

Similarly, we non-dimensionalise the rotational equations of motion, eq. (2.8)

$$\dot{\Psi}\sin\phi = kc_P\Phi\Theta + ((kc_P - 2)\cos\phi - hk\sin\phi)\Phi\Psi, \tag{2.11a}$$

$$\dot{\Theta}\sin\phi = (-kc_P\cos\phi + hk\sin\phi)\Phi\Theta + (-kc_P\cos^2\phi - ka_P\sin^2\phi + hk\sin 2\phi + 2)\Phi\Psi, \tag{2.11b}$$

$$\dot{\Phi}(a_P + 1) = ((a_P - c_P)\sin\phi\cos\phi - h\cos 2\phi)\Psi^2 - (c_P\sin\phi + h\cos\phi)\Theta\Psi + (h\sin\phi - \cos\phi), \tag{2.11c}$$

$$\dot{\phi} = \Phi. \tag{2.11d}$$

where the cyclic equations $\dot{\psi} = \Psi$ and $\dot{\theta} = \Theta$ have been discarded. The variables x, y and z do not appear in the equations of motion, eq. (2.11) and may be solved for separately. The constants

$$a_P = a + h^2, \quad c_P = c + 1, \tag{2.12}$$

are the scaled moments of inertia a and c taken about the contact point $\underline{P}$. We also introduce the quantity

$$k = \frac{c}{a + ca_P}, \tag{2.13}$$

for brevity. Throughout this chapter, we consider an empty food can with mass $m = 0.043\,\mathrm{kg}$, height $H = 5.45 \times 10^{-2}\,\mathrm{m}$, radius $R = 3.7 \times 10^{-2}\,\mathrm{m}$, and moments of inertia $A = 6.97 \times 10^{-5}\,\mathrm{kg\,m^2}$ and $C = 5.89 \times 10^{-5}\,\mathrm{kg\,m^2}$. The moments of inertia are given by the sum of the contributions from the hollow cylinder and the top and bottom faces. The scaled parameters are

$$a = 0.727, \quad c = 0.615, \quad a_P = 2.897, \quad c_P = 1.6156, \quad h = 1.473, \quad k = 0.245. \tag{2.14}$$

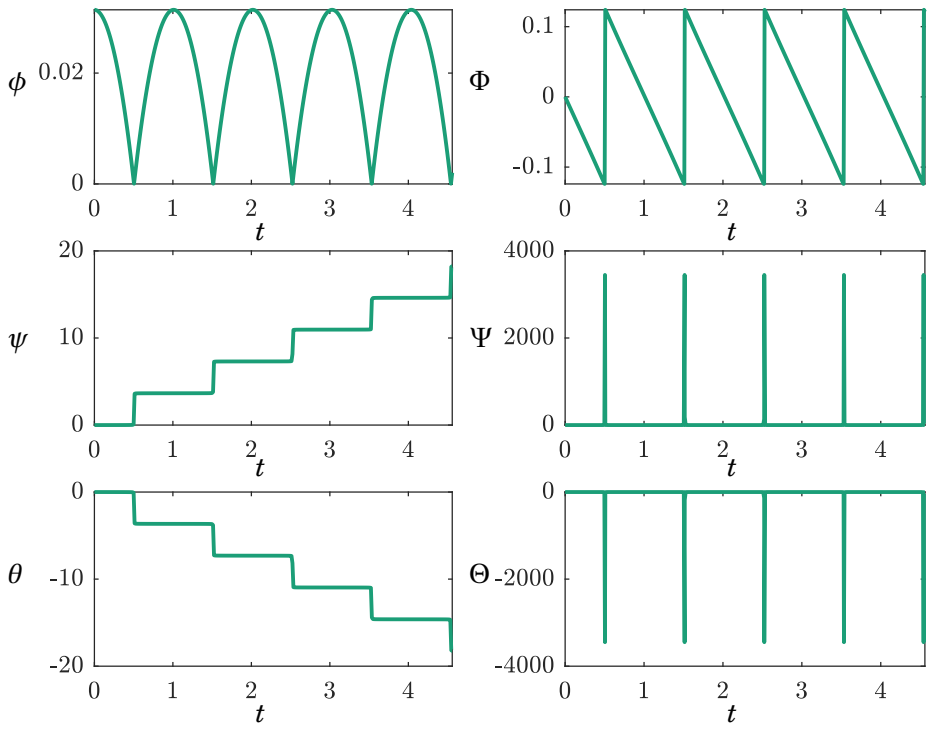

Figure 2.3: Numerical solution of the non-dimensionalised equations of motion, eq. (2.11). Initial conditions and material parameters are given in eqs. (2.14) and (2.15) respectively.

Unless otherwise stated, in this chapter we consider initial conditions that give rise to the rocking can phenomenon

$$(\psi, \dot{\psi}, \phi, \dot{\phi}, \theta, \dot{\theta}) = (0, 0.1001, \pi/100, 0, 0, -0.1000). \tag{2.15}$$

Numerical solutions of eq. (2.11) are shown in fig. 2.3. The numerics were performed in MATLAB using ODE15S to cope with the stiff nature of the ODEs. The nutation angle, ϕ exhibits bouncing behaviour, and the reversal of the angular velocity is visible in the sawtooth profile of the $\dot{\phi}$ plot. Fast changes in the other variables can also be seen at small ϕ. The angle of turn, $|\Delta\psi|$, is the size of the step-like change in ψ, here observed to be 209°. These step changes give rise to the large spikes in the angular velocities, Ψ and Θ. The abrupt, almost discontinuous changes are indicative of slow-fast dynamics, which we study via matched asymptotics in Section 2.5. In the next section, we examine the equilibria and steady motions of eq. (2.11).

2.3 Equilibria and steady motions

In this section, we locate the equilibria and steady motions of eq. (2.11) and determine their stability. Physically, we expect an equilibrium S_{static} of eq. (2.11) when the can is balanced on its

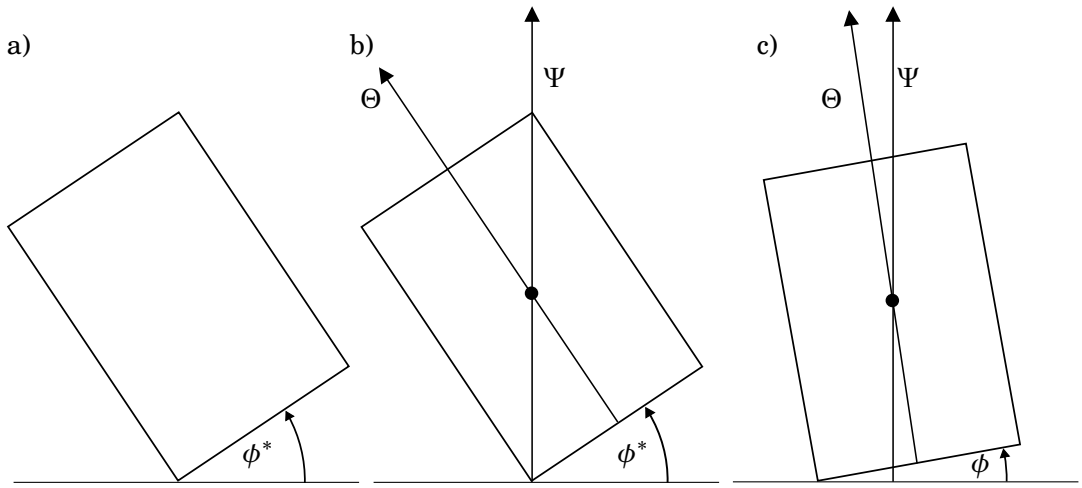

Figure 2.4: Side view of the different steady motions. a) In S_{static} the can is static and balanced on its rim at $\phi^* = \arctan(1/h)$. b) The can is balanced on its rim, but rolling with Θ and Ψ given by S_{bal} eq. (2.20). c) The can is inclined at a constant angle ϕ and rolling with Θ and Ψ given by S_{steady} eq. (2.23).

rim and stationary

$$S_{\text{static}} = \left\{(\Psi, \Theta, \Phi, \phi) = (0,0,0,\phi^*)\right\}, \tag{2.16}$$

where $\phi^* = \arctan(1/h)$. All the angular velocities are zero and the can is tilted at the balancing angle as in fig. 2.4a. The Jacobian, evaluated on this equilibrium, has one positive, one negative and two zero eigenvalues, indicating that S_{static} is a non-hyperbolic saddle. This is to be expected; when balanced, the can shares similarities with a planar inverted compound pendulum. Note that ψ and θ, the cyclic variables, may take any value. S_{static} is the only static equilibrium of the system.

In fact, we may use the static equilibrium to explore the system further. Setting $\Psi = \Theta = 0$, yields an integrable subsystem of eq. (2.11), where the can is not spinning or rolling, but only pivoting about its rim

$$\ddot{\phi} = \frac{h\sin\phi - \cos\phi}{a_P + 1}, \tag{2.17}$$

which exactly describes the dynamics of a planar inverted compound pendulum. Making the transformations

$$\tau = \sqrt{\frac{h^2+1}{a_P+1}}\,t, \quad \phi = x + \arctan(1/h), \tag{2.18}$$

gives the ODE, $\ddot{x} = \sin(x)$. The solution is [98]

$$x = \pm \int (-2\cos\tau + C_1)^{-1/2} \mathrm{d}\tau + C_2, \tag{2.19}$$

with integration constants C_1 and C_2. The solution passes straight through $\phi = 0$, and the can impacts the plane at all points on its rim simultaneously. The rocking can phenomenon in fig. 2.3 is not observed if $\Psi = \Theta = 0$, indicating that the problem is singularly perturbed.

S_{bal} is the set of all steady motions with the can balanced at $\phi = \phi^*$ (as in fig. 2.4 b)

$$S_{\text{static}} \subset S_{\text{bal}} = \left\{(\Psi, \Theta, \Phi, \phi) = (\Psi, \Theta, 0, \phi^*)\right\}, \tag{2.20}$$

where it is required that $\Psi \sin\phi^* \left((a-c)\cos\phi^* \Psi - c\Theta\right) = 0$ from eq. (2.11c). If $\Psi = 0$, then the steady motion corresponds to the can rolling in a straight line. S_{bal} has two non-zero eigenvalues, which may be real or imaginary,

$$\lambda_{12} = \pm\sqrt{\frac{\sqrt{h^2+1} - \Theta^2 c_P h k (h + c_P)}{a_P + 1}}, \tag{2.21}$$

and two zero eigenvalues. Setting $\Theta = 0$ in eq. (2.21) recovers the eigenvalues for the static equilibrium, eq. (2.16). We see that for

$$\Theta^2 > \Theta_c^2 = \frac{\sqrt{h^2+1}}{h k c_P (h + c_P)}, \tag{2.22}$$

the steady motion S_{bal}, is centre-like and otherwise it is saddle-like. Therefore, there is a critical rolling speed Θ_c, faster than which the rolling motion will persist. For a thin disk, the critical rolling speed has been explored by Przybylska and Rauch-Wojciechowski [81], Paris and Zhang [79] and O'Reilly [76]. Non-zero Ψ in S_{bal} gives a 1-D manifold of spinning and rolling solutions with $\Theta = (a-c)\cos\phi^* \Psi / c$. Steady rolling motions also occurs for angles of ϕ other than the balancing angle ϕ^*. Requiring only that $\Phi = 0$, we obtain the set of all steady motions

$$S_{\text{bal}} \subset S_{\text{steady}} = \left\{(\Psi, \Theta, \Phi, \phi) = (\Psi, \Theta, 0, \phi)\right\}, \tag{2.23}$$

where

$$((a_P - c_P)\sin\phi\cos\phi - h\cos 2\phi)\Psi^2 - (c_P \sin\phi + h\cos\phi)\Theta\Psi + (h\sin\phi - \cos\phi) = 0. \tag{2.24}$$

The set, S_{steady}, shown in fig. 2.4c, is a 2-D manifold comprising all possible steady motions. In addition to steady motions at small ϕ, there exist equilibria for $\phi > \phi^*$ where the can is 'overbalanced'. These equilibria are central to the 'mysterious spinning cylinder' explored by Jackson et al. [57], which consists of a slender cylinder undergoing a steady motion close to $\phi \approx \pi/2$. Upon spinning, symbols drawn on the cylinder disappear or appear to remain stationary depending on their position. An example of an overbalanced steady motion is obtained by setting $\phi = \pi/2$, $\Psi = \Theta = \pm\sqrt{h/(c_P - h)}$.

The can rolls in a circle for all steady motions, S_{steady}. The x and y velocities of the centre of mass are given in unscaled form in eq. (2.5). Applying the scalings from eq. (2.9), we obtain

$$\dot{x} = -(\Phi(\sin\phi + h\cos\phi)\cos\psi - (\Psi(\cos\phi - h\sin\phi) + \Theta)\sin\psi, \tag{2.25a}$$

$$\dot{y} = (\Psi(\cos\phi - h\sin\phi) + \Theta)\cos\psi - (\Phi(\sin\phi + h\cos\phi))\sin\psi. \tag{2.25b}$$

On S_{steady} the nutation angle ϕ and the angular velocities Ψ and Θ are constant. Therefore, $\Phi = \frac{\mathrm{d}\Psi}{\mathrm{d}t} = \frac{\mathrm{d}\Theta}{\mathrm{d}t} = 0$ and we integrate for the position of the centre of mass

$$x(t) = \frac{\Psi(\cos\phi - h\sin\phi) + \Theta}{\Psi}\cos(\Psi t), \tag{2.26a}$$

$$y(t) = \frac{\Psi(\cos\phi - h\sin\phi) + \Theta}{\Psi}\sin(\Psi t), \tag{2.26b}$$

showing circular motion with radius

$$r_{\text{circ}} = \left|\frac{\Psi(\cos\phi - h\sin\phi) + \Theta}{\Psi}\right|. \tag{2.27}$$

If $\Psi(\cos\phi - h\sin\phi) + \Theta = 0$, then the centre of mass does not move. Steady motions with the centre of mass at rest are called 'stationary motions'. A can undergoing stationary motion experiences no friction force. Therefore, this particular steady motion is shared with the frictionless can. Requiring that $r_{\text{circ}} = 0$ in S_{steady}, eq. (2.23), gives the 1-D set of frictionless orbits

$$S_{\text{rest}} = \left\{(\Psi, \Theta, \Phi, \phi) = (\Psi, \Theta, 0, \phi)\right\}, \tag{2.28}$$

where

$$\Psi^2 = \frac{\cos\phi - h\sin\phi}{a\sin\phi\cos\phi + ch\sin^2\phi}, \quad \Theta = -\Psi(\cos\phi - h\sin\phi). \tag{2.29}$$

The set S_{rest} only exists for $\phi < \phi^*$. Stationary motion is discussed by McDonald and McDonald [73] and Le Saux et al. [67] and has consequences for the analysis of Euler's disk in Chapter 4. In the next section, we reduce the equations of motion, eq. (2.11), to a single second order ODE, eq. (2.63).

2.4 Reduction of the equations of motion

There is additional structure that can be exploited in the equations of motion, eq. (2.11). Take the equations of motion for Θ and Ψ, eqs. (2.11a) and (2.11b), divide by $\Phi = \frac{\mathrm{d}\phi}{\mathrm{d}t}$ and then apply the chain rule

$$\frac{\mathrm{d}\Psi}{\mathrm{d}\phi}\sin\phi = kc_P\Theta + \left((kc_P - 2)\cos\phi - hk\sin\phi\right)\Psi, \tag{2.30a}$$

$$\frac{\mathrm{d}\Theta}{\mathrm{d}\phi}\sin\phi = (-kc_P\cos\phi + hk\sin\phi)\Theta + (-kc_P\cos^2\phi - ka_P\sin^2\phi + hk\sin 2\phi + 2)\Psi. \tag{2.30b}$$

Equation (2.30) is a closed subsystem of eq. (2.11), so integration will yield conserved quantities which may be used to reduce the number of variables. To solve eq. (2.30) we firstly, differentiate eq. (2.30a) with respect to ϕ

$$\Psi'' = \frac{kc_P\Theta'}{\sin\phi} - \frac{kc_P\Theta\cot\phi}{\sin\phi} - \left(\frac{kc_P - 2}{\sin^2\phi}\right)\Psi + ((kc_P - 2)\cot\phi - hk)\Psi', \tag{2.31}$$

where $[]'$ indicates differentiation with respect to ϕ. We eliminate Θ' using eq. (2.30b) and rearrange eq. (2.30a) to eliminate Θ, leaving

$$\Psi'' + 3\cot\phi\Psi' - (2 + k + kh\cot\phi)\Psi = 0, \tag{2.32}$$

a regular, singular ODE, also derived by Batista [12, (6)] with different notation. A solution exists, in terms of hypergeometric functions

$$\begin{aligned}\Psi(\phi) = &\frac{C_1}{\sin(\phi)^{3/2}}(\cot(\phi)+i)^{-\sqrt{\bar{\rho}}}(\cot(\phi)-i)^{\sqrt{\rho}}\times \\ &{}_2F_1\left(\sqrt{\rho}-\frac{1}{2}-\sqrt{\bar{\rho}},\sqrt{\rho}+\frac{3}{2}-\sqrt{\bar{\rho}};1-2\sqrt{\bar{\rho}},\frac{1}{2}-\frac{i}{2}\cot\phi\right) \\ &+\frac{C_2}{\sin(\phi)^{3/2}}(\cot(\phi)+i)^{\sqrt{\bar{\rho}}}(\cot(\phi)-i)^{\sqrt{\rho}}\times \\ &{}_2F_1\left(\sqrt{\rho}+\frac{3}{2}+\sqrt{\bar{\rho}},\sqrt{\rho}-\frac{1}{2}+\sqrt{\bar{\rho}};1+2\sqrt{\bar{\rho}},\frac{1}{2}-\frac{i}{2}\cot\phi\right).\end{aligned} \tag{2.33}$$

where $\rho = \frac{1}{16}(9+4(2+k)+4ikh)$, $\bar{\rho}$ is the complex conjugate and ${}_2F_1$ is the hypergeometric function. The presence of $\sin(\phi)^{-3/2}$ suggests a singular dependence of Ψ on ϕ. It is known that 'Numerical evaluation of the Gauss hypergeometric function... is notoriously difficult' [35], especially for complex arguments. We evaluate the solution, eq. (2.33), using MATLAB's implementation HYPERGEOM. This analytic solution is shown alongside the numerical solution to the full equations of motion, eq. (2.11). A strong dependence of Ψ on $1/\phi^2$ is observed in both solutions. However, eq. (2.33) is not very informative, so we turn to other solution methods. For our can, the maximum angle attained is the balancing angle $\phi^* = \arctan(1/h) \approx 34°$. Furthermore, the rocking can phenomenon occurs when ϕ is at a minimum. Therefore ϕ is assumed to be small and we solve eq. (2.32) with a Frobenius series.

2.4.1 Frobenius series solution

For brevity, we define $\gamma = 2 + k$ and $\beta = kh$ and the subsystem, eq. (2.32), becomes

$$\Psi'' + 3\cot\phi\Psi' - (\gamma + \beta\cot\phi)\Psi = 0. \tag{2.34}$$

The singular point at $\phi = 0$ is regular as both $\phi(3\cot\phi)$ and $\phi^2(\gamma+\beta\cot\phi)$ have valid Taylor series expansions. We assume a Frobenius series solution at $\phi = 0$

$$\Psi(\phi) = \sum_{n=0}^{\infty} p_n \phi^{n+r}, \tag{2.35}$$

for $n \in \mathbb{N}$. Differentiating the series, eq. (2.35), and substituting into eq. (2.34) gives

$$\sum p_n(n+r)(n+r-1)\phi^{n+r-2} + 3\cot\phi\sum p_n(n+r)\phi^{n+r-1} - (\gamma+\beta\cot\phi)\sum p_n\phi^{n+r} = 0, \tag{2.36}$$

where the series expansion of $\cot\phi$ is given by

$$\cot\phi = \phi^{-1} - \frac{\phi}{3} - \frac{\phi^3}{45} + \mathcal{O}\left(\phi^5\right). \tag{2.37}$$

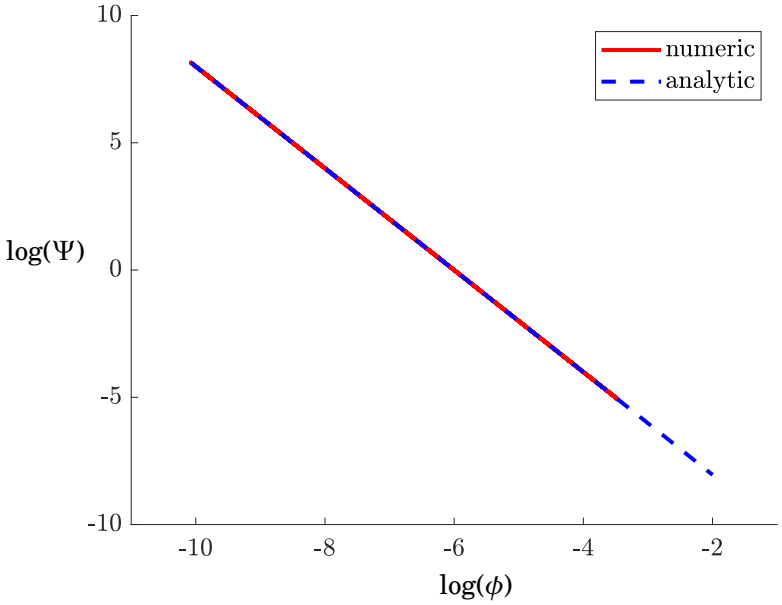

Figure 2.5: Comparison of numerical solutions to the equations of motion eq. (2.11), and the analytic solution of the integrable subsystem, eq. (2.33). The solutions agree and show a clear $\Psi \propto 1/\phi^2$ dependency. Initial conditions and material parameters are given in eqs. (2.14) and (2.15) respectively. The Ψ' initial condition is computed from eq. (2.30a).

To obtain the indicial equation, we match the leading order terms $\mathcal{O}\left(\phi^{r-2}\right)$, in eq. (2.36), given by $n = 0$

$$p_0 r(r-1) + 3p_0 r = 0. \tag{2.38}$$

To obtain a non-trivial solution we require $p_0 \neq 0$. Therefore $r_1 = 0$ and $r_2 = -2$ and two series solutions exist for eq. (2.34), one for each root. As r_1 and r_2 differ by an integer we expect the presence of log terms in the r_2 solution. Beginning with $r_1 = 0$, we suppose a solution

$$\Psi_0(\phi) = \sum_{n=0}^{\infty} p_n \phi^n. \tag{2.39}$$

which upon substitution into eq. (2.34) yields

$$\sum p_n n(n-1)\phi^{n-2} + 3\cot\phi \sum p_n n \phi^{n-1} - \left(\gamma + \beta\cot\phi\right)\sum p_n \phi^n = 0. \tag{2.40}$$

Equating the orders determines the coefficients, p_n, of the series

$$\begin{aligned} \phi^{-2}: &\qquad 0 = 0, \\ \phi^{-1}: &\qquad p_1 = \frac{p_0\beta}{3}, \\ \phi^{0}: &\qquad p_2 = p_0\frac{\beta^2 + 3\gamma}{24}, \\ \phi^{1}: &\qquad p_3 = \frac{\beta p_0(\beta^2 + 11\gamma)}{360}. \end{aligned} \tag{2.41}$$

The arbitrary constant p_0 is determined by the initial conditions. The first series solution is

$$\Psi_0(\phi) = p_0\left(1+\frac{\beta}{3}\phi+\frac{\beta^2+3\gamma}{24}\phi^2+\frac{\beta(\beta^2+11\gamma)}{360}\phi^3\right)+\mathcal{O}\left(\phi^4\right), \tag{2.42}$$

where higher order terms in the expansion may be computed if desired. The second series solution for $r_2 = -2$ has the form

$$\Psi_2(\phi) = D\Psi_1(\phi)\log(\phi)+\sum_{n=0}^{\infty} q_n\phi^{n-2} \tag{2.43}$$

where D is a constant, determined in the process of equating orders. Both q_0 and q_2 are arbitrary constants: q_2 because it corresponds to multiples of the other solution $\Psi_0(\phi)$ and q_0 because it is determined by the initial conditions. Inserting the series eq. (2.43). into eq. (2.34) gives

$$\begin{aligned}&\left[D\Psi_0''\log\phi+\frac{2D\Psi_0'}{\phi}-\frac{D\Psi_0}{\phi^2}+\sum q_n(n-2)(n-3)\phi^{n-4}\right]\\&+3\cot\phi\left[D\Psi'\log\phi+\frac{D\Psi_0}{\phi}+\sum q_n(n-2)\phi^{n-3}\right]+(\gamma+\beta\cot\phi)\left[D\Psi_0\log\phi+\sum q_n\phi^{n-2}\right]=0.\end{aligned} \tag{2.44}$$

We discard all the $\log\phi$ terms as they satisfy the original ODE eq. (2.34), leaving

$$\begin{aligned}&\left[\frac{2D\Psi_0'}{\phi}-\frac{D\Psi_0}{\phi^2}+\sum q_n(n-2)(n-3)\phi^{n-4}\right]\\&+3\cot\phi\left[\frac{D\Psi_0}{\phi}+\sum q_n(n-2)\phi^{n-3}\right]-(\gamma+\beta\cot\phi)\left[\sum q_n\phi^{n-2}\right]=0.\end{aligned} \tag{2.45}$$

Expanding and equating orders determines the coefficients, q_n of the series solution

$$\begin{aligned}\phi^{-4}:&\quad 0=0,\\ \phi^{-3}:&\quad q_1=-\beta q_0,\\ \phi^{-2}:&\quad (\beta^2-\gamma+2)q_0+2Dp_0=0,\\ \phi^{-1}:&\quad (-\gamma+1)q_1+\frac{\beta}{3}(q_0-3q_2)+4Dp_1+3q_3=0.\end{aligned} \tag{2.46}$$

The first order is trivial, because r_2 satisfies the indicial equation. The second order gives q_1. The third order gives D, the coefficient of the log term. At the fourth expansion, we obtain q_3 in terms of known coefficients and similarly for higher orders. Setting the arbitrary constant $q_2 = 0$, we construct the second solution

$$\Psi_2(\phi) = \frac{-q_0(\beta^2-\gamma+2)}{2p_0}\Psi_0(\phi)\log\phi+q_0\left(\frac{1}{\phi^2}-\frac{\beta}{\phi}-\frac{1}{9}\beta\left(-2\beta^2+5\gamma-6\right)\phi\right)+\mathcal{O}\left(\phi^2\right). \tag{2.47}$$

Again, higher order terms may be computed if desired. The general solution to eq. (2.34) is given by a linear combination of the two solutions $\Psi_0(\phi)$ and $\Psi_2(\phi)$

$$\Psi(\phi) = B_0\Psi_0(\phi)+B_{-2}\Psi_2(\phi), \tag{2.48}$$

where we have replaced p_0 and q_0 with B_0 and B_{-2}. We truncate the solution eq. (2.48) to order $\mathcal{O}\left(\phi^2\right)$ and replace the original parameters $\beta = kh$ and $\gamma = 2+k$

$$\begin{aligned}\Psi(\phi) =& B_0\left(1+\frac{kh}{3}\phi\right) - \frac{B_{-2}((kh)^2-k)}{2}\left(1+\frac{kh}{3}\phi+\frac{(kh)^2+6+3k}{24}\phi^2\right)\log\phi \\ &+ B_{-2}\left(\frac{1}{\phi^2}-\frac{kh}{\phi}-\frac{1}{9}kh\left(-2(kh)^2+4+5k\right)\phi\right)+\mathcal{O}\left(\phi^2\right).\end{aligned} \tag{2.49}$$

As predicted by the analytic solution shown in fig. 2.5, Ψ has a ϕ^{-2} dependence at leading order. In the next subsection we compute the analogous series solution for Θ.

2.4.2 Computing the series solution for Θ

With a series solution for $\Psi(\phi)$ in eq. (2.49), we recall that Θ and Ψ are related through eq. (2.30a). Therefore, we compute the series solution for $\Theta(\phi)$ by rearranging eq. (2.30a)

$$\Theta = \frac{\sin\phi}{kc_P}\left(\Psi' - ((kc_P-2)\cot\phi - hk)\Psi\right). \tag{2.50}$$

Then we insert the solution for $\Psi(\phi)$, eq. (2.49), and its derivative $\Psi'(\phi)$. We expand the trigonometric functions and keep terms up to but not including $\mathcal{O}\left(\phi\right)$.

$$\begin{aligned}\Theta(\phi) =& -\frac{B_{-2}}{\phi^2}+\frac{B_{-2}kh}{\phi}+\frac{-9B_{-2}h^2k^2+((4c_P+3)B_{-2}-6B_0c_P)k+12B_0-4B_{-2}}{6kc_P} \\ &+ B_{-2}\frac{h^2k-1}{2c_P}\left((c_Pk-2)+\frac{kh(c_Pk-6)}{3}\phi\right)\log\phi+\mathcal{O}\left(\phi\right).\end{aligned} \tag{2.51}$$

Discarding $\mathcal{O}\left(\phi^2\log\phi\right)$ terms in eq. (2.49), the series solutions for Ψ and Θ read

$$\Theta(\phi) = \frac{-B_{-2}}{\phi^2}+\frac{B_{-2}kh}{\phi}+\Theta_{00}+(\Theta_{l0}+\Theta_{l1}\phi)\log\phi, \tag{2.52a}$$

$$\Psi(\phi) = \frac{B_{-2}}{\phi^2}+\frac{-B_{-2}kh}{\phi}+\Psi_{00}+(\Psi_{l0}+\Psi_{l1}\phi)\log\phi \tag{2.52b}$$

For the first two orders, the two expansions are equal, but have opposite sign, suggesting $\Theta+\Psi=\mathcal{O}(1)$. The unspecified coefficients Θ_{00}, Θ_{l0}, Θ_{l1}, Ψ_{00}, Ψ_{l0} and Ψ_{l1} in eq. (2.52) are given in Section A.1. Equation (2.52) represents an improvement on the formal relations found by Srinivasan and Ruina [87, (7) and (9)] as both $\Psi(\phi)$ and $\Theta(\phi)$ may be expanded to arbitrary orders of ϕ. In section 2.4.4, we use eq. (2.52) to eliminate $\Psi(\phi)$ and $\Theta(\phi)$ from the equations of motion, eq. (2.11), in favour of the conserved quantities B_0 and B_{-2}. However, B_0 and B_{-2} are determined by the initial conditions, eq. (2.15). In the next subsection, we compute B_0 and B_{-2} in terms of these initial conditions and give physical justification for their existence.

2.4.3 Computing the conserved quantities B_0 and B_{-2}

The two integration constants B_0 and B_{-2} are conserved quantities, which generally have physical meanings in mechanical systems. Furthermore, their values are required for numerical

simulations. To determine B_0 and B_{-2}, we require initial conditions for eq. (2.34). However, the only initial conditions are those supplied to the original rocking can problem: $\Psi_{t=0}$, $\Theta_{t=0}$, $\phi_{t=0}$ and $\Phi_{t=0}$. Therefore, we compute Ψ' in terms of Ψ, Θ and ϕ from eq. (2.30a), assuming small ϕ

$$\Psi' = \frac{kc_P(\Psi+\Theta)-2\Psi}{\phi} - hk\Psi + \frac{kc_P(\Theta-2\Psi)+4\Psi}{6}\phi + \mathcal{O}\left(\phi^3\right). \tag{2.53}$$

The initial condition, $\Psi'_{t=0}$, is given by evaluating eq. (2.53) at $t=0$. Differentiating eq. (2.49) with respect to ϕ we obtain two simultaneous equations for B_0 and B_{-2}

$$\Psi_{t=0} = B_0\Psi_0(\phi_{t=0}) + B_{-2}\Psi_2(\phi_{t=0}), \tag{2.54a}$$

$$\Psi'_{t=0} = B_0\Psi'_0(\phi_{t=0}) + B_{-2}\Psi'_2(\phi_{t=0}). \tag{2.54b}$$

We solve for B_0 and B_{-2} and obtain a series solution in terms of the initial conditions

$$\begin{aligned} B_0 = &\frac{kc_P}{2}(\Theta_{t=0}+\Psi_{t=0}) - \frac{hk^2c_P}{2}(\Theta_{t=0}+\Psi_{t=0})\phi_{t=0}, \\ &- \frac{h^2k^2-k}{4}(kc_P(\Theta_{t=0}+\Psi_{t=0})-2\Psi_{t=0})\phi_{t=0}^2\log(\phi_{t=0}) + \mathcal{O}\left(\phi_{t=0}^2\right) \end{aligned} \tag{2.55}$$

$$B_{-2} = -\frac{kc_P}{2}(\Theta_{t=0}+\Psi_{t=0})\phi_{t=0}^2 + \Psi_{t=0}\phi_{t=0}^2 + \mathcal{O}\left(\phi_{t=0}^3\right). \tag{2.56}$$

As conserved quantities B_0 and B_{-2} should remain constant throughout the motion of the can. In fig. 2.6 we plot the expressions for B_0 and B_{-2} in eqs. (2.55) and (2.56), computed from the numerical solution in fig. 2.3. The values of B_0 and B_{-2} are not conserved exactly, due to the truncation of the series, but the fluctuations are small, justifying the inclusion of an additional order in eq. (2.55). Including more terms in the expansions reduces the fluctuations even further.

For a physical understanding of the meaning of B_0 and B_{-2} eqs. (2.55) and (2.56), compare with the angular momentum about the global z axis, $z^{\mathcal{G}}$, and the body z axis, $z^{\mathcal{B}}$

$$H_z^{\mathcal{B}} = c(\Psi\cos\phi+\Theta) \approx c(\Psi+\Theta) - \frac{c\Psi\phi^2}{2} + \mathcal{O}\left(\phi^4\right), \tag{2.57}$$

$$H_z^{\mathcal{G}} = a\Psi\sin^2\phi + c\cos\phi(\Psi\cos\phi+\Theta) \approx c(\Psi+\Theta) + \left(-\frac{c}{2}(\Psi+\Theta) + \left(a-\frac{c}{2}\right)\Psi\right)\phi^2 + \mathcal{O}\left(\phi^4\right) \tag{2.58}$$

We notice that $B_0 \propto H_z^{\mathcal{B}}$ and $B_{-2} \propto H_z^{\mathcal{B}} - H_z^{\mathcal{G}}$ at leading order, suggesting that they correspond to components of angular momentum. In the frictionless case, the angular momenta $H_z^{\mathcal{B}}$ and $H_z^{\mathcal{G}}$ are conserved exactly and emerge naturally in the Lagrangian formulation of the equations of motion (see Section A.2). To understand why they are conserved, consider fig. 2.7: without friction the only contact force is the normal force $\underline{N}$, acting in the same plane as $z^{\mathcal{B}}$ and $z^{\mathcal{G}}$. Therefore, these components of angular momentum must be conserved in the frictionless case.

Upon including friction, the conserved quantities no longer correspond exactly to the angular momenta, but approximately so. It is possible to offer some insight as to why. In the slipping case, it is clear why $H_z^{\mathcal{B}}$ and $H_z^{\mathcal{G}}$ are conserved: there are no frictional forces providing a moment to affect them. In the rolling case, friction affects the angular momenta, as shown in fig. 2.7.

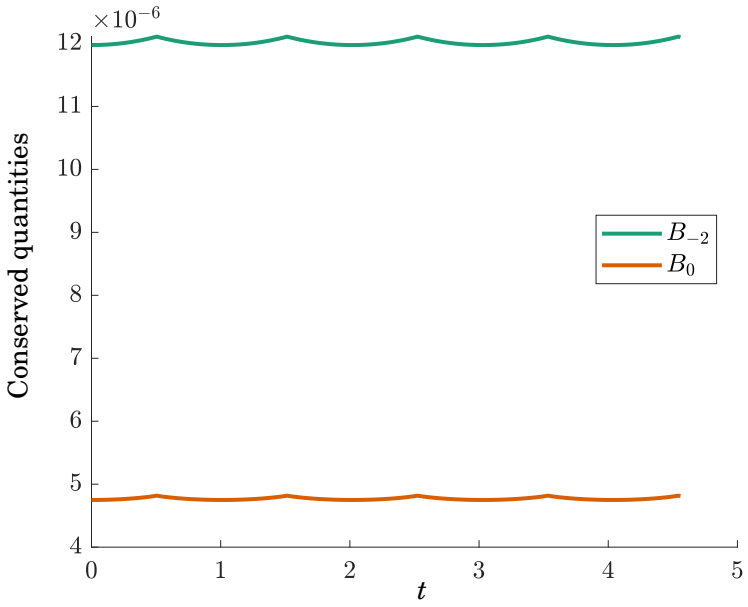

Figure 2.6: The conserved quantities B_0 and B_{-2} computed from the non-dimensionalised equations of motion eq. (2.11). Small oscillations are visible, due to the truncation of eqs. (2.55) and (2.56). Initial conditions and material parameters are given in eqs. (2.14) and (2.15) respectively.

Shifting the friction force into the intermediate frame $\mathcal{I}$, the component $F_x^{\mathcal{I}}$ points in the radial direction. Its line of action intersects with both the cans symmetry axis $z^{\mathcal{B}}$ and the global vertical $z^{\mathcal{G}}$ axis, effecting no change in $H_z^{\mathcal{B}}$ and $H_z^{\mathcal{G}}$. However, the component $F_y^{\mathcal{I}}$ acts in the tangential direction and can affect the angular momentum. It is given by

$$F_y^{\mathcal{I}} = (\mathrm{R}_{\mathcal{G}\mathcal{I}}\underline{F}^{\mathcal{G}})\cdot\underline{\hat{y}}^{\mathcal{I}} = mgk\Phi(a\Psi\sin\phi + ch(\Psi\cos\phi+\Theta)). \tag{2.59}$$

At small ϕ, the size of the tangential friction is proportional to $\Theta+\Psi$, in turn proportional to B_0 at leading order. If B_0 is also small, then the effects of the tangential force on the angular momenta are small and the angular momentum is conserved. We proceed to reduce the equations of motion, eq. (2.11), using the conserved quantities B_0 and B_{-2}.

2.4.4 The reduced equations of motion

We substitute the series solutions for Ψ and Θ, eq. (2.52), into the equation of motion for ϕ, eq. (2.11c), to obtain a single, second order, nonlinear ODE

$$\ddot{\phi} = \frac{a_3}{\phi^3} + \frac{a_{l2}\log\phi}{\phi^2} + \frac{a_2}{\phi^2} + \frac{a_{l1}\log\phi}{\phi} + \frac{a_1}{\phi} + a_{ll}(\log\phi)^2 + a_{l0}\log\phi + a_0 - 1 + \mathcal{O}\left(\phi(\log\phi)\right), \tag{2.60}$$

where the $\cos\phi$ and $\sin\phi$ terms have been replaced by their series expansions. All coefficients a_{ij} are bivariate quadratics in B_0 and B_{-2}, containing only B_0^2, B_{-2}^2 and B_0B_{-2} terms. The coefficients depend on the can's material parameters h, k, a_P and c_P. We have also rescaled time by $\sqrt{a_P+1}$

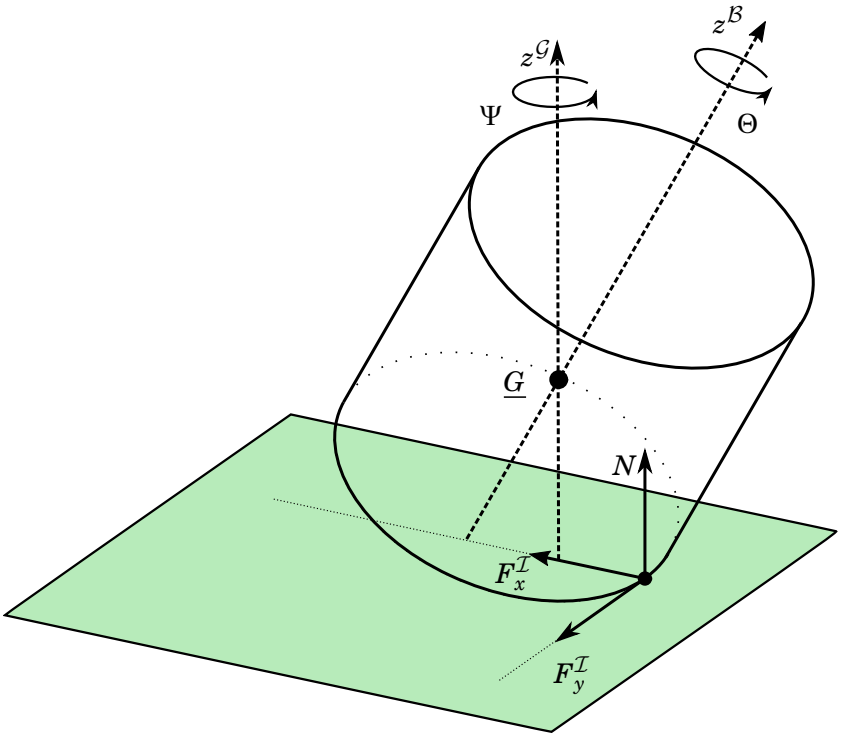

Figure 2.7: The contact forces on the can. The lines of action of both N and $F_x^{\mathcal{I}}$ intersect with the axes $z^{\mathcal{G}}$ and $z^{\mathcal{B}}$ and, therefore, cannot affect the angular momenta about those axes. Only the tangential component of friction $F_y^{\mathcal{I}}$ can affect the angular momenta and this is shown to be small in eq. (2.59).

and overloaded the $\dot{[]}$ notation. The leading order coefficient, $a_3 = B_{-2}^2 a_P$, is positive and higher order coefficients are consigned to Section A.3.

The angle of turn phenomenon occurs when the can is released as in fig. 2.1, with some angular momentum in the $y^{\mathcal{I}}$ direction, but only a small component of angular momentum in the other two axes. This implies that B_0 and B_{-2} are small. Setting $B_0 = B_{-2} = 0$ in eq. (2.60) results in $\ddot{\phi} = -1$, the linearised, scaled, version of the inverted pendulum discussed in eq. (2.17). Instead, let both B_0 and B_{-2} be small and of the same order. Specifically, introduce ϵ, a small parameter such that

$$|B_{-2}| = \epsilon^{1/2}, \tag{2.61}$$

$$B_0 = \zeta \epsilon^{1/2}, \tag{2.62}$$

where $\zeta = \mathcal{O}(1)$ and $0 < \epsilon \ll 1$. Then, upon discarding the $\mathcal{O}\left(\phi \log \phi\right)$ terms we obtain

$$\ddot{\phi} = \epsilon\left(\frac{a_3}{\phi^3} + \frac{a_{l2}\log\phi}{\phi^2} + \frac{a_2}{\phi^2} + \frac{a_{l1}\log\phi}{\phi} + \frac{a_1}{\phi} + a_{ll}(\log\phi)^2 + a_{l0}\log\phi + a_0\right) - 1, \tag{2.63}$$

the governing equation for the remainder of this chapter. We have extracted a factor of ϵ from each a_{ij} and overloaded the notation, such that $a_3 = a_P$. Note that eq. (2.63) is a Hamiltonian

system. In Section A.4, we compute the Hamiltonian and show numerically that there exist closed curves corresponding to periodic orbits.

In figure 2.8, we compare the numerical solutions of the exact equations, eq. (2.11), with the reduced equation obtained using the Frobenius series, eq. (2.63). The initial conditions, eq. (2.15), fix the values of $\epsilon = 1.43 \times 10^{-10}$ and $\zeta = 0.40$. The reduced equation, eq. (2.63), show some drift in the period after the second oscillation. The error arises due to the discarded $\mathcal{O}\left(\phi \log \phi\right)$ terms. The truncation also removes the equilibrium, S_{static}, where the can is balanced on the rim at $\phi = \phi^* = \arctan(1/h)$. Therefore, in eq. (2.63) the can is unable to overturn. These errors are unimportant for the angle of turn phenomenon, which occurs at small $\phi \ll \phi^*$. Small differences in the extremal values of Ψ and Θ are also visible.

Figure 2.9 shows solutions of eq. (2.63) for different values of ϵ. For large ϵ, we see almost sinusoidal oscillations in ϕ and an oval shaped phase portrait. We reconstruct Ψ from the numerical solution using eq. (2.52b), giving a small, smoothed spikes around the minima of ϕ. As we decrease ϵ, the solutions get sharper, the nutation angle ϕ exhibits the bouncing behaviour and ψ shows the step-like increases that correspond to the angle of turn. This behaviour indicates that ϵ mediates the angle of turn phenomenon. The phase portrait shows clearly the repulsion from the singular line $\phi = 0$ due to the ϕ^{-3} term in eq. (2.63).

Equation (2.63) is similar in form to the system $u_{xx} = \frac{\lambda}{(1+u)^2}\left(1 - \frac{\epsilon^2}{(1+u)^2}\right)$ studied by Iuorio et al. [54]. This singularly perturbed boundary-value problem describes the behaviour of a micro-electro-mechanical system or MEMS. Iuorio et al. study the system using geometric singular perturbation theory and blowup to resolve the singularity at $u = -1$. The 'bouncing' or 'touchdown' solutions obtained in their Figure 2 are closely related to ϕ time series in fig. 2.8.

The reduced system, eq. (2.63), also bears similarities to the ODEs studied by Lazer and Solimini [66], and Rojas and Torres [83]. These ODEs are characterised by repulsive singularities and have the form $\ddot{u} - 1/u^{\alpha} = h(t)$. Lazer and Solimini [66] show that such systems have periodic solutions, while Rojas and Torres [83] show that the solutions experience elastic collisions with the singularity. Trajectories approach $u = 0$ zero and then veer away with a sharp change in derivative, as in fig. 2.9.

2.5 Asymptotic analysis

In this section we study the reduced equation of motion, eq. (2.63), using a matched asymptotic expansion [49]. A slow-fast approach is also possible, but the system is in non-standard form [97] and requires more advanced techniques from GSPT and blowup [64].

The small parameter, ϵ, loosely represents an amount of angular momentum in the vertical, $z^{\mathcal{G}}$, and symmetry, $z^{\mathcal{B}}$, directions. When ϵ is small, the rocking can has two obvious regimes: one at large ϕ, where the can acts like a compound pendulum (the outer region), and one at small ϕ, where the bounce occurs (the inner region). Matching the two solutions yields a uniformly valid

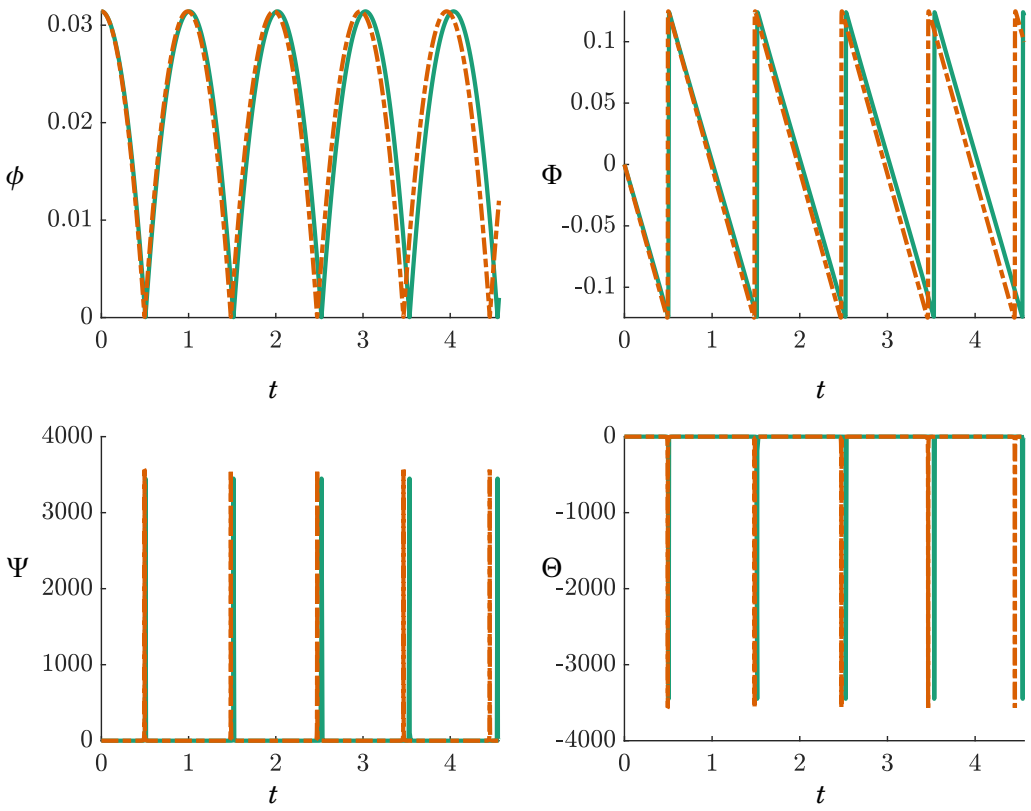

Figure 2.8: Numerical comparison of the exact equations of motion, eq. (2.11), (solid green) and the reduced equation, eq. (2.63), (dashed orange). For fair comparison the additional time scaling $t = \sqrt{a_P + 1}\tau$ in eq. (2.63) is reversed. Initial conditions and material parameters are given in eqs. (2.14) and (2.15) respectively.

solution for one half period of the motion.

2.5.1 The outer solution

The outer problem in a matched asymptotics is given by assuming a regular perturbation. The system is subject to initial conditions, $\phi(0) = I/2$ and $\dot{\phi}(0) = 0$, where the factor of 1/2 simplifies the algebra. These initial conditions are consistent with those in eq. (2.15) for $I = \pi/50$. We propose a regular asymptotic expansion of ϕ in the small parameter ϵ

$$\phi(t) \sim \phi_0(t) + \epsilon\phi_1(t) + \mathcal{O}\left(\epsilon^2\right). \tag{2.64}$$

Upon substitution of the expansion into the reduced equation of motion, eq. (2.63), the leading order problem is given by the $\mathcal{O}(1)$ terms

$$\ddot{\phi}_0 = -1. \tag{2.65}$$

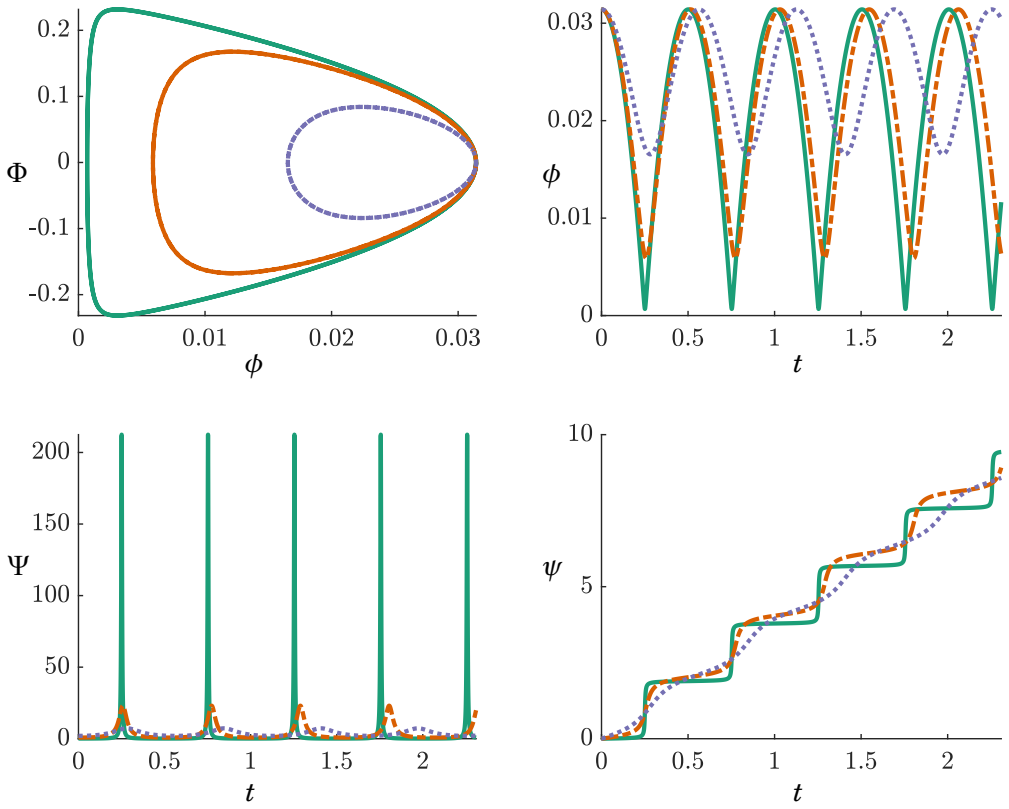

Figure 2.9: Numerical solutions of the reduced equation of motion, eq. (2.63), with $\epsilon = 10^{-8}$ (green solid), 6.4×10^{-7} (orange dashed) and 4×10^{-6} (blue dotted) and $\zeta = 1$. Initial conditions are $(\phi, \Phi) = (\pi/100, 0)$. The material parameters are given in eq. (2.14).

It describes the can falling under a scaled gravity. The solution after applying the initial conditions is

$$\phi_0(t) = \frac{I - t^2}{2}, \tag{2.66}$$

which gives the expected quadratic form. In the absence of angular momentum in the $z^{\mathcal{B}}$ and $z^{\mathcal{G}}$ directions, we expect the disk to fall flat at $t = \sqrt{I} = \sqrt{\phi(0)/2}$.

Balancing the $\mathcal{O}(\epsilon)$ terms yields the next order of approximation

$$\ddot{\phi}_1(t) = \frac{a_3}{\phi_0^3} + \frac{a_{l2}\log\phi_0}{\phi_0^2} + \frac{a_2}{\phi_0^2} + \frac{a_{l1}\log\phi_0}{\phi_0} + \frac{a_1}{\phi_0} + a_{ll}(\log\phi_0)^2 + a_{l0}\log\phi_0 + a_0, \tag{2.67}$$

and substituting in the leading order solution, eq. (2.66), gives the $\mathcal{O}(\epsilon)$ problem for ϕ_1

$$\begin{aligned}\ddot{\phi}_1 = &\frac{8a_3}{(I-t^2)^3} + \frac{4a_{l2}\log\left(\frac{I-t^2}{2}\right)}{(I-t^2)^2} + \frac{4a_2}{(I-t^2)^2} + \frac{2a_{l1}\log\left(\frac{I-t^2}{2}\right)}{I-t^2} + \frac{2a_1}{I-t^2} \\ &+ a_{ll}\log^2\left(\frac{I-t^2}{2}\right) + a_{l0}\log\left(\frac{I-t^2}{2}\right) + a_0,\end{aligned} \tag{2.68}$$

subject to the initial conditions, $\phi_1(0) = \dot{\phi}_1(0) = 0$. The RHS of eq. (2.68) is only a function of t and, therefore, each term may be integrated separately. To simplify the integration, we scale time such that $t = \sqrt{I}\tau$ and then use the properties of logarithms to give

$$\ddot{\phi}_1 = \frac{b_3}{(1-\tau^2)^3} + \frac{b_{l2}\log(1-\tau^2)}{(1-\tau^2)^2} + \frac{b_2}{(1-\tau^2)^2} + \frac{b_{l1}\log(1-\tau^2)}{1-\tau^2} + \frac{b_1}{(1-\tau^2)} + b_{ll}\log^2(1-\tau^2) + b_{l0}\log(1-\tau^2) + b_0, \tag{2.69}$$

where the additional factors have been absorbed into the new coefficients, b_i. The highest order coefficient is $b_3 = 8a_P/I^2$ and the rest are given in Section A.5. The solution to the $\mathcal{O}(\epsilon)$ problem is written

$$\phi_1(\tau) = \sum_{i=0}^{3} b_i J_i(\tau) + \sum_{n=0}^{2} b_{li} J_{li}(\tau) + b_{ll} J_{ll}(\tau), \tag{2.70}$$

where

$$J_i = \int\int \frac{1}{(1-\tau^2)^i} \mathrm{d}\tau\mathrm{d}\tau, \tag{2.71a}$$

$$J_{li} = \int\int \frac{\log(1-\tau^2)}{(1-\tau^2)^i} \mathrm{d}\tau\mathrm{d}\tau, \tag{2.71b}$$

$$J_{ll} = \int\int \log^2(1-\tau^2) \mathrm{d}\tau\mathrm{d}\tau, \tag{2.71c}$$

and each individual integral is evaluated in Section A.6. Many of the integrals involve log terms can be evaluated in terms of the dilogarithm $\mathrm{Li}_2(\tau)$, defined by the power series

$$\mathrm{Li}_2(\tau) = \sum_{n=1}^{\infty} \frac{\tau^n}{n^2}. \tag{2.72}$$

Therefore the entire outer solution up to and including $\mathcal{O}(\epsilon)$ terms is

$$\phi(t) \sim \frac{I-t^2}{2} + \epsilon\left(\sum_{n=0}^{3} b_i J_i\left(\frac{t}{\sqrt{I}}\right) + \sum_{n=0}^{2} b_{li} J_{li}\left(\frac{t}{\sqrt{I}}\right) + b_{ll} J_{ll}\left(\frac{t}{\sqrt{I}}\right)\right) + \mathcal{O}\left(\epsilon^2\right). \tag{2.73}$$

Particularly important is the term J_3, for which the integral is

$$\begin{aligned} J_3 = \int\int \frac{1}{(1-\tau^2)^3} \mathrm{d}\tau\mathrm{d}\tau &= \frac{1}{8(1-\tau^2)} + \frac{3\tau}{8}\operatorname{arctanh}(\tau) \\ &= \frac{I}{8(I-t^2)} + \frac{3t}{8\sqrt{I}}\operatorname{arctanh}\left(\frac{t}{\sqrt{I}}\right). \end{aligned} \tag{2.74}$$

As $t \to \sqrt{I}$, the first term of eq. (2.74) grows larger than the $\mathcal{O}(1)$ solution, $(I-t^2)/2$. Therefore, a change in the dominant balance occurs and the outer solution is not valid as $t \to \sqrt{I}$. As stated in Section 2.3, the problem is singularly perturbed because the regular asymptotic series, eq. (2.64), is not valid over the whole domain. The $\mathcal{O}(1)$ term in the outer solution, eq. (2.73), gives the solution to the problem with no vertical angular momentum and the $\mathcal{O}(\epsilon)$ term gives a small correction. A plot of the outer solution is shown in fig. 2.10, showing the quadratic fall.

2.5.2 The inner solution

The inner solution to a matched asymptotic problem is the solution in the region where the outer solution fails. In this case, the outer solution, eq. (2.73), fails as $t \to \sqrt{I}$. We propose a scaling of the equation of motion, eq. (2.63), such that $\phi = \delta\varphi$ and $t = \eta T + \sqrt{I}$ in the inner region where both η and δ are small quantities. The shift in t centres the inner time, T, on the breakdown of the asymptotic balance. After applying the scalings we obtain

$$\frac{\delta}{\eta^2}\varphi'' = \epsilon\left(\frac{a_P}{\delta^3\varphi^3} + \frac{a_{l2}\log\delta\varphi}{\delta^2\varphi^2} + \frac{a_2}{\delta^2\varphi^2} + \frac{a_{l1}\log\delta\varphi}{\delta\varphi} + \frac{a_1}{\delta\varphi} + a_{ll}(\log\delta\varphi)^2 + a_{l0}\log\delta\varphi + a_0\right) - 1, \tag{2.75}$$

where $[]'$ now denotes differentiation with respect to T. To balance the derivative term and the φ^{-3} term, we require

$$\frac{\delta}{\eta^2} \sim \frac{\epsilon}{\delta^3}. \tag{2.76}$$

To remove the constant term, -1, we require it to be dominated by the φ^{-3} term, necessitating $\frac{\epsilon}{\delta^3} \gg 1$ such that $\delta = o\left(\epsilon^{1/3}\right)$. However, choosing $\delta = \epsilon^{1/3}$ and $\eta = 1$ removes the derivative term from the dominant balance, leaving an algebraic equation. We therefore require the time scaling η, which leads to a set of allowable scalings. To map with the outer region, δ and η should be the same scale, as t and ϕ are both $\mathcal{O}(1)$ in the outer region. Setting $\delta = \eta$ gives $\delta = \eta = \varepsilon^{1/2}$ in the asymptotic balance, eq. (2.76). Therefore, the inner scaling is

$$\phi = \varepsilon^{1/2}\varphi, \quad t = \sqrt{I} + \varepsilon^{1/2}T. \tag{2.77}$$

Applying the scalings to the equation of motion, eq. (2.63), and multiplying through by $\epsilon^{1/2}$ gives the inner problem

$$\begin{aligned}\varphi'' = &\frac{a_3}{\varphi^3} + \epsilon^{1/2}\frac{a_{l2}\log\epsilon^{1/2}\varphi}{\varphi^2} + \epsilon^{1/2}\frac{a_2}{\varphi^2} + \epsilon\frac{a_{l1}\log\epsilon^{1/2}\varphi}{\varphi} + \epsilon\frac{a_1}{\varphi} + \epsilon^{3/2}a_{ll}\left(\log\epsilon^{1/2}\varphi\right)^2 \\ &+ \epsilon^{3/2}a_{l0}\log\epsilon^{1/2}\varphi + \epsilon^{3/2}a_0 - \varepsilon^{1/2},\end{aligned} \tag{2.78}$$

which may now be solved by a regular asymptotic series, $\varphi \sim \varphi_0 + \epsilon^{1/2}\varphi_1 + \mathcal{O}(\epsilon)$. Only the leading order problem is required

$$\varphi_0'' = \frac{a_p}{\varphi_0^3}. \tag{2.79}$$

Equation (2.79) is equivalent to the equation found by Srinivasan and Ruina [87, (13)] in their treatment of the rocking can problem. The solution is

$$\varphi(T) = \sqrt{P^2 + \frac{\left(\sqrt{a_p}T - Q\right)^2}{P^2}} + \mathcal{O}\left(\epsilon^{1/2}\log\epsilon\right), \tag{2.80}$$

where P and Q are integration constants. Both initial conditions have already been used when determining the integration constants for the outer solution. Therefore, P and Q must be determined by matching with the outer solution.

2.5.3 Matching the outer and inner solutions

In the previous subsections we obtained two, approximate, analytic solutions to the equation of motion, eq. (2.63). The outer approximation is valid for $0 < t \ll \sqrt{I}$ and large ϕ and the inner approximation is valid for $0 \ll t < \sqrt{I}$ at small ϕ. In this section we match the two solutions to obtain a uniformly valid solution for one half period of the motion. We appeal to Van Dyke's matching rule [49], which is commonly stated as

$$E_n H_m \phi = H_m E_n \phi, \tag{2.81}$$

where E_n refers to the outer limit of the solution ϕ as $\epsilon \to 0$, while keeping the outer variable ϕ fixed and retaining $n+1$ terms. H_m refers to the inner limit as $\epsilon \to 0$, keeping the inner variable φ fixed and retaining $m+1$ terms. The left side of eq. (2.81) is obtained by computing the inner solution to $m+1$ terms and converting to outer variables. We then take the limit as $\epsilon \to 0$, retaining $n+1$ terms. Repeating the process in reverse gives the right hand side. Requiring both sides to be equal matches the inner and outer solutions and determines the integration constants P and Q.

In eq. (2.80), we have computed the inner solution to one term ($m = 1$). To write the inner solution in outer variables, we apply the reverse transformation to eq. (2.77), $\varphi = \epsilon^{-1/2}\phi$ and $T = \epsilon^{-1/2}(t - \sqrt{I})$

$$\phi \sim \epsilon^{1/2} \sqrt{P^2 + \frac{\left(\epsilon^{-1/2}\sqrt{a_p}(\tau_2 - \sqrt{I}) - Q\right)^2}{P^2}}. \tag{2.82}$$

Expanding, taking the limit as $\epsilon \to 0$ and retaining two terms ($n = 2$) gives the LHS of Van Dyke's matching rule

$$E_2 H_1 \phi = \frac{\sqrt{a_p}(\sqrt{I} - t)}{P} + \varepsilon^{1/2}\frac{Q}{P} + \mathcal{O}(\epsilon). \tag{2.83}$$

Two terms of the inner solution written in the outer variables are required for both matching constants P and Q to appear.

We computed the outer solution, eq. (2.73), to two terms. Writing the outer solution in inner variables using eq. (2.77), then expanding it to a single order gives

$$H_1 E_2 \varphi = -\sqrt{I}T - \frac{a_P}{2I^{5/2}T} + \mathcal{O}\left(\epsilon^{1/2}\log\epsilon\right), \tag{2.84}$$

where the first term $-\sqrt{I}T$ arises due to the leading order approximation ϕ_0 and the second term arises due to the J_3 term. When written in equivalent variables the left and right hand sides of eq. (2.81), eqs. (2.83) and (2.84), should match. Writing eq. (2.84) in outer variables and equating with eq. (2.83) gives

$$E_2 H_1 \phi = \frac{\sqrt{a_p}(\sqrt{I} - t)}{P} + \epsilon^{1/2}\frac{Q}{P} = -\sqrt{I}(t - \sqrt{I}) - \epsilon\frac{a_p}{2I^{5/2}(t - \sqrt{I})} = H_1 E_2 \phi. \tag{2.85}$$

Matching orders of ϵ determines P and Q

$$P = \sqrt{\frac{a_P}{I}}, \quad Q = 0. \tag{2.86}$$

Therefore the one term, matched inner solution is

$$\varphi = \sqrt{\frac{a_p}{I} + IT^2}. \tag{2.87}$$

To construct a uniformly valid solution for $0 < t < \sqrt{I}$, we add the inner and outer solutions and subtract the common form in the overlap. The common form is $-\sqrt{I}(\sqrt{I} - t)$, given by inserting the values of P and Q into eq. (2.85). The uniformly valid solution to the governing equation eq. (2.63) is

$$\begin{aligned} \phi \sim & \frac{I - t^2}{2} + \epsilon^{1/2}\sqrt{\frac{a_p}{I} + I\epsilon^{-1}(t - \sqrt{I})^2} + \sqrt{I}(t - \sqrt{I}) \\ = & -\frac{\left(\sqrt{I} - t\right)^2}{2} + \sqrt{\frac{\epsilon a_p}{I} + I(t - \sqrt{I})^2}. \end{aligned} \tag{2.88}$$

The inner, outer and matched solutions are shown in fig. 2.10 for the standard initial conditions eq. (2.15). It can be seen that the outer solution has a quadratic form and passes straight through $\phi = 0$. The inner solution is backwards asymptotic to $\phi = \sqrt{I}(t - \sqrt{I})$, but as the solution approaches $t = \sqrt{I}$ the trajectory veers away from $\phi = 0$.

The uniformly valid solution fails after $t = \sqrt{I}$. However, the governing equation eq. (2.63), is a periodic, time reversible ODE, so, if required, a solution for all time may be constructed by reflecting and repeating the matched solution, eq. (2.88).

2.5.4 Reconstructing the state variables

In the previous section we obtained a matched solution to the rocking can problem. We now reconstruct the remaining state variables in the inner region where the bounce takes place.

Recall the series solution for $\Psi(\phi)$, eq. (2.52b). We compute the inner solution for Ψ by shifting to the inner variables, eq. (2.77). The time scaling, $t = \sqrt{a_P + 1}T$, from eq. (2.60) must also be applied

$$\frac{1}{\sqrt{a_P + 1}}\frac{\mathrm{d}\psi}{\mathrm{d}T} = \frac{\operatorname{sign}(B_{-2})}{\varphi^2} - \frac{\epsilon^{1/2}\operatorname{sign}(B_{-2})kh}{\varphi} + \mathcal{O}(\log\epsilon), \tag{2.89}$$

To obtain $\frac{\mathrm{d}\psi}{\mathrm{d}T}$ as a function of the inner time T, we insert the inner solution, eq. (2.80), and take the leading order term in ϵ. It is not possible to retain any higher order terms because eq. (2.80) only includes terms of $\mathcal{O}(1)$

$$\frac{\mathrm{d}\psi}{\mathrm{d}T} = \frac{\sqrt{a_P + 1}\operatorname{sign}(B_{-2})}{\left(\frac{a_3}{I} + IT^2\right)} \tag{2.90}$$

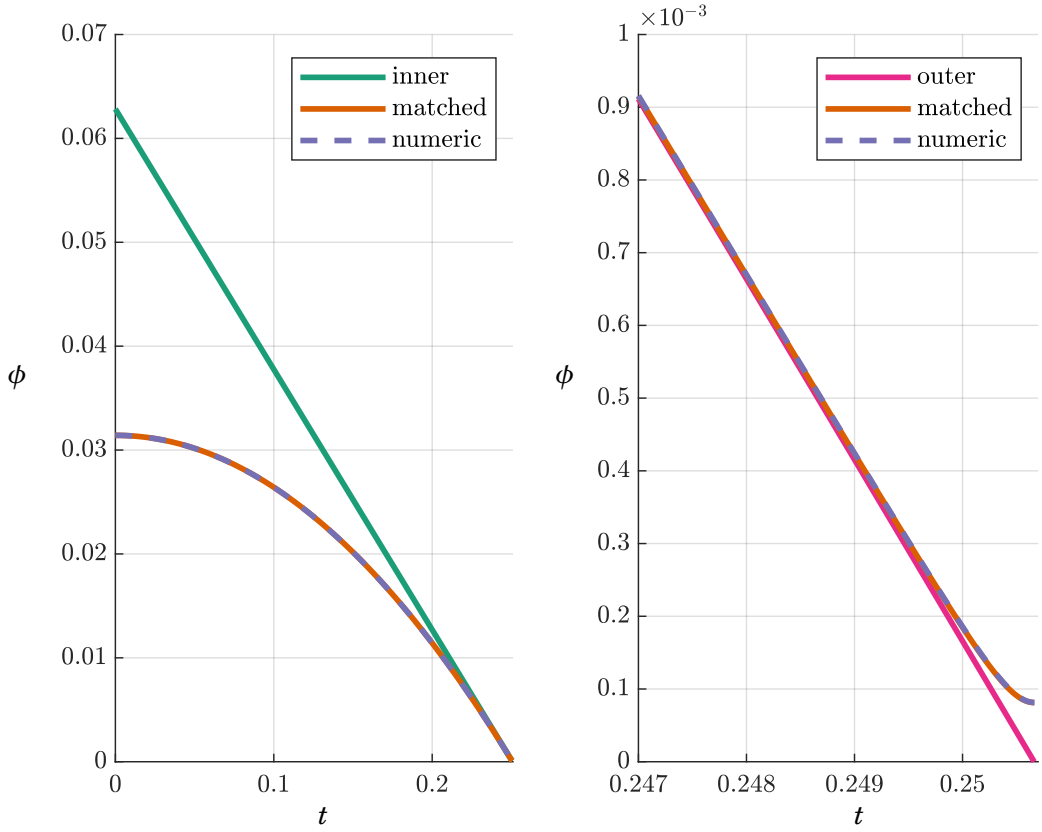

Figure 2.10: Comparison of inner eq. (2.80), outer eq. (2.73), matched eq. (2.88), and numeric solutions of the reduced equation of motion, eq. (2.63). Left: the time series for $0 < t < \sqrt{I} = 0.2507$. The matched and numeric solutions lie on top of one another. Right: the time series for $0.247 < t < 0.251$ showing the divergence of the outer solution from the matched and numeric solutions. Initial conditions and material parameters are given in eqs. (2.14) and (2.15) respectively. The small parameter $\epsilon = B_{-2}^2 = 1.43 \times 10^{-10}$ and $I = \pi/50$.

This solution is only valid for $0 < t < \sqrt{I}$, or equivalently $T < 0$. However, RHS of eq. (2.90) is symmetric about $T = 0$, so we may look at positive and negative T. The maximum angular velocity $\frac{\mathrm{d}\psi}{\mathrm{d}T}$ is attained at $T = 0$ and in the non-dimensionalised scalings of eq. (2.63) it reads

$$\left.\frac{\mathrm{d}\psi}{\mathrm{d}t}\right|_{\max} = \frac{I\sqrt{a_P + 1}\,\mathrm{sign}(B_{-2})}{\epsilon^{1/2} a_P}. \tag{2.91}$$

The presence of $\epsilon^{1/2}$ causes the large spikes visible in fig. 2.8. For the standard parameter values and initial conditions, eqs. (2.14) and (2.15), the maximum value of $\frac{\mathrm{d}\psi}{\mathrm{d}t} = 3449$. Numerical integration of the full, non-dimensionalised equations eq. (2.11) gives $\frac{\mathrm{d}\psi}{\mathrm{d}t} = 3575$. The error is to be expected due to the small ϕ and small ϵ approximations. The same procedure of transforming

and scaling is applied to the Θ expression, eq. (2.52a)

$$\frac{\mathrm{d}\theta}{\mathrm{d}T} = -\frac{\sqrt{a_P+1}\,\mathrm{sign}(B_{-2})}{\left(\frac{a_3}{I}+IT^2\right)} = -\frac{\mathrm{d}\psi}{\mathrm{d}T}, \tag{2.92}$$

where we see that $\frac{\mathrm{d}\theta}{\mathrm{d}T}$ and $\frac{\mathrm{d}\psi}{\mathrm{d}T}$ are identical but opposite in sign. The two angles ψ and θ are determined by integration of eqs. (2.90) and (2.92). First, ψ

$$\psi(T) = \int \frac{\sqrt{a_P+1}\,\mathrm{sign}(B_{-2})}{\frac{a_3}{I}+IT^2}\mathrm{d}T = \frac{\sqrt{a_P+1}\,\mathrm{sign}(B_{-2})}{a_P}\arctan\left(\frac{IT}{\sqrt{a_P}}\right)+C_\psi, \tag{2.93}$$

and secondly, θ

$$\theta(T) = -\frac{\sqrt{a_P+1}\,\mathrm{sign}(B_{-2})}{a_P}\arctan\left(\frac{IT}{\sqrt{a_P}}\right)+C_\theta, \tag{2.94}$$

where C_ψ and C_θ are integration constants. We compute $\frac{\mathrm{d}\varphi}{\mathrm{d}T}$ by differentiating the inner solution eq. (2.80)

$$\frac{\mathrm{d}\varphi}{\mathrm{d}T} = \frac{IT}{\sqrt{\frac{a_3}{I}+IT^2}}, \tag{2.95}$$

thus completing the set of angular velocities and positions describing the can's motion during the bounce. The presence of arctan in eqs. (2.93) and (2.94) cause the angles ψ and θ to exhibit a fast change over the bounce, and resemble smoothed step functions. The size of the step is equal to the angle of turn $\Delta\psi$. The scaled angle φ evolves according to a smoothed modulus function, avoiding $\varphi = 0$. In unscaled variables the minimum angle reached by ϕ is $\phi_{\min} = \sqrt{\epsilon a_p/I}$.

2.6 Physical phenomena

The rocking can phenomenon consists of a slow, inverted pendulum-like rock downwards, before a fast bouncing motion where the state variables undergo an abrupt change in value. In Section 2.5 these two motions were separated into the outer and inner regions respectively. In this section we use the expressions for the state variables in the inner region to understand the physical behaviour of the can as it undergoes the bounce. We explore the angle of turn and its sign, the motion of the contact point and the coefficient of friction required for the phenomenon.

2.6.1 The angle of turn

The angle of turn, $\Delta\psi$, is defined as the change in the precession angle ψ over the bounce. We compute $\Delta\psi$ from the inner solution for ψ, eq. (2.93). Recalling that the solution is only valid for $T < 0$, but appealing to the symmetry of eq. (2.90), the angle of turn is

$$\Delta\psi = 2(\psi(T=0) - \psi(T=-\infty)) = \pi\sqrt{\frac{a_P+1}{a_p}}\,\mathrm{sign}(B_{-2}). \tag{2.96}$$

In the case of large a_P then $|\Delta\psi| \to \pi$, the minimum value of the angle of turn. It is interesting that the can rotates by at least π before rising back up, regardless of the material parameters. In the case of small a_P then $|\Delta\psi| \to \infty$, suggesting that the can completes many revolutions before rising back up. The feasibility of such a large angle of turn is discussed in Section 2.6.3. Reverting to unscaled units, the size of the angle of turn is

$$|\Delta\psi| = \pi\sqrt{\frac{A + mH^2 + mR^2}{A + mH^2}}, \tag{2.97}$$

agreeing with the work of Srinivasan and Ruina [87], which used formal assumptions on ψ, θ and ϕ to reduce the problem. For the empty food can we calculate $|\Delta\psi| = 209°$ or $29°$ past the centre line; the solution of the non-dimensionalised equations of motion in fig. 2.3 also show jumps of $|\Delta\psi| = 209°$. The difference in $|\Delta\psi|$ with respect to Srinivasan and Ruina [87] is attributed to the differences in the can's parameters, eq. (2.14).

Equation (2.96) also contains information about the direction of the angle of turn, through sign(B_{-2}). The dividing line between the clockwise and anticlockwise rotating solutions has been investigated for the thin disk by Cushman and Duistermaat [33], who find a 'codimension one semi-analytic subset F of the phase space such that the disk falls flat in finite time'. Falling flat corresponds to the singular solution described in eq. (2.17), where the entire rim of the disk contacts the plane simultaneously. Recall the expression for B_{-2}, eq. (2.56)

$$B_{-2} = -\frac{kc_P}{2}(\Theta_0 + \Psi_0)\phi_0^2 + \Psi_0\phi_0^2 + \mathcal{O}\left(\phi_0^3\right) \tag{2.98}$$

Disregarding $\mathcal{O}\left(\phi_0^3\right)$ terms, the sign of B_{-2} is determined by whether the initial conditions lie to the left or the right of the dividing line

$$\Theta(0) = \left(\frac{2}{c_P k} - 1\right)\Psi(0). \tag{2.99}$$

Close to this line, the asymptotic series of ϕ_0 in eq. (2.98) breaks down and we should consider higher order terms. In fig. 2.11, we test the boundary, (2.99), numerically by solving the equations of motion, eq. (2.11), for different initial conditions and noting to which side the disk falls. A green square indicates that the can falls clockwise and orange indicates that the can falls in the anticlockwise direction.

2.6.2 The contact locus

As the can approaches the bounce, the instantaneous contact point races quickly around the rim of the can. Cushman and Duistermaat [33], numerically integrate the equations of motion for the thin disk and plot the paths traced out by the contact locus. Using the inner solutions in section 2.5.4, we analytically investigate the paths for the thick disk.

The instantaneous contact point $\underline{P}$ is stationary due to the rolling constraint. It is located at $\underline{GP}^{\mathcal{B}}$ in the body frame. To see the movement of this contact point over the horizontal plane

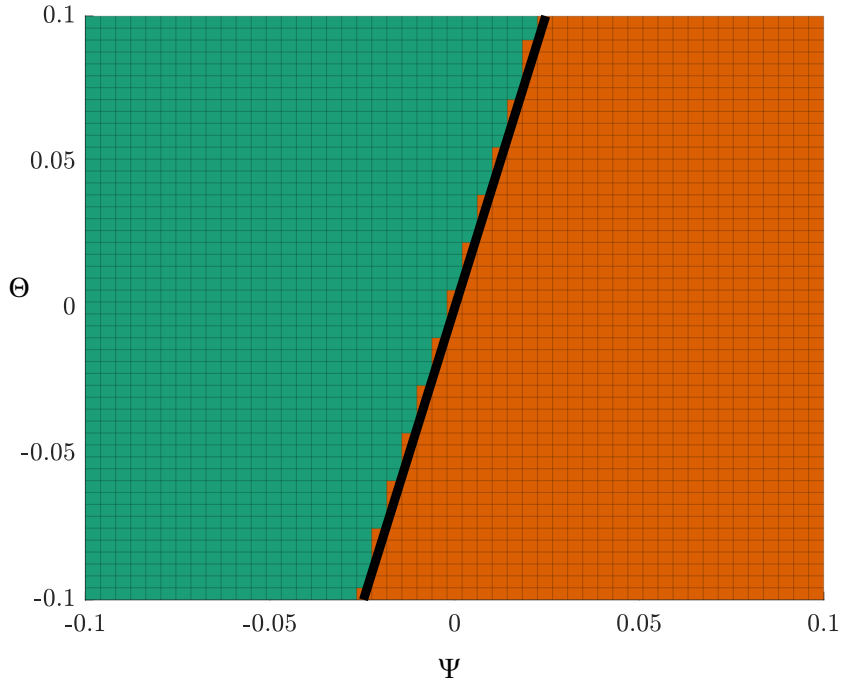

Figure 2.11: Numerical validation of the boundary eq. (2.99), between clockwise and anticlockwise falling trajectories. The unscaled initial conditions are $(\dot{\psi}, \phi, \dot{\phi}, \dot{\theta}) = (\dot{\psi}(0), \pi/100, 0, \dot{\theta}(0))$, and both $\dot{\psi}(0)$ and $\dot{\theta}(0)$ are varied. The corresponding square is coloured orange if $\Delta\psi < 0$ and the can falls anticlockwise. A square is coloured green if $\Delta\psi > 0$ and the can falls clockwise. The black line is the analytical prediction for the boundary, eq. (2.99).

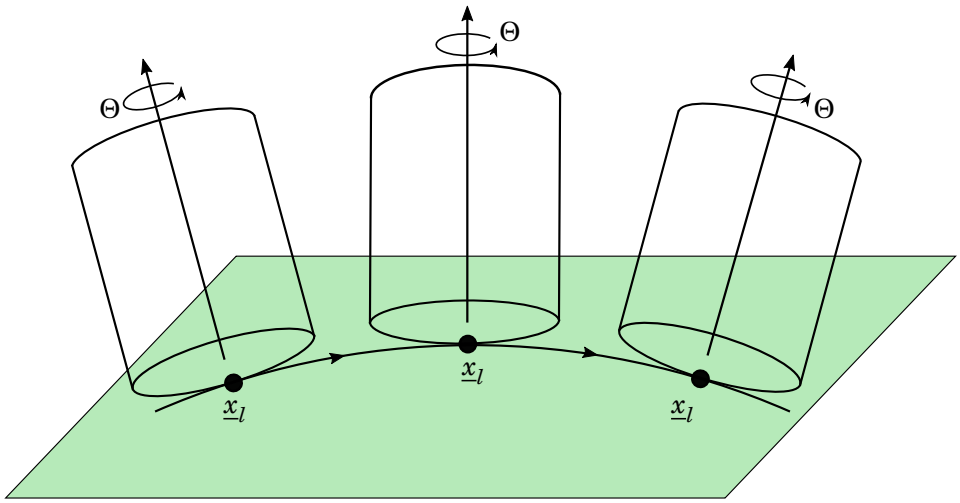

Figure 2.12: The instantaneous contact point, $\underline{P}$, is fixed with respect to the can and stationary at the moment of contact. The path that the instantaneous contact point traces out as the can moves over the plane is called the contact locus, $\underline{x}_l$.

we introduce the contact locus $\underline{x}_l$. As the can rolls, the contact locus, $\underline{x}_l$ traces out a path on the horizontal plane. It is not fixed to a point on the can, but instead follows the contact point.

Subtracting the rotation in θ from the can's angular velocity, we compute the velocity of the contact locus, $\underline{V}_l$ ensuring that $\underline{x}_l$ remains in contact with the plane

$$\underline{V}_l^{\mathcal{G}} = \underline{V}_g^{\mathcal{G}} + \mathrm{R}_{\mathcal{BG}}\left((\underline{\Omega}^{\mathcal{B}} - \Theta\underline{\hat{z}}^{\mathcal{B}}) \times \underline{GP}^{\mathcal{B}}\right). \tag{2.100}$$

The centre of mass velocity is given in eq. (2.5) and we apply the scalings, eq. (2.9), to non-dimensionalise. The velocity of the contact locus over the horizontal plane is

$$\frac{\mathrm{d}\underline{x}_l}{\mathrm{d}t}^{\mathcal{G}} = \Theta\begin{pmatrix} -\sin\psi \\ \cos\psi \end{pmatrix}. \tag{2.101}$$

Converting to inner variables and noting that $\frac{\mathrm{d}\psi}{\mathrm{d}T} = -\frac{\mathrm{d}\theta}{\mathrm{d}T}$ from eq. (2.92)

$$\frac{\mathrm{d}\underline{x}_l}{\mathrm{d}T}^{\mathcal{G}} = -\frac{\mathrm{d}\psi}{\mathrm{d}T}\begin{pmatrix} -\sin\psi \\ \cos\psi \end{pmatrix}, \tag{2.102}$$

which is integrable. Therefore, the leading order, inner solution for the contact locus describing the path traced out by the can is

$$x_l(T) = -\cos\left(\frac{\sqrt{a_P+1}\,\mathrm{sign}(B_{-2})}{a_P}\arctan\left(\frac{IT}{\sqrt{a_P}}\right) + C_\psi\right) + C_{xl}, \tag{2.103a}$$

$$y_l(T) = \sin\left(\frac{\sqrt{a_P+1}\,\mathrm{sign}(B_{-2})}{a_P}\arctan\left(\frac{IT}{\sqrt{a_P}}\right) + C_\psi\right) + C_{yl}, \tag{2.103b}$$

where C_{xl} and C_{yl} are constants of integration related to the initial position of the contact locus. Therefore, during the bounce the contact locus moves in a circular trajectory with radius 1. The size of the circular arc traced out by the contact locus is $|\Delta\psi|$.

To understand how the contact locus moves in the outer region we recall the series solutions for $\Theta(\phi)$ and $\Psi(\phi)$, eqs. (2.52a) and (2.52b). Rescaling time T by $\frac{1}{\sqrt{a_P+1}}$ brings the series into the same scale as eq. (2.63). Then, inserting the outer solution, eq. (2.73), and discarding the $\mathcal{O}(\epsilon)$ terms we obtain

$$\frac{\mathrm{d}\psi}{\mathrm{d}t} = \frac{4\epsilon^{1/2}\,\mathrm{sign}(B_{-2})\sqrt{a_P+1}}{(I-t^2)^2} = -\frac{\mathrm{d}\theta}{\mathrm{d}t}. \tag{2.104}$$

Integrating gives the outer solution for $\psi(t)$

$$\psi(t) = 2\epsilon^{1/2}\,\mathrm{sign}(B_{-2})\sqrt{a_P+1}\left(\frac{t}{I(I-t^2)} + \operatorname{arctanh}\left(\frac{t}{\sqrt{I}}\right)\right) + C_\psi, \tag{2.105}$$

and inserting this into the contact locus equation, eq. (2.101), gives

$$x_l(t) = -\cos\left(2\epsilon^{1/2}\,\mathrm{sign}(B_{-2})\sqrt{a_P+1}\left(\frac{t}{I(I-t^2)} + \operatorname{arctanh}\left(\frac{t}{\sqrt{I}}\right)\right) + C_\psi\right) + C_{xl}, \tag{2.106a}$$

$$y_l(t) = \sin\left(2\epsilon^{1/2}\,\mathrm{sign}(B_{-2})\sqrt{a_P+1}\left(\frac{t}{I(I-t^2)} + \operatorname{arctanh}\left(\frac{t}{\sqrt{I}}\right)\right) + C_\psi\right) + C_{yl}. \tag{2.106b}$$

The presence of the small parameter in eq. (2.106) suggests that the contact locus position barely changes in the outer solution until the asymptotic balance is broken as $t \to \sqrt{I}$. For small ϵ, the contact locus trajectories are circular with large arcs in the inner solution and small arcs in the outer solution. The numerical solutions of eq. (2.11) in fig. 2.13a show exactly this behaviour. Sections of the trajectory where ϕ is large are plotted in red showing that the majority of the motion occurs in the inner region at small ϕ.

In Cushman and Duistermaat's [33] study of the thin disk with $H = 0$, the contact locus rotates clockwise at small ϕ. After overturning at $\phi > \pi/2$, the disk then rotates anticlockwise (or vice versa). The thick disk cannot overturn without having multiple points of contact, therefore we restrict $\phi \in (0, \pi/2)$. The change in rotation direction is not visible in the inner and outer solutions presented in eqs. (2.103) and (2.106), both solutions rotate clockwise if $\text{sign}(B_{-2}) > 0$ and anticlockwise otherwise.

Figure 2.13 also shows the contact locus trajectory for three other sets of initial conditions. The trajectories are calculated numerically using the non-dimensionalised equations of motion, eq. (2.11). The variety of different types of motion is evident, but note that at small ϕ, shown in blue, all trajectories appear to be circular arcs. Figure 2.13b shows motion with initial conditions just off the balancing angle $\phi^* = \arctan(1/h)$ with a large $\dot{\theta}$. The can rolls in a straight line before falling almost flat, turning around and repeating, producing a spirographic, flower-like pattern. Such a pattern cannot be seen in the reduced system (2.63), because it requires the presence of the saddle equilibrium at $\phi^* = \arctan(1/h)$ which is destroyed when discarding $\mathcal{O}\left(\phi\right)$ terms.

In fig. 2.13c the initial conditions are small ϕ, but with large ϵ. We see a roughly circular trajectory, but with wobbles caused by the large vertical angular momentum ϵ. In fig. 2.13c, the initial conditions are small ϕ with large $\dot{\theta}$ and ϵ. Close to the boundary defined by eq. (2.99), we see circular movement, but along the top we see small cusp-like projections from the circle where the can reverses its direction. These trajectories have some striking patterns, but our analysis only applies to the circular trajectory in fig. 2.13a.

Further work is required to explain the cusp-like trajectories of the simulation in fig. 2.13d. Figure 2.13d also raises another question: for what initial conditions does the can's position remain bounded? If the initial conditions belong to the steady motion S_{bal}, eq. (2.23), with $\Psi = 0$, then the can rolls in a straight line with velocity $R\Theta$ and the position is unbounded. In fig. 2.12d, the contact locus appear to be prescribe a larger circle, but it is unclear if the position remains bounded. In the case of the thin disk, Borisov et al. [20] show that the contact locus is bounded for almost all initial conditions.

2.6.3 The coefficient of Coulomb friction

To ensure the equations of motion, eq. (2.11), are valid we require that the coefficient of Coulomb friction $\mu > |\underline{F}(t)|/N(t)$ for all time. The maximum value of $|\underline{F}|/N$ is the required coefficient of Coulomb friction between the can and the surface. Srinivasan and Ruina [87, fig. 5] find sharp

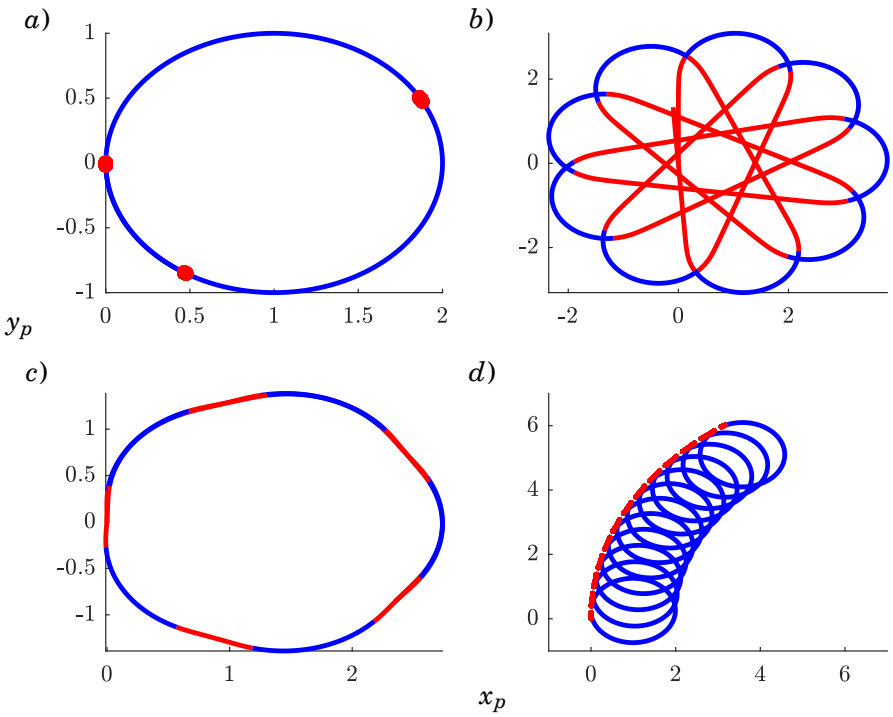

Figure 2.13: Contact locus trajectories for different initial conditions. Portions of a trajectory where ϕ is small compared to the initial condition are coloured blue ($\phi < \phi_0/10$). To obtain the trajectories the contact point velocity eq. (2.101) is integrated numerically using solutions of eq. (2.11). The unscaled initial conditions are: a) as in eq. (2.15), b) $(\dot{\psi}, \phi_0, \dot{\phi}, \dot{\theta}) = (0, \phi^* - 1 \times 10^{-5}, 0, 2)$, c) $(\dot{\psi}, \phi, \dot{\phi}, \dot{\theta}) = (0.72667, \pi/100, 0, 7)$ and d) $(\dot{\psi}, \phi, \dot{\phi}, \dot{\theta}) = (1.7267, \pi/100, 0, 7)$. The material parameters are given in eq. (2.14).

changes in the friction ratio $|\underline{F}|/N$ when solving the equations of motion. The required coefficient of Coulomb friction appears to remain finite despite its singular appearance. In this section we investigate the dependence of the friction ratio on the material characteristics of the can.

The contact forces F_x, F_y and N are computed in eqs. (2.7a) to (2.7c). The ratio $|\underline{F}|/N$ is

$$\frac{|\underline{F}|}{N} = \frac{\sqrt{F_x^2 + F_y^2}}{N}, \tag{2.107}$$

and in non-dimensionalised variables

$$\frac{|\underline{F}|}{N} = \frac{\sqrt{\left(\dot{\Phi}(\sin\phi + h\cos\phi) + \Theta\Psi + (\Phi^2 + \Psi^2)(\cos\phi - h\sin\phi)\right)^2 + \left(\dot{\Psi}(\cos\phi - h\sin\phi) + \dot{\Theta} - 2\Phi\Psi(\sin\phi + h\cos\phi)\right)^2}}{1 + \dot{\Phi}(\cos\phi - h\sin\phi) - \Phi^2(\sin\phi + h\cos\phi)}. \tag{2.108}$$

In fig. 2.14, we plot the friction ratio, eq. (2.108), during the can's motion. Similar behaviour to Srinivasan and Ruina [87, fig. 5] is observed, but it differs due to the choice of parameter values and initial conditions. In fig. 2.14, we colour the inner region blue, for $\phi < \phi_0/10$, and we colour

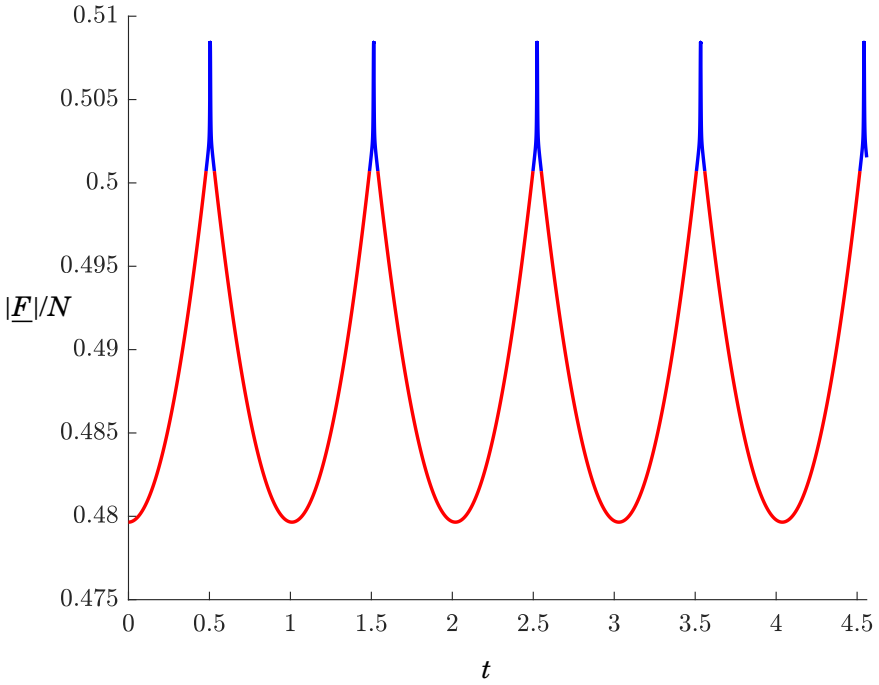

Figure 2.14: The ratio of friction to normal force versus time. The plot is coloured blue if the can is close to the bounce and $\phi < \phi_0/10$. The data is obtained by solving the equations of motion, eq. (2.11), with initial conditions and material parameters from eqs. (2.14) and (2.15) respectively.

the outer region red. In this case, the outer region requires less friction than the inner region. This is not true for all initial conditions and parameter values. The outer region may require a higher coefficient of friction than the inner region, particularly if the initial conditions have large Φ. The peak of the ratio $|\underline{F}|/N$ in fig. 2.14 is 0.508, suggesting that if $\mu > 0.508$ the can will roll without slip. This quite a large coefficient of friction, suggesting that the can may slip.

We write the friction ratio, eq. (2.108), in inner variables and insert the inner solutions, eqs. (2.87), (2.90) and (2.92), along with their derivatives. Expanding and keeping only the leading order term in ϵ gives an approximate lower bound on the required coefficient of friction

$$\frac{|\underline{F}|}{N} \approx \frac{h}{a_P} = \frac{mRH}{A + mH^2}. \tag{2.109}$$

There is no time dependence in eq. (2.109), it must appear at higher orders of ϵ. Equation (2.109) predicts a required coefficient of friction of $\mu_{req} = 0.508$, agreeing with the numerical value. We note that this lower bound on the required coefficient of friction is indeed finite, as suggested by Srinivasan and Ruina [87], despite the sharp appearance in fig. 2.14. Unexpectedly, there is no dependence of the ratio $\frac{|\underline{F}|}{N}$ on the initial conditions in eq. (2.109). Again, the dependence is likely to appear at higher orders of ϵ.

In Section 2.6.1, the expression for the angle of turn $|\Delta\psi|$ predicts arbitrarily large values, resulting in many complete rotations of ψ. Large angles of turn are predicted if the non-symmetry

moment of inertia about the contact point, a_P, is small. However, small a_P in eq. (2.109) results in a large required coefficient of friction, rendering large angles of turn infeasible. This explains why large angles of turn are not seen in practice: the can slips.

For a uniform density cylinder, R, H, C and A are not independent quantities and the required coefficient of friction may be simplified further

$$\frac{|\underline{F}|}{N} \approx \frac{RH}{\frac{1}{12}(3R^2+H^2)+H^2} = \frac{12h}{3+13h^2}. \tag{2.110}$$

Therefore for a uniform density cylinder the maximum required coefficient of friction is $\mu = 0.96$, occurring when $h = \sqrt{39}/13 \approx 0.48$. A coefficient of $\mu = 0.96$ is not one easily achieved in tabletop experiments.

2.7 Discussion and conclusion

In Section 2.2, we rederived the equations of motion for a can rolling on a rough, horizontal plane. The equilibria and steady motions of the equations are examined and the problem is reduced to a second order ODE using a small angle approximation. Two approximately conserved quantities B_0 and B_{-2} are found that correspond to angular momenta about the global vertical and symmetry axes, justifying the formal assumptions made by Srinivasan et al. [87, (7) and (9)]. Setting $B_0 = B_{-2} = 0$ is a singular perturbation, prompting the introduction of the small parameter $\epsilon = B_0^2$. The singular limit, $\epsilon = 0$, yields a flat-falling solution, which is studied by Cushman and Duistermaat [33] for the thin disk.

Two distinct regimes are visible when reproducing the rocking can phenomenon. Therefore, we split the problem into inner and outer regions using a matched asymptotic approach, taking advantage of the small parameter ϵ. In the outer region the can's dynamics evolve according to an inverted pendulum, while the inner region contains the dynamics underpinning the angle of turn phenomenon.

Solving the inner problem results in approximate solutions for all the variables of the can, enabling exploration of the characteristic features of the angle of turn phenomenon. We compute the minimum angle $\phi_{\min}$ achieved by the disk and the maximum angular velocity $\dot{\psi}_{\max}$ attained over the bounce. We recompute the angle of turn $|\Delta\psi|$ derived by Srinivasan and Ruina [87] and gain more information about the direction of the angle of turn. This extends the work of Cushman and Duistermaat [33] to a thick disk with $H \neq 0$. The key characteristics of the dynamics are confirmed by numerical solutions of the full, nonlinear equations, eq. (2.11), in MATLAB. We examine the motion of the contact locus and see a range of different trajectories, from circular to petaloid motion and even cusp-like behaviour. However, at small ϕ and ϵ all trajectories of the contact locus are circular.

Finally, we examine the friction ratio, eq. (2.108), over the course of the motion. Previous analysis by Srinivasan and Ruina [87] shows sharp changes in the ratio over the bounce. Using

the inner solutions we obtain an approximate lower bound for the required coefficient of friction to avoid slip. We see that for small ϵ and ϕ the lower bound is independent of the initial conditions and dependent only on the material characteristics of the can. For the empty food tin considered in this chapter, a coefficient of friction $\mu \approx 0.508$ is required to avoid slipping.

The tabletop experiments of Srinivasan and Ruina [87] show reasonable agreement for the size of the angle of turn. Slow-motion video footage similar to that presented in Chapter 3 may provide the necessary data to corroborate analytic estimates of $\phi_{\min}$ and $\dot{\psi}_{\max}$. It may also be possible to detect the presence of slipping events.

An interesting extension to the rocking can problem is the addition of a forced horizontal plane, considered in the context of Euler's disk by Takano et al. [92]. In the planar case, Hogan [50] explored the dynamics of a rigid rectangular block rocking and impacting with a sinusoidally-forced horizontal plane. The system contains a range of dynamical behaviour including period-doubling cascades. If excited by seismic activity, three-dimensional structures such as classical columns or grain silos may undergo similar behaviour to both the rocking can and the rocking block. The literature concerning these structures [89, 94] may benefit from the approach in this work.

CHAPTER 3

EXPERIMENTAL ANALYSIS OF EULER'S DISK

3.1 Introduction

The commercial Euler's disk consists of a small, heavy, polished, steel disk and an accompanying concave, mirrored base-plate. An example is shown in fig. 1.3. The bottom rim of the disk is gently curved, ensuring smooth contact with the base-plate, while the top rim is sharper. The designs around the cylindrical and top faces produce striking patterns as the disk spins. The concavity of the base-plate keeps the spinning disk confined to a central area of the plate. It also increases the duration of the motion by providing a smooth surface for the disk to roll upon. A technical diagram of the disk on a horizontal plane is shown in fig. 3.1. The orientation of the disk is specified by the Euler angles ψ, ϕ and θ. The first angle ψ, the *precession* angle, describes a rotation around the global vertical axis, $z^{\mathcal{G}}$. The second angle ϕ, the *nutation* angle, describes a rotation about the intermediate frame axis $y^{\mathcal{I}}$ and the third angle θ, the *rotation* angle, describes a rotation around the body vertical axis $z^{\mathcal{B}}$.

Contrary to its name, Euler's disk was invented by Joseph Bendik in 1987 [14]. Bendik spun polishing chucks on a hard desk and noted the long duration of the motion: around thirty to forty seconds. Captivated, Bendik sought disks that would spin for even longer. After prototyping, the commercial Euler's disk was born, which can spin for times in excess of two minutes. The Euler moniker is attributed to the great Leonhard Euler for his interest in spinning and rolling (or *spolling*) bodies. Indeed, the moniker is particularly appropriate, given that most analyses make use of both Euler angles and Euler's equations.

On spinning the disk about the vertical, it remains upright for some time. After a while the disk 'falls' and it adopts a more horizontal attitude. As the nutation angle ϕ with respect to the horizontal plane decreases, the disk rolls faster and faster. Towards the end of the motion, the

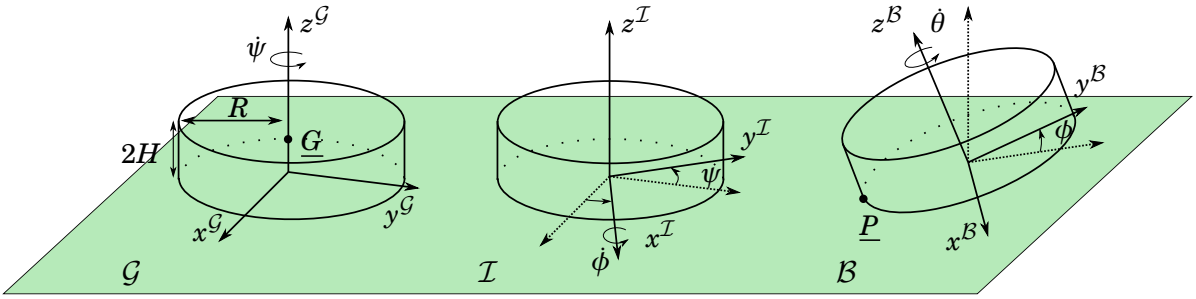

Figure 3.1: Technical diagram of Euler's disk. The three reference frames, the global $\mathcal{G}$, intermediate $\mathcal{I}$ and body frame $\mathcal{B}$ are given by successive rotations ψ and ϕ. The vectors $\underline{G}$ and $\underline{P}$ refer to the positions of the centre of mass and the contact point respectively.

disk is almost flat and spinning very quickly. The contact point races over the base-plate at a speed of up to $60\,\mathrm{km\,h^{-1}}$ causing a whirring rattling noise. The sound increases in pitch as ϕ decreases further. Finally, the disk halts abruptly and falls flat.

The equations of a dissipation-free disk spinning on a horizontal plane have been generally understood since the research of Korteweg, Appell, Vierkandt and Chapylgin [10, 25, 62, 95] around the end of the 19^{th} century. However, the specific problem of Euler's disk is focused on the final moments of the disk's motion. Counterintuitively, the disk appears to spin faster and faster before an abrupt stop. The velocity of the contact point approaches a singularity in a continuous analogue to the chattering ping pong ball which, when dropped onto a hard surface, undergoes successive impacts with decreasing intervals. For the case of the ping pong ball, the dissipation mechanism which removes energy from the system is clear: impacts. For the disk, it is less obvious; there are many candidates: Coulomb friction, rolling friction, elasticity, impacts, and even vibrations [11, 32, 68, 96]. Coulomb friction, the go-to candidate for dissipation in mechanical systems has been discounted for being unable to bring the disk to a halt [68].

Euler's disk has been analysed experimentally many times. The halt is a simple phenomenon to replicate but it is difficult to obtain meaningful data due to the high frequency and small amplitude of the disk at the end of the motion. Air resistance was proposed by Moffatt [74] in 2000 as the dissipative mechanism that brings the disk to a halt. Subsequently, van den Engh et al. [93] and Borisov et al. [17] spun disks in a vaccuum and observed the same qualitative behaviour. Note that these experiments do not necessarily mean that Moffatt was mistaken, other dissipation mechanism may also bring the disk to a halt with the same qualitative appearance as air resistance. Many other experiments have been performed over the next two decades. In two simple experiments, Borisov et al. [19] showed that the disk actually loses contact with the plane. The final loss of contact is very short, lasting between 12 and 40 ms. Other experiments are more conventional. Ma et al. [71] filmed the disk's motion using two high-speed cameras, reconstructed all the state variables and concluded that a form of rolling friction is the most likely culprit for the dissipation mechanism. Leine [68] and Cross [32] also filmed the disk with a high-speed camera and reconstructed some of the state variables. Leine's analysis [68] pointed to the contour

friction variant of rolling friction as the dominant mechanism [68]. Cross [32] suggested that as the disk falls flatter, it comes into contact with more 'high spots' in the base-plate, resulting in a rolling friction that depends on the nutation angle, ϕ.

Dissipation mechanisms explored in the literature predict that the energy decreases according to a power law, eq. (3.2), with a parameter-free energy exponent, n. For example, the energy exponent associated with clasical rolling friction is $n = 2$ [68], resulting in a quadratic decrease in energy regardless of material parameters. Leine [68] remarks that 'the results were always qualitatively similar' when spinning the disk on glass and aluminium base-plates. Ma et al. [71] also spun the disk on glass and noted the same behaviour, albeit with slightly different exponents. Finally, Caps et al. [23] spun the disk on glass, plastic and aluminium and found different energy exponents. This suggests that n does have some material dependence, in contrast to analytical calculations.

In this chapter we present the results of two sets of experiments focused on the disk's final moments. The first experiment in Section 3.2 examines the effect of the base-plate material on the energy profile of the disk. We spin the commercial Euler's disk and a similarly sized brass disk on eight base-plates of different materials, including the mirrored concave base-plate, then extract the energy from the footage. Fitting the experimental energy to the power law, eq. (3.2), determines the energy exponent. For a stainless steel base-plate, we find that the energy exponent agrees with [68], but it varies by as much as 0.24 depending on the base-plate material.

The second experiment, presented in Section 3.3, was motivated by an observation in the first experiment. On viewing the footage, it appeared that the disk continued to rotate about the vertical axis after falling flat. Such continued rotation may invalidate the so-called 'stationary rolling' assumption employed in mathematical analysis of Euler's disk [11, 67, 68, 74]. Stationary rolling motion, sometimes known as adiabatic [74] or precession-free [11] motion, refers to rolling motion where the centre of mass is stationary. It is often applied in a quasi-static form, and the disk is assumed to 'slowly drift(s) along this 1-parameter family of steady rolling solutions' [11, 68] as it comes to a halt. This assumption is particularly advantageous because it reduces the dimensionality of the equations of motion. For Euler's disk, a 3D rigid body with six degrees of freedom, any simplification, approximation or assumption is vital to analysis.

We use a mirror to film both the top and side of the disk and mark the top face of the disk to track the rotation as it spins. The footage suggests that the disk continues to rotate after falling flat. Furthermore, there is a qualitative change in the vertical rotation after the disk falls flat, suggesting that the continued rotation corresponds to a different type of motion. The length of time that the disk rotates can be extended by lubricating the surface with oil and decreased by spinning the disk on the concave base-plate. Therefore, on flat base-plates, it would appear that the disk is briefly supported by a thin layer of fluid before making contact and sliding to a halt. By contrast, on the concave base-plate, the disk falls flat and is immediately brought to a halt by Coulomb friction.

3.2 A material dependent energy exponent

In this section we examine the effect of the base-plate material on the motion of Euler's disk, challenging the analytical result that the energy exponent is parameter-free [36, 68, 73]. First, we discuss the power law used to describe the energy of the disk. We then estimate the energy of the disk analytically, in terms of its state variables, before describing the experimental setup. In section 3.2.4, we extract the state variables from the slow-motion footage. The disk's energy is then estimated from the experimental data and used to fit the parameters of the power law. Finally, we analyse the results of the experiments in Section 3.2.6.

3.2.1 The energy exponent

The search for the dominant dissipation mechanism can be traced back to Moffatt [74], who analysed the disk in terms of energy. Mofatt proposed that at small nutation angles, ϕ, the energy dissipation is caused by a viscous layer of air between the disk and the base-plate, resulting in a decrease in energy of the form

$$E(t) \propto (t_0 - t)^{\frac{1}{3}}, \tag{3.1}$$

where t_0 is the time of the abrupt stop (subsequent analysis by Bildsten [16] revised the exponent upwards to $n = 4/9$). Moffatt [74] showed that this theory breaks down before the finite-time stop, noting that 'nature abhors a singularity'. This seminal analysis sparked a number of works examining other mechanisms.

Many of the attempts to explain the disk's motion involve finding an energy power law of the form

$$E(t) = A_e(t_0 - t)^n, \tag{3.2}$$

where n is the energy exponent and A_e is a multiplicative constant. In general, A_e is dependent on the material parameters, such as the coefficient of Coulomb friction, radius of the disk, etc. On the other hand, n is typically determined by the form of the dissipation mechanism. Figure 3.2 compares the energy profile for a number of different values of n. All experimental evidence predicts $n < 1$ resulting in a perpendicular decrease to zero energy, rather than tangential decrease for $n > 1$ [32, 68, 71]. The perpendicular decrease in energy causes the halt to appear abrupt.

The key question for Euler's disk is, What mechanism brings the disk to a halt? The mechanism with the smallest energy exponent dominates the dissipation and therefore can be credited with bringing the disk to a halt. The term 'dominant' is used here in the asymptotic sense. The rate of energy loss is given by differentiating eq. (3.2)

$$\frac{\mathrm{d}E(t)}{\mathrm{d}t} = -nA_e(t_0 - t)^{n-1}. \tag{3.3}$$

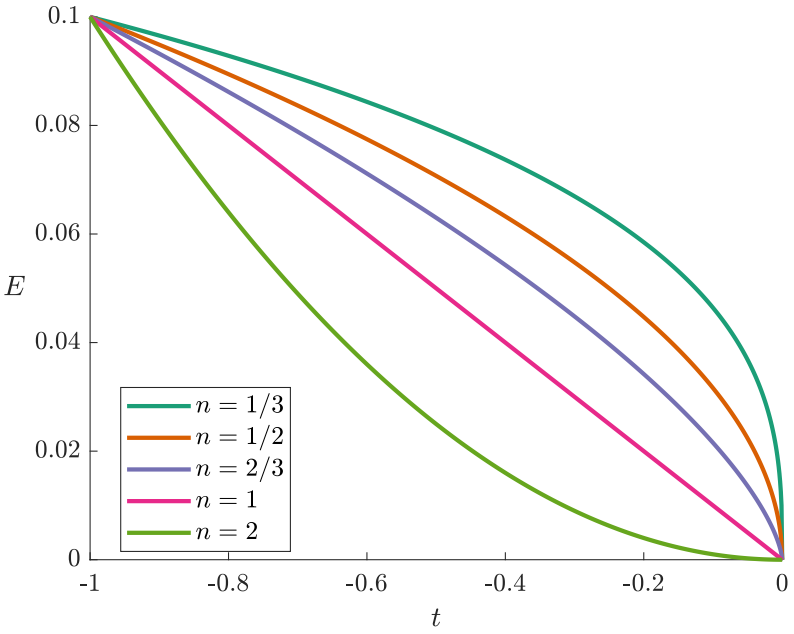

Figure 3.2: Comparison of different energy exponents in the power law, eq. (3.2). Experiments predict $n < 1$ for a perpendicular decrease in energy. Here $t_0 = 0$.

Clearly, if $n < 1$ the rate of energy loss is singular at $t = t_0$. Therefore a mechanism with a lower energy exponent, n, dominates other mechanisms with larger n as $t \to t_0$. For example, $n = 1/3$ dominates the other power laws in fig. 3.2. Much analysis has focused on finding the dissipation mechanism with the smallest exponent, but n must agree with the data gathered from experiments.

3.2.2 Estimating the energy of Euler's disk

The total energy of the disk is the sum of the linear and rotational kinetic energies and the potential energy

$$E = \frac{m(\underline{V}_G \cdot \underline{V}_G)}{2} + \frac{\underline{\underline{\mathrm{I}}}\underline{\Omega} \cdot \underline{\Omega}}{2} + mg(R\sin\phi + H\cos\phi), \tag{3.4}$$

where $\underline{V}_G = (\dot{X}_G, \dot{Y}_G, \dot{Z}_G)^\intercal$ is the velocity of the centre of mass, $\underline{\Omega} = (\dot{\psi}\sin\phi, -\dot{\phi}, \dot{\psi}\cos\phi + \dot{\theta})^\intercal$ is the angular velocity of the disk and $\dot{[]}$ indicates differentiation with respect to time. $\mathrm{I} = \mathrm{diag}(A, A, C)$ is the moment of inertia tensor for the disk and A and C are the components about the nonsymmetry and symmetry axes respectively. For Euler's disk, $m = 0.443\,\mathrm{kg}$, $R = 0.0381\,\mathrm{m}$ and $H = 0.006\,35\,\mathrm{m}$ and, for the brass disk, $m = 0.421\,\mathrm{kg}$, $R = 0.04\,\mathrm{m}$ and $H = 0.005\,\mathrm{m}$. The moments of inertia are given by $A = \frac{m}{12}\left(3R^2 + H^2\right)$ and $C = \frac{mR^2}{2}$.

Estimating the energy requires knowledge of the state variables, not all of which are computable from the experimental footage. Therefore, some assumptions are required. Firstly, it is

assumed that the disk is rolling, so the contact point $\underline{P}$ has zero velocity. Rather than recompute the velocity of the centre of mass, we note that when rolling, Euler's disk is identical to the rocking can studied in Chapter 2. The velocity of the centre of mass is given in eq. (2.5), repeated here

$$\dot{X}_G = -\dot{\phi}\cos\psi(R\sin\phi + H\cos\phi) - \dot{\psi}\sin\psi(R\cos\phi - H\sin\phi) - R\dot{\theta}\sin\psi, \tag{3.5a}$$

$$\dot{Y}_G = -\dot{\phi}\sin\psi(R\sin\phi + H\cos\phi) + \dot{\psi}\cos\psi(R\cos\phi - H\sin\phi) + R\dot{\theta}\cos\psi, \tag{3.5b}$$

$$\dot{Z}_G = \dot{\phi}(R\cos\phi - H\sin\phi). \tag{3.5c}$$

Substituting eq. (3.5) and $\underline{\Omega}$ into the energy, eq. (3.4), gives

$$\begin{aligned} E = {} & \frac{\dot{\phi}^2}{2}\left(A + mH^2 + mR^2\right) + \frac{C}{2}\left(\dot{\theta} + \dot{\psi}\cos\phi\right)^2 + \frac{m}{2}\left(R(\dot{\theta} + \dot{\psi}\cos\phi) - H\dot{\psi}\sin\phi\right)^2 \\ & + \frac{A}{2}\dot{\psi}^2\sin^2\phi + mg\left(R\sin\phi + H\cos\phi\right). \end{aligned} \tag{3.6}$$

Knowledge of $\dot{\psi}$, $\dot{\theta}$, ϕ and $\dot{\phi}$ is still required to compute the energy. Therefore, we assume that the disk undergoes stationary rolling motion, such that the centre of mass has zero velocity

$$\sqrt{\dot{X}_G^2 + \dot{Y}_G^2} = \dot{\psi}(R\cos\phi - H\sin\phi) + R\dot{\theta} = 0 \tag{3.7}$$

and $\dot{\phi} = 0$ from eq. (3.5). The stationary rolling motion assumption will be investigated further in Section 3.3, but here it is used to eliminate $\dot{\phi}$ and $\dot{\theta}$ from the energy, eq. (3.6). Subtracting the potential energy mgH, ensures that $E = 0$ when the disk comes to a halt. Hence,

$$E = \frac{C}{2}\left(\frac{H}{R}\dot{\psi}\sin\phi\right)^2 + \frac{A}{2}\dot{\psi}^2\sin^2\phi + mg(R\sin\phi + H\cos\phi) - mgH. \tag{3.8}$$

Therefore, to estimate the energy exponent, it suffices to obtain only ϕ and ψ from experiments. Numerical differentiation gives $\dot{\psi}$. The other quantities, A, m, R and H are known constants.

3.2.3 Experimental set up

To obtain the relevant dynamical variables, ϕ and ψ, we film Euler's disk in 480fps, 720×1280px footage on a OnePlus 6T smartphone. The curved surface and top face of the disk are wrapped in white paper and masking tape to dull reflections and provide contrast with the background. The bottom surface is untouched to avoid interfering with the rolling motion.

In fig. 3.3, the camera captures the front elevation of Euler's disk at rest on a $30 \times 30 \times 0.3$cm, flat, mild-steel base-plate. The base-plate rests on a silicone mat to dampen vibrations and keep it fixed. Although spun by hand, care was taken to spin the disk in approximately the same way each time. A single frame of the disk in motion is shown in fig. 3.4.

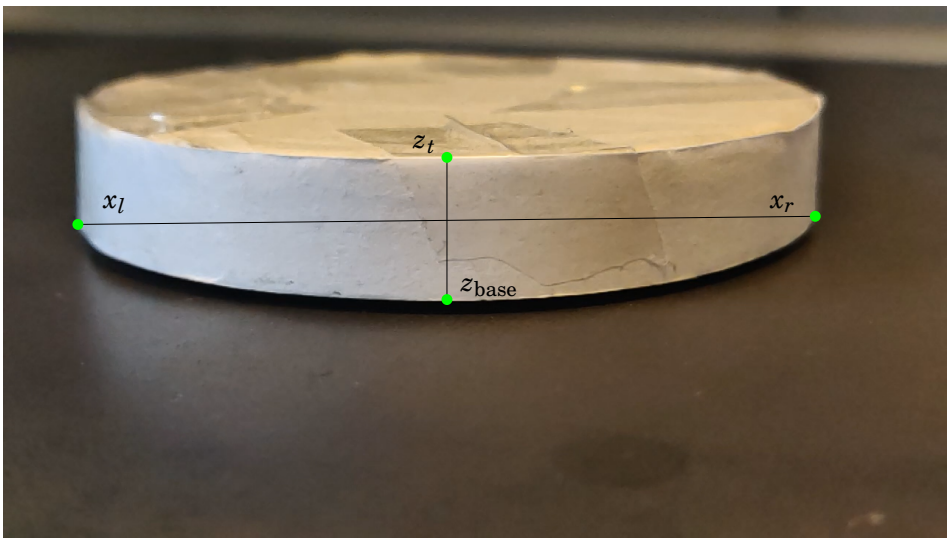

Figure 3.3: A single frame of the footage showing Euler's disk at rest on mild steel. The manually identified edge points, x_l, x_r, z_t and z_{base} are shown in green. The disk is flush with the base-plate and $z_{\text{rim}} = 0$.

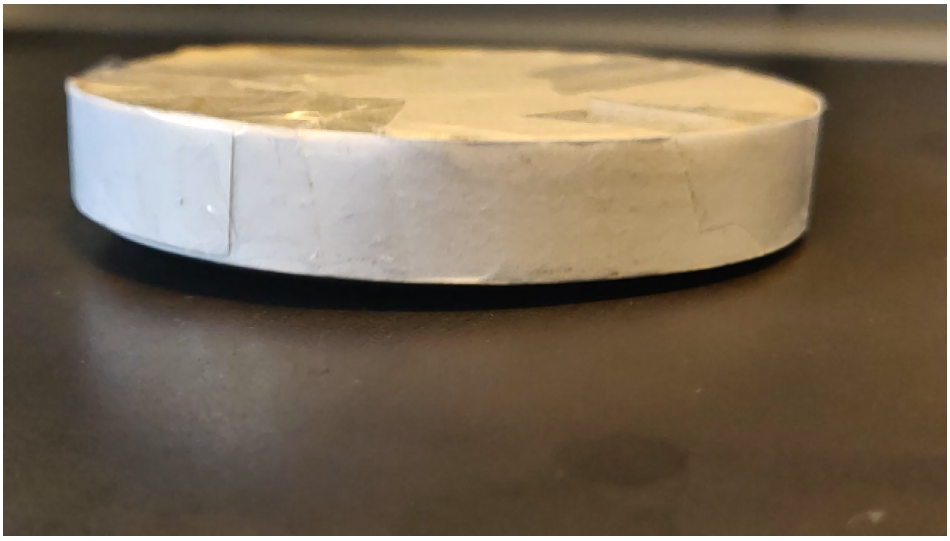

Figure 3.4: Euler's disk in motion on the mild-steel base-plate, roughly 0.5 s before the halt.

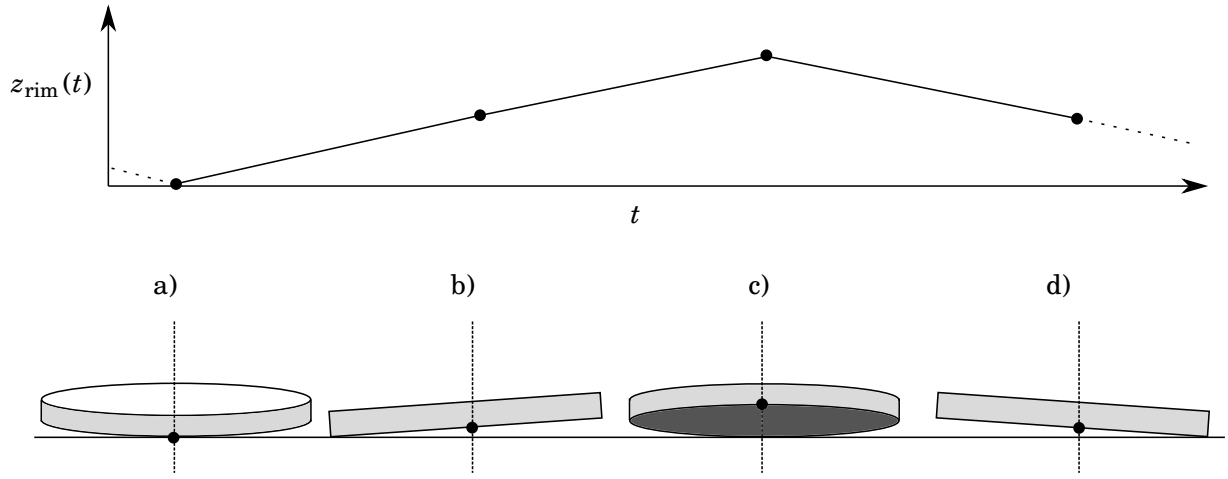

Figure 3.5: The variable z_{rim} denotes the height of the bottom rim of the disk along the centre line. As the disk rotates z_{rim} increases and decreases. In c) z_{rim} reaches a maximum and the disk is facing the camera.

3.2.4 Extracting data from the footage

There are a number of methods to compute ϕ and ψ from the footage. Some authors have filmed from different angles and fitted ellipses to the top face, or tracked markings on the disk [68, 70]. For the experiment, we use a less computationally intensive method to compute ϕ. First, we find $z_{\text{rim}}(t)$, the instantaneous height of the midpoint of the bottom rim above the base-plate, as shown in fig. 3.5. At maxima of $z_{\text{rim}}(t)$ the orientation of the disk is known, as shown in fig. 3.6. We compute ϕ using trigonometry

$$\phi = \sin\left(\frac{z_{\text{rim}}}{2R}\right). \tag{3.9}$$

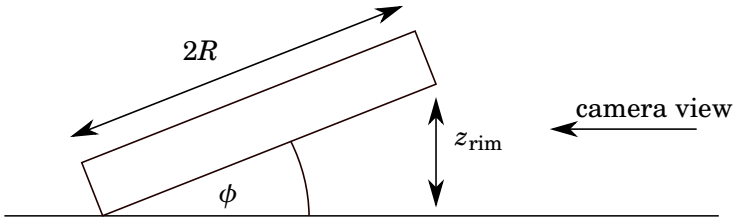

Figure 3.6: Orientation of the disk at maxima in z_{rim} corresponding to a side view in fig. 3.5c.

To extract $z_{\text{rim}}(t)$, we consider the disk after it has come to a halt in fig. 3.3. We compute the final position of the disk by manually finding the pixels corresponding to the left and rightmost edges of the bottom of the disk, denoted x_l and x_r. The centre line of the disk is $(x_{\text{centre}}, z) = ((x_r - x_l)/2, z)$. In the resting state of fig. 3.3, the disk is flush with the base-plate and the intersection of the centre line with the bottom rim occurs at $z = z_{\text{base}}$, the height of the base-plate. In preceding frames, where the disk is in motion, such as fig. 3.4, it is assumed that the disk

has barely moved horizontally and the intersection corresponds to the position of the midpoint of the bottom rim, $z_{\text{int}}(t)$. This is the aforementioned stationary rolling assumption, eq. (3.7). It is not valid for times long before the halt, but close to the halt it is a reasonable approximation. The height of the midpoint above the base-plate is given by computing $z_{\text{rim}}(t) = z_{\text{int}}(t) - z_{\text{base}}$ for every frame of the footage.

Figure 3.7: A single frame of the footage, showing the disk on mild steel base-plate. The pixels are converted from RGB to binary with a threshold of $\gamma = 0.35$

To find the intersection of the centreline with the bottom edge, we must first find the bottom edge of the disk. We convert each frame to black and white, thresholding on the intensity of the RGB image. Pixels are coloured white if the mean RGB value $(1/3)(R/256 + G/256 + B/256)$ is greater than some threshold $\gamma \in [0,1]$ and coloured black otherwise. Differences in light levels, position of the disk and base-plate colours mean that the threshold is not constant for all experiments. In fig. 3.7, an intensity threshold of $\gamma = 0.35$ is used which clearly outlines the bottom of the disk. There is a large patch of white in the bottom left of the figure, caused by the reflection of the disk in the steel, but we only require a clean image close to the centre line, (x_{centre}, z).

Applying MATLAB's edge detection procedure[1] on the black and white frame yields fig. 3.8, where the outline of the disk is clearly visible. The vertical position of the rim, $z_{\text{rim}}(t)$ is given by the intersection of bottom edge with the centre line shown in green in fig. 3.8. For other base-plate materials, such as acrylic and Teflon, the base-plate is white. We rely on the shadow beneath the disk to give the necessary contrast to detect the bottom rim, as shown in fig. 3.9. In that

[1] edge, Copyright 1992-2020 The MathWorks, Inc.

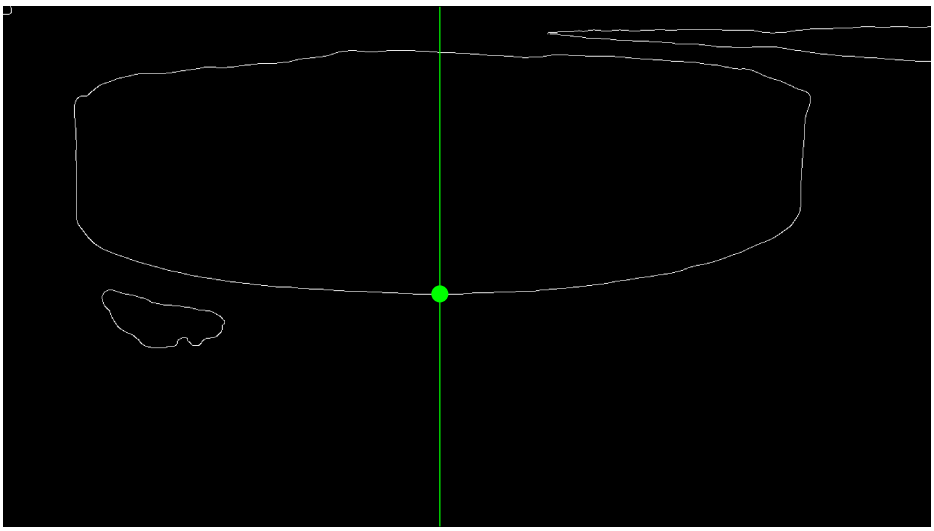

Figure 3.8: A single frame of the footage on the mild steel base-plate after applying edge detection. The height of the bottom rim is given by the green dot which is located at the intersection of centre line and the bottom rim of the disk.

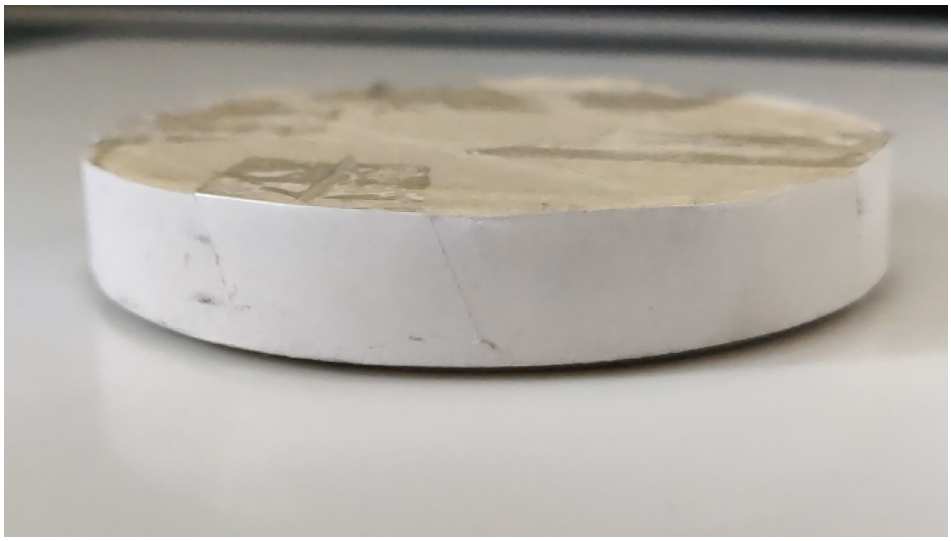

Figure 3.9: A single frame of the footage showing Euler's disk at rest on a Teflon base-plate. The light coloured base-plate requires a different approach to identify the rim of the disk. The shadow between the base-plate and the disk provides the required contrast.

case there are two edges: the beginning of the shadowed region and the beginning of the disk. Therefore, for light coloured base-plates, we compute $z_{\text{rim}}(t)$ using the intersection of the centre line with the second edge from the bottom.

Computing $z_{\text{rim}}(t)$ for each frame gives fig. 3.10. Just after release, the disk can move considerably from side to side, violating the stationary rolling assumption. Oscillations in the envelope of z_{rim} between frames 0 and 1000 are visible, but it is unclear if these are due to the lateral movement of the disk. Towards the end of the motion the lateral movement has disappeared. Therefore, we only focus on the final 0.5 s of the motion, with the additional benefit of cutting down on computation time.

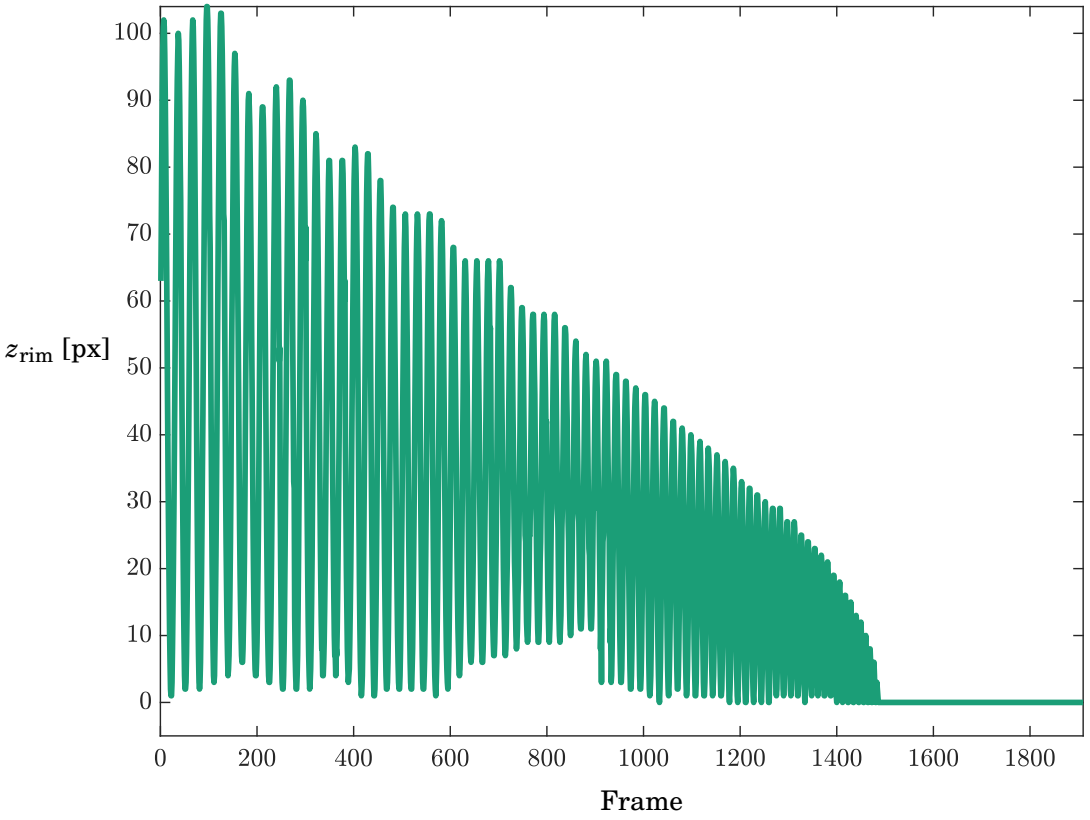

Figure 3.10: The vertical position of the bottom edge of the disk in pixels. Footage was filmed at 480fps capturing about 3 s of motion.

To convert $z_{\text{rim}}(t)$ from pixels to metres, we compute the size of a single pixel. Disregarding error due to the elevated perspective of the camera, the length of the centre line from z_t to z_{base} in fig. 3.3 is equal to the height of the disk, $2H$. Therefore the vertical length of a single pixel is

$$\delta = \frac{2H}{z_t - z_{\text{rim}}}, \tag{3.10}$$

defining the resolution of the data and thus the minimum detectable amplitude of oscillations. The resolution δ is not fixed for every experiment, because the disk may wander in the course of its motion and halt closer or further from the camera. For the experiment in fig. 3.3, $\delta = 6.58 \times 10^{-5}$m, or roughly 1/20th of a millimetre.

Multiplying by δ converts the $z_{\text{rim}}(t)$ data from pixels to metres and the frame number is converted to time using the frame rate of 480fps. The stopping time, t_0, is easily identified in fig. 3.10, occurring at frame 1486, or $t_0 = 3.096\,\text{s}$. All data points after t_0 are discarded and time is shifted so that the disk stops at $t = 0$. Finally we discard data points before $t = -0.5\,\text{s}$ to capture only the end of the motion.

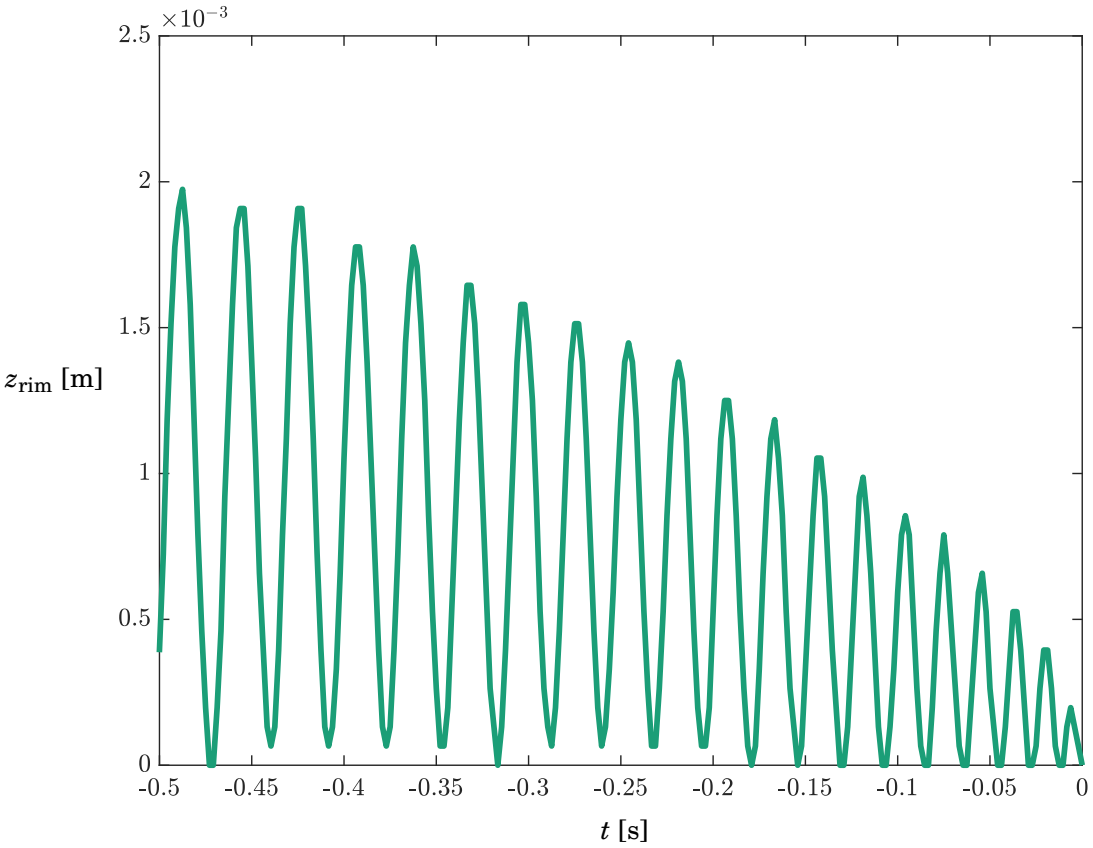

Figure 3.11: The vertical height of the bottom edge of the disk during the last 0.5 s of the motion.

The resultant $z_{\text{rim}}(t)$ data, plotted in fig. 3.11, shows oscillations increasing in frequency and decreasing in amplitude. Even in $z_{\text{rim}}(t)$ the abrupt nature of the stop is visible. The disk completes roughly 20 oscillations in the final 0.5 s, giving an average frequency of 40 Hz. The final oscillation has an instantaneous frequency of 72 Hz. This is less than the estimates of McDonald and McDonald [73], but likely due to the differences in sampling rate and resolution. During the final oscillation, the contact point is moving at $17\,\text{m}\,\text{s}^{-1}$ or around $60\,\text{km}\,\text{h}^{-1}$.

In the final oscillation shown in fig. 3.11, peaking around $t = -0.006\,\text{s}$, the rim is only 0.2 mm

above the base-plate. Such small oscillations are close to the resolution of the data δ, resulting in rough data. Furthermore, the high frequency of the oscillations caused some of the peaks and troughs to be truncated by the time sampling. This is ignored in the subsequent analysis, but could be mitigated by an appropriate smoothing.

3.2.5 Computing the state variables ϕ and ψ

While $z_{\text{rim}}(t)$ carries useful information, ϕ and $\dot{\psi}$ are required to estimate the energy in eq. (3.8). At each peak of $z_{\text{rim}}(t)$, the underside of the disk faces the camera directly, as in fig. 3.6, and the nutation angle of the disk, ϕ, is given by eq. (3.9).

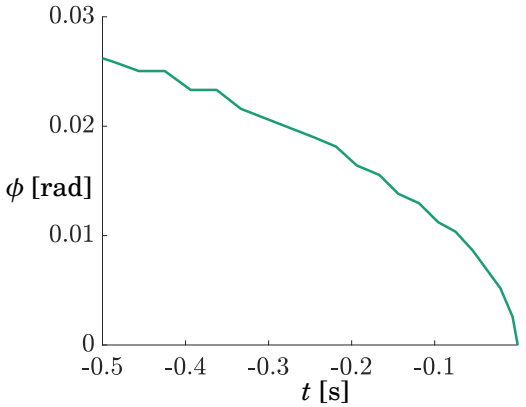

Figure 3.12: Reconstruction of ϕ from the experiment footage.

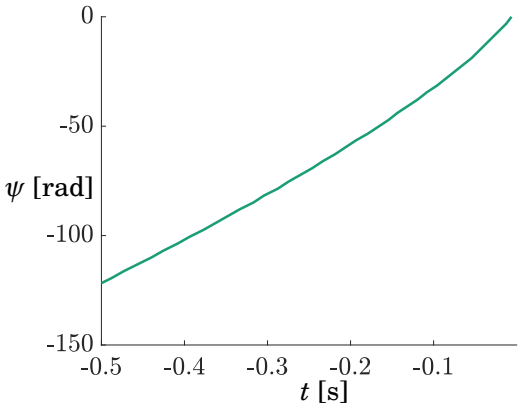

Figure 3.13: Reconstruction of ψ from the experiment footage.

This sampling reduces the time resolution of the data from one data point every $1/480^{\text{th}}$ of a second to one data point per peak in $z_{\text{rim}}(t)$. Improvements are discussed in Section 3.2.7. Between each peak, the disk precesses by 2π. Therefore we compute ψ by incrementing 2π each peak in $z_{\text{rim}}(t)$. Alternatively, the resolution may be doubled by incrementing ψ by π each peak or trough. As with $z_{\text{rim}}(t)$, we zero the ψ time series such that the motion ends at $\psi = 0$. McDonald & McDonald [73] determine ψ by the same method. The ϕ and ψ data are shown in figs. 3.12 and 3.13. In fig. 3.12, we see the classic perpendicular decrease in ϕ that has been observed in other experiments [68, 71]. The ϕ variable does not appear to oscillate, but this may be due to the sampling frequency.

We require $\dot{\psi}$ to estimate the energy of the disk. The derivative at a time t_i is estimated using the slope of the succeeding line segment

$$\frac{\mathrm{d}\psi_i}{\mathrm{d}t} \approx \frac{\psi_{i+1} - \psi_i}{t_{i+1} - t_i}. \tag{3.11}$$

We compute the energy using eq. (3.8) and show the results in fig. 3.14. Note the similarity with the ϕ time series which suggests that the potential energy dominates the energy.

To determine the energy exponent, n, we fit the power law, eq. (3.2), to the energy in fig. 3.14. By shifting time so that the stop occurs at $t = 0$, the energy power law is simply $E = A_e t^n$.

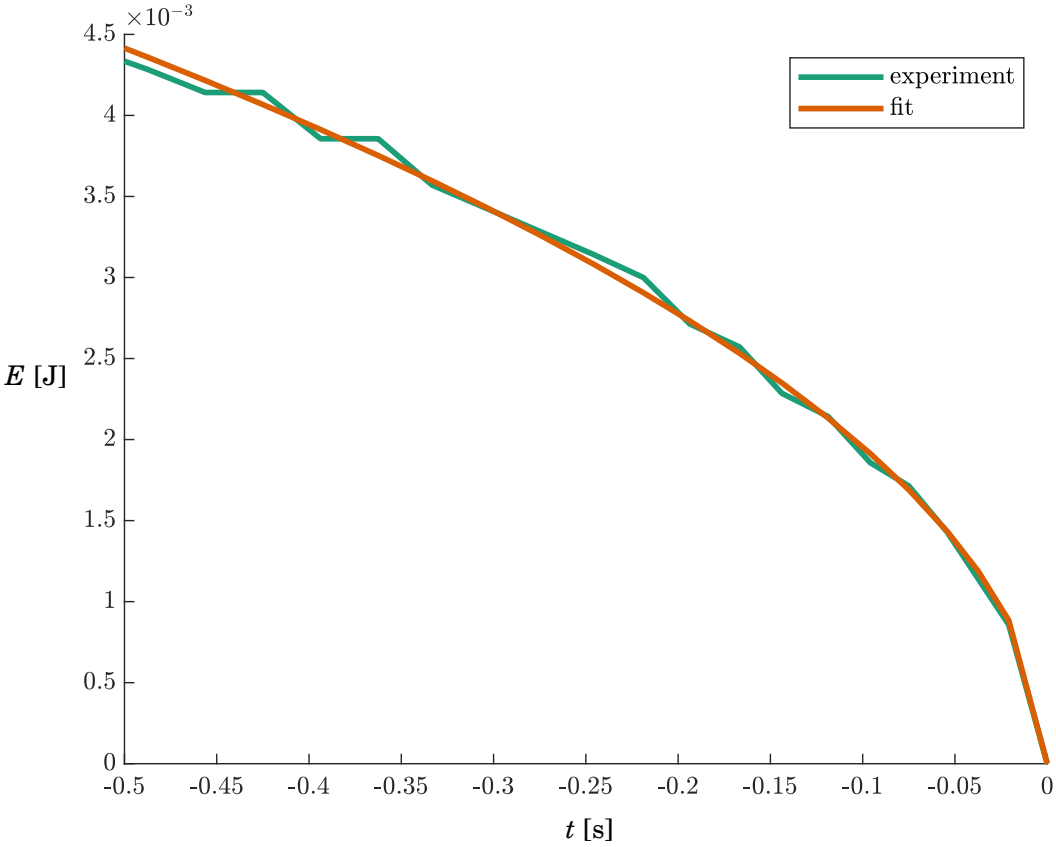

Figure 3.14: The energy power law that best fits the experimental data. We fit $E = A_e t^n$ to the experimental energy data using a least squares approach. The fit has $A_e = 0.0063$ and $n = 0.502$, very close to square root-like behaviour.

Minimising the squared error between the experimental energy and the power law gives estimates for A_e and n. In fig. 3.14, the fit for this experiment is shown with $A_e = 0.0063$ and $n = 0.502$ which shows a good agreement with the literature [68, 73].

3.2.6 Results

Due to the noise in the data we repeat the experiment twelve times on base-plates made of mild steel, stainless steel, pine, oak, acrylic, Teflon and silicone to determine if the energy power law depends on the material of the base-plate. We also spin the disk on the concave base-plate that accompanies the commercial Euler's disk.

These materials were chosen for their wide range of physical properties. For example, mild and stainless steel have a very high Young's modulus, 210 GPa and 180 GPa respectively, while silicone and Teflon have a much lower Young's modulus, 0.4 GPa and 0.0793 GPa respectively. Other material values are shown in table 3.1.

Accurate values of the coefficient of Coulomb friction are difficult to find and dependent upon

Material	Poisson ratio, ν	YM, GPa	μ
mild steel	0.303	210	0.147
stainless steel	0.305	180	0.134
oak	0.369	11	0.181
pine	0.335	9	0.201
acrylic	0.37	3.2	0.204
Teflon	0.42	0.4	0.094
silicone	0.5	0.0793	0.373

Table 3.1: Table of base-plate material properties [34, 37, 38, 41, 72]. Coefficient of Coulomb friction, μ, is calculated from data obtained in an inclined plane experiment. The concave base-plate is omitted.

the surface finish of both the disk and the base-plate material. To obtain approximate values we repeat the classical experiment of a block on an inclined plane. We place Euler's disk on each base-plate and tilt the base-plate until slipping occurs. The angle of the base-plate, α, at the onset of slip determines the coefficient of Coulomb friction via $\mu = \tan\alpha$. The average coefficients of Coulomb friction after 10 repeats are recorded in table 3.1. Teflon has a famously low coefficient of Coulomb friction, measured to be $\mu = 0.094$, while silicone has the largest coefficient at $\mu = 0.373$.

The energy exponents for each set of experiments are shown in a box plot in fig. 3.15. All the exponents lie in the range $n \in [0,1]$: the perpendicular decrease in energy is common to all base-plates. However, there are differences between the materials. For example, the mean energy exponent for silicone is $n = 0.69$ while for mild and stainless-steel it is $n = 0.49$ and $n = 0.45$ respectively. There is no overlap between the box plots for steel and silicone suggesting that the difference in material properties translates to a difference in energy exponent. It remains to be seen which material properties affect the motion of the disk. We discuss four properties: Young's Modulus, Poisson's ratio, coefficient of Coulomb friction and surface roughness.

Figure 3.16 shows the variation of n as a function of the material parameters. Young's modulus measures the stiffness of a solid and is defined as the ratio of stress to axial strain. A material with a large Young's modulus is difficult to extend or compress. Although frequently modelled as rigid bodies, the disk and base-plate are not perfectly rigid. Instead of contacting the base-plate at a point, the disk touches the base-plate over a contact region. The size of this contact region is partly determined by the material's Young's modulus [58]. Stiffer materials with larger Young's moduli have smaller contact regions [58] and smaller contact regions result in decreased rolling resistance. Correspondingly, a rough negative trend of n with Young's modulus is visible in fig. 3.16a.

Poisson's ratio is defined as the ratio of transverse to axial strain. In the elastic Hertzian model of contact, Poisson's ratio also affects the size and shape of the contact region [58]. Figure 3.16b shows the energy exponent, n, as a function of the Poisson's ratio. Unlike Young's Modulus, we see a positive trend, suggesting that larger Poisson's ratios give rise to larger exponents.

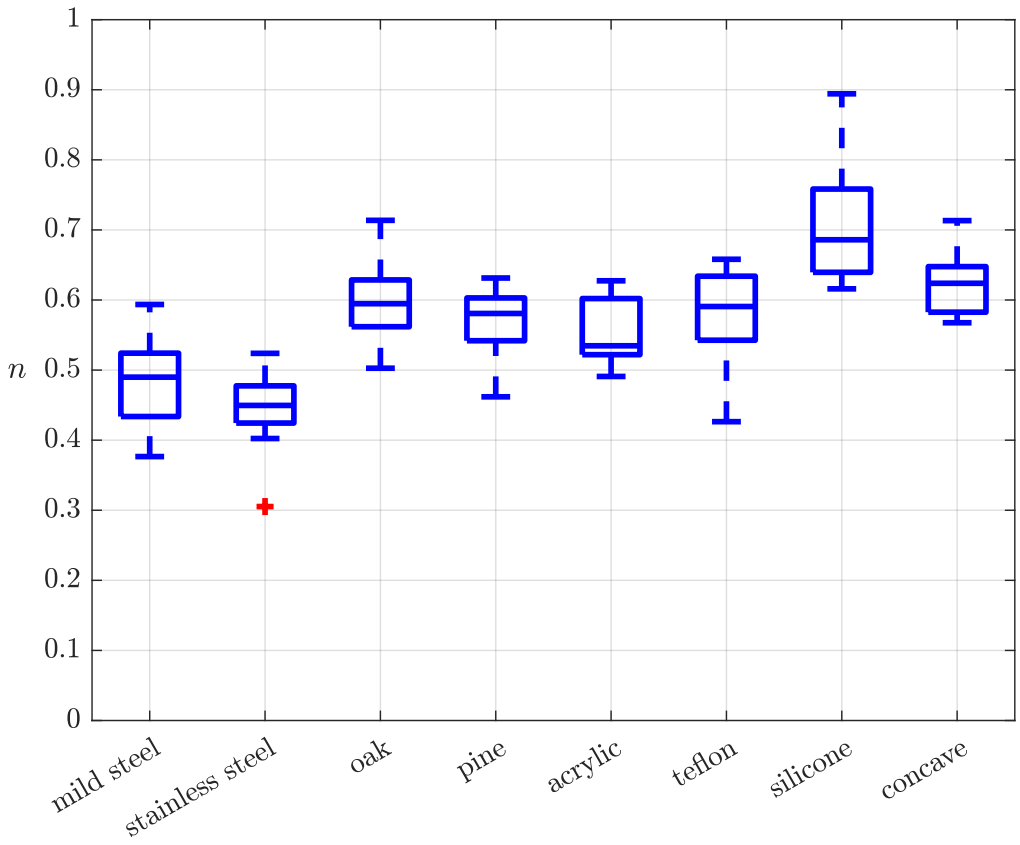

Figure 3.15: Box plots of the energy exponent, n, estimated from experiments. Euler's disk was spun twelve times on each base-plate material. Materials are ordered by decreasing Young's modulus, except for the concave base-plate for which the Young's modulus is not known. Outlier shown in red.

Teflon was included in the experiments for its low coefficient of Coulomb friction but the exponent does not stand out in fig. 3.15. In fig. 3.16c there is a similar weak positive trend when compared to the Poisson's ratio. It is perhaps surprising that a trend is visible. If as assumed, the disk is rolling at the end of the motion, then the coefficient of friction does not affect the energy dissipation. Even if the disk does slip, Coulomb friction has been shown to be dominated by other dissipation mechanisms [68].

It is likely that surface roughness affects the energy exponent. Mild and stainless steel are similar materials, but the base-plates have differing finishes. The stainless steel base-plate has a far smoother finish, possibly translating into a lower energy exponent. However, the two exponents for mild and stainless steel are too close to draw conclusions.

A possible reason for silicone's large exponent is its short spinning time. A short spinning time means that the 0.5 s sample may capture other dissipation mechanisms as well, not just the dominant mechanism. For example, if the sample length is the whole motion, from release to

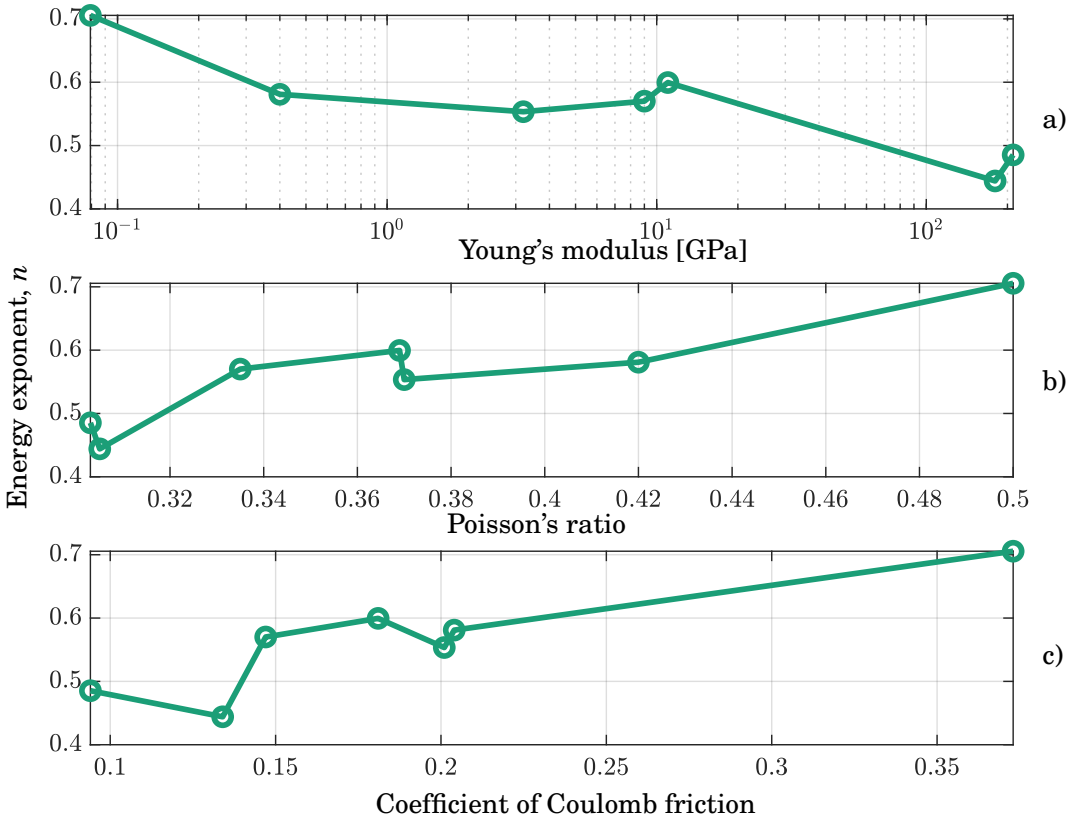

Figure 3.16: Plots of the energy exponent, n, as a function of the material parameters. Young's modulus in log scale shows a negative trend, while Poisson's ratio and the coefficient of Coulomb friction show a positive trend. The concave base-plate is not included.

halt, then the energy loss at the beginning of the motion may be almost entirely due to classical rolling friction with an exponent of $n = 2$. Towards the end of the motion, the mechanism with the lowest n will dominate, but the fit may be skewed by classical rolling friction, thereby increasing the apparent energy exponent. Leine [68], noted that $n = 2/3$ for $t \ll t_0$ and $n = 1/2$ for $t \approx t_0$, and suggested that dry and viscous contour friction are capable of explaining the motion. Although not possible for these data, it would be interesting to compute the energy exponent, n, for different sample lengths, e.g. 1 s, 0.1 s. A shorter sample length would not contain enough data points for an accurate fit and longer sample lengths run into the problem of frame skips in the data, an issue discussed further in Section 3.2.7.

The disk spins for the longest time on the concave base-plate, which has a relatively large energy exponent, $n = 0.62$. This could be due to the base-plates' material properties. An alternative explanation is that the flat base-plates experience dissipation due to a thin layer of air between the disk and base-base-plate. Bildsten [16] estimated that the energy exponent for this air resistance mechanism is $n = 4/9$ [16]. The concave base-plate does not experience the air resistance

mechanism due to the large gap between the disk and the base-plate, resulting in a larger observed energy exponent. We are further encouraged by the proximity of $n = 0.62$ to the estimate of dry contour friction $n = 2/3$. This suggests that dry contour friction dominates on the concave base-plate, but further investigation is required.

Material combination	s. steel	oak	pine	acrylic	Teflon	silicone	concave
m.steel	0.1123	0.0003	0.0018	0.0075	0.0017	0.000	0.000
s. steel		0.0000	0.0000	0.0000	0.0000	0.0000	0.0000
oak			0.2248	0.0556	0.4900	0.0019	0.2749
pine				0.4097	0.6541	0.000	0.0123
acrylic					0.2476	0.000	0.0012
Teflon						0.0004	0.0721
concave							0.0085

Table 3.2: Comparison of p-values between energy exponents for different materials in fig. 3.15. Comparisons with a p-value less than 0.0018 are highlighted blue, suggesting that there is a statistically significant difference between these materials.

We apply a two-sample t-test for equal means to each pair of materials to determine if the difference in the mean energy exponent is statistically significant. The p-value describes the likelihood that the two sets of experimental data have the same mean values of energy exponent. Multiple samples are compared, so we apply the Bonferroni correction [84] to reduce the number of false positives. The correction divides the original critical p-value of 0.05 by the number of unique comparisons, 28, to give the critical p-value, $p = 0.0018$. The results of the statistical tests are shown in table 3.2. Silicone differs from almost all other materials, as do stainless and mild steel. The other materials, oak, pine, acrylic and Teflon do not have statistically significant differences in means.

We may be sure that the differences in energy exponent for the steel base-plates is not due to randomness or noise in the experimental measurements. The question for the analytic models in Chapter 4 is, Where does the material dependence come from?

3.2.6.1 Effect of the disk's rim on the energy exponent

The commercial Euler's disk has a rounded bottom rim, facilitating smooth contact with the base-plate. The top rim of the disk is much less rounded. Therefore, repeating the experiments with the disk upside-down gives an easy comparison between the two rims. The same experiments were also performed with a brass disk mentioned in section 3.2.2. Machined on a CNC router, it has approximately the same size and weight as Euler's disk, but with an even sharper rim. The results can be found in Tables B.2 and B.3. A sharper rim results in a narrower contact region, and may affect the energy exponent. The concave base-plate was omitted to avoid scratches from the brass disk.

A collection of the results is shown in fig. 3.17. It is difficult to see any correlation between sharpness of edge and exponent. The energy exponent for the brass disk is very similar to Euler's disk despite the material and physical differences. Again, we perform a two-sample t-test for equal means between disks, keeping the material constant. The p-values are shown in Table 3.3. Again, we apply a Bonferroni correction to the critical p-value. The number of comparisons is 21, three per base-plate material for each of the seven materials (the concave base-plate was omitted to avoid scratches). Therefore, the critical p-value is $p = 0.05/21 = 0.0024$. There is only one case in Table 3.3 where the difference in means is statistically significant: the brass and flipped Euler's disk on the oak base-plate. This suggests that the sharpness of rim is not an important factor in determining n.

Material combination	Euler & Brass	Euler & Euler flipped	Euler flipped & Brass
mild steel	0.0252	0.0208	0.8258
stainless steel	0.1232	0.7246	0.0319
oak	0.0408	0.3982	0.0024
pine	0.0110	0.0027	0.6723
acrylic	0.7054	0.0303	0.1046
Teflon	0.1353	0.4736	0.1452
silicone	0.0443	0.1352	0.3668

Table 3.3: Comparison of p-values between energy exponents for different materials in fig. 3.17. Combinations with a p-value less than 0.0024 are highlighted blue, denoting statistically significant differences between disks.

3.2.7 Issues and improvements to the experiments

The experiment was limited by the temporal resolution of the data. By only computing ϕ and ψ once per oscillation in $z_{\text{rim}}(t)$, many potential data points are discarded. For example, in fig. 3.11, there are 20 oscillations in the final 0.5 s corresponding to 20 data points in fig. 3.12. Compare this with the 240 frames captured in the same time. To compute ϕ every frame requires a more involved setup, but could be achieved by an improved data analysis algorithm or another synchronised camera. However, the simplicity and robustness of the approach enabled many repeats for statistical analysis.

Another issue is the lack of knowledge of all the state variables. We use the stationary rolling assumption to eliminate $\dot{\theta}$ from the energy in eq. (3.8). However, as seen in Section 3.3, the stationary rolling assumption may not be accurate. An improved experiment might compute θ directly, eliminating the need for the simplifying assumption. This issue could also be solved by filming the disk with multiple, synchronised cameras and then making use of markings on the disk to determine the rotation angle θ.

The disk's horizontal position drifts in the course of its motion. This is most obvious in the footage on a stainless steel base-plate. The drift slows towards the end of the motion, so it is

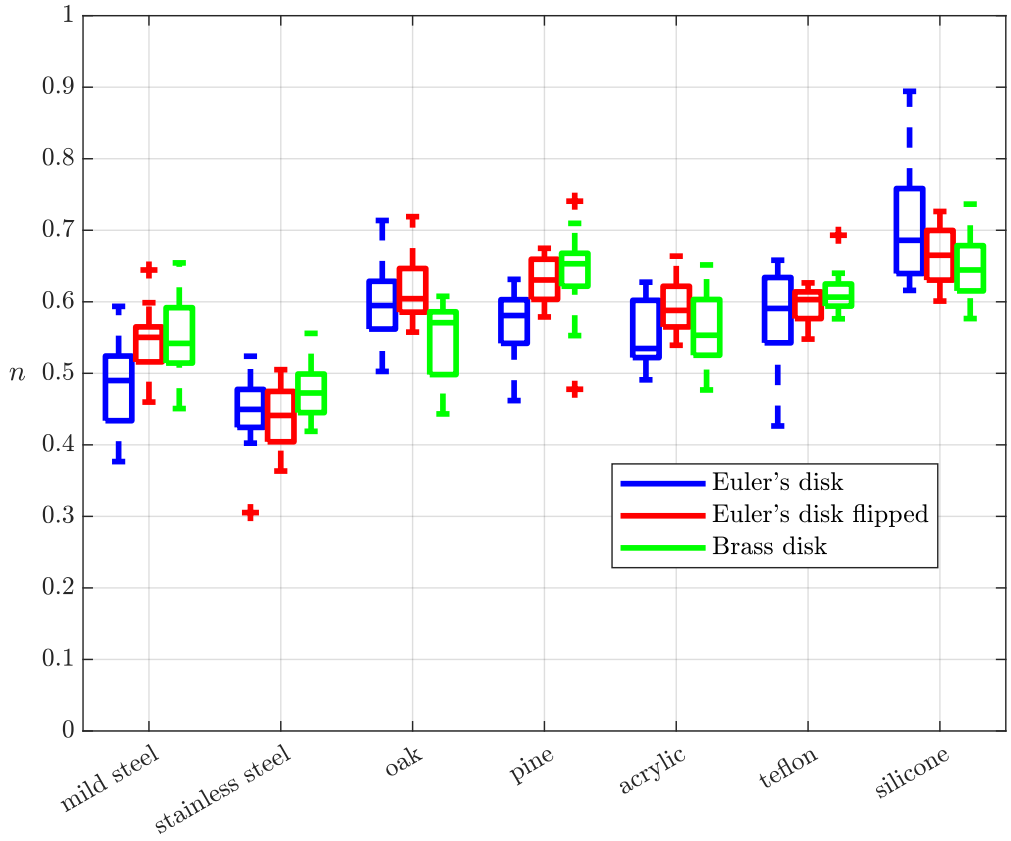

Figure 3.17: Box plots of the energy exponent, n, for the Euler's disk, flipped Euler's disk and the brass disk experiments. The raw data is given in Section B.

assumed that the disk is oscillating in place for the final 0.5 s before the halt. Small errors in the position of the disk are unimportant, because the middle of the rim of the disk appears very flat to the camera (fig. 3.8) so any lateral movement results in only a small error. If the position of the disk could be computed at each frame then good quality data could be obtained for the entirety of the disk's motion and not just the final 0.5 s.

The footage suffered from occasional frame skips due to the camera's inability to cope with the quantity of data being produced. This is a common issue with slow-motion cameras where the limiting factor is the bandwidth required to save the data. A trade-off between resolution and frame-rate takes place. The issue was mitigated by simply repeating the experiment if any frame-skips were visible in the final 0.5 s. The peak of $z_{\text{rim}}(t)$'s final oscillation was 3.7px, averaged over all the experiments, which is practically at the limit of the camera's capability, suggesting that the experiment might benefit from higher resolution cameras. Purpose-made slow-motion cameras with higher resolutions and frame-rates would eliminate these issues. Flickering lights at 50 Hz due to the mains power supply was visible in the footage. Flicker-free lights were obtained for Section 3.3.

3.3 Continued vertical rotation experiments

On viewing the final frames in the experiments of the previous section, it was noticed that the disk appears to continue to rotate about the vertical axis after falling flat. If true, there are a number of consequences for Euler's disk. Firstly, the presence of continued rotation invalidates the stationary rolling approximation eq. (3.7). This is explored further in Chapter 4. Secondly, the rotation agrees with the experiments of Borisov et al. [19], which predict that the disk loses contact with the base-plate at the halt. Thirdly, it suggests slippage: if the disk falls flat and continues to rotate then it is Coulomb friction that must remove the remaining energy and bring the disk to a stop.

In this section, we perform an experiment to isolate the continued rotation. We expose the vertical rotation by drawing a strip across the diameter of the top of the disk and filming the disk from above. By appropriate placement of a mirror, we track the rotation and inclination of Euler's disk simultaneously. A diagram of the experimental setup is shown in fig. 3.18 and fig. 3.19 shows a single frame of the footage. We proceed to compute the rotation of the strip in terms of the state variables. Then in section 3.3.2, we outline the data extraction before discussing the results in section 3.3.3.

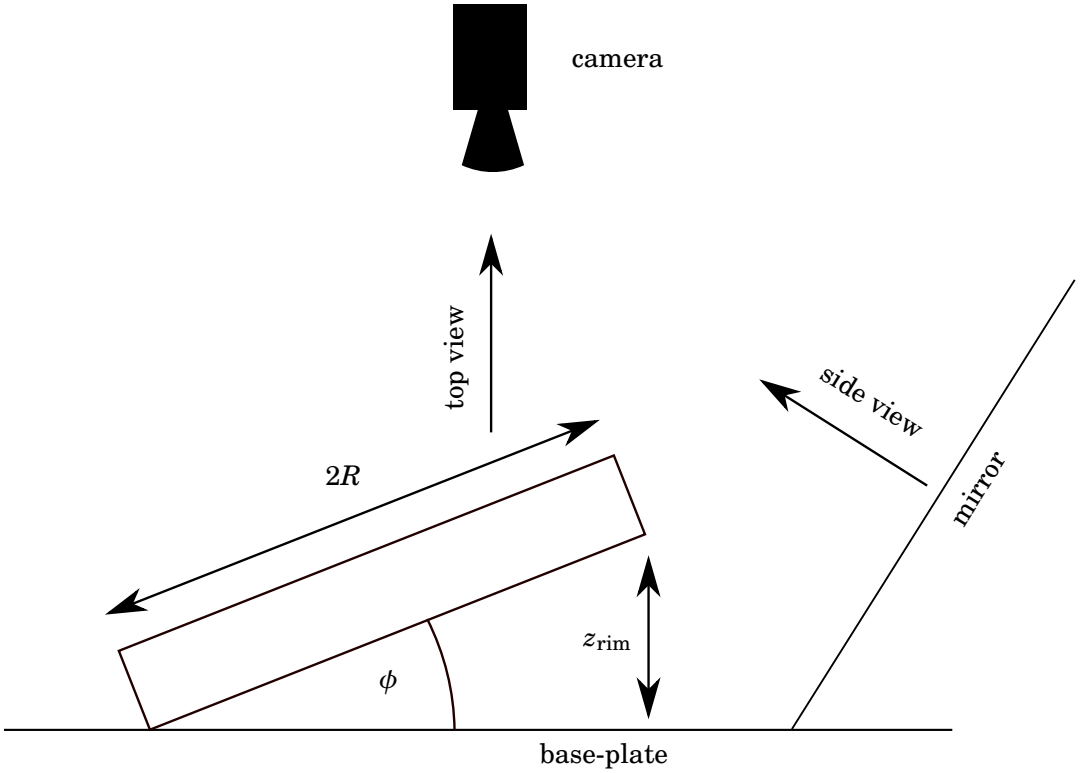

Figure 3.18: Experimental set up for the vertical rotation experiments. Footage is captured from above. A frame is shown in fig. 3.19.

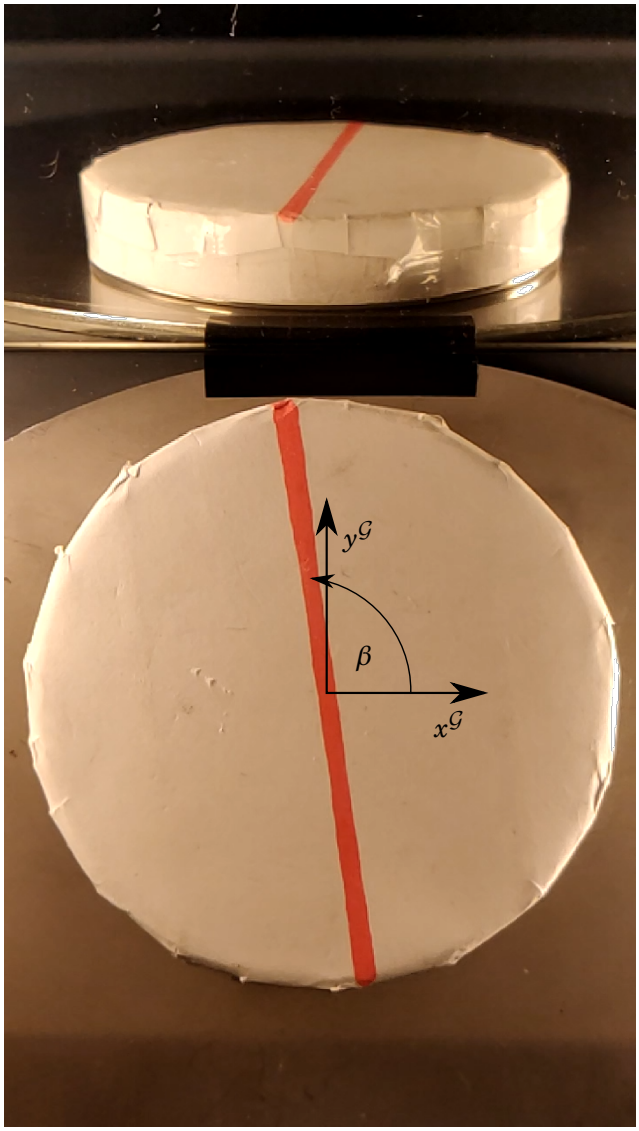

Figure 3.19: Frame from the vertical rotation experiments on stainless steel. The image contains two views of the disk: the top view shows the disk from the side through the mirror and is used to compute ϕ in the manner of Section 3.2. The bottom shows the plan view of the disk. The red strip is used to calculate the vertical rotation, $\dot{\beta}$. The black tape placed on the base-plate was used to increase contrast.

3.3.1 Rotation of the strip

To break the rotational symmetry of the disk, a red strip is drawn across the diameter of the disk. Let β be the angle that the strip makes with the $x^{\mathcal{G}}$ axis in fig. 3.19. The angle β does not correspond exactly to the disk's rotation about its symmetry axis, because the angle of the strip seen by the camera changes as ϕ increases or decreases. Therefore, we must compute β in terms of the state variables ϕ, ψ and θ. We define the top face of disk, D, in polar coordinates. The radius is parametrised by r and the angle by α

$$D = \left\{(r\cos\alpha, r\sin\alpha, 2H)^\intercal \,|\, 0 < r < R, -\pi < \alpha < \pi\right\}. \tag{3.12}$$

The strip, L, is aligned with an initial angle $\alpha = \beta_0$ and stretches across the diameter of the disk such that

$$L = \left\{(r\cos\beta_0, r\sin\beta_0, 2H)^\intercal \,|\, -R < r < R\right\}. \tag{3.13}$$

The orientation of the disk in fig. 3.1 was determined up to the final rotation, θ. The strip is fixed to the disk and rotates with θ in the final frame $\mathcal{F}$, but it is filmed by the camera in the global frame $\mathcal{G}$. Therefore, we must shift the strip from the frame $\mathcal{F}$ to $\mathcal{G}$. The rotation matrices defining successive transformations between frames are

$$\mathrm{R}_{\mathcal{GI}} = \begin{pmatrix} \cos\psi & \sin\psi & 0 \\ -\sin\psi & \cos\psi & 0 \\ 0 & 0 & 1 \end{pmatrix}, \quad \mathrm{R}_{\mathcal{IB}} = \begin{pmatrix} \cos\phi & 0 & \sin\phi \\ 0 & 1 & 0 \\ -\sin\phi & 0 & \cos\phi \end{pmatrix}, \quad \mathrm{R}_{\mathcal{BF}} = \begin{pmatrix} \cos\theta & \sin\theta & 0 \\ -\sin\theta & \cos\theta & 0 \\ 0 & 0 & 1 \end{pmatrix}. \tag{3.14}$$

The combined rotation from $\mathcal{G}$ to $\mathcal{F}$ is given by the composition

$$\mathrm{R}_{\mathcal{GF}} = \mathrm{R}_{\mathcal{BF}}\mathrm{R}_{\mathcal{IB}}\mathrm{R}_{\mathcal{GI}}, \tag{3.15}$$

and the rotation from $\mathcal{F}$ to $\mathcal{G}$ is given by the inverse matrix $\mathrm{R}_{\mathcal{FG}} = \mathrm{R}_{\mathcal{GF}}^{-1}$. The position of the strip in the global frame is

$$L^{\mathcal{G}} = \mathrm{R}_{\mathcal{FG}} L. \tag{3.16}$$

Filming from above, the camera views a projection of $L^{\mathcal{G}}$ in the $x^{\mathcal{G}}$-$y^{\mathcal{G}}$ plane. The $x^{\mathcal{G}}$ and $y^{\mathcal{G}}$ components of $L^{\mathcal{G}}$ are

$$\begin{aligned} L_x^{\mathcal{G}} =& (\cos\theta\cos\phi\cos\psi - \sin\theta\sin\psi) r\cos\beta_0 + (-\sin\theta\cos\phi\cos\psi - \cos\theta\sin\psi) r\sin\beta_0 \\ & - 2H\sin\phi\cos\psi, \end{aligned} \tag{3.17}$$

$$\begin{aligned} L_y^{\mathcal{G}} =& (\cos\theta\cos\phi\sin\psi + \sin\theta\cos\psi) r\cos\beta_0 + (-\sin\theta\cos\phi\sin\psi + \cos\theta\cos\psi) r\sin\beta_0 \\ & - 2H\sin\phi\sin\psi, \end{aligned} \tag{3.18}$$

where r ranges over the diameter of the disk $[-R,R]$. The angle, β, that the strip makes with the $x^{\mathcal{G}}$ axis is

$$\begin{aligned}\beta &= \arctan\left(\frac{L_y^{\mathcal{G}}|_{r=R} - L_y^{\mathcal{G}}|_{r=-R}}{L_x^{\mathcal{G}}|_{r=R} - L_x^{\mathcal{G}}|_{r=-R}}\right), \\ &= \arctan\left(\frac{\sin\psi\cos\phi(\sin\theta\sin\beta_0 - \cos\beta_0\cos\theta) - \cos\psi(\sin\theta\cos\beta_0 + \sin\beta_0\cos\theta)}{\cos\psi\cos\phi(\sin\theta\sin\beta_0 - \cos\beta_0\cos\theta) + \sin\psi(\sin\theta\cos\beta_0 + \sin\beta_0\cos\theta)}\right).\end{aligned} \tag{3.19}$$

The dependence on the height of the disk, H, has disappeared and does not affect the angle β. Applying multiple angle formulae to eq. (3.19) gives

$$\beta = \arctan\left(\frac{\tan\psi\cos\phi + \tan(\theta+\beta_0)}{\cos\phi - \tan\psi\tan(\theta+\beta_0)}\right). \tag{3.20}$$

Differentiating eq. (3.20) with respect to time yields the angular velocity of the strip

$$\dot{\beta} = \dot{\psi} + \frac{\dot{\phi}\sin\phi\sin(\theta+\beta_0)\cos(\theta+\beta_0) + \dot{\theta}\cos\phi}{1 - \sin^2\phi\cos^2(\theta+\beta_0)}, \tag{3.21}$$

then taking a small ϕ approximation we obtain

$$\dot{\beta} = \dot{\psi} + \dot{\theta} + \mathcal{O}\left(\phi^2\right). \tag{3.22}$$

As one would expect the angular velocity of the strip is approximately the same as the angular velocity of the disk about the $z^{\mathcal{G}}$ axis, $\omega_z^{\mathcal{G}} = \dot{\psi} + \dot{\theta}\cos\phi$. Therefore, $\dot{\beta}$ may be thought of as an $\mathcal{O}\left(\phi^2\right)$ approximation to the global vertical angular velocity. Computing ψ, as described in Section 3.2, would enable a complete description of the state of the disk through $\beta \approx \psi + \theta$. However, the $z_{\text{rim}}(t)$ data obtained in the following experiment has larger errors caused by a decrease in resolution. In Section 3.3, the disk was roughly 200px tall from rim to rim, while in fig. 3.19 the disk is about 100px tall.

In the next section, we compute β and ϕ from the experimental data and show that the disk continues to rotate after it has fallen flat.

3.3.2 Extracting data from the footage

Filming the disk in portrait with a mirror allows both ϕ and β to be obtained simultaneously avoiding the need for two synchronised cameras. For each experiment, the frame in fig. 3.19 is split into two images and analysed separately. The top portion of the frame views the disk from the side and is analysed as in Section 3.3, giving both ϕ and ψ. Due to the reduction in resolution, the derivatives are noisy and not computed. The bottom portion of the frame views the disk from above showing the strip.

To compute the angle β, we extract the pixels corresponding to the strip. The intensity of the frame is normalised by the mean RGB value of the pixels in the image, mitigating the changes in ambient light levels due to the oscillating top face of the disk. The individual RGB components of

the image are thresholded to produce a binary image. The red strip is characterised by high red and low blue and green values suggesting the following filter

$$\begin{cases} 1 & \text{if} \quad R(i,j) > r_{\text{thresh}} \quad \text{and} \quad G(i,j) < g_{\text{thresh}} \quad \text{and} \quad B(i,j) < b_{\text{thresh}} \\ 0 & \text{otherwise} \end{cases} \tag{3.23}$$

A pixel is assigned a value of 1 if it passes all the thresholds and a value of 0 if not. Applying this filter to fig. 3.19 results in a binary image of the strip. As with the intensity threshold in Section 3.2, the colour thresholds, r_{thresh}, b_{thresh} and g_{thresh} all require adjustment between experiments. After filtering, some frames contained a small number of isolated white pixels that did not correspond to the strip. To remove them we compute the largest connected component of pixels in the image using the MATLAB function BWCONNCOMP. The erroneous isolated pixels are discarded, leaving just the pixels corresponding to the red strip in fig. 3.20.

Having isolated the strip, we compute the angle β with respect to the horizontal. Consider the pixels in the connected component as a set of data points with x and y values equal to their position in the image. The obvious method to compute the angle of the strip is least squares regression, which solves for the line passing through the strip that minimises the sum of the squared errors in the y direction. However, least squares suffers from difficulties when the strip is aligned with the y axis.

Instead, we use Principal Component Analysis (PCA) [59], which computes a series of orthogonal vectors that correspond to the directions with maximum variation in the data. The first principal component, $\underline{v}$, is aligned with the long axis of the strip, the direction with the most variation. This component defines a line that minimises the sum of the squared perpendicular (rather than y) distances from the pixels [59]. The second principal component is orthogonal to the first and aligned with the short axis of the strip. Both principal components are plotted in fig. 3.20. To compute the angle of the strip, β, we take the arctan of the x and y components of the first principal component, $\underline{v}$

$$\beta = \arctan\left(\frac{v_y}{v_x}\right). \tag{3.24}$$

However, $\frac{v_y}{v_x}$ is discontinuous. At each $v_x = 0$, we increment β by $\pm\pi$ depending on direction of rotation to ensure β is continuous. The time series in β is shown in fig. 3.21, where β is shifted such that the disk stops at $\beta = 0$.

The β data has a far higher temporal resolution than the ϕ data in Section 3.2 because a new data point is produced at every frame rather than every oscillation of the disk. To estimate the spatial resolution, we zoom in on the end of motion, as shown in fig. 3.22. After the disk has come to a halt in fig. 3.22, the noise in β is roughly on the order of 5×10^{-3} rad or $3/100^{\text{th}}$ of a degree. The last half second of z_{rim} data is shown in fig. 3.23. The reduction in resolution results in worse quality data compared to fig. 3.11 in the experiments of Section 3.3.

The end of the motion is difficult to determine. To estimate it, we choose a point in fig. 3.22 after which β has certainly settled down. For example, we may safely say that the disk has

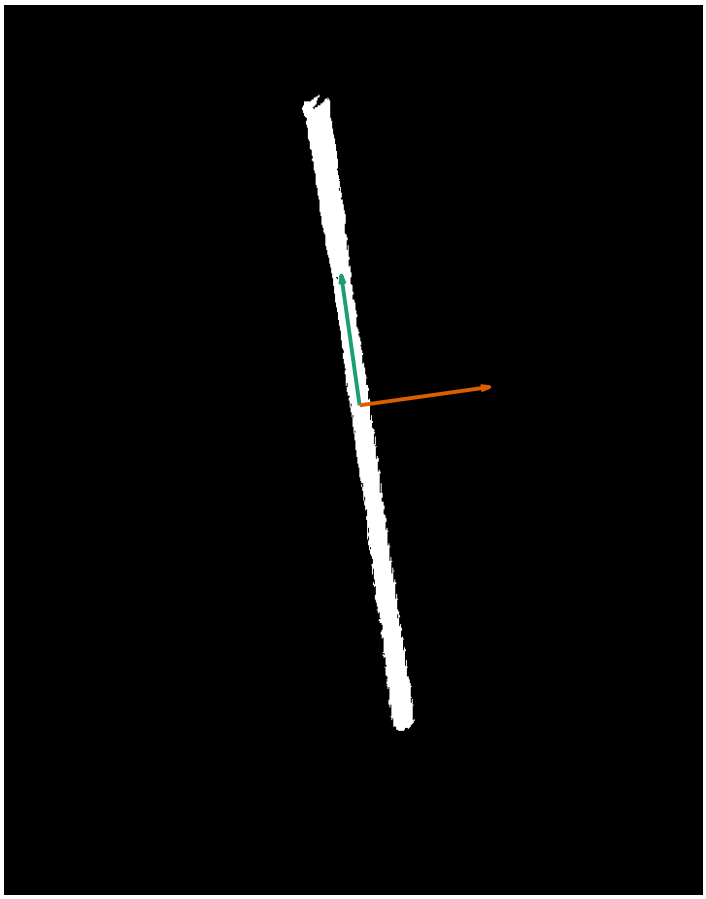

Figure 3.20: The bottom image of fig. 3.19 after filtering according to eq. (3.23) and removing the isolated pixels with BWCONNCOMP. The first principal component, aligned with the long axis of the strip, is shown in green. The second principal component, aligned with the short axis, is shown in orange.

come to a halt by $t = 6.92\,\mathrm{s}$ in fig. 3.22. Take a band in β, defined by the maxima and minima of the angle after $t = 6.92\,\mathrm{s}$. When the trajectory first intersects with this band, it is assumed the disk has stopped. After the intersection, β is as large as the noise, so further measurements are meaningless. The band is shown in fig. 3.22. The blue circle shows the first intersection with the band at $t = 6.879\,\mathrm{s}$. This time is denoted t_β, the stopping time for β. This extra stopping condition is not necessary when calculating the stopping time for ϕ, t_ϕ because of the discrete nature of z_{rim}. For example, in fig. 3.23, there are no more fluctuations in z_{rim} after $t_\phi = 6.833\,\mathrm{s}$. The disk therefore continues to rotate for $t_\beta - t_\phi \approx 0.05\,\mathrm{s}$. The difference in β and ϕ stopping times is explored further in Section 3.3.3 and fig. 3.27.

We also compute the angular velocity of the strip, $\dot{\beta}$ by numerically differentiating β with

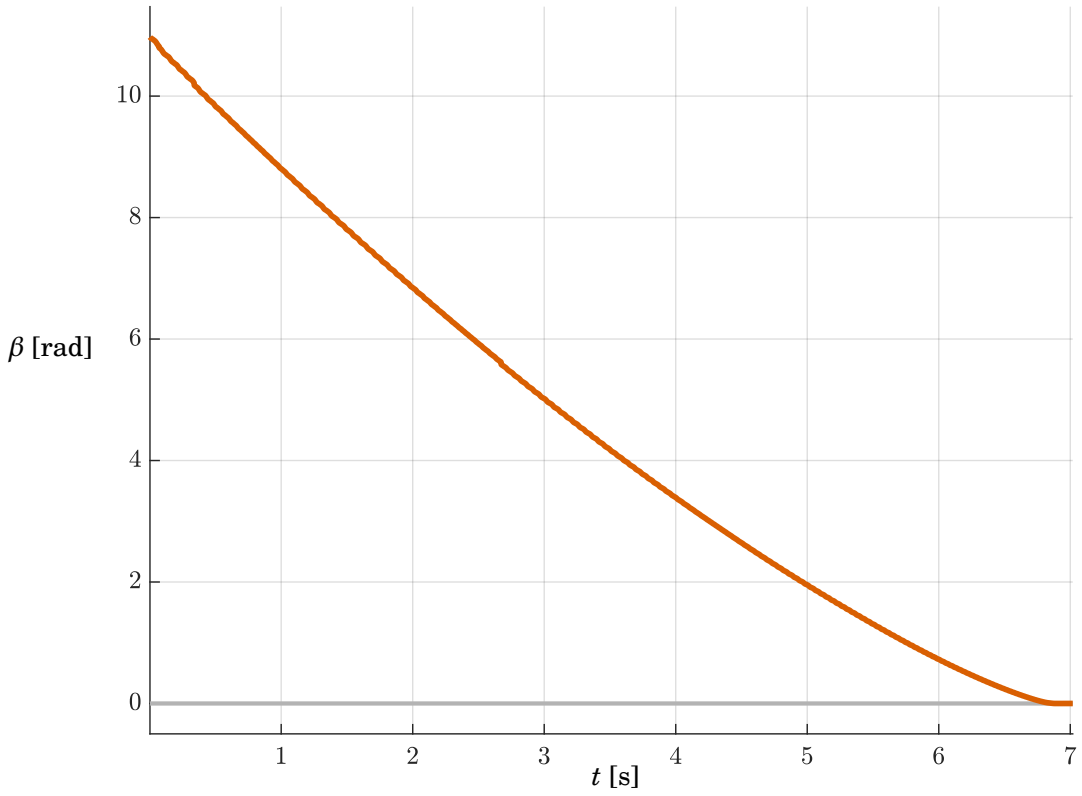

Figure 3.21: Time series of β extracted from the experimental footage.

eq. (3.11). The resultant data, shown in fig. 3.24, is rather rough, but the number of data points obtained means it is possible to smooth the data. We smooth β with a 5-point moving average and then numerically differentiate to give $\dot{\beta}$, also shown in fig. 3.24. Comparing the smoothed and unsmoothed time series during the final 0.5 s in fig. 3.25, the smoothed data captures all of the relevant behaviour.

Note the large spikes at $t \approx 0.1$, 0.3 and 2.7 in fig. 3.24. These spikes appear due to frame skips occurring in the footage, the small jumps in β are just visible in fig. 3.21 at the same times. The skips do not affect the analysis as none are present during the last half second of the motion.

In fig. 3.26, we show the smoothed $\dot{\beta}$ for the last half second of the motion and plot the stopping times t_β and t_ϕ. Not only are the stopping times unequal, suggesting that the disk continues to rotate after falling flat, but they divide $\dot{\beta}$ into two qualitatively different sections. Prior to t_ϕ, there are oscillations in $\dot{\beta}$, but after t_ϕ, there is a short constant section before a decrease towards $\dot{\beta} = 0$. The small increase in $\dot{\beta}$ that is visible after the stopping time, t_β, is due to the 5-point moving average. We may be sure that this effect is not due to the smoothing, because there are 21 frames between t_ϕ and t_β, larger than the window of the 5-point moving average. We repeat the experiment on mild and stainless steel base-plates, both lubricated and unlubricated

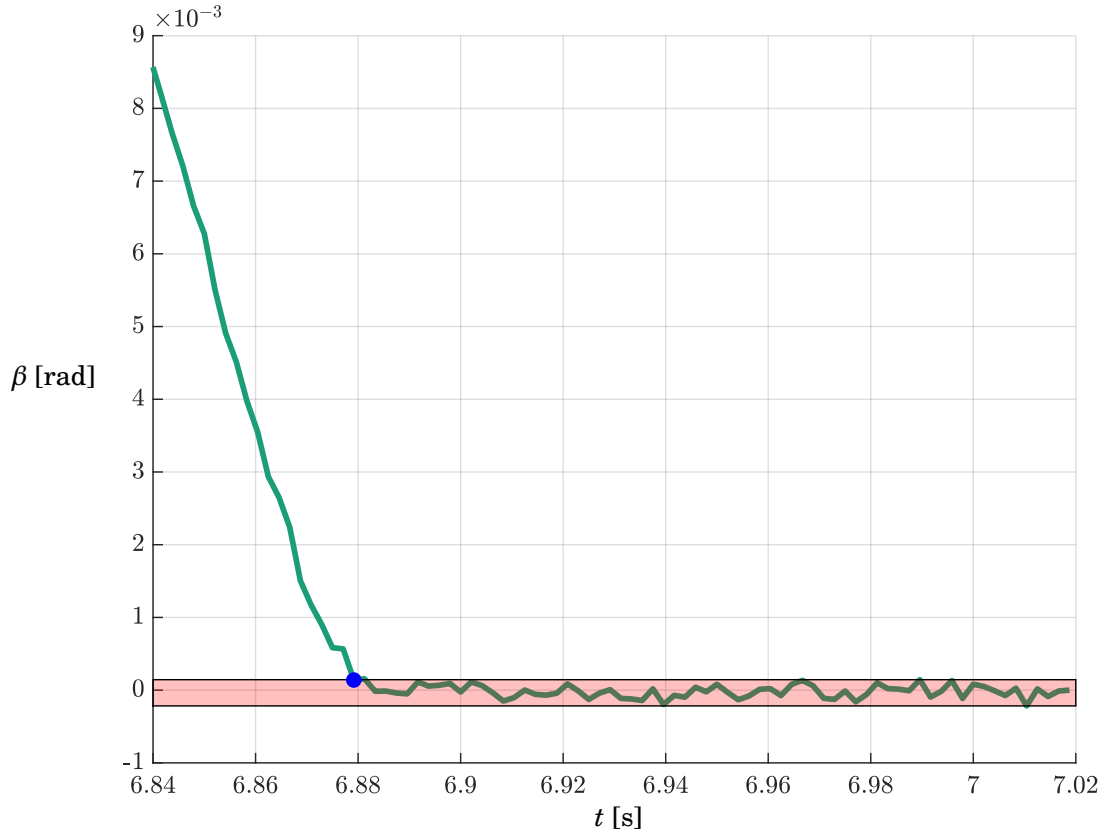

Figure 3.22: The end of the motion is taken to be the first intersection of β with the band defined by the maxima and minima of β after $t = 6.92\,\mathrm{s}$ when the disk has settled. The blue dot denotes this intersection. The maxima and minima also define the size of the noise, here roughly $5 \times 10^{-4}\,\mathrm{rad}$.

with a general purpose oil. We also perform the experiment on the concave base-plate.

3.3.3 Results

To explore the difference in stopping times we plot both β and $z_{\mathrm{rim}}(t)$ in fig. 3.27. It appears that the angle of the strip is still changing even after the disk has fallen flat. There is time for three more oscillations of $z_{\mathrm{rim}}(t)$, but, following the trend line, the disk should have fallen flat well before it stops spinning vertically.

In fig. 3.28, we show $\dot{\beta}$ from six experiments on the unlubricated stainless steel base-plate. Just as in fig. 3.26, the $\dot{\beta}$ dynamics appear to change at $t = t_\phi$. Before $t = t_\phi$, $\dot{\beta}$ is oscillatory and slowly decreasing. There is some variation between the size of the oscillations: for example, fig. 3.28b has oscillations of size about $0.4\,\mathrm{rad\,s^{-1}}$, while the fig. 3.28c has oscillations around $1.1\,\mathrm{rad\,s^{-1}}$ in size. After $t = t_\phi$, there is a qualitative change and $\dot{\beta}$ appears constant for a small period of time before decreasing to zero. Similar results were obtained for the mild steel base-

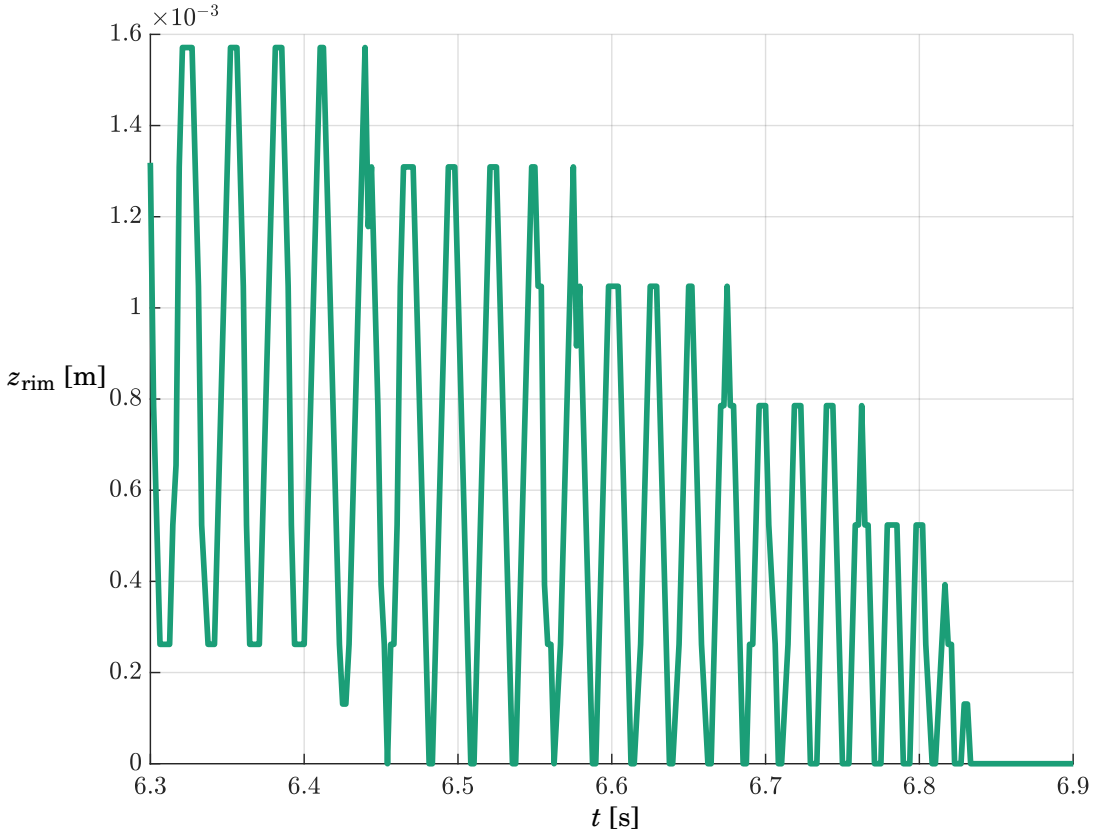

Figure 3.23: The z_{rim} data from the continued rotation experiments.

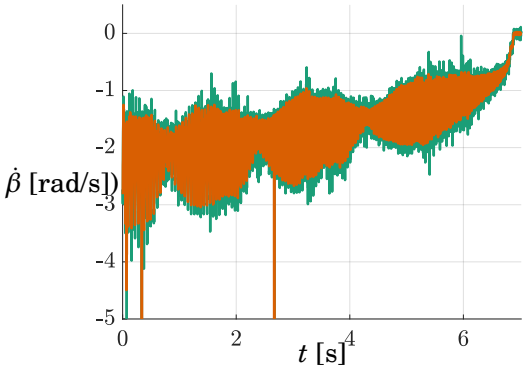

Figure 3.24: Unsmoothed and smoothed $\dot{\beta}$ time series. Three frame skips are visible at $t \approx 0.1$, 0.3 and 2.3.

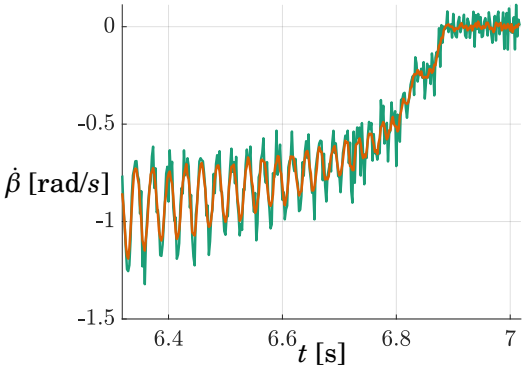

Figure 3.25: Unsmoothed and smoothed time series of $\dot{\beta}$ during the last 0.5 s.

plate.

If the disk has fallen flat but continues to rotate, one would expect that lowering the coefficient of Coulomb friction of the base-plate might increase $t_\beta - t_\phi$. The experiments on a stainless steel

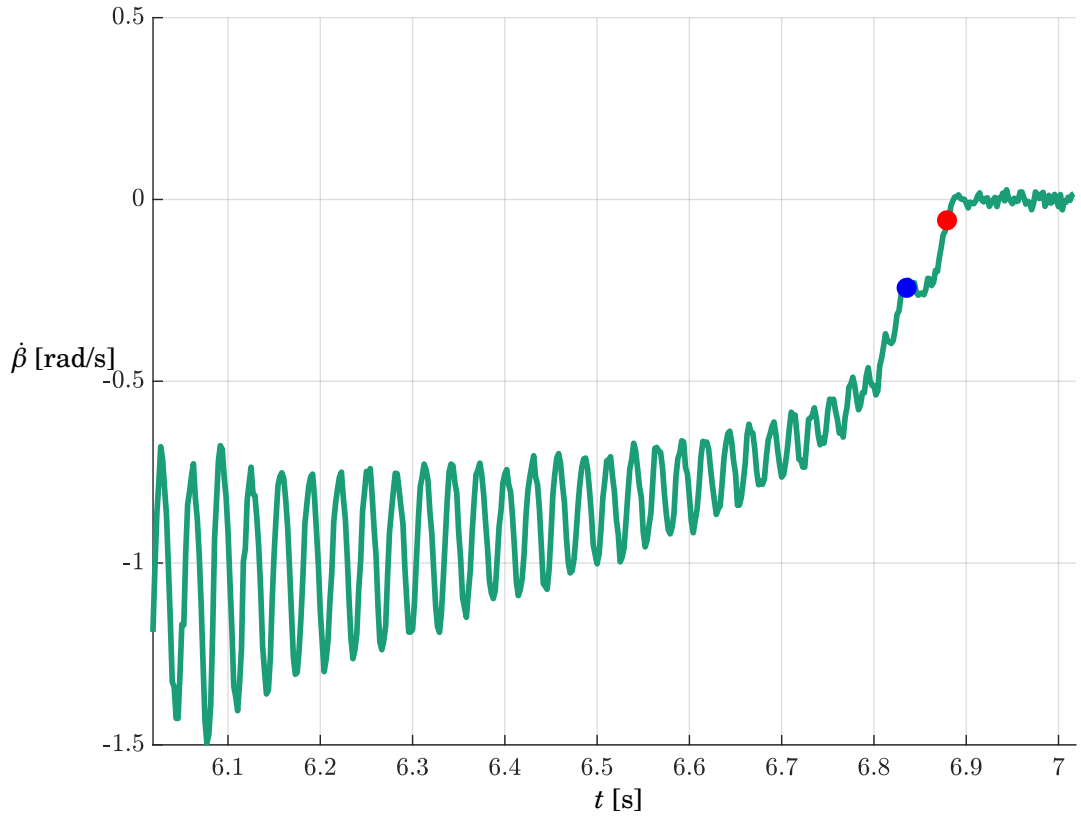

Figure 3.26: The smoothed angular velocity $\dot{\beta}$ during the last second of the data. The circles correspond to the stopping times t_ϕ (blue) and t_β (red).

base-plate, lubricated with general purpose oil, result in fig. 3.29. The time series look very similar to the unlubricated case, but the interval $t_\beta - t_\phi$ has increased and the constant portions are more visible. Figure 3.29c is an outlier caused by an abundance of lubricant; the disk fell flat and slid on a thin film of oil. Again, similar results were obtained for a lubricated mild steel base-plate. The mean interval, $t_\beta - t_\phi$, is 0.0403 s and 0.0600 s for unlubricated and lubricated stainless steel respectively (after discarding the outlier). For the mild-steel base-plate the intervals were 0.0385 s and 0.0431 s. In both cases, the interval increases. The 50% increase in $t_\beta - t_\phi$ for the stainless steel versus the 12% increase for mild steel is perhaps due to the differences in surface roughness allowing for more effective lubrication.

On repetition with the concave base-plate in fig. 3.30, the mean interval is $t_\beta - t_\phi = 0.0058$ s, far shorter than the other two base-plates. This interval is less than three frames in length. The discrepancy between the flat and concave base-plates can be explained by supposing that after falling flat, the disk is briefly supported by a layer of air. When supported by a thin film of air, there is negligible resistance to the continued rotation, resulting in the constant section of $\dot{\beta}$, observed in fig. 3.29. Then, when the disk makes contact with the base-plate, the rotation is

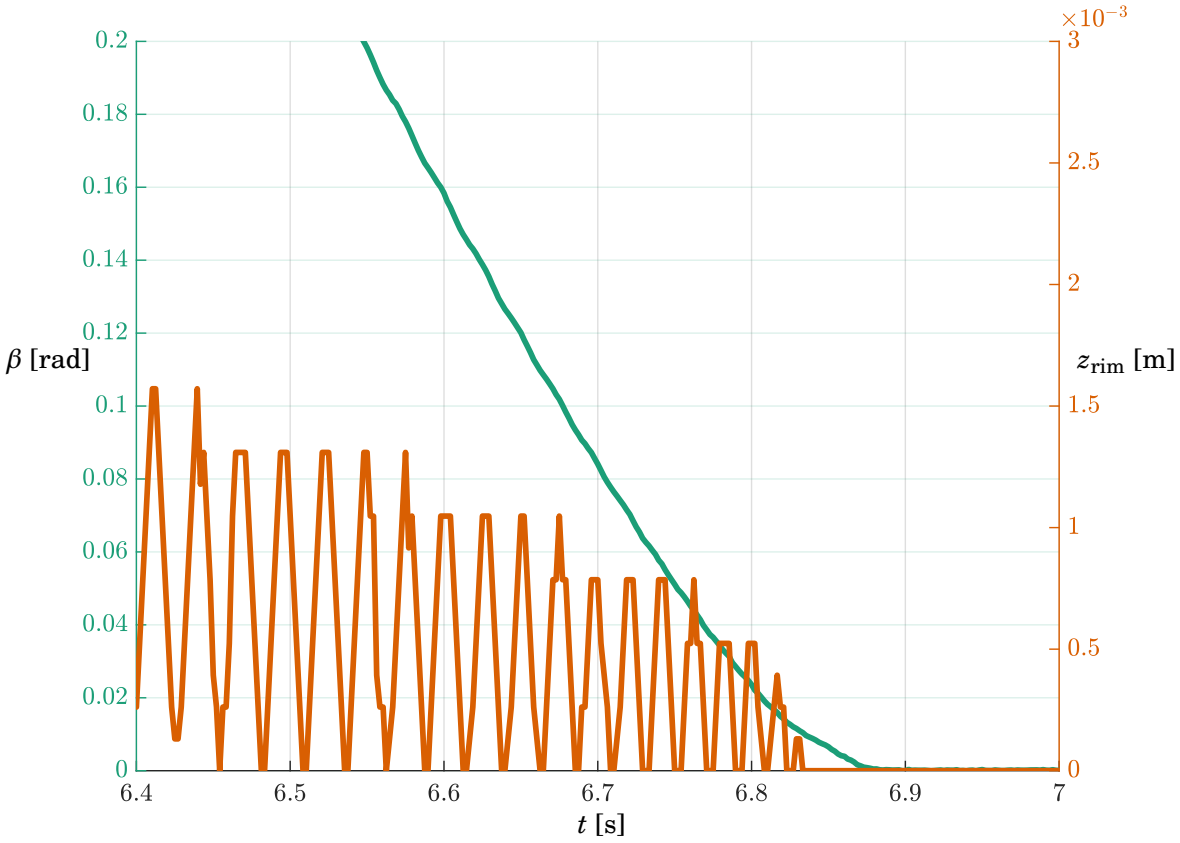

Figure 3.27: Comparison of the β and z_{rim} experimental data. The disk appears to have fallen flat before β comes to a halt.

brought to a halt by Coulomb friction. In the case of the concave base-plate, it is not possible for the disk to trap a thin layer of air. The disk makes contact immediately then slips to a halt, explaining the shorter interval.

This sequence of events is supported by fig. 3.31, in which we plot $\dot{\beta}$ after the disk has fallen flat at $t = t_\phi$. To compare the experiments, we scale the initial angular velocity $\dot{\beta}(t_\phi)$ and the interval, $t_\beta - t_\phi$. The constant section is visible from $\tau = -1$ to $\tau = -0.3$, before a linear decrease towards zero angular velocity. This supports the presence of an contactless phase, followed by a Coulomb-governed slip to a halt.

In Chapter 4, we analyse this post-flat falling phase analytically.

3.4 Discussion and conclusions

In Section 3.2, we investigated the dependence of the energy exponent, n, on the base-plate material. We spun the Euler's disk and the brass disk on different materials and estimated the energy. It was shown that the energy exponent does vary and therefore must depend upon the

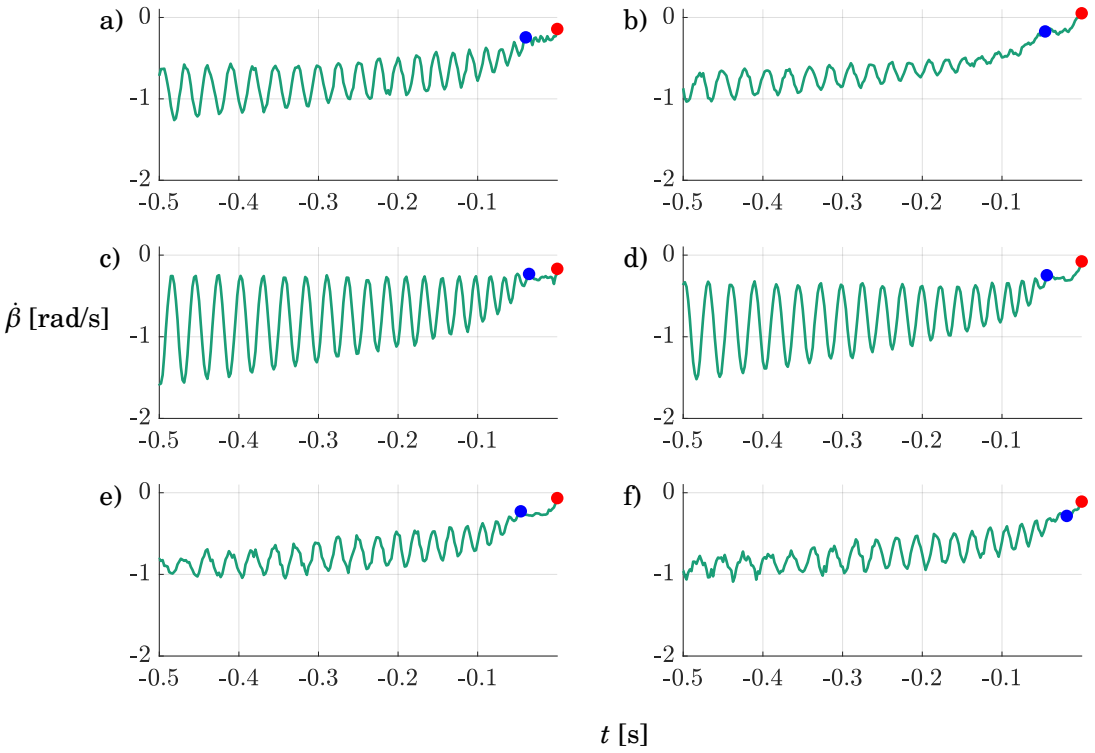

Figure 3.28: Six time series of $\dot{\beta}$ from the experiments of Euler's disk on stainless steel. The blue dot is placed at $t = t_\phi$ and the red dot at $t = t_\beta$.

material. All materials gave $n < 1$, suggesting the finite-time abrupt halt is ubiquitous. Therefore, the dynamics look qualitatively the same for each material. However, the mean exponents varied from $n = 0.69$ for the silicone base-plate to $n = 0.45$ for the stainless steel base-plate. It appears that harder, smoother materials tend to have a lower exponent, but more thorough experiments are required to understand the dependence. We do not see a clear dependence of n on the sharpness of the disk's rim.

Typically, dissipation mechanisms give rise to different energy exponents through differing dependencies on the nutation angle, ϕ. Variation in the energy exponent, n, with the base-plate material suggests that the dissipation mechanism's dependence on ϕ could have a material component. This is not something that has been explored in the literature, where dissipation mechanisms have a constant energy exponent [68].

Alternatively, the variation might be due to the experimental sample period of 0.5 s. Different exponents are known to be visible at different time scales, possibly caused by multiple dissipation mechanisms acting at once. Leine [68] observed in experiments that the exponent is 1/2 or 2/3, depending on whether the sample is at $t \ll t_\phi$, or $t \approx t_\phi$ respectively. The estimates of Ma et al. [71] predict $n = 0.6$ to 0.7 for a sample window of 3 s. The exponents for stainless steel, $n = 0.45$ and silicone $n = 0.69$ are close to these observed values, 1/2 and 2/3. Such exponents

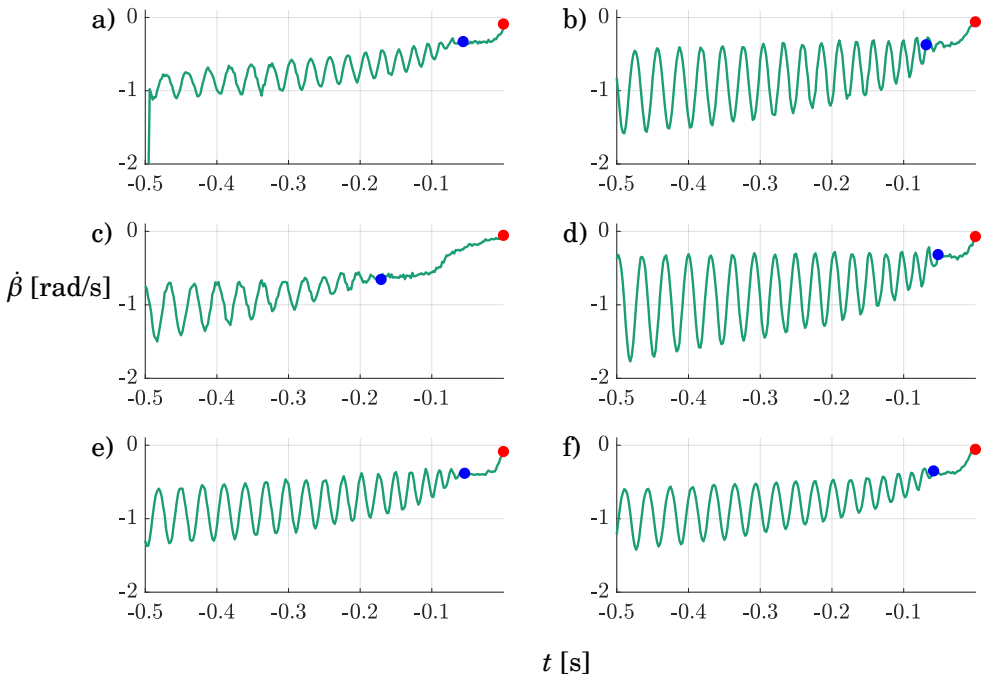

Figure 3.29: Six time series of $\dot{\beta}$ from the experiments of Euler's disk on lubricated stainless steel. The blue dot is placed at $t = t_\phi$ and the red dot at $t = t_\beta$.

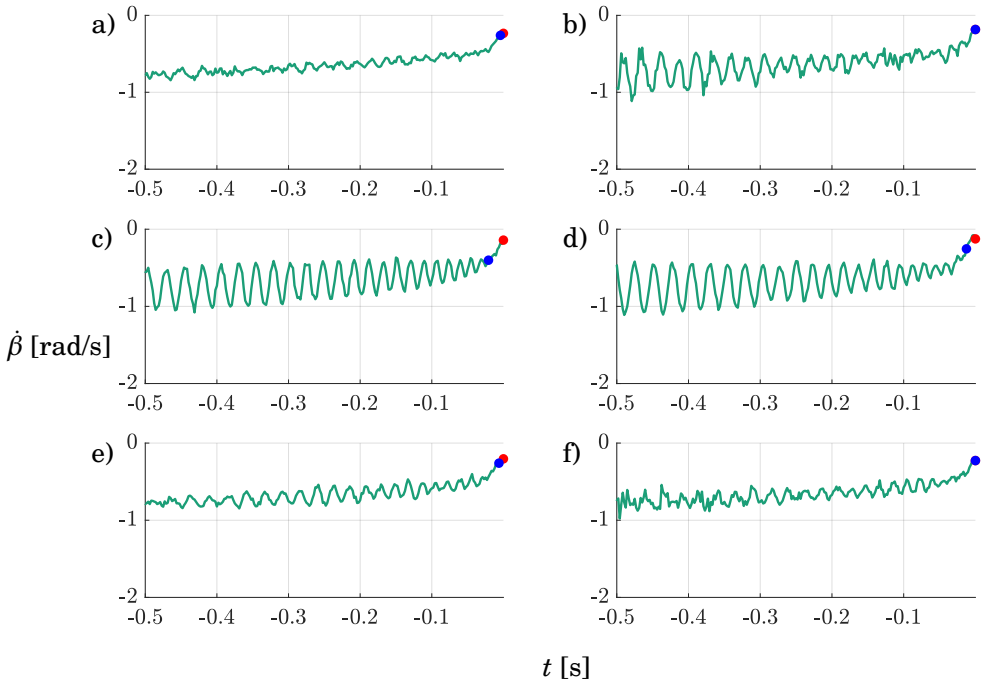

Figure 3.30: Six time series of $\dot{\beta}$ from the experiments for Euler's disk on the concave base-plate. The blue dot is placed at $t = t_\phi$ and the red dot at $t = t_\beta$.

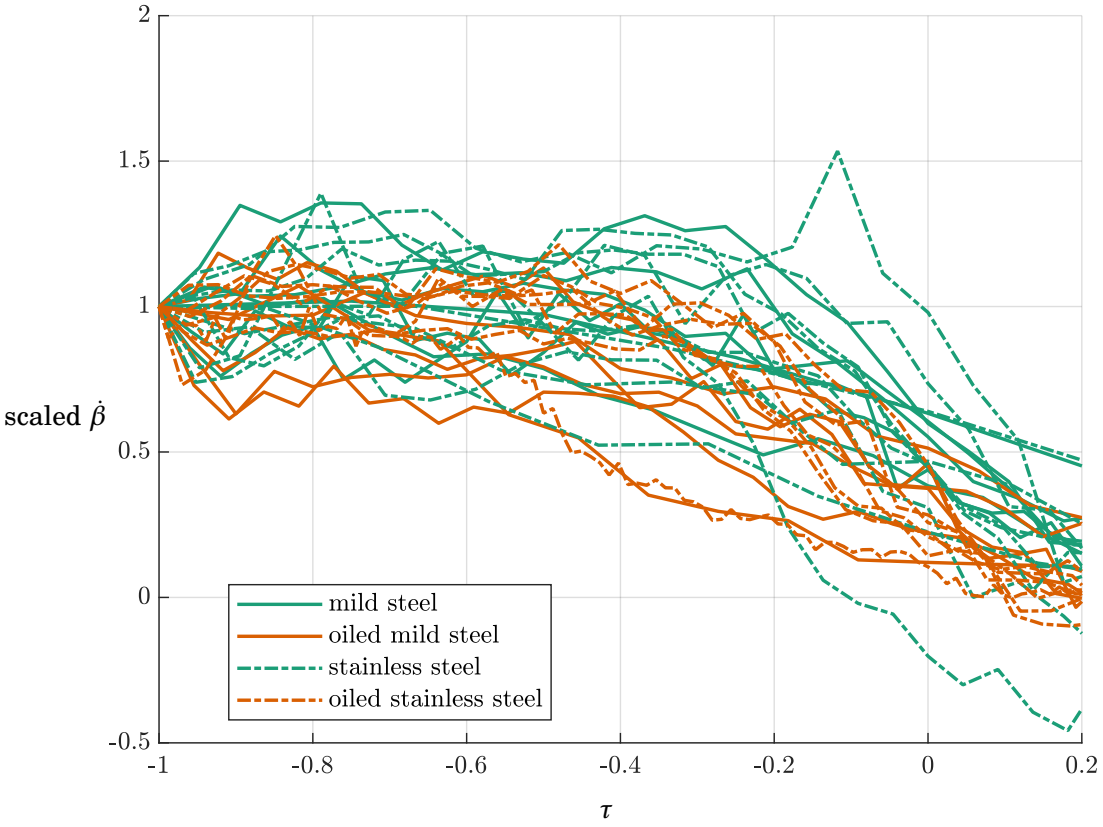

Figure 3.31: The behaviour of $\dot{\beta}$ in the interval $t_\phi < t < t_\beta$. Time, τ has been scaled by the t_ϕ and $\dot{\beta}$ has been scaled by $\dot{\beta}(t_\phi)$. A flat section from $\tau = -1$ to $\tau = -0.4$ is visible, succeeded by a decreasing section until the stop at $\tau = 0$. Trajectories may not reach $\beta = 0$ due to the stopping condition in fig. 3.22. The concave base-plate is excluded due to insufficient data points.

could be caused by viscous and dry contour friction respectively [68]. However, air resistance predicts an energy exponent of $n = 4/9$ [15], close to the experimental value of n for stainless steel. Unexpectedly, the concave base-plate was found to have the second largest energy exponent of $n = 0.62$, despite the long spinning times. Perhaps this larger than expected energy exponent can be explained by the gap between the disk and base-plate, which excludes the air resistance mechanism.

In Section 3.3, we examined the angular velocity of the disk about the vertical axis. The experiment was motivated by the slow-motion footage in Section 3.2, which appeared to show the disk continuing to rotate after falling flat. Tracking a strip drawn on the top face of the disk corroborates this. Estimates from experiments suggest that the disk continues to rotate for about $t_\beta - t_\phi$ =0.04 s after falling flat. This phenomenon is repeatable and augmentable by lubrication of the surface. The dynamics of $\dot{\beta}$, the angular velocity of the strip, appear to change qualitatively after the disk has fallen flat, as seen in figs. 3.28 and 3.29. The oscillations in $\dot{\beta}$ are no longer

possible after the disk has fallen flat.

We propose that the disk loses contact with the plane at $t = t_\phi$, before being supported by a layer of fluid. Then, upon making contact with the base-plate the disk is brought to a halt by Coulomb friction. The final loss of contact has been observed before by Borisov et al. [19], lasting for up to 0.04 s and agreeing with the experiments in Sections 3.2 and 3.3.

In comparison to air, oil has a much higher viscosity. Therefore, one would expect the duration of the contactless phase to be longer on the lubricated base-plate. Oil also reduces the coefficient of friction, so after making contact the disk should rotate for longer. This is the case in fig. 3.29 and fig. 3.28, where lubrication results in a 50% increase in post-falling flat spinning time for the stainless steel base-plate and a 12% increase for the mild steel base-plate. The hypothesis of a loss of contact is supported by the experiments on the concave base-plate, where the interval between falling flat and and coming to a halt is only 0.0058 s. The geometry of the base-plate removes the possibility of a thin, supporting layer of fluid. The disk makes contact immediately and Coulomb friction brings it to a halt. This is strong evidence for the presence of air-related factors that affect the motion of the disk.

These findings give rise to a few observations. If the disk is still rotating when it falls flat, then the stationary rolling assumption, eq. (3.7), is violated. In addition, the disk may not even roll in the final stages. The disk slips after making contact, so it seems wise to reinvestigate the assumption that the disk is rolling prior to the halt. It is obvious that, if there is slip, then the amount must be very small, as it is not visible to the naked eye or in the footage.

The key problem for Euler's disk is determining the dissipation mechanism that brings it to a halt. The dissipation mechanism must be compatible with the observed behaviour. From the results in this chapter, we refine the desired dissipation mechanism. It is already known that, on stainless steel, the disk undergoes an abrupt finite-time stop with an approximate energy exponent of $n = 0.45$. It is also known that the disk loses contact with the base-plate [19]. We now require that the candidate dissipation mechanism predicts energy exponents with a material dependence and continued rotation of the disk after falling flat.

In the next chapter we search for an analytical explanation for the motion of Euler's disk. We derive the equations of motion, subject to a number of candidate dissipation mechanisms. Numerical analysis of these equations allows relaxation of the stationary rolling assumption and quantitative comparisons with the experimental data in this chapter. Additionally, we provide an analytical explanation for the observed post-falling flat motion.

CHAPTER 4

THE HALTING OF EULER'S DISK

4.1 Introduction

In Chapter 1 and Section 3.1, we discussed the halting of Euler's disk and its associated literature. We begin this chapter with a short review of the phenomenon and the relevant findings of Chapter 3, before exploring Euler's disk numerically and analytically.

When a coin is spun on a hard, smooth surface it quickly and loudly rattles to a stop. The rate of rotation increases as the coin approaches the halt, resulting in a whirring noise followed by a sudden bang. The effect is magnified in Euler's disk, a desk toy machined out of steel. Euler's disk is accompanied by a concave, mirrored base-plate and holographic decorations. The decorations produce striking patterns during the high frequency motion and the base-plate serves as the hard, smooth surface for the disk to roll upon. Upon release, Euler's disk continues to spin for durations of around two minutes. The rotation and speed of the contact point approach a finite-time singularity, which is avoided by the sudden and abrupt halt.

Moffatt's seminal work [74] attributed the abrupt stop to a thin layer of air between the disk and base-plate, removing energy from the system via viscous dissipation. In subsequent experiments, by van den Engh et al. [93] and Borisov et al. [17], the disk was spun in a vacuum and the same qualitative behaviour was observed. Such observations do not necessarily invalidate Moffatt's findings, but may suggest that different dissipation mechanisms dominate in different regimes. Experiments by Ma et al. [71], Cross [32], Leine [68] and others all observe the same behaviour: an abrupt halt with a decrease in energy that closely follows a power law, eq. (1.2), governed by the energy exponent n.

It was found in the experiments of Chapter 3 that $n \in [0.45, 0.69]$ depending on the material of the base-plate. The energy shows square-root-like behaviour, gently decreasing before dropping

abruptly to zero. The central question surrounding Euler's disk is: what physical mechanism can produce such a decrease in energy? Many mechanisms have been considered: air resistance, rolling friction, impacts, Coulomb friction, etc. With appropriate assumptions, energy power laws can be derived from most mechanisms. The mechanism that predicts the smallest value of n is dominant, as it results in the largest rate of dissipation as the disk approaches the halt. However, the mechanism must also agree with the experimentally determined values of n and other qualitative features of the motion.

In the second experiment of Section 3.3, we filmed the motion from two angles, the top and the side to obtain information about the vertical rotation as the disk approached the halt. The disk appears to fall flat *before* the vertical rotation has stopped, implying continued rotation. This finding casts doubt on the applicability of the assumption of 'stationary rolling motion', where the disk rolls with the centre of mass approximately stationary [11, 68, 74]. Differences in behaviour were observed between the disk spinning on the flat and concave base-plates, suggesting that the presence of air may affect the motion. A candidate dissipation mechanism must explain, or at least be consistent with these findings.

Different narratives describing the stages of motion have been proposed. Leine [68] noted that the energy resembles different power laws at different time scales. It was tentatively suggested that dry contour friction ($n = 2/3$) followed by viscous contour friction ($n = 1/2$) could explain the behaviour of Euler's disk. Borisov et al. [19] finds that the disk loses contact with the base-plate and does so in phases. The first phase is repeated microlosses of contact, before a phase of constant contact followed by a lift-off at the halt. Ma et al. [70] find that the disk appears to pass through a fast sliding stage, where 'sliding friction plays a dominant role in dissipating energy', followed by a slow creeping stage where both 'sliding and rolling frictions dissipate the energy'. Finally, the disk undergoes a purely rolling stage where rolling friction dominates. Kessler and O'Reilly [60] suggest that vibrations in the disk and base-plate result in a loss of contact with the surface, then the subsequent impacts bring the disk to a halt. Numerical simulations by Le Saux et al. [67] examine combinations of friction models and find periods of slip and stick interspersed throughout the motion. In this chapter, we attempt to unify these narratives with the experimental results from Chapter 3.

In Section 4.2, we derive the equations of motion for Euler's disk subject to Coulomb friction and an unspecified dissipative moment. Coulomb friction is discontinuous and gives rise to two states, rolling and slipping. We derive the equations for these states in Section 4.2.2 and Section 4.2.3 respectively. The transitions between the two states are defined and the equations non-dimensionalised. Then, in Section 4.3, we analyse the disk subject to Coulomb friction in the absence of a dissipative moment.

In Section 4.2, we rederive the various rolling frictions discussed by Leine [68]. Then, in Section 4.5, we derive new rolling frictions via a relaxation of the rigid body assumption, finding equivalences with classical rolling friction and contour friction. We compute the associated energy

exponents for each mechanism in Section 4.6 and analyse the dynamics of the disk subject to Coulomb friction and contour friction, the most likely mechanism. We compare the numerical results with the experimental results.

Section 4.8 provides an explanation for the dynamics of the disk during the final 0.05 s of its motion. In Section 3.3, it was observed that the disk falls flat but continues to rotate. We find good agreement with the experiments by assuming a contactless phase, where the disk rests on a lubricating layer of air, followed by a Coulomb friction-governed phase where the disk is in contact with the base-plate. We discuss the results and conclude in section 4.9.

4.2 Derivation of the equations of motion

In this section, we derive the equations of motion for Euler's disk rolling on a rough, horizontal plane. The disk experiences both Coulomb friction and rolling friction. The configuration and notation is the same as Chapter 2. The disk is a rigid, rotationally symmetric cylinder with height $2H$, radius R and mass m, as shown in fig. 4.1. The moment of inertia tensor is $\mathrm{I} = \mathrm{diag}(A, A, C)$, where $C = \frac{mR^2}{2}$ and $A = \frac{m}{12}\left(3R^2 + H^2\right)$ are the moments of inertia about the symmetry and non-symmetry axes respectively. The rim of the disk contacts the plane at a point $\underline{P}$, where the contact forces $\underline{N}$ and $\underline{F}$ act. Additionally, the dissipative moment applies a torque $\underline{Q}$. This system is a generalisation of the rocking can, studied in Chapter 2, and is subject to external forces and moments that reduce the energy. The disk is allowed to slip if the friction ratio $|\underline{F}|/|N|$ grows too large.

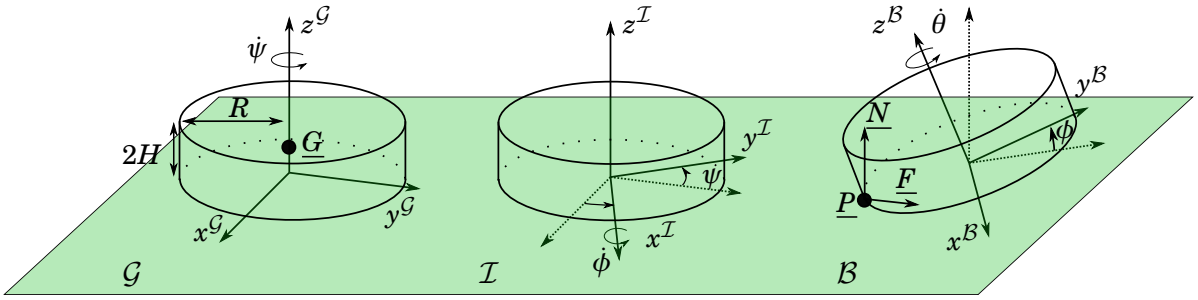

Figure 4.1: Technical diagram of Euler's disk, reproduced from fig. 3.1. The three reference frames global $\mathcal{G}$, intermediate $\mathcal{I}$ and body frame $\mathcal{B}$ are given by successive rotations ψ and ϕ. The vectors $\underline{G}$ and $\underline{P}$ refer to the positions of the centre of mass and the contact point respectively.

A three-dimensional rigid body has six degrees of freedom. To describe the disk, we select three coordinates, X_G, Y_G and Z_G, to specify the position of the centre of mass and three Euler angles ψ, ϕ and θ to specify the orientation. The angles are defined by successive rotations about different axes, see fig. 4.1. The global reference frame $\mathcal{G}$, is fixed with respect to the horizontal plane. Rotating by the *precession* angle, ψ, around the $z^{\mathcal{G}}$ axis yields the intermediate frame, $\mathcal{I}$. Rotating $\mathcal{I}$ around the $y^{\mathcal{I}}$ axis by the *nutation* angle, ϕ, gives the body frame, $\mathcal{B}$. The final frame, $\mathcal{F}$, is given by rotating about the $z^{\mathcal{B}}$ axis by the *rotation* angle, θ. The transformations are

defined by rotation matrices, R_{ij}, that convert from frame i to j

$$\mathrm{R}_{\mathcal{GI}} = \begin{pmatrix} \cos\psi & \sin\psi & 0 \\ -\sin\psi & \cos\psi & 0 \\ 0 & 0 & 1 \end{pmatrix}, \quad \mathrm{R}_{\mathcal{IB}} = \begin{pmatrix} \cos\phi & 0 & \sin\phi \\ 0 & 1 & 0 \\ -\sin\phi & 0 & \cos\phi \end{pmatrix}, \quad \mathrm{R}_{\mathcal{BF}} = \begin{pmatrix} \cos\theta & \sin\theta & 0 \\ -\sin\theta & \cos\theta & 0 \\ 0 & 0 & 1 \end{pmatrix}. \tag{4.1}$$

Successive transformations are given by composition. A force and moment balance yields the equations of motion

$$m\underline{a}_G^{\mathcal{G}} = -mg\hat{\underline{z}}^{\mathcal{G}} + \underline{N}^{\mathcal{G}} + \underline{F}^{\mathcal{G}}, \tag{4.2a}$$

$$\mathrm{I}\dot{\underline{\Omega}}^{\mathcal{B}} + \underline{\omega}^{\mathcal{B}} \times \mathrm{I}\underline{\Omega}^{\mathcal{B}} = \underline{GP}^{\mathcal{B}} \times \mathrm{R}_{\mathcal{GB}}\left(\underline{N}^{\mathcal{G}} + \underline{F}^{\mathcal{G}}\right) + \underline{Q}^{\mathcal{B}}, \tag{4.2b}$$

where $\underline{a}_G$ is the linear acceleration of the centre of mass, $\underline{\Omega}^{\mathcal{B}} = (\dot{\psi}\sin\phi, -\dot{\phi}, \dot{\psi}\cos\phi + \dot{\theta})^{\mathsf{T}}$ is the angular velocity vector of the disk and $\underline{\omega}^{\mathcal{B}} = (\dot{\psi}\sin\phi, -\dot{\phi}, \dot{\psi}\cos\phi)^{\mathsf{T}}$ is the angular velocity of the frame $\mathcal{B}$. The vector $\underline{GP}^{\mathcal{B}} = (-R, 0, -H)^{\mathsf{T}}$ is the displacement of the contact point, $\underline{P}$, from the centre of mass, $\underline{G}$. The external force, $\underline{F}$, is due to friction and the torque $\underline{Q}$ represents the dissipative moment. The vector $\hat{\underline{z}}^{\mathcal{G}}$ denotes a unit vector in the $z^{\mathcal{G}}$ direction. Other unit vectors are defined analogously. The normal force acts in the vertical direction, such that $\underline{N} = N\hat{\underline{z}}^{\mathcal{G}}$.

It is simplest to examine the force balance, eq. (4.2a), in the global frame $\mathcal{G}$ and the moment balance eq. (4.2b) in the body frame $\mathcal{B}$ frame due to the alignment of the moment of inertia tensor with the disk. To determine the unknown contact forces $\underline{F}$, $\underline{N}$ and $\underline{Q}$ in the equations of motion, eq. (4.2), we define Coulomb friction and the dissipative moment.

4.2.1 Dissipative forces

There are two dissipative terms in eq. (4.2), $\underline{F}$ and $\underline{Q}$, representing Coulomb friction and a rolling friction respectively. Sliding friction resists relative velocity between two bodies and many models exist such as dry, viscous, Stribeck, etc. In this chapter, we employ the most well known model, Coulomb friction, which gives rise to two states: slip and stick. The system is slipping if the contact point is moving with respect to the surface, and sticking if the contact point is stationary with respect to the surface. For the disk, the sticking state refers to rolling, sometimes referred to as 'rolling without slip'.

In Chapter 2, it was assumed that the coefficient of Coulomb friction, μ, was large enough to prevent slip. In this chapter, that assumption is relaxed and we allow the disk to slip if the friction ratio $|\underline{F}|/N$ grows larger than μ. For planar bodies, Coulomb friction is defined by

$$F \begin{cases} = -\mu N \operatorname{sign}(V_P) & \text{if} \quad |V_P| > 0 \\ \in [-\mu N, \mu N] & \text{if} \quad |V_P| = 0 \end{cases}, \tag{4.3}$$

where V_P is the velocity of the contact point.[1]. Coulomb friction provides a constant force that opposes the contact point velocity. If this velocity is zero, then Coulomb friction provides a force in the range $-\mu N < F < \mu N$ to keep the contact point stationary. The additional information needed to determine F is supplied by the constraint $V_P = 0$. For bodies in 3D, spatial Coulomb friction may act in any direction tangent to the plane of intersection between the two bodies

$$\underline{F} \begin{cases} = -\mu N \hat{\underline{V}}_P & \text{if} \quad |\underline{V}_P| > 0 \\ \in \left\{ \underline{F} \;\middle|\; |\underline{F}| \leq \mu N \right\} & \text{if} \quad |\underline{V}_P| = 0 \end{cases}, \tag{4.4}$$

where $\underline{V}_P$ is now the contact point velocity vector. As in the planar case, if the body is slipping then $\underline{F}$ acts in the opposite direction to the contact point velocity with magnitude μN. If the body is rolling, then $\underline{V}_P = 0$ and the friction force is determined by the constraint $\underline{V}_P = 0$, subject to the condition that its magnitude cannot be greater than μN. Coulomb friction contains an isolated codimension-2 discontinuity at $\dot{X}_P = \dot{Y}_P = 0$. The stability of the transitions from slipping to rolling behaviour and vice versa have been studied by Cheesman et al. [27] and Antali and Varkonyi [7].

Like sliding friction, rolling friction has many different formulations and we leave derivation of specific models to Section 4.4 and Section 4.5. In this chapter, we consider the class of rolling frictions that give rise to a torque, $\underline{Q}$, of the form

$$\underline{Q} = -\eta N R \begin{pmatrix} q_x \\ q_y \\ q_z \end{pmatrix}, \tag{4.5}$$

where η is the coefficient of rolling friction and R is the radius of the disk, present to ensure that $\underline{Q}$ represents a torque instead of a force. Not all dissipation mechanisms can be placed in the form of eq. (4.5): vibrations, impacts and air resistance, for example, are unlikely to take this form. The components q_x, q_y and q_z are specific to the dissipation mechanism and will be determined in Sections 4.4 and 4.5. Furthermore, these components may contain discontinuities similar to Coulomb friction in eq. (4.4). For rolling friction, we are only concerned with the dynamics off the discontinuity set as the dynamics on the discontinuity set do not dissipate energy. We proceed to derive the rolling and slipping equations of motion of Euler's disk.

4.2.2 The rolling subsystem

The rolling equations of motion, in the absence of a dissipative moment, are identical to the rocking can equations, eq. (2.8). Here, we briefly derive the equations of motion with the dissipative moment. The rolling constraint requires that the contact point has zero velocity

$$\underline{V}_P^{\mathcal{G}} = \underline{V}_G^{\mathcal{G}} + \mathrm{R}_{\mathcal{BG}} \left(\underline{\Omega}^{\mathcal{B}} \times \underline{GP}^{\mathcal{B}} \right) = \underline{0}, \tag{4.6}$$

[1] ODEs with such terms as eqs. (4.3) and (4.4) are called *differential inclusions*. In the case of Coulomb friction, these ODEs are called Filippov systems [40] In this chapter, we retain the slipping and rolling definitions and avoid conflicting terminology from non-smooth dynamics and Filippov systems.

where $\underline{V}_G = \left(\dot{X}_G, \dot{Y}_G, \dot{Z}_G\right)^\mathsf{T}$ is the velocity of the centre of mass. We expand the rolling constraint, eq. (4.6), componentwise to obtain the velocities of the centre of mass

$$\dot{X}_G = (-R\sin\phi - H\cos\phi)\dot{\phi}\cos\psi - (R(\dot{\psi}\cos\phi + \dot{\theta}) - H\dot{\psi})\sin\psi, \tag{4.7a}$$

$$\dot{Y}_G = (-R\sin\phi - H\cos\phi)\dot{\phi}\sin\psi + (R(\dot{\psi}\cos\phi + \dot{\theta}) - H\dot{\psi})\sin\psi, \tag{4.7b}$$

$$\dot{Z}_G = (R\cos\phi - H\sin\phi)\dot{\phi}, \tag{4.7c}$$

identical to eq. (2.5). Differentiation with respect to time gives the equations of motion for the centre of mass, equivalent to eq. (2.6)

$$\begin{aligned}\ddot{X}_G = &\left(-(R\sin\phi + H\cos\phi)\ddot{\phi} - (R\cos\phi - H\sin\phi)(\dot{\psi}^2 + \dot{\phi}^2) - R\dot{\theta}\dot{\psi}\right)\cos\psi \\ &+ \left(-\ddot{\psi}(R\cos\phi - H\sin\phi) - R\ddot{\theta} + 2(R\sin\phi + H\cos\phi)\dot{\phi}\dot{\psi}\right)\sin\psi,\end{aligned} \tag{4.8a}$$

$$\begin{aligned}\ddot{Y}_G = &\left((R\cos\phi - H\sin\phi)\ddot{\psi} + R\ddot{\theta} - 2(R\sin\phi + H\cos\phi)\dot{\phi}\dot{\psi}\right)\cos\psi \\ &+ \left(-(R\sin\phi + H\cos\phi)\ddot{\phi} - (R\cos\phi - H\sin\phi)(\dot{\psi}^2 + \dot{\phi}^2) - R\dot{\psi}\dot{\theta}\right)\sin\psi,\end{aligned} \tag{4.8b}$$

$$\ddot{Z}_G = \ddot{\phi}(R\cos\phi - H\sin\phi) - \dot{\phi}^2(R\sin\phi + H\cos\phi). \tag{4.8c}$$

We substitute the accelerations into the force balance, eq. (4.2a), to determine the normal and friction forces, as given in eq. (2.7),

$$\begin{aligned}F_x = &m\left(-(R\sin\phi + H\cos\phi)\ddot{\phi} - (R\cos\phi - H\sin\phi)(\dot{\psi}^2 + \dot{\phi}^2) - R\dot{\theta}\dot{\psi}\right)\cos\psi \\ &+ m\left(-\ddot{\psi}(R\cos\phi - H\sin\phi) - R\ddot{\theta} + 2(R\sin\phi + H\cos\phi)\dot{\phi}\dot{\psi}\right)\sin\psi,\end{aligned} \tag{4.9a}$$

$$\begin{aligned}F_y = &m\left((R\cos\phi - H\sin\phi)\ddot{\psi} + R\ddot{\theta} - 2(R\sin\phi + H\cos\phi)\dot{\phi}\dot{\psi}\right)\cos\psi \\ &+ m\left(-(R\sin\phi + H\cos\phi)\ddot{\phi} - (R\cos\phi - H\sin\phi)(\dot{\psi}^2 + \dot{\phi}^2) - R\dot{\psi}\dot{\theta}\right)\sin\psi,\end{aligned} \tag{4.9b}$$

$$N = mg + m\ddot{\phi}(R\cos\phi - H\sin\phi) - m\dot{\phi}^2(R\sin\phi + H\cos\phi), \tag{4.9c}$$

where F_x and F_y are the $x^{\mathcal{G}}$ and $y^{\mathcal{G}}$ components of $\underline{F}$. Substituting the contact forces, eq. (4.9), into the moment balance, eq. (4.2b), determines the external torque and subsequently, the equations of motion for the rolling disk

$$\begin{aligned}\left((A + mH^2)\sin\phi - mHR\cos\phi\right)\ddot{\psi} - mHR\ddot{\theta} = &(C - 2A - 2mH^2)\dot{\psi}\dot{\phi}\cos\phi \\ &+ C\dot{\phi}\dot{\theta} - 2mHR\dot{\psi}\dot{\phi}\sin\phi + Q_x,\end{aligned} \tag{4.10a}$$

$$\begin{aligned}\left(mR^2 + mH^2 + A\right)\ddot{\phi} = &\left((A + mH^2 - C - mR^2)\sin\phi\cos\phi - mRH\cos(2\phi)\right)\dot{\psi}^2 \\ &- mg(R\cos\phi - H\sin\phi) - ((C + mR^2)\sin\phi + mRH\cos\phi)\dot{\theta}\dot{\psi} - Q_y,\end{aligned} \tag{4.10b}$$

$$(C + mR^2)(\dot{\psi}\cos\phi + \ddot{\theta}) - mRH\ddot{\psi}\sin\phi = \left((C + 2mR^2)\sin\phi + 2mRH\cos\phi\right)\dot{\psi}\dot{\phi} + Q_z, \tag{4.10c}$$

$$\ddot{X}_P = 0, \tag{4.10d}$$

$$\ddot{Y}_P = 0, \tag{4.10e}$$

where Q_x, Q_y and Q_z are the $x^{\mathcal{G}}$, $y^{\mathcal{G}}$ and $z^{\mathcal{G}}$ components of the external torque $\underline{Q}$. We have appended the trivial differential equations for the contact point for a complete description of

the disk (the z component is not required due to the unilateral constraint). In the absence of a dissipative moment, $\underline{Q}$, eq. (4.10) reduces to the rocking can, eq. (2.8). In the next subsection we derive the equations of motion for the slipping subsystem.

4.2.3 The slipping subsystem

If the disk is slipping, the friction force is given by

$$\underline{F} = -\mu N \frac{\underline{V}_P}{|\underline{V}_P|} = -\frac{\mu N}{\sqrt{\dot{X}_P^2 + \dot{Y}_P^2}} \begin{pmatrix} \dot{x}_P \\ \dot{y}_P \\ 0 \end{pmatrix}, \tag{4.11}$$

and depends upon on the normal force, N. We compute the normal force by considering the unilateral constraint, $Z_P = 0$, ensuring that the disk does not penetrate the plane

$$Z_G = R\sin\phi + H\cos\phi. \tag{4.12}$$

Differentiating eq. (4.12) twice with respect to time and inserting into the Z_G component of the force balance, eq. (4.2a), yields the normal force

$$N = mg + m(R\cos\phi - H\sin\phi)\ddot{\phi} - m\dot{\phi}^2(R\sin\phi + H\cos\phi). \tag{4.13}$$

The contact forces, $\underline{F}$ and N, are now known and we compute the equations of motion for the orientation of the disk by expanding the moment balance, eq. (4.2b), componentwise

$$A\ddot{\psi}\sin\phi + 2A\dot{\psi}\dot{\phi}\cos\phi - C\dot{\phi}(\dot{\theta} + \dot{\psi}\cos\phi) - H(-F_x\sin\psi + F_y\cos\psi) - Q_x = 0, \tag{4.14a}$$

$$\begin{aligned} A\ddot{\phi} + C\dot{\psi}(\dot{\theta} + \dot{\psi}\cos\phi)\sin\phi - A\dot{\psi}^2\sin\phi\cos\phi \\ - (F_x\cos\psi + F_y\sin\psi)(R\sin\phi + H\cos\phi) + N(R\cos\phi - H\sin\phi) + Q_y = 0, \end{aligned} \tag{4.14b}$$

$$C\ddot{\theta} + C\ddot{\psi}\cos\phi - C\dot{\psi}\dot{\phi}\sin\phi + R(-F_x\sin\psi + F_y\cos\psi) - Q_z = 0. \tag{4.14c}$$

The equations of motion for the position of the disk are still required. These are best expressed in terms of the contact point rather than the centre of mass, due to the dependence of friction on the contact point velocity, $\underline{V}_P$. The velocity of the contact point is

$$\underline{V}_P^{\mathcal{G}} = \underline{V}_G^{\mathcal{G}} + \mathrm{R}_{\mathcal{BG}}\left(\underline{\Omega}^{\mathcal{B}} + \underline{GP}^{\mathcal{B}}\right). \tag{4.15}$$

Again, by expanding componentwise and differentiating with respect to time we obtain the accelerations of the contact point

$$\begin{aligned} \ddot{X}_P = &\left(\ddot{\psi}(R\cos\phi - H\sin\phi) - 2\dot{\psi}\dot{\phi}(R\sin\phi + H\cos\phi) + R\ddot{\theta}\right)\sin\psi \\ &+ \left(\ddot{\phi}(R\sin\phi + H\cos\phi) + (\dot{\psi}^2 + \dot{\phi}^2)(R\cos\phi - H\sin\phi) + R\dot{\psi}\dot{\theta}\right)\cos\psi + \ddot{X}_G, \end{aligned} \tag{4.16a}$$

$$\begin{aligned} \ddot{Y}_P = &-\left(\ddot{\psi}(R\cos\phi - H\sin\phi) - 2\dot{\psi}\dot{\phi}(R\sin\phi + H\cos\phi) + R\ddot{\theta}\right)\cos\psi \\ &+ \left(\ddot{\phi}(R\sin\phi + H\cos\phi) + (\dot{\psi}^2 + \dot{\phi}^2)(R\cos\phi - H\sin\phi) + R\dot{\psi}\dot{\theta}\right)\sin\psi + \ddot{Y}_G, \end{aligned} \tag{4.16b}$$

where the $\ddot{Z}_P$ equation has been discarded due to unilateral constraint, eq. (4.12). The force balance, eq. (4.2a), determines the centre of mass accelerations

$$\begin{aligned}\ddot{X}_P = &\left(\ddot{\psi}(R\cos\phi - H\sin\phi) - 2\dot{\psi}\dot{\phi}(R\sin\phi + H\cos\phi) + R\ddot{\theta}\right)\sin\psi \\ &+ \left(\ddot{\phi}(R\sin\phi + H\cos\phi) + (\dot{\psi}^2 + \dot{\phi}^2)(R\cos\phi - H\sin\phi) + R\dot{\psi}\dot{\theta}\right)\cos\psi + F_x/m,\end{aligned} \tag{4.17a}$$

$$\begin{aligned}\ddot{Y}_P = &-\left(\ddot{\psi}(R\cos\phi - H\sin\phi) - 2\dot{\psi}\dot{\phi}(R\sin\phi + H\cos\phi) + R\ddot{\theta}\right)\cos\psi \\ &+ \left(\ddot{\phi}(R\sin\phi + H\cos\phi) + (\dot{\psi}^2 + \dot{\phi}^2)(R\cos\phi - H\sin\phi) + R\dot{\psi}\dot{\theta}\right)\sin\psi + F_y/m.\end{aligned} \tag{4.17b}$$

Equations (4.14) and (4.17) describe the orientation and position of the can in the slipping state. In the next subsection we define the transitions between rolling and slipping states.

4.2.4 The rolling-to-slipping transition and vice versa

Together the rolling, eq. (4.10), and the slipping subsystems, eqs. (4.14) and (4.17), determine the dynamics of Euler's disk. However, it remains to define the transition between rolling and slipping and vice versa. The rolling-to-slipping transition occurs when the friction force required to keep the disk rolling becomes too large. In other words, when trajectories of the rolling system hit the discontinuity set, S_{rs}, defined by

$$S_{rs} = \left\{ \underline{X} \middle| \frac{|\underline{F}(\underline{X})|}{N(\underline{X})} = \mu \right\}, \tag{4.18}$$

where $\underline{X} = (\psi, \dot{\psi}, \phi, \dot{\phi}, \theta, \dot{\theta}, X_P, \dot{X}_P, Y_P, \dot{Y}_P)^\intercal$ is the vector of state variables and the contact forces $\underline{F}$ and N are given in eq. (4.9). When transitioning from rolling to slipping the disk begins to slip on the horizontal plane in the direction opposing friction

$$\underline{V}_{\text{slip}} = \begin{pmatrix} \cos\xi \\ \sin\xi \end{pmatrix}, \tag{4.19}$$

where $\xi = \arctan(F_y/F_x) - \pi$, as shown in fig. 4.2.

The slipping-to-rolling transition occurs when the contact point velocity equals zero

$$S_{sr} = \left\{ \underline{X} \middle| \sqrt{\dot{X}_P^2 + \dot{Y}_P^2} = 0 \right\}. \tag{4.20}$$

Other issues with the transitions arise when solving the equations numerically, but these are dealt with in Section 4.3.1.

4.2.5 Non-dimensionalisation and reduction of the equations of motion

We non-dimensionalise the equations of motion with the same scalings used for the rocking can, eq. (2.9), which are repeated here

$$h = \frac{H}{R}, \quad x_P = \frac{X_P}{R}, \quad y_P = \frac{Y_P}{R}, \quad z = \frac{Z_P}{R}, \quad a = \frac{A}{mR^2}, \quad c = \frac{C}{mR^2}, \quad \tau = \sqrt{\frac{g}{R}}t. \tag{4.21}$$

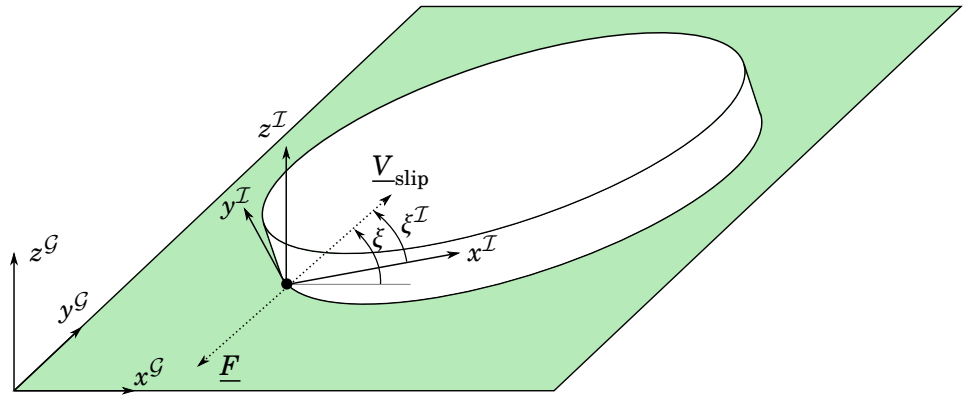

Figure 4.2: When the disk transitions from rolling to slipping, we compute the friction force $\underline{F}$ and let the disk slip in the opposite direction. This direction is defined by the slipping angle, $\xi = \arctan\left(F_y/F_x\right) - \pi$, measured with respect to $x^{\mathcal{G}}$. In the intermediate frame this angle is $\xi^{\mathcal{I}}$, measured with respect to the $x^{\mathcal{I}}$ axis.

First we apply the scalings to the rolling subsystem eq. (4.10), overloading the notation so that $[\dot{]}$ refers to differentiation with respect to the new time, τ. We also insert the rolling friction definition for $\underline{Q}$ from eq. (4.5) to obtain

$$\left(a_p \sin\phi - h\cos\phi\right)\ddot{\psi} - h\ddot{\theta} = (c-2a_p)\dot{\psi}\dot{\phi}\cos\phi + c\dot{\phi}\dot{\theta} - 2h\dot{\psi}\dot{\phi}\sin\phi - \eta q_x n(\phi,\dot{\phi},\ddot{\phi}), \tag{4.22a}$$

$$\left(a_p+1\right)\ddot{\phi} = \left((a_p-c_p)\sin\phi\cos\phi - h\cos(2\phi)\right)\dot{\psi}^2 - (c_p\sin\phi + h\cos\phi)\dot{\theta}\dot{\psi} - (\cos\phi - h\sin\phi) + \eta q_y n(\phi,\dot{\phi},\ddot{\phi}), \tag{4.22b}$$

$$(c_p\cos\phi - h\sin\phi)\ddot{\psi} + c_p\ddot{\theta} = \left((c_p+1)\sin\phi + 2h\cos\phi\right)\dot{\psi}\dot{\phi} - \eta q_z n(\phi,\dot{\phi},\ddot{\phi}), \tag{4.22c}$$

$$\ddot{x}_P = 0, \tag{4.22d}$$

$$\ddot{y}_P = 0, \tag{4.22e}$$

where $n(\phi,\dot{\phi},\ddot{\phi}) = N/mg$ in scaled variables.

$$n(\phi,\dot{\phi},\ddot{\phi}) = 1 + \ddot{\phi}(\cos\phi - h\sin\phi) - \dot{\phi}^2(\sin\phi + h\cos\phi). \tag{4.23}$$

Next, we manipulate eq. (4.22) so that only a single second derivative appears on the left-hand side. We also introduce the constant $k = c/(ca_p + a)$ for brevity and the functions g_i which describe the dissipation free dynamics. The definitions are given in Section C.

$$\ddot{\phi} = g_\phi + \frac{\eta q_y n(\phi,\dot{\phi},\ddot{\phi})}{a_p+1}, \tag{4.24a}$$

$$\ddot{\psi} = g_\psi - \frac{\eta k n(\phi,\dot{\phi},\ddot{\phi})}{c\sin\phi}(c_p q_x + h q_z), \tag{4.24b}$$

$$\ddot{\theta} = g_\theta - \frac{\eta k n(\phi,\dot{\phi},\ddot{\phi})}{c}\left(q_x(h - c_p\cot\phi) + q_z(a_p - h\cot\phi)\right), \tag{4.24c}$$

$$\ddot{x}_P = 0, \tag{4.24d}$$

$$\ddot{y}_P = 0. \tag{4.24e}$$

However, eq. (4.24) is still implicit due to the normal force, $n(\phi,\dot{\phi},\ddot{\phi})$, which depends upon $\ddot{\phi}$. Numerical solutions therefore require the use of slower, less accurate, implicit solvers such as ODE15i. We substitute the normal force, eq. (4.23), into the $\ddot{\phi}$ equation, eq. (4.24a) and solve for $\ddot{\phi}$

$$\ddot{\phi} = \frac{g_\phi(a_p+1)+\eta q_y(1-\dot{\phi}^2(\sin\phi+h\cos\phi))}{a_p+1-\eta q_y(\cos\phi-h\sin\phi)}, \tag{4.25a}$$

$$\ddot{\psi} = g_\psi - \frac{\eta k n(\phi,\dot{\phi},\ddot{\phi})}{c\sin\phi}(c_p q_x + h q_z), \tag{4.25b}$$

$$\ddot{\theta} = g_\theta - \frac{\eta k n(\phi,\dot{\phi},\ddot{\phi})}{c}\left(q_x(h-c_p\cot\phi)+q_z(a_p-h\cot\phi)\right), \tag{4.25c}$$

$$\ddot{x}_P = 0, \tag{4.25d}$$

$$\ddot{y}_P = 0. \tag{4.25e}$$

These equations are not quite in explicit form, but when solving numerically, we first compute $\ddot{\phi}$ explicitly in eq. (4.25b). Then, $n(\phi,\dot{\phi},\ddot{\phi})$ is determined by eq. (4.23) for the remaining equations, enabling the use of stiff solvers such as ODE15s. To save space, we do not substitute $n(\phi,\dot{\phi},\ddot{\phi})$ into the other components of eq. (4.25). Equation (4.25) is the governing equation for the rolling dynamics.

We now apply the same scalings to the slipping subsystem, eqs. (4.14) and (4.17),

$$\begin{aligned} a\ddot{\phi} =& (a-c)\cos\phi\sin\phi\dot{\psi}^2 - c\sin\phi\dot{\psi}\dot{\theta} + \eta n q_y + (f_x\cos\psi + f_y\sin\psi)(h\cos\phi+\sin\phi) \\ & - (\cos\phi - h\sin\phi)n(\phi,\dot{\phi},\ddot{\phi}), \end{aligned} \tag{4.26a}$$

$$a\sin\phi\ddot{\psi} = c\dot{\theta}\dot{\phi} - (2a-c)\cos\phi\dot{\psi}\dot{\phi} + h(-f_x\sin\psi + f_y\sin\psi) - \eta q_x n(\phi,\dot{\phi},\ddot{\phi}), \tag{4.26b}$$

$$\begin{aligned} ac\sin\phi\ddot{\theta} =& ((ca-c^2)\cos^2\phi + ca)\dot{\psi}\dot{\phi} - c^2\dot{\theta}\cos\phi + \eta(cq_x\cos\phi - aq_z\sin\phi)n(\phi,\dot{\phi},\ddot{\phi}) \\ & + (\sin\psi f_x - f_y\cos\psi)(ch\cos\phi + a\sin\phi), \end{aligned} \tag{4.26c}$$

$$\begin{aligned} \ddot{x}_P =& \left(\ddot{\psi}(\cos\phi - h\sin\phi) - 2\dot{\psi}\dot{\phi}(\sin\phi+h\cos\phi) + \ddot{\theta}\right)\sin\psi \\ & + \left(\ddot{\phi}(\sin\phi+h\cos\phi) + (\dot{\psi}^2+\dot{\phi}^2)(\cos\phi - h\sin\phi) + \dot{\psi}\dot{\theta}\right)\cos\psi + f_x, \end{aligned} \tag{4.26d}$$

$$\begin{aligned} \ddot{y}_P =& -\left(\ddot{\psi}(\cos\phi - h\sin\phi) - 2\dot{\psi}\dot{\phi}(\sin\phi+h\cos\phi) + \ddot{\theta}\right)\cos\psi \\ & + \left(\ddot{\phi}(\sin\phi+h\cos\phi) + (\dot{\psi}^2+\dot{\phi}^2)(\cos\phi - h\sin\phi) + \dot{\psi}\dot{\theta}\right)\sin\psi + f_y, \end{aligned} \tag{4.26e}$$

accompanied by the scaled friction forces

$$f_x = -\mu n(\phi,\dot{\phi},\ddot{\phi})\frac{\dot{x}_P}{\sqrt{\dot{x}_p^2+\dot{y}_p^2}}, \tag{4.27a}$$

$$f_y = -\mu n(\phi,\dot{\phi},\ddot{\phi})\frac{\dot{y}_P}{\sqrt{\dot{x}_p^2+\dot{y}_p^2}}. \tag{4.27b}$$

A transformation of the contact point velocities from the global to the intermediate frame removes

the $\sin\psi$ and $\cos\psi$ terms from eqs. (4.26d) and (4.26e). This transformation is

$$\dot{x} = \dot{x}_p \cos\psi + \dot{y}_p \sin\psi, \tag{4.28a}$$

$$\dot{y} = -\dot{x}_p \sin\psi + \dot{y}_p \cos\psi, \tag{4.28b}$$

which, upon differentiation, yields the new equations of motion for the contact point position

$$\ddot{x} = \ddot{x}_p \cos\psi + \ddot{y}_p \sin\psi + \dot{\psi}\dot{y}, \tag{4.29a}$$

$$\ddot{y} = -\ddot{x}_p \sin\psi + \ddot{y}_p \cos\psi - \dot{\psi}\dot{x}. \tag{4.29b}$$

Applying the transformation, (4.28), to the slipping equations of motion, eq. (4.26), gives

$$\begin{aligned} a\ddot{\phi} =& (a-c)\cos\phi\sin\phi\dot{\psi}^2 - c\sin\phi\dot{\psi}\dot{\theta} - \mu n(\phi,\dot{\phi},\ddot{\phi})\frac{\dot{x}}{\sqrt{\dot{x}^2+\dot{y}^2}}(h\cos\phi+\sin\phi) \\ & -(\cos\phi - h\sin\phi)n(\phi,\dot{\phi},\ddot{\phi}) + \eta q_y n(\phi,\dot{\phi},\ddot{\phi}), \end{aligned} \tag{4.30a}$$

$$a\sin\phi\ddot{\psi} = c\dot{\theta}\dot{\phi} - (2a-c)\dot{\psi}\dot{\phi}\cos\phi - \mu h n(\phi,\dot{\phi},\ddot{\phi})\frac{\dot{y}}{\sqrt{\dot{x}^2+\dot{y}^2}} - \eta q_x n(\phi,\dot{\phi},\ddot{\phi}), \tag{4.30b}$$

$$\begin{aligned} ac\sin\phi\ddot{\theta} =& ((ca-c^2)\cos^2\phi + ca)\dot{\psi}\dot{\phi} - c^2\dot{\theta}\dot{\phi}\cos\phi + \eta(cq_x\cos\phi + aq_z\sin\phi)n(\phi,\dot{\phi},\ddot{\phi}) \\ & + \mu n(\phi,\dot{\phi},\ddot{\phi})\frac{\dot{y}}{\sqrt{\dot{x}^2+\dot{y}^2}}(ch\cos\phi + a\sin\phi), \end{aligned} \tag{4.30c}$$

$$\ddot{x} = \ddot{\phi}(\sin\phi + h\cos\phi) + (\dot{\psi}^2+\dot{\phi}^2)(\cos\phi - h\sin\phi) + \dot{\psi}\dot{\theta} - \frac{\mu n(\phi,\dot{\phi},\ddot{\phi})\dot{x}}{\sqrt{\dot{x}^2+\dot{y}^2}} + \dot{\psi}\dot{y}, \tag{4.30d}$$

$$\ddot{y} = -\ddot{\psi}(\cos\phi - h\sin\phi) + 2\dot{\psi}\dot{\phi}(\sin\phi + h\cos\phi) - \ddot{\theta} - \frac{\mu n(\phi,\dot{\phi},\ddot{\phi})\dot{y}}{\sqrt{\dot{x}^2+\dot{y}^2}} - \dot{\psi}\dot{x}. \tag{4.30e}$$

We introduce the functions h_i to describe the dissipation-free components of the slipping motion

$$\ddot{\phi} = h_\phi + \frac{n(\phi,\dot{\phi},\ddot{\phi})}{a}\left(\eta q_y - \mu\frac{\dot{x}}{\sqrt{\dot{x}^2+\dot{y}^2}}(h\cos\phi+\sin\phi) - (\cos\phi - h\sin\phi)\right), \tag{4.31a}$$

$$\ddot{\psi} = h_\psi - \frac{n(\phi,\dot{\phi},\ddot{\phi})}{a\sin\phi}\left(\mu h\frac{\dot{y}}{\sqrt{\dot{x}^2+\dot{y}^2}} - \eta q_x\right), \tag{4.31b}$$

$$\ddot{\theta} = h_\theta + \frac{n(\phi,\dot{\phi},\ddot{\phi})}{ac\sin\phi}\left(\eta c q_x\cos\phi - \eta a q_z\sin\phi + \mu\frac{\dot{y}}{\sqrt{\dot{x}^2+\dot{y}^2}}(ch\cos\phi + a\sin\phi)\right), \tag{4.31c}$$

$$\ddot{x} = \ddot{\phi}(\sin\phi + h\cos\phi) + (\dot{\psi}^2+\dot{\phi}^2)(\cos\phi - h\sin\phi) + \dot{\psi}\dot{\theta} - \frac{\mu n(\phi,\dot{\phi},\ddot{\phi})\dot{x}}{\sqrt{\dot{x}^2+\dot{y}^2}} + \dot{\psi}\dot{y}, \tag{4.31d}$$

$$\ddot{y} = -\ddot{\psi}(\cos\phi - h\sin\phi) + 2\dot{\psi}\dot{\phi}(\sin\phi + h\cos\phi) - \ddot{\theta} - \frac{\mu n(\phi,\dot{\phi},\ddot{\phi})\dot{y}}{\sqrt{\dot{x}^2+\dot{y}^2}} - \dot{\psi}\dot{x}. \tag{4.31e}$$

The definitions of h_i are given in Section C. Again, we make the $\ddot{\phi}$ component explicit by eliminating $n(\phi,\dot{\phi},\ddot{\phi})$ from eq. (4.31a). Then $n(\phi,\dot{\phi},\ddot{\phi})$ is determined by eq. (4.23) for the other

equations

$$\ddot{\phi} = \frac{h_\phi + (1 - \dot{\phi}^2(\sin\phi + h\cos\phi))f_\phi}{a - (\cos\phi - h\sin\phi)f_\phi}, \tag{4.32a}$$

$$\ddot{\psi} = h_\psi - \frac{n(\phi,\dot{\phi},\ddot{\phi})}{a\sin\phi}\left(\mu h\frac{\dot{y}}{\sqrt{\dot{x}^2+\dot{y}^2}} - \eta q_x\right), \tag{4.32b}$$

$$\ddot{\theta} = h_\theta + \frac{n(\phi,\dot{\phi},\ddot{\phi})}{ac\sin\phi}\left(\eta c q_x\cos\phi - a\eta q_z\sin\phi + \mu\frac{\dot{y}}{\sqrt{\dot{x}^2+\dot{y}^2}}(ch\cos\phi + a\sin\phi)\right), \tag{4.32c}$$

$$\ddot{x} = \ddot{\phi}(\sin\phi + h\cos\phi) + (\dot{\psi}^2 + \dot{\phi}^2)(\cos\phi - h\sin\phi) + \dot{\psi}\dot{\theta} - \frac{\mu n(\phi,\dot{\phi},\ddot{\phi})\dot{x}}{\sqrt{\dot{x}^2+\dot{y}^2}} + \dot{\psi}\dot{y}, \tag{4.32d}$$

$$\ddot{y} = -\ddot{\psi}(\cos\phi - h\sin\phi) + 2\dot{\psi}\dot{\phi}(\sin\phi + h\cos\phi) - \ddot{\theta} - \frac{\mu n(\phi,\dot{\phi},\ddot{\phi})\dot{y}}{\sqrt{\dot{x}^2+\dot{y}^2}} - \dot{\psi}\dot{x}. \tag{4.32e}$$

The function f_ϕ represents the contact forces affecting ϕ and the definition is given in Section C. Setting $\mu = \eta = 0$ in eq. (4.32) recovers the dissipation-free, frictionless, slipping system. The rolling and slipping systems in eq. (4.25) and eq. (4.32) are the governing equations for this chapter. By inserting different expressions for $\underline{q} = (q_x, q_y, q_z)^\mathsf{T}$, it is possible to numerically analyse different dissipation mechanisms.

Before proceeding to the analysis, we scale the transitions between rolling and slipping states. The rolling-to-slipping transition, eq. (4.18), becomes

$$S_{rs} = \left\{ \underline{X} \middle| \frac{|\underline{F}|}{N} = \frac{\sqrt{\left(f_x^{\mathcal{I}}\right)^2 + \left(f_y^{\mathcal{I}}\right)^2}}{1 + \ddot{\phi}(\cos\phi - h\sin\phi) - \dot{\phi}^2(\sin\phi + h\cos\phi)} = \mu \right\}, \tag{4.33}$$

where $f_x^{\mathcal{I}}$ and $f_y^{\mathcal{I}}$ are the components of the scaled friction force in the intermediate frame $\mathcal{I}$

$$f_x^{\mathcal{I}} = -(\sin\phi + h\cos\phi)\ddot{\phi} - (\cos\phi - h\sin\phi)\dot{\psi}^2 - \dot{\theta}\dot{\psi} - (\cos\phi - h\sin\phi)\dot{\phi}^2, \tag{4.34a}$$

$$f_y^{\mathcal{I}} = -\ddot{\psi}(\cos\phi - h\sin\phi) - \ddot{\theta} + 2(\sin\phi + h\cos\phi)\dot{\phi}\dot{\psi}. \tag{4.34b}$$

The initial direction of slip is now determined by the angle the friction force makes with the $x^{\mathcal{I}}$ axis

$$\underline{v}_{\text{slip}} = \begin{pmatrix} \cos\xi^{\mathcal{I}} \\ \sin\xi^{\mathcal{I}} \end{pmatrix} \tag{4.35}$$

where $\xi^{\mathcal{I}} = \arctan\left(f_y^{\mathcal{I}}/f_x^{\mathcal{I}}\right) - \pi$, as shown in fig. 4.2. The slipping-to-rolling discontinuity surface is almost unchanged and reads

$$S_{sr} = \left\{ \underline{X} \middle| \sqrt{\dot{x}^2 + \dot{y}^2} = 0 \right\}. \tag{4.36}$$

The variables ψ, θ, x and y are cyclic because they do not appear in the governing equations, eqs. (4.25) and (4.32), or the transition rules. Therefore, rather than five second-order ODEs,

the system may be reduced to six first-order ODEs. However, we retain the cyclic variables for comparison with experimental data.

Having defined the equations of motion, along with the transitions between rolling and slipping states, we proceed to analyse the Euler's disk subject only to Coulomb friction.

4.3 Coulomb friction analysis

In this section, we explore the motion of Euler's disk in the presence of Coulomb friction and no additional dissipation mechanism. To obtain these equations of motion, we simply set $\eta = 0$ in eqs. (4.25) and (4.32).

McDonald and McDonald [73] suggest that Coulomb friction is insufficient to bring the disk to a halt. We confirm this for the disk in the rolling case. Then, we numerically solve the equations of motion with experimentally determined initial conditions to determine the behaviour of the disk when slipping occurs. We then discuss Painlevé paradoxes and their applicability to Euler's disk.

Equation (4.25), with $\eta = 0$, is identical to the equations of motion for the rocking can, eq. (2.11). It was shown in Section 2.3 that these equations have an equilibrium, or steady motion, given by

$$S_{\text{bal}} \subset S_{\text{steady}} = \left\{(\psi, \dot{\theta}, \dot{\phi}, \phi, \dot{x}, \dot{y}) = (\psi, \dot{\theta}, 0, \phi, 0, 0)\right\}, \tag{4.37}$$

subject to the condition

$$((a_p - c_p)\sin\phi\cos\phi - h\cos 2\phi)\dot{\psi}^2 - (c_p \sin\phi + h\cos\phi)\dot{\theta}\dot{\psi} + (h\sin\phi - \cos\phi) = 0, \tag{4.38}$$

where the cyclic variables ψ, θ, x and y have been discarded. On this equilibrium the disk rolls at a fixed angle ϕ with constant angular velocities $\dot{\psi}$ and $\dot{\theta}$. Setting $\dot{\phi} = 0$ in the equations of motion, eq. (4.25), recovers the condition eq. (4.38). If the coefficient of Coulomb friction is sufficient that the disk does not slip, then the can will continue to roll indefinitely, even in the presence of Coulomb friction. Furthermore, there exists a special steady motion where the centre of mass is at rest, called stationary rolling motion, given in eq. (2.28), and repeated here

$$S_{\text{rest}} = \left\{(\psi, \dot{\theta}, \dot{\phi}, \phi, \dot{x}, \dot{y}) = (\psi, \dot{\theta}, 0, \phi, 0, 0)\right\}, \tag{4.39}$$

with the additional requirements

$$\dot{\psi}^2 = \frac{\cos\phi - h\sin\phi}{a\sin\phi\cos\phi + ch\sin^2\phi}, \quad \dot{\theta} = -\dot{\psi}(\cos\phi - h\sin\phi). \tag{4.40}$$

By Newton's second law, if the centre of mass is stationary then there is no applied friction force. Therefore, there exists a steady motion for all values of μ and Coulomb friction is unable to generically bring the disk to a halt. However, it is not known if Coulomb friction is capable of bringing the disk to a halt in other circumstances. For example, if initial conditions prescribe slipping or the friction ratio $|\underline{F}|/N$ becomes too large. To investigate, we numerically solve the equations of motion, eqs. (4.25) and (4.32), with $\eta = 0$.

4.3.1 Numerical simulations with Coulomb friction

We solve the equations of motion, eqs. (4.25) and (4.32), using MATLAB's ODE15S, an adaptive time-step solver capable of dealing with stiff ODEs. The absolute tolerance is set to 10^{-13} and event functions are used to detect slipping-to-rolling transitions and vice versa. A similar scheme is used by Ma and Liu [70] and Kessler and O'Reilly [60]. The integration is halted in three cases:

1. ϕ becomes too small. If $\phi < 10^{-10}$, we judge the disk to have fallen flat.
2. The integration has surpassed a predetermined time interval, $t > T_{\text{end}}$.
3. The integration crosses the rolling friction discontinuity set, detected to an accuracy of 10^{-10}.

The rolling-to-slipping, eq. (4.33), and slipping-to-rolling, eq. (4.36), transitions are also detected to an accuracy of 10^{-10}. These tolerances are less stringent than the absolute tolerance of 10^{-13} to ensure that no transitions or conditions are missed. In the rolling-to-slipping transition, the end state of the rolling system is used as the initial conditions for the slipping system with an additional slipping velocity, given by

$$\begin{pmatrix} \dot{x}_0 \\ \dot{y}_0 \end{pmatrix} = 1.1 \times 10^{-10} \underline{v}_{\text{slip}}, \tag{4.41}$$

where $\underline{v}_{\text{slip}}$ is given in eq. (4.35). The factor of 1.1 ensures the system does not begin too close to the slipping-to-rolling transition boundary, eq. (4.36).

When transitioning from slipping to rolling, we check that rolling is indeed feasible using eq. (4.33). If it is, then we set $\dot{x} = \dot{y} = 0$ and solve the rolling system. If rolling is not feasible, then the disk continues to slip and we compute the direction of initial slip as above. This ensures that we avoid missing events where the disk slips through zero contact point velocity without rolling.

The materials parameters of Euler's disk are given in Section 3.2.2 and repeated here

$$m = 0.443\,\text{kg}, \quad H = 0.0635\,\text{m}, \quad R = 0.0381\,\text{m}, \quad A = 1.62 \times 10^{-4}\,\text{kg}\,\text{m}^2, \quad C = 3.22 \times 10^{-4}\,\text{kg}\,\text{m}^2. \tag{4.42}$$

The coefficient of Coulomb friction of Euler's disk on the stainless steel base-plate was measured to be $\mu = 0.134$ in Table 3.1. Initial conditions are computed from the data provided by the experiments in Section 3.3. The disk was spun on a stainless steel base-plate, and filming from the side, we obtained data for ϕ and ψ. Numerical differentiation gives rough estimates for $\dot{\phi}$ and $\dot{\psi}$. Filming from above, we also tracked the rotation of a strip drawn on the face of the disk. The angular velocity of this strip was denoted by $\dot{\beta}$ and a relationship, eq. (3.22), derived that enabled estimation of $\dot{\theta}$. The initial conditions are given 0.5 s before the disk comes to a halt. In unscaled variables they read

$$\underline{X}_0 = \left(\psi, \dot{\psi}, \phi, \dot{\phi}, \theta, \dot{\theta}, x, \dot{x}, y, \dot{y}\right)^{\mathsf{T}} = (0, -188.5, 0.0243, 0, 0, 187.2, 0, 0, 0, 0)^{\mathsf{T}}. \tag{4.43}$$

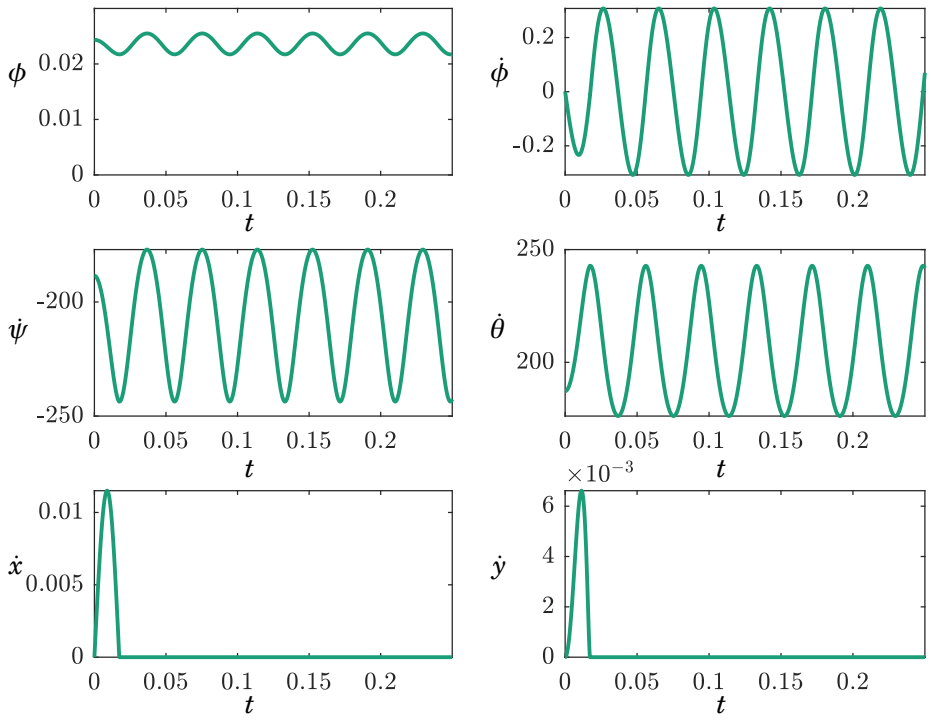

Figure 4.3: Numerical solution of the equations of motion, eqs. (4.25) and (4.32), with ICs and parameter values from eqs. (4.42) and (4.43). Variables are unscaled. A brief period of slip is visible before settling down to rolling motion.

The initial conditions for the cyclic variables x, y, ψ and θ are set to zero without loss of generality. It is not possible to accurately compute the velocity of the contact point from the experiments, so we check the feasibility of rolling using eq. (4.33) and find that the disk must slip. We then compute the initial direction of slip and find $\xi^{\mathcal{I}} = 0$ and the disk initially slips in the positive $x^{\mathcal{I}}$ direction.

The results of the numerical simulation are shown in fig. 4.3 in unscaled units for comparison with later simulations and the experimental results. An initial period of slip lasts for around 0.02 s before a transition to rolling which continues for the remainder of the integration. The disk does not come to a halt in fig. 4.3.

In fig. 4.4, we plot the friction ratio for the solution and find that, after the initial period of slip, the required coefficient of friction remains low. The system does not slip again, suggesting that the disk rolls indefinitely with these initial conditions.

It remains to be seen if the indefinite rolling behaviour occurs for all initial conditions. There is known to be error in the estimates of the initial conditions. So, in fig. 4.5 we alter the initial conditions such that $\dot{\psi} = -388.5$ and $\dot{\theta} = 387.2$, corresponding to releasing the disk with more spin. Different behaviour is observed in the numerical solution, again, we see a period of contact

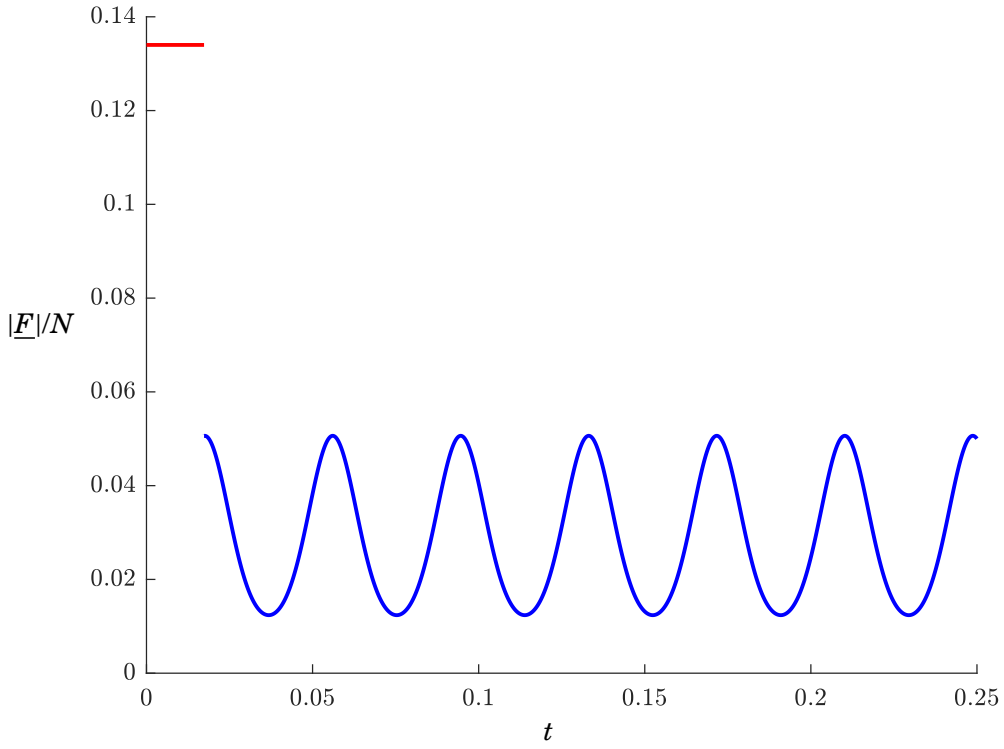

Figure 4.4: The friction ratio, $|\underline{F}|/N$, for the numerical solution in fig. 4.3. The short slipping phase is shown in red. The disk then undergoes periodic rolling motion.

point movement in fig. 4.5 and apparent oscillatory behaviour. However, the disk is repeatedly switching between slipping and rolling motion. This is clearly demonstrated in fig. 4.6, which shows many small periods of slip when the friction ratio, $|\underline{F}|/N$, the coefficient of Coulomb friction. Each slipping phase dissipates energy, however, it does not appear to be bring the disk to a halt. The long time limit appears to be a purely rolling phase, like in fig. 4.3.

Before discussing rolling frictions as the primary mechanism of dissipation, we must address another mechanism by which Coulomb friction could bring Euler's disk to a halt: the Painlevé paradox.

4.3.2 The Painlevé paradox

Under certain conditions, a rigid body subject to Coulomb friction and unilateral constraints may have none or multiple solutions. This is known as the Painlevé paradox. Specifically, Painlevé [78] discussed a slender rod slipping along a rough surface, which was later analysed in detail by Génot and Brogliato [42]. The paradox in two and three dimensions can be resolved by regularisation. Allowing some compliance in the surface results in a so-called 'impact-without-collision', where the disk lifts off to escape the paradox [26, 51]. For Euler's disk, repeated lift-off followed by

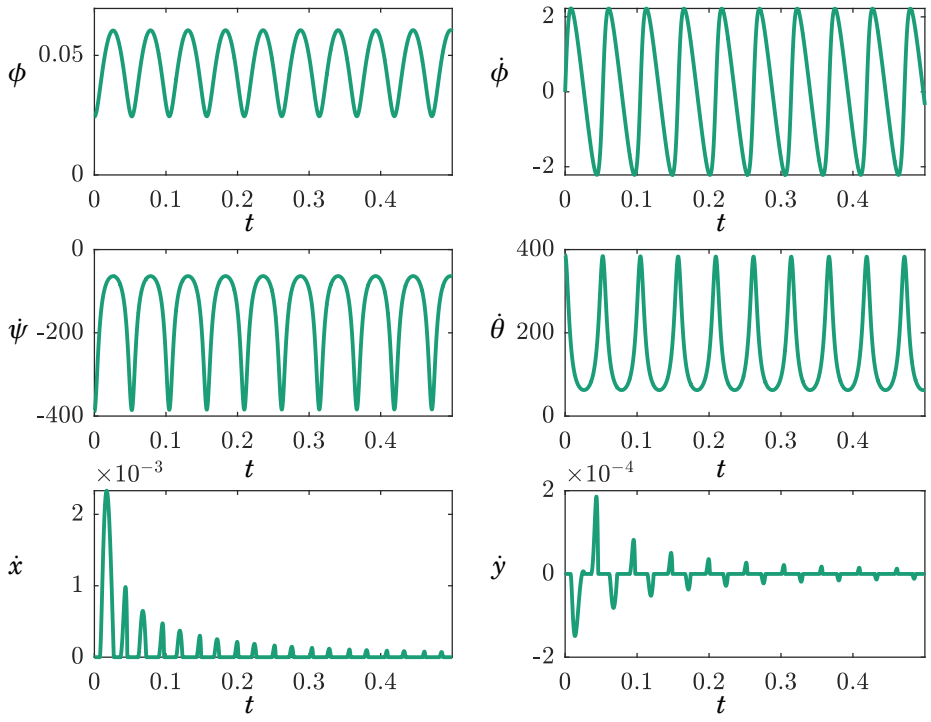

Figure 4.5: Numerical solution of the equations of motion, eqs. (4.25) and (4.32), with altered initial conditions: $\dot{\psi} = -388.5$ and $\dot{\theta} = 387.2$ and a increased simulation time to make the many small slipping phases visible. The material parameters are given in eq. (4.42).

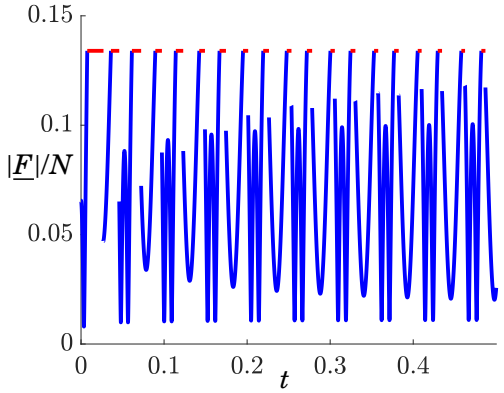

Figure 4.6: The friction ratio, $|\underline{F}|/N$, for the numerical solution in fig. 4.5. Many slipping sections are visible in red where $|\underline{F}|/N = 0.134$.

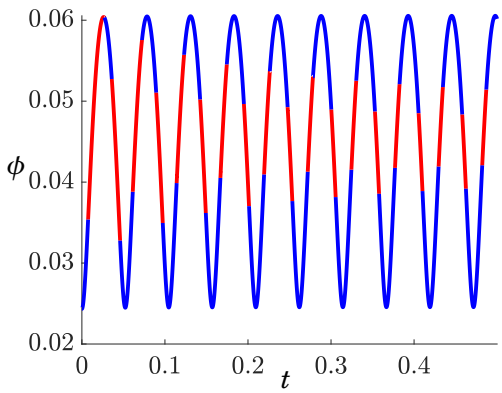

Figure 4.7: The time series of ϕ from the numerical solution in fig. 4.5, with the slipping sections in red and rolling in blue.

impacts with the plane represents a dissipation mechanism that could explain the losses of contact found by Borisov et al. [19]. In this subsection, we determine if it is possible for Euler's

disk to experience a Painlevé paradox. Rather than the thin rod studied by Painlevé [78], Hogan and Kristiansen [51] , and Cheesman et al. [26], we have a thick disk. This example is examined by Ivanov [55] who finds that 'in a neighborhood of stationary motions, detachments do not occur'. Liu et al. [69] examine the Painlevé paradox for a ball impacting disk system and also find that the Painlevé paradox does not occur at large values of ϕ. Here, we search for the Painlevé paradox at all values of ϕ and consider the effect of rolling friction.

To determine if the Painlevé paradox can occur, we compute the normal force $n(\phi,\dot{\phi},\ddot{\phi})$ explicitly. We also insert the slipping ODE for $\ddot{\phi}$, eq. (4.30a) to give

$$n(\phi,\dot{\phi},\ddot{\phi}) = \frac{-b}{p} = \frac{a - a\dot{\phi}^2(s_\phi + hc_\phi) + (c_\phi - hs_\phi)((a-c)s_\phi c_\phi \dot{\psi}^2 - cs_\phi \dot{\psi}\dot{\theta})}{a + (c_\phi - hs_\phi)^2 + \frac{\mu\dot{x}(hc_\phi + s_\phi)(c_\phi - hs_\phi)}{\sqrt{\dot{x}^2+\dot{y}^2}} - \eta q_y(\cos\phi - h\sin\phi)}, \tag{4.44}$$

where we have borrowed notation from Cheesman et al. [26] and denoted the numerator by $-b$ to describe the scaled free acceleration. We denote the denominator by p where $pn(\phi,\dot{\phi},\ddot{\phi})$ describes the acceleration of the contact point due to the interaction with the surface. There exist four distinct cases described by Cheesman et al. [26]:

- $b<0$, $p>0$ then $n(\phi,\dot{\phi},\ddot{\phi})>0$ and the rod slips along the rough surface.
- $b>0$, $p>0$ then $n(\phi,\dot{\phi},\ddot{\phi})<0$ and lift-off occurs.
- $b<0$, $p<0$ then $n(\phi,\dot{\phi},\ddot{\phi})<0$ and both the free and contact accelerations act downwards, inconsistent with the assumption of a rigid plane and solutions do not exist.
- $b>0$, $p<0$ then $n(\phi,\dot{\phi},\ddot{\phi})>0$ but, because the free acceleration is upwards, lift-off is still possible. Motion is indeterminate and solutions are non-unique.

To obtain a paradox, we require $p<0$, but this may not be achievable for realistic values of μ. In the absence of a dissipative moment, $\eta=0$, we set $p=0$ and solve for μ. First, we define a change of variables for $\bar{\phi}$ which represents the angle that $\underline{GP}$ makes with respect to the horizontal plane in fig. 4.1

$$\sin\phi + h\cos\phi = \sqrt{h^2+1}\sin\left(\bar{\phi}\right), \tag{4.45a}$$

$$\cos\phi - h\sin\phi = \sqrt{h^2+1}\cos\left(\bar{\phi}\right). \tag{4.45b}$$

Then p is reduced to

$$p = a + (h^2+1)\cos^2\bar{\phi} - \mu(h^2+1)\cos\bar{\phi}\sin\bar{\phi}\frac{\dot{x}}{\sqrt{\dot{x}^2+\dot{y}^2}} = 0. \tag{4.46}$$

Dividing eq. (4.46) by a factor of the moment of inertia, a, gives

$$0 = 1 + \lambda\cos^2\bar{\phi} - \mu\lambda\cos\bar{\phi}\sin\bar{\phi}\frac{\dot{x}}{\sqrt{\dot{x}^2+\dot{y}^2}}, \tag{4.47}$$

where $\lambda = (h^2 + 1)/a$. Setting $\dot{x} = -1$, and $\dot{y} = 0$ makes the problem planar and maximises the negative part of p. We obtain the same expression as Hogan and Kristiansen [51, (2.6)], but with a shifted angle $\bar{\phi}$. The critical coefficient of Coulomb friction for the planar Painlevé paradox is

$$\mu_p = \frac{2\sqrt{1+\lambda}}{\lambda}. \tag{4.48}$$

For the commercial Euler's disk $h = 0.167$ and $a = 0.252$ giving $\lambda = 4.08$ and $\mu_p = 1.11$. This value of the coefficient of Coulomb friction is much larger than those found in Table 3.1 and in the 3D case, with $(\dot{x}, \dot{y}) \in \mathcal{R}^2$, the required coefficient is even larger [26]. The Painlevé paradox has no place in the Euler's disk phenomenon and the loss of contact must arise due to other causes.

The additional term $-\eta q_y(\cos\phi - h\sin\phi)$ in eq. (4.44) acts to make p more negative, reducing the critical value of the coefficient of friction needed for a Painlevé paradox. However, rolling friction is typically far weaker than sliding friction; η is orders of magnitude smaller than μ. Therefore, the rolling term will only have a small effect on μ_p. In the next section, we derive various rolling frictions and determine the components of the dissipative moments, q_x, q_y and q_z.

4.4 Rolling friction formulations

It is clear that Coulomb friction is not the main driver of energy loss in Euler's disk [68, 73]. We turn to formulations of rolling friction to explain the abrupt halt of Euler's disk and its power law governed decrease in energy. Rolling contact and, by extension, rolling friction have many engineering applications. Pacejka and Bakker [77] developed the so-called 'magic formula tyre model' describing the slipping, self-righting and other dynamic properties of tyres. Euler's disk is far more rigid than rubber tyres and therefore requires a different physical description. In the 19$^{\text{th}}$ century, Reynolds [82] experimented with cast iron rollers on glass and wood. It was shown that slip occurs at the rear of the contact region, thus giving rise to rolling friction. Tabor [90] performed experiments rolling a hard steel sphere over metal surfaces and measured the amount of plastic deformation and also found slip. He posited that, even in metals, the source of rolling resistance arises from elastic hysteresis losses. More recently, Ivanov [56] suggested that rolling friction is inherently viscous, citing the example of a pencil rolling down an inclined slope. Other, more complicated rolling friction models exist such as the viscoelastic model studied by Goryacheva and Zobova [46]. Johnson [58] identifies three sources of energy dissipation in rolling contact :

- Micro-slip and friction at the contact interface.
- Inelastic properties of the material.
- Roughness of the rolling surfaces.

To avoid overcomplication, we assume simple rolling friction models that straightforwardly correspond to moments that oppose angular velocity, as in eq. (4.5). In planar systems, such as

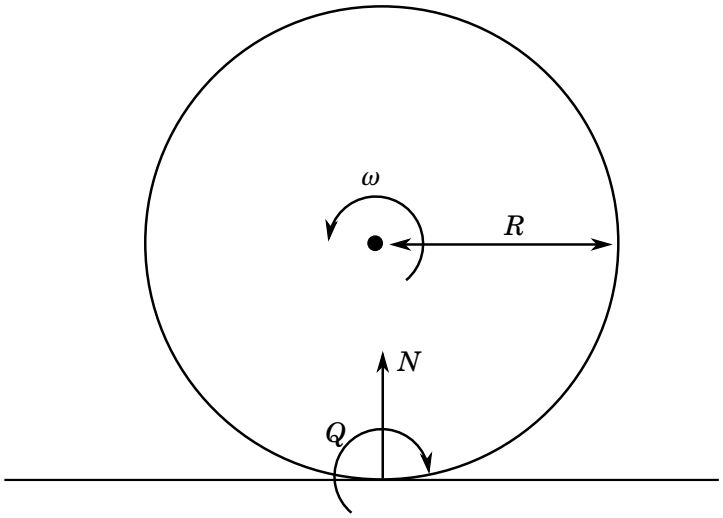

Figure 4.8: Planar rolling friction. The torque, Q, opposes the angular velocity, ω.

fig. 4.8, rolling friction is commonly modelled as an angular version of Coulomb friction in the form of a torque, Q, that opposes an angular velocity, ω. In unscaled variables,

$$Q \begin{cases} = -\eta R N(\phi, \dot{\phi}, \ddot{\phi}) \operatorname{sign}(\omega) & \text{if} \quad \omega \neq 0 \\ \in [-\eta R N(\phi, \dot{\phi}, \ddot{\phi}), \eta R N(\phi, \dot{\phi}, \ddot{\phi})] & \text{if} \quad \omega = 0 \end{cases} . \tag{4.49}$$

Just as with Coulomb friction, eq. (4.49) contains a discontinuity at $\omega = 0$. If $\omega \neq 0$, the system is off the discontinuity set and provides a constant arresting moment, while if $\omega = 0$, the system is on the discontinuity set and rolling friction provides a moment that acts to keep $\omega = 0$.

For a body rolling in three dimensions, the formulation of rolling friction becomes less clear. There are three axes about which the body may roll and spin. A number of formulations have been proposed: classical, contour, pivoting and rolling, along with viscous variants. The formulations capture different effects: rolling motions compress the plane, while spinning motions shear the plane. In three dimensions, Coulomb friction has an isolated codimension-2 discontinuity but, with the right choice of rolling friction, one can obtain codimension-3 discontinuities [9].

In this work, we disregard the dynamics on the discontinuity set. Just as Coulomb friction dissipates no energy when rolling without slip, rolling friction dissipates no energy when the system is on the discontinuity set. Therefore, we assume rolling friction formulations consistent with eq. (4.5), ignoring the differential inclusions. If required, the dynamics on the discontinuity set could be found using the constraint $\omega = 0$. In this chapter, we derive expressions for the different formulations of rolling friction, before analysis in Section 4.6.

4.4.1 Classical rolling friction

Johnson [58] defines rolling contact as 'relative angular motion between two bodies in contact about an axis parallel to their common tangent plane'. Classical rolling friction assumes that

there is a resistance to such rolling contact, that is, angular velocities about the $x^{\mathcal{G}}$ and $y^{\mathcal{G}}$ axes. Angular velocity about the $z^{\mathcal{G}}$ axis is called pivoting and is not considered in classical rolling friction. We compute the angular velocity about the horizontal axes $x^{\mathcal{G}}$ and $y^{\mathcal{G}}$

$$\omega_x^{\mathcal{G}} = \left(\mathrm{R}_{\mathcal{BG}}\underline{\Omega}^{\mathcal{B}}\right)\cdot\underline{\hat{x}}^{\mathcal{G}} = -\sin\phi\cos\psi\dot{\theta} + \sin\psi\dot{\phi}, \tag{4.50a}$$

$$\omega_y^{\mathcal{G}} = \left(\mathrm{R}_{\mathcal{BG}}\underline{\Omega}^{\mathcal{B}}\right)\cdot\underline{\hat{y}}^{\mathcal{G}} = -\sin\phi\sin\psi\dot{\theta} - \cos\psi\dot{\phi}. \tag{4.50b}$$

We construct classical rolling friction by finding the moment opposing the angular velocity and dividing by the factor $\sqrt{\left(\omega_x^{\mathcal{G}}\right)^2 + \left(\omega_y^{\mathcal{G}}\right)^2}$ to ensure that the modulus of the moment is ηRN

$$\underline{Q}^{\mathcal{G}} = -\frac{\eta RN(\phi,\dot{\phi},\ddot{\phi})}{\sqrt{\left(\omega_x^{\mathcal{G}}\right)^2 + \left(\omega_y^{\mathcal{G}}\right)^2}}\begin{pmatrix}\omega_x^{\mathcal{G}}\\ \omega_y^{\mathcal{G}}\\ 0\end{pmatrix} = -\frac{\eta RN(\phi,\dot{\phi},\ddot{\phi})}{\sqrt{\dot{\phi}^2+\dot{\theta}^2\sin^2\phi}}\begin{pmatrix}-\sin\phi\cos\psi\dot{\theta} + \sin\psi\dot{\phi}\\ -\sin\phi\sin\psi\dot{\theta} - \cos\psi\dot{\phi}\\ 0\end{pmatrix}. \tag{4.51}$$

Writing eq. (4.51) in the body frame, $\mathcal{B}$, and non-dimensionalising, we obtain classical rolling friction

$$\underline{Q}^{\mathcal{B}} = -\frac{\eta n(\phi,\dot{\phi},\ddot{\phi})}{\sqrt{\dot{\phi}^2+\sin^2\phi\dot{\theta}^2}}\begin{pmatrix}-\cos\phi\sin\phi\dot{\theta}\\ -\dot{\phi}\\ \dot{\theta}\sin^2\phi\end{pmatrix}, \tag{4.52}$$

defining the components of $\underline{q}$ in the equations of motion eqs. (4.25) and (4.32)

$$\underline{q} = \begin{pmatrix}q_x\\ q_y\\ q_z\end{pmatrix} = \begin{pmatrix}\frac{-\cos\phi\sin\phi\dot{\theta}}{\sqrt{\dot{\phi}^2+\dot{\theta}^2\sin^2\phi}}\\ \frac{-\dot{\phi}}{\sqrt{\dot{\phi}^2+\dot{\theta}^2\sin^2\phi}}\\ \frac{\dot{\theta}\sin^2\phi}{\sqrt{\dot{\phi}^2+\dot{\theta}^2\sin^2\phi}}.\end{pmatrix} \tag{4.53}$$

Equation (4.52) agrees with the definition of rolling friction given by Leine [68], who neglects the q_y term as it is assumed that $\dot{\phi}$ is small. Note that eq. (4.52) defines the moment away from the discontinuity at $\dot{\phi}^2+\dot{\theta}^2\sin^2\phi \neq 0$. If $\dot{\phi}^2+\dot{\theta}^2\sin^2\phi = 0$, then the moment can take any value $|\underline{Q}^{\mathcal{B}}| \in [0, \eta n(\phi,\dot{\phi},\ddot{\phi})]$ to oppose the angular velocity. A viscous version of the dissipation mechanism assumes linear dependence on the angular velocity and can be obtained by discarding the square-root term in eq. (4.52).

4.4.2 Pivoting friction

In contrast to classical rolling friction, pivoting friction assumes a resistance to spinning motion or angular velocity about the $z^{\mathcal{G}}$. We compute the vertical angular velocity

$$\omega_z^{\mathcal{G}} = \left(\mathrm{R}_{\mathcal{BG}}\underline{\Omega}^{\mathcal{B}}\right)\cdot\underline{\hat{z}}^{\mathcal{G}} = \dot{\psi} + \dot{\theta}\cos\phi. \tag{4.54}$$

After shifting to the body frame and non-dimensionalising, the dissipative moment is

$$\underline{Q}^{\mathcal{B}} = -\eta n(\phi, \dot{\phi}, \ddot{\phi}) \operatorname{sign}(\dot{\psi} + \dot{\theta}\cos\phi) \begin{pmatrix} \sin\phi \\ 0 \\ \cos\phi \end{pmatrix}, \tag{4.55}$$

defined for $\dot{\psi} + \dot{\theta}\cos\phi \neq 0$, which agrees with Leine [68]. The components of $\underline{q}$ are defined analogously to eq. (4.52). The zero of $\dot{\psi} + \dot{\theta}\cos\phi$ is a co-dimension one discontinuity.

4.4.3 General rolling friction

General rolling friction simply opposes the total angular velocity of the disk, without differentiating between rolling and pivoting motion

$$\underline{Q}^{\mathcal{B}} = -\eta n(\phi, \dot{\phi}, \ddot{\phi}) \underline{\hat{\Omega}} = -\frac{\eta n}{\sqrt{\dot{\psi}^2 \sin^2\phi + \dot{\phi}^2 + (\dot{\psi}\cos\phi + \dot{\theta})^2}} \begin{pmatrix} \dot{\psi}\sin\phi \\ -\dot{\phi} \\ \dot{\psi}\cos\phi + \dot{\theta} \end{pmatrix}. \tag{4.56}$$

This formulation has a co-dimension three discontinuity that occurs when $\dot{\phi} = \dot{\psi} = \dot{\theta} = 0$. Examples of such discontinuities are discussed by Antali and Varkonyi [9]. Other formulations of rolling friction can be constructed by weighted combinations of pivoting and classical rolling friction.

4.4.4 Contour friction

Contour friction differs to the previous formulations. Le Saux et al. [67] defines it as a moment 'which models resistance against the movement of the contact point along the contour of the disk'. We recall the movement of the contact point from eq. (2.100) in Chapter 2 repeated here

$$\underline{V}_P^{\mathcal{G}} = \underline{V}_G^{\mathcal{G}} + \mathrm{R}_{\mathcal{BG}} \left(\left(\underline{\Omega}^{\mathcal{B}} - \dot{\theta}\underline{\hat{z}}^{\mathcal{B}} \right) \times \underline{GP}^{\mathcal{B}} \right), \tag{4.57}$$

which, when converted to the intermediate frame $\mathcal{I}$, gives the unscaled contact point velocity

$$\underline{V}_p^{\mathcal{I}} = (0, R\dot{\theta}, 0)^{\mathsf{T}}. \tag{4.58}$$

Contour friction opposes the velocity of the contact point $\underline{V}_P$. Leine [68] derives the moment through virtual power considerations. After placing in the body frame and non-dimensionalising

$$\underline{Q}^{\mathcal{B}} = -\eta n(\phi, \dot{\phi}, \ddot{\phi}) \operatorname{sign}(\dot{\theta}) \begin{pmatrix} -\cot\phi \\ 0 \\ 1 \end{pmatrix}. \tag{4.59}$$

Contour friction, in contrast to previous mechanisms, is singular at $\phi = 0$. Therefore, the strength of the moment increases as the disk falls flat. In fact, the formulation is closely related to classical

rolling friction. Contour friction may be obtained by neglecting the $\dot{\phi}$ term in eq. (4.52) and multiplying by a factor of $1/\sin\phi$. Contour friction also has a codimension-1 discontinuity

$$D_c = \left\{ \underline{X} \;\middle|\; \dot{\theta} = 0 \right\}, \tag{4.60}$$

which has implications for the continued rotation of the disk, discussed further in Section 4.7.

In Section 4.5, we find a justification for the existence of contour friction by relaxing the rigid body assumption.

4.5 Rolling frictions that arise from a contact region

The rolling friction formulations set out in Section 4.4 are phenomenological models designed to describe behaviour in different rolling regimes. For the disk, there is no a priori reason to choose one model over another. In this section, we derive rolling frictions for the disk by relaxing the rigid body assumption. As seen in fig. 4.9, rolling friction requires the presence of a contact region, a fact neglected in the phenomenological models of section 4.4. If the disk contacts the plane at a point, then there is no distance over which to exert a dissipative moment. However, the disk and the plane are not perfectly rigid: they deform and contact over an area known as the contact region. The normal force is replaced by a normal pressure, $p(x)$ over the contact region. If the disk rolls, then the pressure distribution skews (fig. 4.9, right) resulting in a moment that acts to slow the body down. In this section, we explore different contact region models and their resulting dissipation mechanisms.

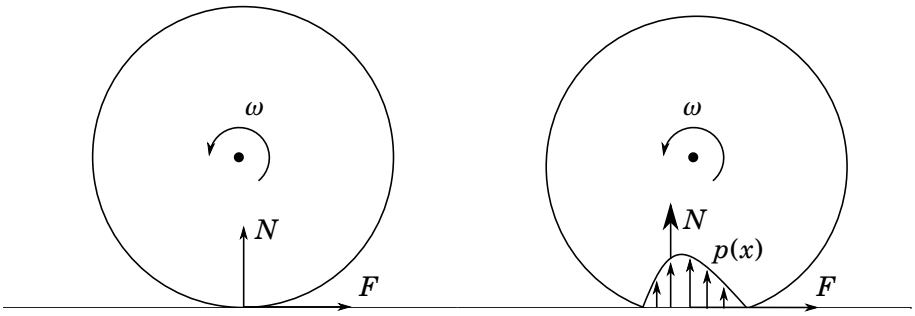

Figure 4.9: Rolling friction requires the presence of a contact region over which there is a skewed pressure distribution, $p(x)$.

4.5.1 Constant offset model

In the first instance, we assume the presence of a contact region with a skewed pressure distribution. The normal force is offset by a small distance, $\underline{\delta}^{\mathcal{I}} = (U, V, 0)$, from the rigid body contact point limit, as shown in fig. 4.10. The offset opposes the motion of the disk. For example, if the disk rolls such that $\underline{G}$ moves in the positive $y^{\mathcal{I}}$ direction, then V must be positive to oppose the

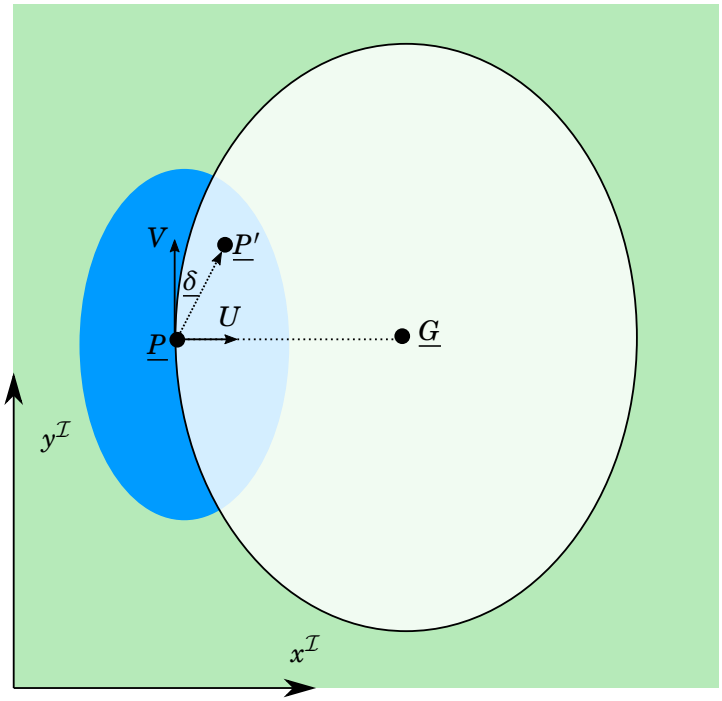

Figure 4.10: Top view of the disk shown in white. An enlarged contact region is shown in blue. The centre of pressure $\underline{P}'$ is offset by $\underline{\delta}$ from the rigid body contact point $\underline{P}$.

motion. The moment balance, eq. (4.2b), is altered such that

$$\mathrm{I}\dot{\underline{\Omega}}^{\mathcal{B}} - \underline{\omega}^{\mathcal{B}} \times \mathrm{I}\underline{\Omega}^{\mathcal{B}} = \underline{GP}^{\mathcal{B}} \times \mathrm{R}_{\mathcal{GB}}\underline{F}^{\mathcal{G}} + (\underline{GP}^{\mathcal{B}} + \underline{\delta}^{\mathcal{B}}) \times \mathrm{R}_{\mathcal{GB}}\underline{N}^{\mathcal{G}} \tag{4.61}$$

where we have assumed no changes in the friction force. The offset, $\underline{\delta}$, results in a dissipative moment $\underline{Q}$ that acts to slow the disk down. The dissipative moment is given by

$$\underline{\delta}^{\mathcal{B}} \times (\mathrm{R}_{\mathcal{GB}}\underline{N}^{\mathcal{G}}) = \underline{Q}^{\mathcal{B}} = -n \begin{pmatrix} -v\,\mathrm{sign}(\dot{\theta})\cos\phi \\ -u\,\mathrm{sign}(\dot{\phi}) \\ v\,\mathrm{sign}(\dot{\theta})\sin\phi \end{pmatrix}, \tag{4.62}$$

where we introduce $U = uR\,\mathrm{sign}(\dot{\phi})$ and $V = vR\,\mathrm{sign}(-\dot{\theta})$ to non-dimensionalise and ensure that u and v are the correct sign. Note that this formulation is similar to classical rolling friction in eq. (4.52), reaching equality at $\dot{\phi} = 0$ or $\dot{\theta} = 0$. The contact region is expected to be long and thin as contact is made along the rim of the disk, hence we assume that $q_y = u = 0$ to give

$$\underline{Q}^{\mathcal{B}} = -n(\phi, \dot{\phi}, \ddot{\phi})v\,\mathrm{sign}(\dot{\theta}) \begin{pmatrix} -\cos\phi \\ 0 \\ \sin\phi \end{pmatrix}, \tag{4.63}$$

in agreement with the classical rolling friction discussed by Leine [68]. The offset in the $y^{\mathcal{I}}$ direction, v, takes the place of the coefficient of rolling friction, η.

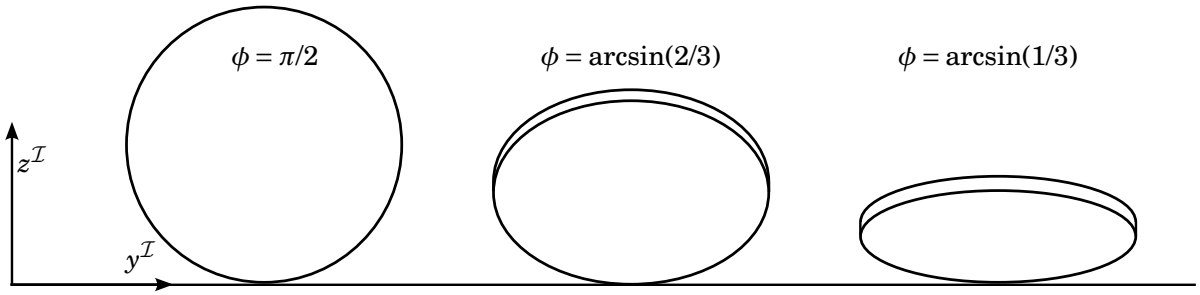

Figure 4.11: As the disk's angle of inclination decreases, the radius of curvature increases.

4.5.2 Curvature dependent offset model

Cross [31] noted that, if the offset distance, V, varies inversely with $\sin\phi$, then 'the rate of fall increases with time'. Therefore, we extend the constant offset model by assuming that the size and shape of the contact region is dependent on the orientation of the disk. As the disk falls flatter, the radius of curvature seen by the plane increases, resulting in a thinner, longer contact region, as shown in fig. 4.11. We compute the radius of curvature at the contact point by considering the bottom face of the disk flush with the plane in the intermediate frame $\mathcal{I}$. The bottom rim of the disk is parametrised by the angle α

$$(x, y, z)^{\mathsf{T}} = (R\cos\alpha, R\sin\alpha, 0)^{\mathsf{T}}. \tag{4.64}$$

To tilt the disk upwards about the contact point we rotate by ϕ about the $x^{\mathcal{I}}$ axis, by applying the rotation matrix $\mathrm{R}_{\mathcal{IB}}$. A translation upwards of $R\sin\phi$ ensures contact at $z = 0$. The new coordinates of the rim are

$$(x, y, z)^{\mathsf{T}} = (R\cos\alpha\cos\phi, R\sin\alpha, R\cos\alpha\sin\phi + R\sin\phi)^{\mathsf{T}}. \tag{4.65}$$

We project the transformed circle into the $(y,z)^{\mathcal{I}}$ plane of fig. 4.11, giving

$$\frac{y^2}{R^2} + \frac{(z - R\sin\phi)^2}{R^2\sin\phi^2} = 1, \tag{4.66}$$

an ellipse with z semi-axis dependent upon ϕ. The rim touches the plane at $z = 0$, at which point the radius of curvature, seen by the plane in the $y^{\mathcal{I}}$ axis is

$$R_y = \frac{R}{\sin\phi}. \tag{4.67}$$

As ϕ decreases, R_y increases, increasing the length of the contact region in the $y^{\mathcal{I}}$ direction. The width of the contact region in the $x^{\mathcal{I}}$ direction is governed by the constant radius of curvature of the edge of the disk, R_x, where $R_x \ll R_y$. Therefore as a first approximation, we propose that the size of the offsets in the centre of pressure are proportional to the curvatures, $V \propto R_y$ and $U \propto R_x$ such that

$$V = \frac{k_v R\,\mathrm{sign}(\dot\theta)}{\sin\phi}, \quad U = k_u R\,\mathrm{sign}(\dot\phi), \tag{4.68}$$

where k_v and k_u are constants of proportionality. Upon substitution of eq. (4.68) into eq. (4.62), we obtain the dissipative moment arising due to a curvature dependent offset in the centre of pressure

$$\underline{Q}^{\mathcal{B}} = -n(\phi,\dot{\phi},\ddot{\phi}) \begin{pmatrix} -k_v \operatorname{sign}(\dot{\theta}) \cot\phi \\ -k_u \operatorname{sign}(\dot{\phi}) \\ k_v \operatorname{sign}(\dot{\theta}) \end{pmatrix}. \tag{4.69}$$

This dissipation mechanism closely agrees with contour friction, eq. (4.59), and is identical in the case of $k_u = 0$, a reasonable approximation due to the difference in curvatures. If $k_u = 0$, then k_v takes the role of η, the coefficient of rolling friction. However, as discussed in the next subsection, the assumption $V \propto R_y$ appears to overestimate the length of the contact region.

4.5.3 Other contact region models

Thus far, we have ignored the shape of the contact region, assuming only that the centre of pressure is shifted by an amount proportional to the radius of curvature of the disk. In this subsection, we use Hertzian contact theory to determine the size and shape of the contact region and inform our estimates of the offset $\underline{\delta}$. First, we give an overview of Hertzian contact, before examining some common approximations. We follow Johnson's [58] derivation of the contact region for general profiles. The disk and plane are assumed to be smooth, static, frictionless and elastic. The plane is modelled as an elastic half-space with zero curvature everywhere. The disk has two principle radii of curvature: $R_y = R/\sin(\phi)$ and R_x, aligned with the intermediate axes $y^{\mathcal{I}}$ and $x^{\mathcal{I}}$ respectively. We approximate the distance, d, between the disk and the plane by

$$d(x,y) = \frac{x^2}{2R_x} + \frac{y^2}{2R_y}, \tag{4.70}$$

where $(x,y) = (0,0)$ is the centre of the contact region. Cubic terms have been omitted due to the assumption of a small contact region. Hertzian contact theory assumes an elliptic contact region with semi-axes lengths a and b in the $y^{\mathcal{I}}$ and $x^{\mathcal{I}}$ axes respectively. The pressure distribution over the contact region is assumed to be

$$p(x,y) = p_0 \left(1 - \left(\frac{x}{b}\right)^2 - \left(\frac{y}{a}\right)^2\right)^{1/2}, \tag{4.71}$$

where p_0 is the maximum pressure at the centre of the contact region. The three unknowns p_0, a and b are determined by the following set of three equations, adapted from Johnson [58, (4.26a), (4.26b) and (4.27)], and originally derived by considering the surface displacements caused by the pressure distribution eq. (4.71)

$$\frac{1}{2R_x} = \frac{p_0}{E^*} \frac{b}{e^2 a^2} (K(e) - E(e)), \tag{4.72a}$$

$$\frac{1}{2R_y} = \frac{p_0}{E^*} \frac{b}{e^2 a^2} \left((a^2/b^2)E(e) - K(e)\right), \tag{4.72b}$$

$$P = (2/3) p_0 a b. \tag{4.72c}$$

In this quasi-static setting it is assumed that the total load, P, equals the weight of the disk, mg. E^* is a combined measure of the Young's moduli mediated by the Poisson ratios

$$\frac{1}{E^*} = \frac{1-\nu_1^2}{E_1} + \frac{1-\nu_2^2}{E_2}. \tag{4.73}$$

The eccentricity of the contact region, e, is given by

$$e = \left(1 - \frac{b^2}{a^2}\right)^{1/2}, \tag{4.74}$$

for $b < a$. The functions $K(e)$ and $E(e)$ are complete elliptic integrals of the first and second kind, respectively defined by

$$K(e) = \int_0^1 \frac{\mathrm{d}t}{\sqrt{(1-t^2)(1-e^2t^2)}}, \quad E(e) = \int_0^1 \frac{\sqrt{1-e^2t^2}}{\sqrt{1-t^2}}\mathrm{d}t. \tag{4.75}$$

Combining eq. (4.72), we eliminate p_0 and insert the radii of curvatures, R_x and $R_y = R/\sin\phi$, to obtain

$$\frac{R}{R_x \sin\phi} = \frac{\frac{a^2}{b^2}E(e) - K(e)}{K(e) - E(e)}, \tag{4.76a}$$

$$\frac{1}{2}\left(\frac{\sin\phi}{RR_x}\right)^{1/2} = \frac{3mg}{2E^*a^3e^2}\left\{\left((a/b)^2E(e) - K(e)\right)\left(K(e) - E(e)\right)\right\}^{1/2}. \tag{4.76b}$$

It remains to solve eq. (4.76) for the unknown semi-axes a and b of the contact region as a function of ϕ and other material constants. We may then compute the dissipative moment by assuming an offset proportional to the length of the semi-axes,

$$\underline{\delta} = \begin{pmatrix} U \\ V \end{pmatrix} \propto \begin{pmatrix} b \\ a \end{pmatrix} \tag{4.77}$$

However, it is not possible to solve for a and b analytically because eq. (4.76) contain elliptic functions. A number of different approximations have been developed for this purpose. We first compute the semi-axes using the Greenwood approximation [47].

4.5.3.1 Greenwood approximation

Instead of an elliptic contact region, Greenwood [47] assumes an equivalent circular contact with area πc^2, and radius, c, given by the geometric mean of the contact region semi-axes $c^2 = ab$. The radius c and the maximum contact pressure p_0 are determined by [47, (1)]

$$c = \frac{3WR_e}{4E^*}^{1/3}, \qquad p_0 = \frac{3W}{2\pi c^2}. \tag{4.78}$$

The effective radius of curvature, R_e, is an average of the relative curvatures, $\kappa_y = \frac{1}{2R_y}$ and $\kappa_x = \frac{1}{2R_x}$ [47, (2)]

$$R_e = \left(\kappa_y\kappa_x\frac{(\kappa_y + \kappa_x)}{2}\right)^{-1/3}. \tag{4.79}$$

We require the semi-axes a and b of the ellipse, rather than their product $c^2 = ab$. The ratio $\frac{b}{a}$ may be found using the asymptotic equation employed by Greenwood [47] and Johnson [58]

$$\left(\frac{b}{a}\right) \sim \left(\frac{\kappa_y}{\kappa_x}\right)^{2/3}. \tag{4.80}$$

By solving for a and b, substituting the disk curvatures $\kappa_y = \frac{\sin\phi}{2R}$ and $\kappa_x = \frac{1}{2R_x}$ and assuming small ϕ, we obtain estimates for the size of the contact region

$$a = \left(\frac{3W}{4E^*}\right)^{1/3}\left(\frac{R}{R_x\sin\phi}\right)\left(\frac{2R^2R_x^2}{R - x\sin^2\phi + R\sin\phi}\right)^{1/9} \propto \phi^{-4/9}, \tag{4.81a}$$

$$b = \left(\frac{3W}{4E^*}\right)^{1/3}\left(\frac{R_x\sin\phi}{R}\right)\left(\frac{2R^2R_x^2}{R_x\sin^2\phi + R\sin\phi}\right)^{1/9} \propto \phi^{2/9}. \tag{4.81b}$$

The semi-axis a increases according to a singular power of ϕ, while the semi-axis b decreases. Assuming that the offsets u and v are proportional to the semi-axes b and a respectively gives

$$u = k_u\phi^{2/9}, \tag{4.82a}$$

$$v = k_v\phi^{-4/9}. \tag{4.82b}$$

Compared with the curvature dependent offset model in Section 4.5.2, this estimate of the offset v is much smaller as $\phi \to 0$. This suggests that the linear dependence of the offset on the radius of curvature in eq. (4.68) is an overestimate. This is also the case for the other Hertzian derived models.

Substituting the offset into the constant offset dissipation mechanism eq. (4.62) yields

$$\underline{Q}^{\mathcal{B}} = -n(\phi,\dot\phi,\ddot\phi)\begin{pmatrix} -k_v\phi^{-4/9} \\ -k_u\phi^{2/9} \\ k_v\phi^{5/9} \end{pmatrix}. \tag{4.83}$$

A warning must be issued, it is stated that 'This method works well for mildly elliptical contacts' [47]. However, we require very elliptical contacts, for which $a \gg b$, suggesting that other contact models might be more appropriate.

4.5.3.2 Brewe and Hamrock approximation

Brewe and Hamrock [21] consider an elliptic contact region, but approximate the value of the elliptic integral and the semi-axis ratio $k = a/b$. The exact equations for the semi-axes are [47]

$$a = \left(\frac{3k^2E(e)mgR}{\pi E^*}\right)^{1/3}, \qquad b = \left(\frac{3E(e)WR}{\pi kE^*}\right)^{1/3} \tag{4.84}$$

where $1/R = \kappa_y + \kappa_x$. The elliptic integral $E(e)$ and semi-axis ratio are approximated by

$$k \equiv \frac{a}{b} \approx 1.0339\left(\frac{\kappa_x}{\kappa_y}\right)^{0.636}, \quad E(e) \approx 1.0003 + 0.5968\left(\frac{\kappa_y}{\kappa_x}\right). \tag{4.85}$$

Assuming small ϕ and that the offsets are proportional to the semi-axes yields

$$V \approx k_v \phi^{-0.424}, \tag{4.86a}$$

$$U \approx k_u \phi^{0.212}. \tag{4.86b}$$

Inserting into the offset dissipation mechanism eq. (4.62) gives the moment

$$\underline{Q}^{\mathcal{B}} = -n(\phi, \dot{\phi}, \ddot{\phi}) \begin{pmatrix} -k_v \phi^{-0.424} \\ -k_u \phi^{0.212} \\ k_v \phi^{0.576} \end{pmatrix}. \tag{4.87}$$

A similar approximation by Hamrock and Brewe [48] corrects for errors at almost circular contacts, which is not relevant for the very elliptical contacts considered here.

4.5.3.3 Winkler's elastic foundation model

Instead of modelling the plane with an elastic half-space, the Winkler or mattress model described in Johnson [58] assumes an elastic foundation of depth d_f, resting on a rigid base. Shear forces are neglected in this model. The boundary of the contact area is an ellipse with semi-axes

$$a = (2\delta R_y)^{1/2}, \quad b = (2\delta R_x)^{1/2}, \quad \delta = \frac{2 d_f m g}{K \pi a b} \tag{4.88}$$

where δ is the compression at the origin and K is the elastic modulus of the foundation. Inserting $R_y = R/\sin\phi$, solving for a and b and assuming small ϕ gives

$$a = \sqrt{2} \left(\frac{P^2 d_f^2 R^3}{R_x K^2 \pi^2} \right)^{1/8} \sin^{-3/8}\phi \propto \phi^{-3/8}, \tag{4.89a}$$

$$b = \sqrt{2} \left(\frac{P^2 d_f^2 R_x^3}{R K^2 \pi^2} \right)^{1/8} \sin^{-1/8}\phi \propto \phi^{1/8}. \tag{4.89b}$$

Assuming that the offset, $\underline{\delta}$ is proportional to the length of the semi-axes and inserting into the dissipation mechanism, eq. (4.62), gives

$$\underline{Q}^{\mathcal{B}} = n(\phi, \dot{\phi}, \ddot{\phi}) \begin{pmatrix} k_v \phi^{-3/8} \\ k_u \phi^{1/8} \\ -k_v \phi^{5/8} \end{pmatrix}. \tag{4.90}$$

4.5.3.4 Cylindrical contact model

The final approximation considered is the cylindrical contact model. At small ϕ, the radius of curvature in the $y^{\mathcal{I}}$ direction is much larger than the radius of curvature in the $x^{\mathcal{I}}$ direction because $R_y = R/\sin\phi \gg R_x$. Therefore, we assume that the disk contacts the plane in a line instead of an ellipse, reducing the problem to a planar one. Contact is modelled by 'two dimensional

contact of cylindrical bodies' [58]. The plane is modelled by one cylinder with infinite radius of curvature and the disk is modelled by a cylinder with radius of curvature $R/\sin\phi$. Johnson [58, (4.43)] gives the formula for the length of the contact region

$$a = \sqrt{\frac{4PR'}{\pi E^*}} = \sqrt{\frac{4mgR}{\pi E^*}\frac{1}{\sin\phi}} \approx k_v \phi^{-1/2}. \tag{4.91}$$

resulting in the dissipation mechanism

$$\underline{Q}^{\mathcal{B}} = n(\phi, \dot{\phi}, \ddot{\phi}) \begin{pmatrix} k_v \phi^{-1/2} \\ 0 \\ -k_v \phi^{1/2} \end{pmatrix}. \tag{4.92}$$

4.5.4 Hertzian derived models: Issues and improvements

The contact region models set out in Section 4.5.3 inherit many assumptions from Hertzian mechanics. In all cases, the models are static and all dynamic effects of the disk rolling over the plane are ignored. Effects such as viscoelasticity, elastic hysteresis and microslip are all neglected. Furthermore, the size and shape of the contact region is predicated on a symmetric pressure distribution between the disk and the plane, eq. (4.71). However, to provide a dissipative moment, this pressure distribution must be skewed as in fig. 4.9.

In all models, friction is assumed to act identically to the point contact, rigid body limit. However, the Hertzian contact model assumes that the plane is frictionless. We expect that including friction, skewed pressure distributions and surface roughness in the Hertzian models will affect the size and shape of the contact region and introduce microslip, but this is beyond the scope of this thesis.

In the case of rolling frictions derived from viscoelasticity, the rolling resistance is governed by the Deborah number, $\zeta = VT/a$. A non-dimensional quantity, ζ represents 'the ratio of the relaxation time of the material to the time taken for an element to travel through the semi-contact width' [58]. The resistance to rolling is maximum when $\zeta = 1$ and the body travels through the contact region at the same rate as the surface relaxes. At lower speeds, the material relaxes as the body rolls over it, while at higher speeds the material does not have sufficient time to compress resulting in elastic-like behaviour. This is not an observation consistent with Euler's disk.

In the next section, we analyse, via energy methods, the rolling friction formulations set forth in Sections 4.4 and 4.5.

4.6 The energy exponent

Many dissipation mechanisms are defined in Sections 4.4 and 4.5 and each has the potential to explain the motion of Euler's disk. Therefore, we require a means of comparison to differentiate

between them. It is known from experiments that, as the disk comes to a halt, its energy decreases according to a power law of the form

$$E(t) = A_e(t_0 - t)^n, \tag{4.93}$$

where A_e is a multiplicative constant, t_0 is the time of the halt and n is the energy exponent. As noted in Section 3.2.1, an energy exponent of $n > 1$ results in a gentle, tangential decrease towards zero energy, while $n < 1$ results in an abrupt, perpendicular decrease. All experimental evidence from Section 3.2 and the literature [23, 32, 68, 71] indicates that $n < 1$. In Section 3.2, it was found that n can vary from 0.45 to 0.69 depending on the material of the base-plate the disk rolls on. Importantly, different dissipation mechanisms predict different energy exponents, naturally leading to a method of comparison [23, 68, 71]. The mechanism with the lowest, n, dominates the dissipation as $t \to t_0$ and can be said to bring the disk to a halt. However, the dissipation mechanism must be consistent with with experimental data.

We compute the analytical energy exponent for the candidate mechanisms in Sections 4.4 and 4.5, in the manner of Leine [68]. The calculation relies on a number of assumptions, so we also estimate the energy exponent from numerical solutions of the equations of motion. The total energy of Euler's disk is

$$E = \frac{m(\underline{V}_G \cdot \underline{V}_G)}{2} + \frac{\mathrm{I}\underline{\Omega} \cdot \underline{\Omega}}{2} + mg(R\sin\phi + H\cos\phi). \tag{4.94}$$

To reduce eq. (4.94), we apply the non-dimensional scalings in eq. (4.21) and scale the energy by $E = \bar{E}mgR$ and immediately drop the bar notation. We also assume the disk is rolling, such that $\underline{V}_P = 0$, and insert the centre of mass velocity, eq. (4.7), along with the angular velocity, $\underline{\Omega}$

$$\begin{aligned} E =& (-2h\sin\phi\cos\phi + a_P\sin^2\phi + c_P\cos^2\phi)\frac{\dot{\psi}^2}{2} + (c_P\cos\phi - h\sin\phi)\dot{\psi}\dot{\theta} + c_P\frac{\dot{\theta}^2}{2} \\ &+ (a_P + 1)\frac{\dot{\phi}^2}{2} + h\cos\phi + \sin\phi. \end{aligned} \tag{4.95}$$

The disk is assumed to be undergoing stationary rolling motion as defined in eq. (4.39). The expressions for stationary rolling motion in eq. (4.40) are used to eliminate $\dot{\psi}$ and $\dot{\theta}$. We also subtract h, the scaled energy of the disk in the flat configuration, before finally assuming small ϕ to give

$$E \approx \frac{ch^2 + 3a}{2a}\phi, \tag{4.96}$$

a linear relationship between the energy and the nutation angle, ϕ. The rate of energy dissipation is given by the component of the angular velocity in the direction of the dissipative moment

$$\dot{E} = \underline{Q}^{\mathcal{B}} \cdot \underline{\Omega}^{\mathcal{B}}. \tag{4.97}$$

For classical rolling friction, we substitute the dissipative moment $\underline{Q}^{\mathcal{B}}$ derived in eq. (4.52)

$$\dot{E} = -\frac{\eta n(\phi,\dot{\phi},\ddot{\phi})}{\sqrt{\dot{\phi}^2+\sin^2\phi\dot{\theta}^2}}\begin{pmatrix}-\cos\phi\sin\phi\dot{\theta}\\ -\dot{\phi}\\ \dot{\theta}\sin^2\phi\end{pmatrix}\cdot\begin{pmatrix}\dot{\psi}\sin\phi\\ -\dot{\phi}\\ \dot{\psi}\cos\phi+\dot{\theta}\end{pmatrix}, \tag{4.98}$$

and apply the stationary rolling assumption, while taking only the leading order term as $\phi\to 0$

$$\dot{E} = -\frac{\eta n}{\sqrt{\dot{\phi}^2+\sin^2\phi\dot{\theta}^2}}\left(\dot{\phi}^2+\dot{\theta}^2\sin^2\phi\right)\approx -\frac{\eta}{\sqrt{a}}\sqrt{\phi}, \tag{4.99}$$

suggesting that the rate of energy dissipation is proportional to $\sqrt{\phi}$. Other dissipation mechanisms predict rates proportional to different powers of ϕ. Upon inserting the relationship between ϕ and the energy, eq. (4.96), into eq. (4.99), we obtain a solvable differential equation for the energy of the disk, subject to classical rolling friction

$$\dot{E} = -\frac{\eta}{\sqrt{a}}\sqrt{\frac{2a}{ch^2+3a}E}. \tag{4.100}$$

At t_0, the disk is flat with zero energy. The initial conditions are $E(t_0)=0$, and we take the non-trivial solution

$$E(t) = \frac{\eta^2}{2ch^2+6a}(t_0-t)^2, \tag{4.101}$$

which is in the form of the well-known power law, eq. (4.93). The energy exponent, $n=2$, suggests a tangential, quadratic decrease to zero energy, rather than the abrupt halt predicted by experiments. We repeat this analysis for all dissipation mechanisms and give the results in Table 4.1. For reference, Moffatt [74] computed $n=1/3$ for air resistance, before a subsequent revision by Bildsten [15] to $n=4/9$.

Diss Mech.	$\dot{E}\propto$	E	n	numerical n
Classical rolling	$\sqrt{E}$	$A_e(t_0-t)^2$	2.00	2.01
Pivoting	$\sqrt{E}$	$A_e(t_0-t)^2$	2.00	2.13
General	$\sqrt{E}$	$A_e(t_0-t)^2$	2.00	2.01
Contour	$1/\sqrt{E}$	$A_e(t_0-t)^{2/3}$	0.67	0.67
Constant offset	$\sqrt{E}$	$A_e(t_0-t)^2$	2.00	2.00
Curv. dep. offset	$1/\sqrt{E}$	$A_e(t_0-t)^{2/3}$	0.67	0.67
Greenwood [47]	$E^{1/18}$	$A_e(t_0-t)^{18/17}$	1.06	1.06
B & H [21]	$E^{0.076}$	$A_e(t_0-t)^{1.08}$	1.08	1.09
Winkler [58]	$E^{1/8}$	$A_e(t_0-t)^{8/7}$	1.14	1.15
Cylinder [58]	E^0	$A_e(t_0-t)$	1.00	1.00

Table 4.1: Dissipation mechanisms and their associated energy exponents. In some cases, the analytic estimate is a slight underestimate when compared to the numerical estimate.

Except for contour friction and its equivalent formulation, the curvature dependent offset, all models predict $n > 1$ and do not give rise to the abrupt halt. It was noted in Section 4.5.3.1, that the curvature dependent offset model overestimates the size of the offset when compared to other, more realistic models of contact. However, as it predicts $n < 1$, contour friction is the most credible of the mechanisms explored here.

We also compute numerical estimates of n in Table 4.1. These are found by numerically integrating the equations of motion, eqs. (4.25) and (4.32), with each dissipation mechanism according to the scheme outlined in section 4.3.1. The initial conditions are given in eq. (4.43). We tune η, the coefficient of rolling friction to ensure that the motion ends at $t_0 = 0.5\,\mathrm{s}$. We compute the energy using eq. (4.94) and fit the parameters of the power law, A_e, t_0 and n, by minimising the sum of the squared errors. In all cases, the analytic version of n is a slight underestimate when compared to the numeric estimate. The disparity is a little larger for pivoting friction. The coefficient of rolling friction, η, required to bring the disk to a halt in 0.5 s resulted in intersection with the discontinuity set of pivoting friction ($\dot{\psi} + \dot{\theta}\cos\phi = 0$). Therefore, we reduced η and the trajectory avoided the discontinuity set. The disk came to a halt in 0.7 s; the longer sample size perhaps explains the discrepancy.

We have not included any viscous mechanisms in Table 4.1 even though the viscous version of a mechanism may result in a lower value of n. In a simple example of a pencil rolling down a slope, Ivanov [56] observes that rolling friction must have a viscous component. However, contact-mechanics-informed viscous mechanisms, such as those discussed by Goryacheva and Zobova [46] and Hunter [53] lie outside the scope of this thesis, and we restrict ourselves to the dry models obtained from a simple contact region.

In Section 4.7, we numerically analyse Euler's disk subject to contour friction, the mechanism with an energy exponent closest to the experimental observations.

4.7 Numerical analysis with Coulomb friction and contour friction

Of the dissipation mechanisms considered in Sections 4.4 and 4.5, contour friction, or equivalently the curvature dependent offset model, gives the best agreement with experiments. In this section, we numerically solve the equations of motion for Euler's disk subject to both contour and Coulomb friction, a system was also studied by Le Saux et al. [67]. Figure 4.12 shows a number of variables from the numerical solution with experimentally determined initial conditions, eq. (4.43). The variable $\dot{\beta}$, plotted in the bottom left of fig. 4.12, refers to the angular velocity of a strip drawn on the face of the disk, as in the experiments of Section 3.3.1. The angular velocity, $\dot{\beta}$, is related to the state variables through eq. (3.21), reproduced here

$$\dot{\beta} = \dot{\psi} + \frac{\dot{\phi}\sin\phi\sin(\theta+\beta_0)\cos(\theta+\beta_0) + \dot{\theta}\cos\phi}{1 - \sin^2\phi\cos^2(\theta+\beta_0)} \tag{4.102}$$

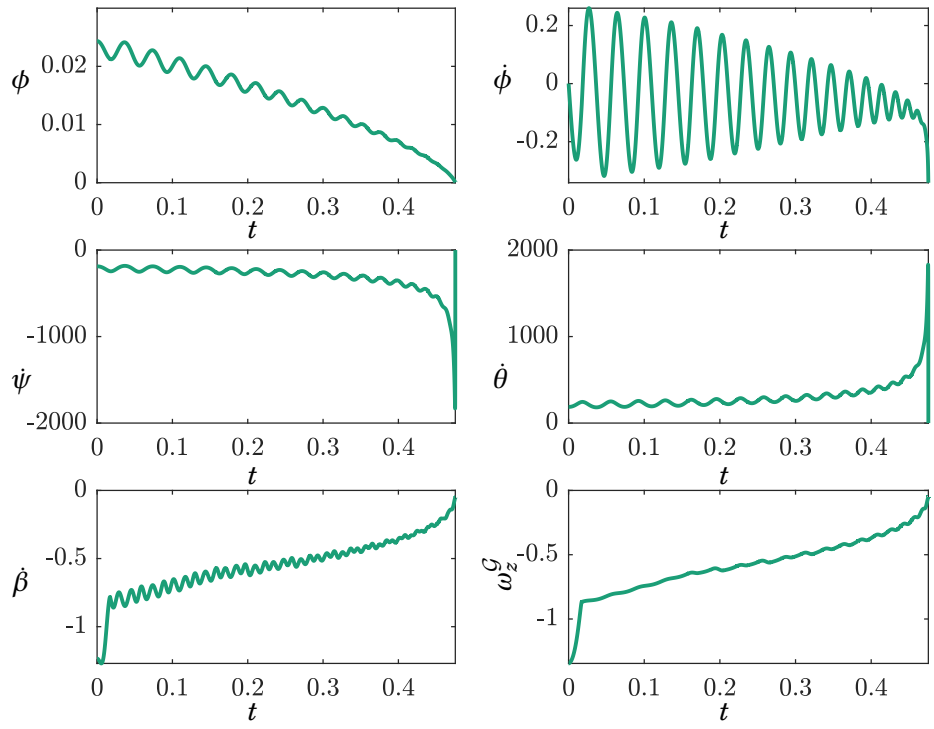

Figure 4.12: The numerical solution of the equations of motion, eqs. (4.25) and (4.32), subject to Coulomb friction and contour friction. The initial conditions are determined from experiments and given in eq. (4.43). The coefficient of contour friction is $\eta = 2.43 \times 10^{-4}$ and other parameters are given in Section 4.3.1.

where β_0 is the initial angle of the strip. The angular velocity $\omega_z^{\mathcal{G}}$, plotted in fig. 4.12 right, is the angular velocity of the disk about the global vertical axis and is closely related to $\dot{\beta}$, but unaffected by the perspective of the camera angle in the experiments.

It is known from experiments that the disk falls flat 0.5 s after the initial conditions. As in the previous section, we tune the coefficient of contour friction, η, to ensure the simulation ends at $t = 0.5$ s. A value of $\eta = 2.43 \times 10^{-4}$ achieves this. The integration ends when the trajectory intersects the discontinuity set of contour friction, $D_c = \{\underline{X} \mid \dot{\theta} = 0\}$, defined in eq. (4.60). This is the third terminal condition of the integration scheme in section 4.3.1. The value of ϕ at the intersection is 3.1×10^{-5}, which is smaller than the minimum observable angle, $\phi = \arcsin(\delta/2R) = 8.6 \times 10^{-4}$, in experiments.

There are a number of interesting features present in fig. 4.12: firstly, the abrupt decrease to zero of $\dot{\psi}$ and $\dot{\theta}$. They appear to be increasing towards a singularity, before quickly decelerating towards zero. We suggest that there is a change in the dominant balance and the dissipation mechanism dominates the equations of motion, snapping $\dot{\theta}$ to a halt. This behaviour is not seen in the numerical analysis by Le Saux et al. [67], but a similar feature appears in Ma et al.

[71]. At the instant of hitting the discontinuity surface, D_c, the disk has some residual angular velocity, $\psi = -0.051\,\mathrm{rad\,s^{-1}}$. Although not solved for numerically, we conjecture that the dynamics are henceforth constrained to D_c, and the disk falls flat. Therefore, the discontinuity could provide a mechanism for the disk to continue to rotate after falling flat, perhaps explaining the experimental results in Section 3.3.

Secondly, we see oscillations in $\dot{\phi}$, followed by a sharp, short decrease just before the halt. This is predicted by the relationship between the energy and ϕ in eq. (4.96). For $n < 1$, as $t \to t_0$, the rate of energy loss and, consequently, $\dot{\phi}$ is singular. A trend towards large singular values just prior to the halt is to be expected.

Finally, $\dot{\beta}$ and $\omega_z^{\mathcal{G}}$ both have fast corrections at the start of the motion. This behaviour is due to errors in the estimated initial conditions. It is possible that the variables are attracted towards a slow manifold. By adjustment of the initial conditions, the fast corrections can be removed.

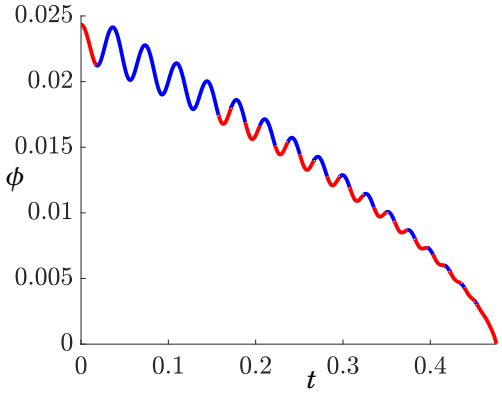

Figure 4.13: Time series of ϕ for the numerical solution subject to Coulomb friction and contour friction and experimentally determined initial conditions. Slipping sections are shown in red, rolling sections are shown in blue.

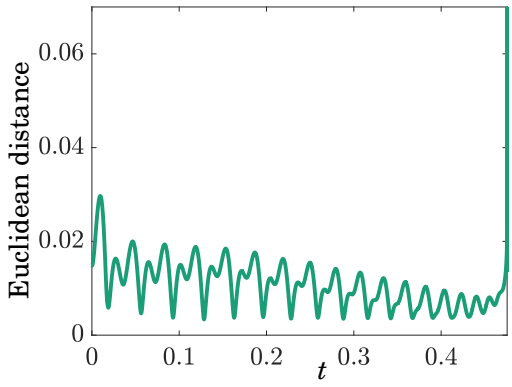

Figure 4.14: Distance of the numerical solution in fig. 4.12 from the stationary rolling manifold, eq. (4.39). The large spike at the end is due to the dissipation mechanism bringing $\dot{\theta}$ to a halt.

In fig. 4.13, we show the time series for ϕ with the rolling and slipping sections highlighted. The disk begins slipping, possibly due to errors in the initial conditions. It then undergoes a period of rolling for roughly four oscillations, before slipping phases begin to appear. These phases increase in length until, in the final few hundreds of a second, the disk is only slipping, contrary to the narrative suggested by Ma et al. [71]. A similar sequence is noticed by Le Saux et al. [67].

If the disk is in slipping state at the end of the motion, then it is not undergoing stationary rolling motion. We test the validity of the stationary rolling assumption [11, 68, 74] by computing the Euclidean distance between each point on the trajectory and the stationary rolling manifold. This distance is shown in fig. 4.14 and, although decreasing, it does not show the exponential decay one would expect if the manifold was attractive. The large increase in distance at the end is due to the dissipation mechanism driving the system towards $\dot{\theta} = 0$, which is incompatible with

the stationary manifold, resulting in a large error. Therefore, we discount the notion that the disk undergoes 'slow drift along a one parameter family of stationary rolling solutions' [11].

4.7.1 Comparison with experimental data

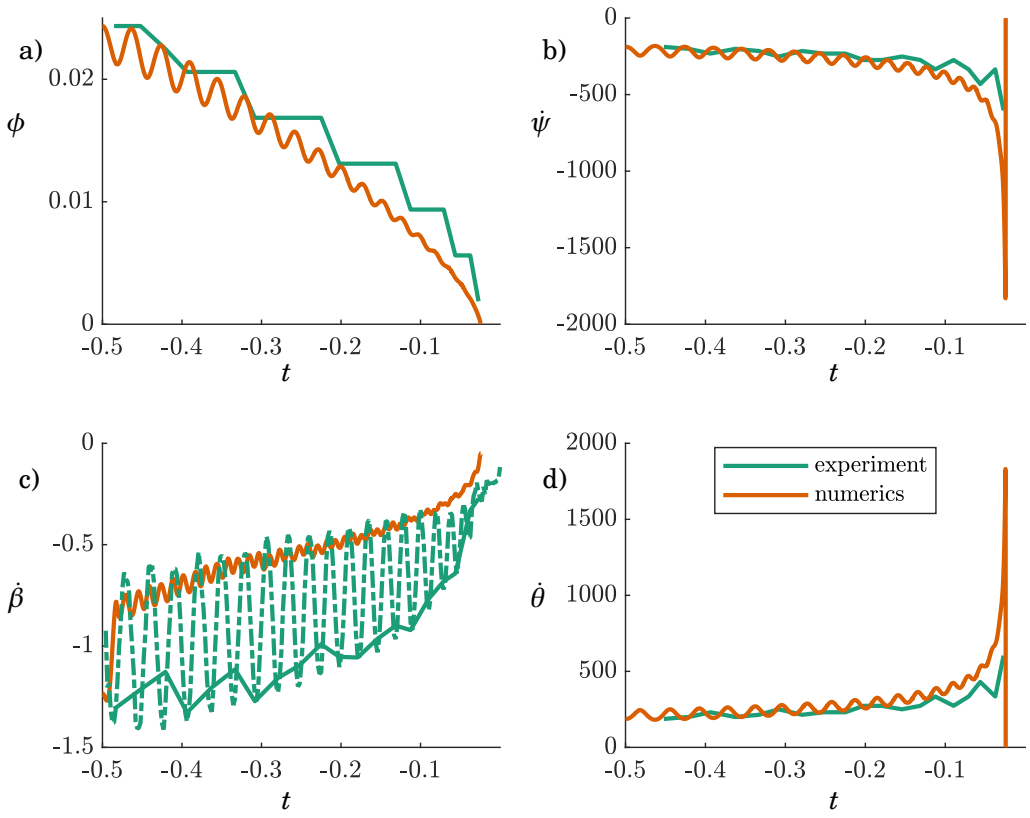

Figure 4.15: Experimental time series (green) of Euler's disk rolling on a stainless steel base-plate in Section 3.3. The bottom left panel shows $\dot{\beta}$ data captured at 480fps in dashed green. For fair comparison, the sampled $\dot{\beta}$ data is also shown, in solid green. The numerical solution of the equations of motion, eqs. (4.25) and (4.32), subject to Coulomb and contour friction, is shown in orange. Initial conditions are given in eq. (4.43), the material parameters in eq. (4.42) and the coefficient of contour friction is $\eta = 2.43 \times 10^{-4}$.

In fig. 4.15, we overlay the numerical solution of fig. 4.12 with data obtained by spinning the disk on the stainless steel base-plate in Section 3.3. In this experiment, the disk was filmed from above and the side. A data point for ϕ is captured once for each 2π rotation in ψ. The time taken to complete the 2π rotation is used to estimate $\dot{\psi}$. The β data describes the rotation of the strip drawn on the top face of the disk. It is captured every frame at 480fps and is smooth enough to allow numerical differentiation. Numerically, $\dot{\beta}$ is computed from eq. (4.102). For fair comparison with the other variables in fig. 4.15, we plot the complete data for $\dot{\beta}$ (dashed green), in addition to

the data sampled at the same instants as ϕ (solid green).

The experimental sampling means the oscillatory behaviour of ϕ, $\dot{\psi}$ and $\dot{\theta}$ is lost. Nevertheless, we see a qualitative agreement for ϕ, $\dot{\psi}$ and $\dot{\theta}$, with the error increasing towards the end of the motion. This error is attributed to mismatch the energy exponents of contour friction. For Euler's disk rolling on stainless steel it was estimated in section 3.2 that $n = 0.45$, while contour friction predicts $n = 0.66$.

The $\dot{\beta}$ comparison in fig. 4.15c is less favourable. Although the experimental and numerical means follow roughly the same trajectory, the amplitude of oscillations is far smaller in the numerical solution than in the experiments. The amplitude of oscillations in the experiments, shown in fig. 3.28, vary in size from around $0.3\,\mathrm{rad\,s^{-1}}$ to $1.2\,\mathrm{rad\,s^{-1}}$. We also plot the sampled $\dot{\beta}$ data which tracks the lower envelope of the oscillations. The larger oscillations are caused by the initial conditions, estimated from experiments in eq. (4.43).

The frequency of oscillations in $\dot{\beta}$ also differs between the numerical solution and the experiments. Again, the discrepancy is attributed to the initial conditions. The numerical solution oscillates at roughly twice the frequency of the experimental data. We suggest that $\dot{\beta}$ reaches a maximum whenever the strip aligns with the contact point, occurring twice for every revolution in ψ. In experiments, the oscillations in ϕ, introduced by the initial conditions, overwhelm this behaviour and result in larger oscillations with half the frequency.

To address the mismatch in energy exponent between contour friction and experiments, we formulate a more singular version of contour friction, heedless of a physical interpretation. Requiring that the energy exponent is $n = 0.45$ implies that the rate of energy dissipation is $\dot{E} \propto E^{1.22}$. Such a rate is achieved by multiplying contour friction, eq. (4.59), by a factor of $\phi^{-0.722}$. The result is a dissipation mechanism with $n = 0.45$, acting in the same direction as contour friction.

The corresponding numerical simulation is shown in fig. 4.16. The coefficient of contour friction is reduced to $\eta = 1.1 \times 10^{-5}$, ensuring that the disk stops after 0.5 s. We observe a much better quantitative fit with the experimental results. All of $\dot{\psi}$, $\dot{\theta}$ and ϕ track the experimental data right up until the halt. The peak in $\dot{\psi}$ and $\dot{\theta}$ is reduced, because the augmented contour friction now dominates the equations before $\dot{\psi}$ and $\dot{\theta}$ become so large. However, the β solution is almost unchanged and the fast correction and a lack of oscillations remain.

Just as in figs. 4.12 and 4.15, the trajectory hits the discontinuity surface, D_c, at $\phi = 4.65 \times 10^{-4}$, leaving a residual angular velocity $\dot{\psi} = -0.14\,\mathrm{rad\,s^{-1}}$. Note that in eq. (4.102) the two angular velocities, $\dot{\beta}$ and $\dot{\psi}$, coincide at $\phi = \dot{\theta} = 0$. The average residual angular velocity observed in the experiments of fig. 3.28 is $\dot{\beta} = -0.23\,\mathrm{rad\,s^{-1}}$, very close to the numerical estimate of $-0.14\,\mathrm{rad\,s^{-1}}$ predicted by contour friction.

It remains to be seen if any physical reasoning exists for the augmented contour friction, but we see good quantitative agreement with the state variables ϕ, $\dot{\psi}$ and $\dot{\theta}$. Discrepancies in β are attributed to errors in the estimates of the initial conditions. Figure 4.16 suggests that a

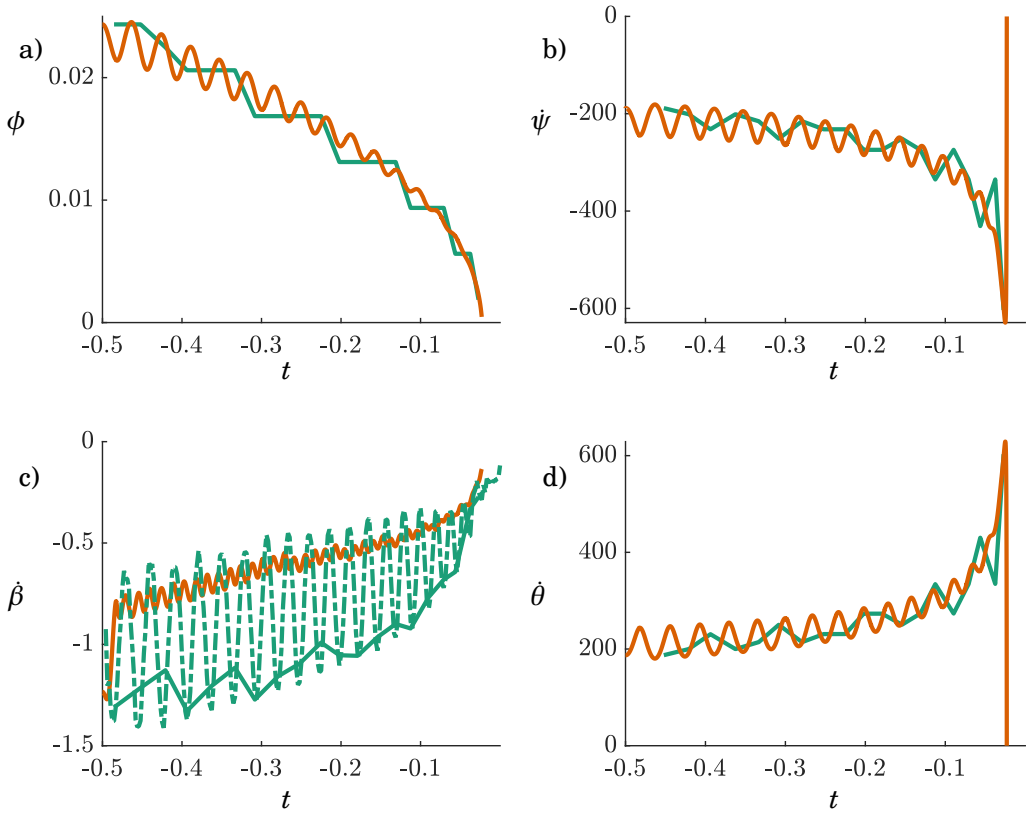

Figure 4.16: Experimental time series (green) of Euler's disk rolling on a stainless steel base-plate from Section 3.3. The bottom left panel shows $\dot{\beta}$ data captured at 480fps in dashed green. For fair comparison, the sampled $\dot{\beta}$ data is shown in solid green. Numerical solution of eqs. (4.25) and (4.32) with Coulomb friction and a strengthened contour friction is shown in orange. Initial conditions are from eq. (4.43) and the coefficient of contour friction is $\eta = 1.1 \times 10^{-5}$.

moment equivalent to augmented contour friction is the cause of the halt of Euler's disk, but the physical origin of the moment is unknown. As $\phi \to 0$, the $x^{\mathcal{B}}$ component of contour friction dominates in eq. (4.59). It may well be the case that, rather than contour friction, a different physical factor gives rise to a moment in the same direction with the correct strength. For example, in Chapter 3 it was seen that the presence of air affects the motion of Euler's disk in its final moments. Bildsten's [16] estimate of $n = 4/9$ for air resistance agrees closely with our experimental estimates. Furthermore, it does not rely upon the arbitrary multiplication of contour friction by $\phi^{-0.722}$ to obtain the correct, quantitative behaviour. However, the author is not aware of any formulation of the moment due to air resistance for Euler's disk, the derivation of which falls outside the scope of eq. (4.49), and therefore, this thesis.

In the next section, we investigate the dynamics of the disk after it has fallen flat, during the last 0.05 s of its motion.

4.8 Post-falling flat dynamics

In the second experiment of Chapter 3 it was observed that, after the disk fell flat on the stainless steel base-plate, it continued to rotate about the vertical axis. On the concave base-plate, the disk fell flat and stopped rotating almost immediately. In this section, we propose an explanation. In the numerical solutions, shown in fig. 4.16, the disk hits the discontinuity surface of contour friction, D_c (fig. 4.17a). It then falls flat with residual angular velocity $\dot{\psi}$. Then, if the base-plate is flat, the thin layer of trapped air beneath the disk causes a loss of contact. Following the loss of contact, the disk undergoes an air-lubricated, contactless phase fig. 4.17b, followed by a contact phase governed by Coulomb friction, fig. 4.17c. Finally, the disk comes to a halt in fig. 4.17d. Such a loss of contact agrees with Borisov et al. [19], who showed the disk loses contact at the end of the motion.[2]

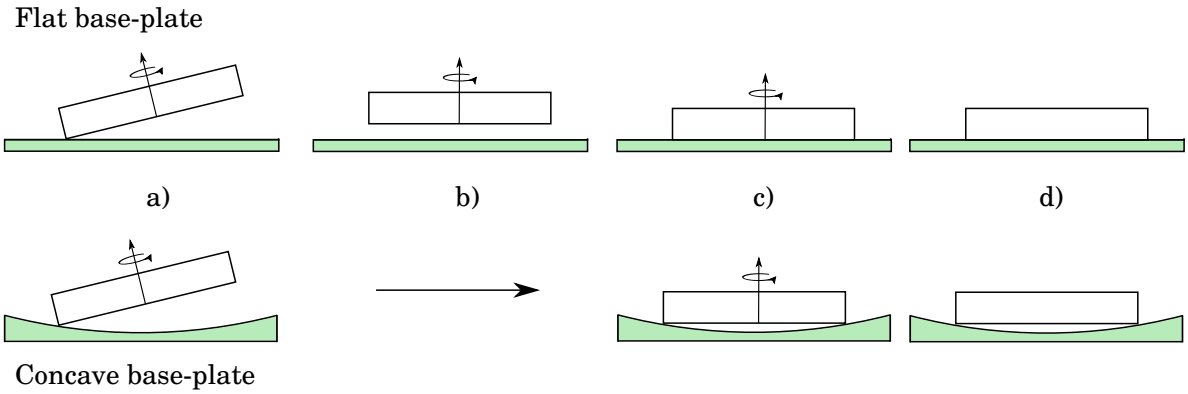

Figure 4.17: The loss of contact on flat and concave base-plates. In a) the disk hits the discontinuity surface, D_c, and falls flat with residual angular velocity $\dot{\psi} = \dot{\beta}$. In b) the disk loses contact due to a thin layer of air between the disk and base-plate. This does not occur on the concave base-plate. In c) the disk makes contact with the base-plate and slips to a halt. In d) The disk has come to rest.

If the base-plate is concave, then there is no thin layer of trapped air. The large gap between disk and base-plate, does not allow for the high pressure gradients necessary to support the disk. The disk therefore skips the contactless phase in fig. 4.17b, immediately makes contact with the base-plate and skids to a halt. In this section, we explore the two phases: contact and contactless and compare with the experimental results of Section 3.3.

4.8.1 Contactless phase

If two bodies are separated by a thin film of viscous fluid, it can take a large force to pull them apart. The force required to separate a disk from a horizontal plane, with a thin layer of viscous

[2]Other losses of contact during the motion can be explained by asperities in the base-plate and disk.

fluid between the two, is given by [6, (7.50)]

$$F = -\frac{3\pi\mu_{\text{air}}R^4}{2}\frac{\dot{Z}_b}{Z_b^3}, \tag{4.103}$$

where Z_b is the height of the disk above the plane and $\mu_{\text{air}} = 1.8\times10^{-5}\text{kg}\,\text{m}^{-1}\,\text{s}^{-1}$ is the viscosity of the fluid, in this case air.

We consider the reverse problem: the disk begins at a height, $Z_b(0)$, above the plane with initial velocity, $\dot{Z}_b(0)$, what is the subsequent motion of the disk? The differential equation governing the motion of the disk is[3]

$$m\ddot{Z}_b = -\frac{3\pi\mu_{\text{air}}R^4}{2}\frac{\dot{Z}_b}{Z_b^3} - mg. \tag{4.104}$$

We wish to solve for the time taken for the disk to fall and make contact at $Z_b = 0$. However, there is no equilibrium in eq. (4.104) for the disk to approach; the layer of fluid repels the disk from the surface. When the disk gets close enough to the base-plate, asperities and surface roughness take affect and the disk makes contact.

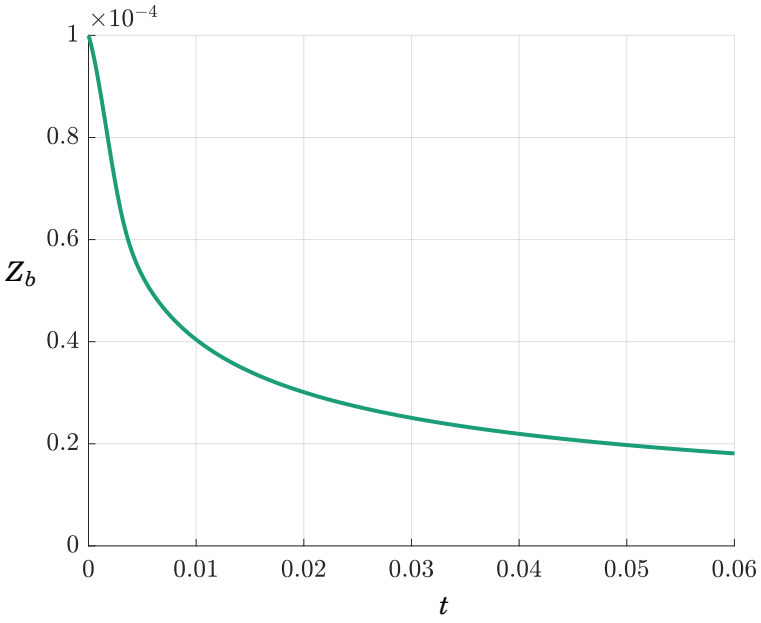

Figure 4.18: The separation, Z_b, between the disk and the plane in eq. (4.104). The initial conditions are $Z_b(0) = 1\times10^{-4}\text{m}$ and $\dot{Z}_b = -0.007\,\text{m}\,\text{s}^{-1}$.

We numerically solve eq. (4.104) with initial conditions $Z_b(0)$ and $\dot{Z}_b(0)$ corresponding to the height of the disk's bottom face and its vertical velocity at the loss of contact. The initial conditions are estimated from the final values of the experiments in Chapter 3. We assume

[3]Note the similarity of eq. (4.104) and the governing equation of the rocking can eq. (2.63), but with the additional damping term $\dot{Z}_b$

that after the disk encounters the discontinuity set, D_c, it loses contact with the base-plate. In Section 3.2, we obtained data about the height of the disk's bottom rim, z_{rim}, which is of sufficient quality for a rough estimate of $Z_b(0)$ and $\dot{Z}_b(0)$. From the final peak in fig. 3.11, $z_{\text{rim}} = 2.0 \times 10^{-4}$m. Therefore the height of the centre of the bottom face of the disk is $Z_b(0) = 1.0 \times 10^{-4}$m. Numerical differentiation of ϕ in fig. 3.12 gives $\dot{\phi} = -0.18\text{rad}\,\text{s}^{-1}$. The vertical velocity of centre of the bottom face is $\dot{Z}_b(0) = \dot{\phi}R = -0.007\,\text{m}\,\text{s}^{-1}$.

The numerical solution is shown in fig. 4.18. The separation between the disk and the plane decreases rapidly until around $t = 0.01$s, before slowing. As predicted, the singular point in eq. (4.104) prevents Z_b from reaching zero. However, at some value of Z_b, surface roughness takes effect and the disk comes into contact with the plane. Coulomb friction then brings the disk to a halt. On stainless steel, the average time between the disk falling flat and coming to a complete stop is $t_\beta - t_\phi = 0.04$s. It is encouraging that this simple model evolves on approximately the same time scale. In addition, the time scale is consistent with the duration of loss of contact observed by Borisov et al. [19] which lasts for between 12 and 40 ms.

In the case of the concave base-plate, the experiments in Section 3.3 observe only a small interval $t_\beta - t_\phi$. Here, eq. (4.104) does not apply as the gap between disk and base-plate is not small. Therefore, we expect the disk to contact the ground immediately.

4.8.2 Contact phase

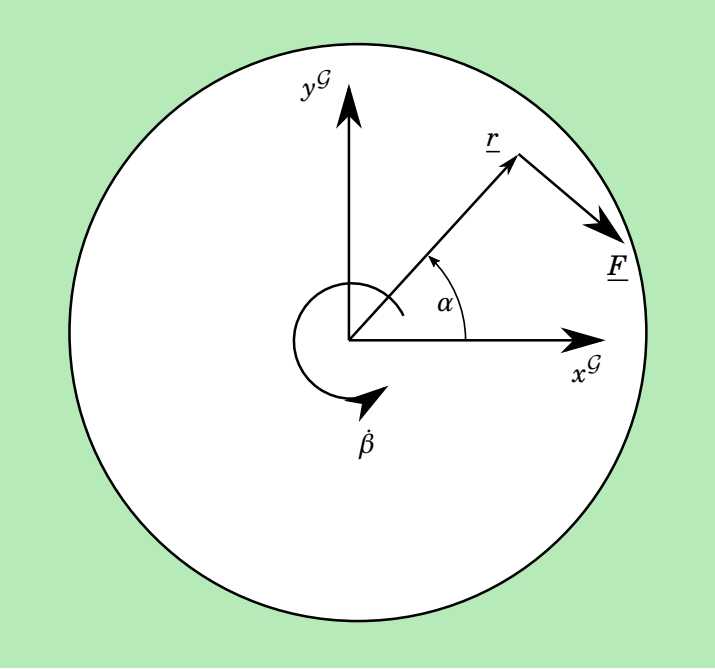

Figure 4.19: Top view of the contact area between the disk and the plane. Coulomb friction acts on the disk over the contact area, bringing the disk to a halt.

Once the disk has made contact with the base-plate, Coulomb friction acts on the face of

the disk to bring the rotation, $\dot{\beta}$, to a halt. To compute the time taken for the disk to come to a halt, we consider the torque produced by Coulomb friction. Assuming uniform contact with the base-plate, the plane exerts a constant pressure, ρ, over the contact area

$$\rho = \frac{mg}{\pi R^2}. \tag{4.105}$$

The disk is slipping, so Coulomb friction acts at each point, as shown in fig. 4.19. The friction force $\underline{F}$ acts over the contact region and opposes the relative velocity. Written in polar coordinates

$$\underline{F} = \frac{-\operatorname{sign}(\dot{\beta})\,\mu mg}{\pi R^2}\begin{pmatrix} -\sin\alpha \\ \cos\alpha \\ 0 \end{pmatrix}, \tag{4.106}$$

where $r \in [0,R]$ and $\alpha \in [0,2\pi)$ parametrise the contact region. The torque, $\underline{T}$, about the centre of the disk is given by integrating the resultant moment over the contact area

$$\underline{T} = \int_0^{2\pi}\int_0^R \left(\underline{r}\times\underline{F}\right) r\,\mathrm{d}r\,\mathrm{d}\alpha. \tag{4.107}$$

where $\underline{r} = (r\cos\alpha, r\sin\alpha, 0)^\intercal$. Computing the cross product and the integral yields a torque in the $z^{\mathcal{G}}$ direction

$$T_z^{\mathcal{G}} = \frac{-2\operatorname{sign}(\dot{\beta})\,\mu mgR}{3}. \tag{4.108}$$

Applying Newton's second law to the disk with the applied torque gives

$$C\ddot{\beta} = -\frac{2\operatorname{sign}(\dot{\beta})\,\mu mgR}{3}, \tag{4.109}$$

where $C = mR^2/2$ is the moment of inertia about the disk's symmetry axis. We note that the torque acts to slow the disk down and cannot change the sign of $\dot{\beta}$. Therefore $\operatorname{sign}(\dot{\beta}) = \operatorname{sign}(\dot{\beta}(0))$. Integration of eq. (4.109) yields the angular velocity of the disk as a function of time

$$\dot{\beta} = -\frac{2\operatorname{sign}(\dot{\beta}(0))\,\mu mgR}{3C}t + \dot{\beta}(0), \tag{4.110}$$

showing that the disk decelerates linearly. The time taken for the disk to come to a halt is

$$t_{\text{stop}} = \frac{3C|\dot{\beta}(0)|}{2\mu mgR}. \tag{4.111}$$

The parameter values in eq. (4.111) are given in Section 4.3.1. The stainless steel experiments in Section 3.3 show that the average value of $\dot{\beta}$ when the disk falls flat is $-0.23\,\mathrm{rad\,s^{-1}}$. It is assumed that the contactless phase does not affect the vertical rotation, so that $\dot{\beta}(0) = -0.23\,\mathrm{rad\,s^{-1}}$. Equation (4.111) gives the stopping time, $t_{\text{stop}} = 0.0050\,\mathrm{s}$, approximately $1/200^{\text{th}}$ of a second. This is not long enough to account for the motion after the disk has fallen flat, experimentally observed to last for 0.04 s, supporting the suggestion that the disk is supported by a thin layer of air before coming to a halt.

For the concave base-plate, the disk makes contact immediately. Rather than the whole bottom face of the disk, it is just the rim of the disk in contact with the base-plate, resulting in a torque

$$T_z^{\mathcal{G}} = -\mu m g R |\dot{\beta}(0)|, \tag{4.112}$$

an increased torque compared to uniform contact over the surface. Computed from the experiments shown in fig. 3.30, the average residual rotational velocity on the concave base-plate is $\dot{\beta}(0) = -0.19\,\mathrm{rad\,s^{-1}}$. The coefficient of Coulomb friction, μ, is unknown for the base-plate, so we estimate with the same value as stainless steel, $\mu = 0.134$. The stopping time on the concave base-plate is

$$t_{\mathrm{stop}} = \frac{R|\dot{\beta}(0)|}{2\mu g} \approx 0.0033\,\mathrm{s}. \tag{4.113}$$

Although a rough estimate, this time is close to the experimentally computed interval, $t_\beta - t_\phi = 0.0058\,\mathrm{s}$, itself close to the time resolution of the experiments, 0.002 s. For the flat base-plate, the sum of the durations of the contact (0.005 s) and contactless ($\approx 0.03\,\mathrm{s}$) phase are consistent with the interval, $t_\beta - t_\phi = 0.04\,\mathrm{s}$ observed in experiments. Furthermore, the experimental results in fig. 3.31 show two phases: a section of flat, constant $\dot{\beta}$, corresponding to the contactless phase, and a linear decrease to $\dot{\beta} = 0$, corresponding to the contact phase. Therefore, the evidence suggests that air resistance does affect the motion of Euler's disk in its final moments, though, not necessarily in the manner predicted by Moffatt [74].

4.9 Discussion and conclusions

In this chapter we explored, analytically and numerically, the halting of Euler's disk. We derived the equations of motion for Euler's disk subject to both Coulomb friction and unspecified dissipative moments. Due to the discontinuous nature of Coulomb friction, the equations of motion take the form of rolling and slipping systems along with transition rules.

Analysis of the disk in the absence of a dissipative moment confirmed that Coulomb friction alone is insufficient to bring the disk to a halt. In section 4.3.2, we proceeded to show that the Painlevé paradox is not present in the Euler's disk problem, but uncovered slipping-rolling trajectories exhibiting interesting non-smooth phenomena.

In Sections 4.4 and 4.5, we derived a number of candidate dissipative moments to explain the motion of Euler's disk. Section 4.4 concentrated on well-known phenomenological dissipation mechanisms such as classical rolling friction, while Section 4.5 derived contact-region based mechanisms by relaxing the rigid body assumption. We find a correspondence between a curvature dependent offset in the normal force and contour friction. For each dissipation mechanism, the energy exponent, n, is derived both analytically and numerically.

We find, as did Leine [68], that contour friction predicts approximately the correct energy exponent, $n = 2/3$. However, on some flat base-plates, contour friction does not appear to be

the dominant factor. On the stainless steel base-plate, the experimental estimate is $n = 0.45$, suggesting dry contour friction is insufficient and a different dissipation model may be more appropriate. On the concave base-plate, it would appear that contour friction is sufficient, close to the experimental estimate, $n = 0.62$. The difference in n between the flat and concave base could be explained by the presence of a viscous contour friction, present only on the flat base-plates, or Moffatt's air resistance mechanism [74]. Despite the experiments of van den Engh et al. [93], performed in vacuo: a *qualitative* difference in the motion might not be visible, but it might be possible to detect *quantitative* differences in n due to air resistance.

In Section 4.7, we numerically solved the equations of motion for the disk subject to both Coulomb friction and contour friction. Qualitative agreement with the experimental data is obtained in fig. 4.15 but, quantitatively, the difference in energy exponent introduces errors. Multiplying contour friction by a factor of $\phi^{-0.722}$ resulted in an augmented mechanism that acts in the same direction as contour friction, but predicts the correct energy exponent. Numerical solutions with the augmented contour friction in fig. 4.16 give much better quantitative agreement with experiments. However, a physical reason for the additional factor of $\phi^{-0.722}$ is unknown. We note that, for both contour friction and augmented contour friction, trajectories hit the discontinuity set, D_c, just before the halt. Upon entering the sticking state, the disk is left with some residual angular velocity, $\dot{\psi} = -0.14\,\mathrm{rad\,s^{-1}}$, close to the experimental estimates of $-0.23\,\mathrm{rad\,s^{-1}}$. Therefore, the discontinuity in contour friction provides a mechanism for the continued rotation of the disk after falling flat.

The numerical solutions predict that the disk slips, contrary to previous numerical analysis [70]. At the end of the motion in fig. 4.13, the disk undergoes alternating periods of slipping and rolling. Slipping behaviour is incompatible with the assumption of stationary rolling motion. In fig. 4.14, we plot the distance from the trajectory to the stationary rolling manifold, eq. (4.39). The error does not decay exponentially and in fact diverges towards the end of the motion, implying that the disk does *not* undergo slow-drift along a one-dimensional manifold of stationary rolling motions [11, 68].

In Section 4.8, we analyse the continued rotation of the disk after it has fallen flat. We assumed the presence of two phases: a contactless phase, where the disk is supported by a thin layer of air, followed by a contact phase where Coulomb friction brings the disk to a halt. We find good agreement between experimental and predicted stopping times for flat base-plates. Furthermore, Borisov et al. [19] observed a final loss of contact of approximately the same duration. As expected, the experimental results for the concave base-plate are best explained by a contact phase with *no* contactless phase.

We tentatively suggest the following explanation for the motion of Euler's disk on a flat base-plate. In agreement with Leine [68], the energy dissipation is first dominated by contour friction (or similar variant) with $n \approx 2/3$. Then, as the disk falls further, a stronger mechanism with $n \approx 1/2$ dominates. Depending on the multiplicative factor of the dissipation mechanism in

eq. (4.93), the experimental data in fig. 3.15 reflects a weighted average of the energy exponents. This gives rise to the observed dependence of n on the base-plate material. As mentioned, viscous contour friction with $n = 1/2$ [68], or air resistance with $n = 4/9$ [16], are viable candidates for the stronger mechanism. Considerable differences in energy exponents for the concave and flat base-plates also suggest that air resistance may play a role.

As the disk enters the final stages of its motion, the dissipative moment grows in strength. Trajectories are forced onto the discontinuity surface, D_c and the disk falls flat with some residual angular velocity, ψ. Depending on the geometry of the base-plate, the disk loses contact and is briefly supported by a thin, lubricating layer of air. The rotation continues until contact is made and Coulomb friction brings the disk to a halt. If the base-plate is concave then the disk simply falls flat with no contactless phase.

We believe that this explanation addresses many of the problems in the literature and agrees with the narratives of Leine [68] and Borisov et al. [19]. It accounts for the apparent material dependence of the energy exponent, the continued rotation, and even the loss of contact with the base-plate.

4.10 Further work

The results of this chapter are verifiable experimentally. Repetition of experiments performed in vacuo by van den Engh et al. [93], along with accurate computation of the energy exponent should confirm if air resistance is the dominant mechanism for flat base-plates. The claim may also be tested using flat and concave base-plates of the same material.

Experimentally determined quantities such as t_{stop} in eq. (4.113) are close to the resolution of the experiments in Chapter 3. Higher frame-rates and resolutions are therefore required. Additional synchronised cameras and improved data processing techniques may enable computation of all the state variables. Such information may validate the observed slipping behaviour in fig. 4.13 and the sharp changes of $\dot{\theta}$ and $\dot{\psi}$ in fig. 4.12.

Moffatt [74] and Bildsten [16] derive the energy exponent for the disk subject to air resistance, but a description of the associated moment is unknown. Numerical simulations of Euler's disk subject to a moment induced by air resistance might confirm or deny its presence when compared with experimental data.

The rolling frictions, derived in Section 4.5.3 by relaxing the rigid body assumption, rely on Hertzian contact mechanics. Therefore, they do not take into account any dynamic effects, such as viscoelasticity. Goryacheva and Zobova [45, 46] and Hunter [53] studied dynamic models of cylinders rolling and sliding on viscoelastic foundations. This is perhaps a starting point for further study. The rolling frictions considered in this chapter also neglect Coulomb friction acting over the contact region. Antali and Varkonyi [9] studied slipping and spinning bodies in the presence of dry friction, taking into account the contact area. Their work might be applied to

Euler's disk to yield new insights into the rolling friction formulations, improving upon the commonly used phenomenological models.

Finally, the equations of motion for Euler's disk, eqs. (4.25) and (4.32), appear intractable, but a more thorough analytic exploration may yield new understanding. The fast corrections, visible in $\dot{\beta}$ and $\omega_z^{\mathcal{G}}$ in fig. 4.12, hint at the presence of a slow manifold. Figure 4.14 suggests that this manifold is *not* the stationary rolling solutions as previously assumed. If such a slow manifold does exist then the system may be amenable to a slow-fast analysis. Furthermore, the sharp, vertical profiles of $\dot{\theta}$ and $\dot{\psi}$ in fig. 4.12 indicate a change in dominant balance, which could be studied using matched asymptotics or slow-fast techniques.

CHAPTER 5

DISCUSSION AND CONCLUSION

In Chapter 2, we analysed the rocking can problem. Srinivasan and Ruina [87, (7) and (9)] first analysed the problem using formal relations arising from numerics to determine the angle of turn. The numerical solutions also showed slow-fast behaviour [64]. Here, we rigorously derived these formal relationships, exploiting the multiple scale behaviour to provide a deeper understanding of the rocking can phenomenon. We reduced the equations of motion from five, second order ODEs, eq. (2.8), to one, singularly perturbed, second order ODE, eq. (2.63), in the nutation angle, ϕ. This equation has an exact solution in terms of the hypergeometric function, eq. (2.33), that we eschewed in favour of a more tractable Frobenius series solution, eq. (2.49). The integration constants B_0 and B_{-2} describe conserved angular momenta and correspond to the formal relationships, identified by Srinivasan and Ruina [87, (7) and (9)]. Physical justification for B_0 and B_{-2} was given in fig. 2.6.

The differences in scale in the numerical simulations of the rocking can are governed by the small parameter ϵ in the reduced equation of motion, eq. (2.63). This small parameter is given by $\epsilon = B_{-2}^2$ or, loosely speaking, a small amount of angular velocity in the global vertical or symmetry axes, $z^{\mathcal{G}}$ and $z^{\mathcal{B}}$, respectively. An appropriate scaling of time and ϕ separates the problem into outer and inner regions. In the outer region, the can behaves as a perturbed inverted compound pendulum, eq. (2.70), while in the inner region, the can exhibits the bounce as ϕ quickly switches from decreasing to increasing in eq. (2.80). Using Van Dyke's matching rule, we obtained a uniformly valid solution, eq. (2.88), for one half-period of the motion.

The inner solution, eq. (2.80), enabled analysis of the bounce. After reconstructing the behaviour of the state variables, we found the expected step-like behaviour in the rotation angle θ, eq. (2.94), and the precession angle ψ, eq. (2.93), that results in the angle of turn $\Delta\psi$. By recomputing $\Delta\psi$, eq. (2.96), we gained information about its sign. Agreement with the

full, nonlinear equations of motion is seen in fig. 2.11, extending the work of Cushman and Duistermaat [33]. Other dynamic features of the phenomenon were also considered. In fig. 2.13, the contact locus is observed to trace out circular arcs. For initial conditions that do not lead to the rocking can phenomenon, petaloid shapes are observed, similar to the thin disk [33].

Finally, we computed the friction ratio, eq. (2.109), in the inner region to obtain an approximate upper bound on the required coefficient of Coulomb friction during the rocking can phenomenon. We see that large $\Delta\psi$ requires prohibitively large coefficients of Coulomb friction.

In Chapters 3 and 4, we explored the related problem of Euler's disk. Many different narratives and mechanisms have been proposed to explain the sudden halt of Euler's disk. In Chapter 3, we carried out a series of experiments, probing the final stages of motion. Chapter 4 then combines analytics and numerical simulations to explain the results of both our own experiments and others'.

In Chapter 3, we investigated the halting of Euler's disk through two experiments. The first experiment measured the energy of Euler's disk as it span on flat surfaces of different materials. In previous experiments [23, 68, 71], it has been observed that the energy of Euler's disk decreases according to a power law eq. (1.2). However, analytic estimates for the energy exponent, n, are parameter-free. One might expect that different material surfaces would give rise to different values of n, therefore, we spun the disk on base-plates of different materials. The disk was filmed from the side and the height of the rim of the disk above the base-plate was used to determine ϕ, the nutation angle. By employing the approach of McDonald and McDonald [73], we also obtained low-resolution data about ψ, the precession angle. We estimated the energy of the disk using the stationary rolling assumption, eq. (3.7), during the final 0.5 s before the halt. An estimate for the energy exponent, n, was obtained by fitting the energy to the power law. In fig. 3.15, the results show a clear material dependence, confirmed by statistical tests in Table 3.2. Energy exponents in the range $n \in [0.45, 0.69]$ are observed. The minimum value of n occurred on the stainless steel base-plate and the maximum on the silicone base-plate. In general, materials with higher Young's moduli and lower coefficients of friction gave the lowest exponents, as shown in fig. 3.16. On a concave base-plate, the observed energy exponent was $n = 0.62$, which is higher than expected, given the longevity of the motion.

In the base-plate material experiments of Section 3.2, it was observed that the disk continued to rotate after falling flat, inspiring a second set of experiments. This rotation was not visible to the naked-eye, but can be seen in the slow-motion footage. Therefore, a strip was drawn on the disk's top face to facilitate tracking of the rotation about the vertical axis. An appropriately angled mirror, as in fig. 3.18, allowed simultaneous tracking of ϕ and the strip without the need for multiple synchronised cameras. We spun the disk on the stainless steel, the mild steel and the concave base-plate. On the stainless and mild steel base-plates, mean intervals of 0.0403 s and 0.0385 s respectively were observed between the disk falling flat and stopping rotating. Lubrication of the surface extended this interval by up to 50%. A qualitative difference in the

dynamics of the disk after falling flat is observed in fig. 3.28. However, when spinning the disk on the concave base-plate, the interval was practically eliminated, lasting for only 0.0058 s. This strongly suggests the presence of a supportive layer of fluid between the disk and the flat base-plate. We hypothesize that the disk loses contact with the surface and continues to rotate while supported, before making contact with the base-plate and coming to a halt. This sequence of events agrees with the loss of contact observed in experiments by Borisov et al. [19], for which the durations were between 0.012 s and 0.04 s in length.

Chapter 4 analysed the halting of Euler's disk analytically and numerically. We derived the equations of motion of the disk, subject to Coulomb friction and another unspecified dissipation mechanism, resulting in two sets of ODEs, eqs. (4.25) and (4.32), that describe the slipping and rolling dynamics. The transition between states is governed by the codimension-2 discontinuity of Coulomb friction [7, 27].

The system, subject only to Coulomb friction, is analysed in Section 4.3 and we confirm the result that Coulomb friction is unable to bring the disk to a halt. On solving the system numerically with initial conditions from experiments, eq. (4.43), the disk slips and then rolls indefinitely fig. 4.4. Altering the initial conditions leads to a scenario where the disk repeatedly switches between slipping and rolling, as shown in fig. 4.6. Although slipping is a dissipative process, Coulomb friction was still unable to bring the disk to a halt, instead the motion tended towards a rolling trajectory.

Dissipation mechanisms capable of bringing the disk to a halt are considered in Sections 4.4 and 4.5. We focussed on rolling friction mechanisms that can be written in a angular version of Coulomb's law, eq. (4.49), rather than impacts, vibrations, etc. We rederived some common mechanisms examined by Leine [68], before deriving others through a relaxation of the rigid body assumption. In fig. 4.10, we assumed a constant offset in the centre of pressure from the rigid body, point contact limit, recovering classical rolling friction. Assuming instead that the offset in pressure is dependent upon the curvature experienced by the base-plate, we recovered contour friction discussed by [67, 68]. However, it appears that the curvature dependent offset overestimates the size of the offset, and therefore, the strength of the moment. Inserting Hertzian mechanics at the contact point yields weaker mechanisms, giving rise to $n \geq 1$. All the mechanisms considered are dry frictions and therefore contain a discontinuity when the appropriate angular velocity is zero. It should be noted that these mechanisms are quasi-static and do not include energy loss through dynamic factors such as hysteresis, viscoelasticity, microslip or other factors. Developing a rolling friction model that includes these factors is an avenue for further work.

The equations of motion, eqs. (4.25) and (4.32), subject to these dissipation mechanisms are solved numerically with initial conditions estimated from experiments at 0.5 s before the halt. For each mechanism, the energy exponent, n, is estimated from the solution, before comparison with analytical estimates in Table 4.1. The analytical estimate for n is slightly lower than the numerical estimate, due to the deviation of the initial conditions from the stationary rolling

manifold, a key assumption in the analytic estimate. The lowest value of n of the mechanisms examined is $n = 2/3$, achieved by dry contour friction.

In Section 4.7, we analysed the disk subject to Coulomb and contour friction and the numerical solutions are shown in fig. 4.12 and the same results as Le Saux [67] are observed. Rolling behaviour is followed by switching between rolling and slipping states. We compute the distance to the stationary rolling manifold, plotted in fig. 4.14, and find that it does not attract solutions, invalidating the commonly used stationary rolling assumption. Furthermore, contour friction predicts that the disk slips rather than rolls at the end of the motion. Comparison of the numerical solution with experimental data shows a good qualitative agreement. Better quantitative agreement is given by augmenting contour friction to match the experimentally observed energy exponent. This was achieved by multiplying contour friction by a factor of $\phi^{-0.722}$, heedless of any physical interpretation.

In simulations of the augmented contour friction, shown in fig. 4.16, the trajectory hit the discontinuity set of contour friction, D_c, defined by eq. (4.60). The intersection occurs when the disk is almost flat, $\phi = 4.65 \times 10^{-4}$, and leaves the disk with residual angular velocity, $\psi = -0.14\,\mathrm{rad\,s^{-1}}$. This agrees with the angular velocity observed in when the disk falls flat in experiments, $\psi = -0.23\,\mathrm{rad\,s^{-1}}$. Therefore, the continued rotation of the disk can be explained by the discontinuity of dissipation mechanism.

We suggest that, on flat base-plates, the disk loses contact with the base-plate after encountering the discontinuity. It is then briefly supported by a thin layer of air, trapped between the disk and the base-plate. Using initial conditions determined from experiments, we estimate the length of time it takes for the disk to make contact with the base-plate. The dynamics evolve on the same timescale as predicted by the experiments in Chapter 3, on the order of 0.03 s. This loss of contact duration agrees nicely with the jump of 0.012 s to 0.04 s occurring at the end of the motion, predicted by Borisov et al. [19]. After falling flat and making contact with the base-plate, Coulomb friction brings the disk to a halt in around 0.005 s on the flat base-plate. The whole post-falling flat motion is predicted to take approximately 0.035 s, consistent with experimental estimates.

In the case of the concave base-plate, there is no thin layer of air supporting the disk. After falling flat, the disk immediately makes contact with the base-plate. Coulomb friction, acting on the rim of the disk, predicts the stopping time t_{stop} =0.0033 s, close to the experimentally determined time of 0.0058 s.

The key problem of Euler's disk is determining the mechanism by which energy is removed. We proposed that for the concave base-plate, contour friction is a good candidate. Contour friction not only provides a close match in energy exponent, but also provides a mechanism for the continued rotation. However, on the flat base-plates, the prediction for dry contour friction is too high ($n = 2/3$) and alternatives such as viscous contour friction ($n = 1/2$ [68]) or air resistance ($n = 4/9$ [16]) should be investigated.

If the disk is subject to multiple dissipation mechanisms with different coefficients and exponents, then, at the end of the motion, the mechanism with the smallest exponent will dominate in the asymptotic sense. However, in experiments, it is not possible to observe the motion as the disk asymptotically approaches the halt; a sample must be taken. In the experiments of Chapter 3, the sample period is the final 0.5 s of the motion. In this time, more than one mechanism might contribute to the energy loss, resulting in an estimated energy exponent, n, that is a compromise between mechanisms.

We propose that the whole motion lasts for a long time on the steel base-plates because the coefficient of contour friction is low. This enables the dominant mechanism with $n = 0.45$ to be seen in the final 0.5 s. However, for the silicone base-plate, the coefficient of contour friction is large, skewing the energy exponent estimate towards $n = 2/3$, that of contour friction. The intermediate values as seen in the other base-plates in fig. 3.15 are a compromise between contour friction and the dominant mechanism. This effect is noted by Leine [68], who observed that for times long before the halt $n = 2/3$, while just before the halt $n = 1/2$, as the dominant mechanism takes over.

However, the disk spins on the concave base-plate for a long time before stopping, suggesting a low coefficient of contour friction. Therefore, we expect to see the exponent corresponding to the dominant mechanism, but instead experiments predict $n = 0.62$, a value that is much larger than the value for stainless steel, $n = 0.45$. We propose that the low exponents observed on the steel base-plates are due to an air resistance based mechanism. If the dominant mechanism was a rolling friction type mechanism such as a viscous contour friction, it would also be observed in the concave base-plate. Furthermore, the results of experiments probing the post-falling flat motion of the disk are in agreement with a supportive layer of air. Therefore, it must be the case that air resistance has *some* effect on Euler's disk. Although experiments by Borisov et al. [17] and van den Engh et al. [93] discounted air resistance as a factor in spinning disks, perhaps it should be revisited in the final stages of the motion of Euler's disk.

Further work

In Chapter 2, we obtained new results for the rocking can. An experimental investigation of the phenomenon that tracks the state variables throughout the motion should confirm the theoretical predictions. Characteristics such as the maximum precession velocity eq. (2.91) and the friction ratio $|\underline{F}|/N$ eq. (2.109) are good candidates for testing.

For Euler's disk, we suggest a number of experiments. Firstly, multiple high speed cameras are capable of providing enough information to compute all the state variables of the disk [71]. Focussing on the final stages of the motion, high-quality data may enable numeric computation of the dissipative moment. By considering different sample lengths, it might be possible to gain more information about the regimes in which different mechanisms dominate.

Although disks and coins have been spun in a vacuum before, we are not aware of any quantitative experiments estimating the energy exponent, n, for Euler's disk in a vacuum compared to atmospheric pressure. If air resistance is a factor, we would expect to observe differences in n between the two scenarios. Furthermore, experiments in vacuo may confirm the presence of a supportive layer of air in the final stages of the disk. Alternatively, one could spin the disk on flat and concave base-plates of the same material and estimate the energy exponent.

There is also scope for further analytical work. In experiments, we examined the behaviour of the disk on the concave base-plate and found the energy exponent to be larger than expected. Derivation and analysis of the equations of motion for the disk on a concave base-plate may confirm if this can be attributed to geometric effects or the dissipation mechanism.

Moffatt [74] and Bildsten [16] computed the energy exponent for the air resistance mechanism, but the actual dissipative moment remains unknown. It is unlikely to be of the same form as the rolling frictions, eq. (4.5), considered here and may predict different dynamics. Furthermore, the commonly used rolling frictions such as classical, pivoting, and even contour friction are phenomenological in nature. In Section 4.5.3, we derive new rolling frictions by considering a contact region. These models are greatly simplified and effects that might be important, such as friction over the contact region and viscoelasticity, are neglected. A first principles approach towards rolling friction, in the manner of Antali and Varkonyi [9], may yield new insights for Euler's disk.

The numerical solutions for Euler's disk subject to Coulomb and contour friction, shown in fig. 4.12, exhibit fast corrections which may be indicative of slow-fast behaviour. Typically, in slow-fast systems, the full problem can be split into the layer and reduced problems, each of lower dimensionality. We have shown that the stationary rolling motion, shown in fig. 4.14, is not an attractive slow manifold. As mentioned in Section 4.10, if such a slow manifold is identified then perhaps Euler's disk can be reduced to a more tractable problem.

APPENDIX A

A.1 Coefficients in eqs. (2.49) and (2.51)

The coefficients of the series solution for $\Psi(\phi)$ and $\Theta(\phi)$ are

$$\begin{aligned}
\Psi_{00} &= B_0, \\
\Psi_{l0} &= \frac{B_{-2}((kh)^2 - k)}{2}, \\
\Psi_{l1} &= \frac{B_{-2}kh((kh)^2 - k)}{6}, \\
\Theta_{00} &= \frac{2 - kc_p}{kc_p} B_0 + \frac{3k(c_p + 1) - 4 - 9h^2k^2}{6kc_p} B_{-2} \\
\Theta_{l0} &= \frac{B_{-2}(h^2k - 1)}{2c_p}(c_pk - 2), \\
\Theta_{l1} &= \frac{B_{-2}(h^2k - 1)}{2c_p} \frac{kh(c_pk - 6)}{3}.
\end{aligned}$$

A.2 The frictionless case

In the frictionless case, for which $\mu = 0$, the Lagrangian approach is more appropriate due to the absence of the non-holonomic constraint on the contact velocity. The Lagrangian, $\mathscr{L} = T - V$ is

$$\mathcal{L} = \frac{\underline{\underline{I}}\underline{\Omega} \cdot \underline{\Omega}}{2} + \frac{m\underline{V}_G \cdot \underline{V}_G}{2} - mgZ_G. \tag{A.1}$$

Upon inserting the unilateral, no penetration constraint, $Z_G = R\sin\phi + H\cos\phi$

$$\mathcal{L} = \frac{A}{2}(\dot{\psi}^2\sin^2\phi + \dot{\phi}^2) + \frac{C}{2}(\dot{\psi}\cos\phi + \dot{\theta})^2 + \frac{m}{2}(\dot{\phi}(R\cos\phi - H\sin\phi))^2 + \frac{m}{2}(\dot{X}_G^2 + m\dot{Y}_G^2) - mg(R\sin\phi + H\cos\phi). \tag{A.2}$$

The equations of motion are found using the Lagrangian equations for the generalised coordinates $q \in \{\phi, \psi, \theta, \dot{X}_G, \dot{Y}_G\}$

$$\frac{\mathrm{d}}{\mathrm{d}t}\frac{\partial\mathcal{L}}{\partial\dot{q}} - \frac{\partial\mathcal{L}}{\partial q} = 0. \tag{A.3}$$

The advantage of the Lagrangian approach is that the conserved quantities appear naturally when there are cyclic coordinates. For example, ψ, θ, $\dot{X}_g$ and $\dot{Y}_G$ only appear in the Lagrangian as first derivatives, we therefore expect to obtain four conserved quantities given by integrating

$$\frac{\mathrm{d}}{\mathrm{d}t}\left(C(\dot{\psi}\cos\phi + \dot{\theta})\right) = 0, \tag{A.4}$$

$$\frac{\mathrm{d}}{\mathrm{d}t}\left(A\dot{\psi}\sin^2\phi + C\cos\phi(\dot{\psi}\cos\phi + \dot{\theta})\right) = 0, \tag{A.5}$$

$$\frac{\mathrm{d}}{\mathrm{d}t}\left(m\dot{X}_G\right) = 0, \tag{A.6}$$

$$\frac{\mathrm{d}}{\mathrm{d}t}\left(m\dot{Y}_G\right) = 0. \tag{A.7}$$

Equations (A.6) and (A.7) simply state that the horizontal velocity of the centre of mass is conserved. Integration of eqs. (A.4) and (A.5) yields two conserved quantities that refer exactly to the angular momentum about the body symmetry axis $z^{\mathcal{B}}$ and the the global axis $z^{\mathcal{G}}$

$$c(\dot{\psi}\cos\phi + \dot{\theta}) = H_z^{\mathcal{B}}, \tag{A.8}$$

$$a\dot{\psi}\sin^2\phi + c\cos\phi(\dot{\psi}\cos\phi + \dot{\theta}) = H_z^{\mathcal{G}}, \tag{A.9}$$

where $H_z^{\mathcal{B}}$ and $H_z^{\mathcal{G}}$ are determined by the initial conditions. The remaining equation of motion for the nutation angle ϕ determines the motion of the can

$$(A + m(R\cos\phi - H\sin\phi)^2)\ddot{\phi} = m\dot{\phi}^2(R\sin\phi + H\cos\phi)(R\cos\phi - H\sin\phi) + \dot{\psi}(A - C)\sin\phi\cos\phi - C\dot{\theta}\dot{\psi}\sin\phi - mg(R\cos\phi - H\sin\phi). \tag{A.10}$$

After applying the scalings from (2.9), we obtain

$$(a + (\cos\phi - h\sin\phi)^2)\ddot{\phi} = \dot{\phi}^2(\sin\phi + h\cos\phi)(\cos\phi - h\sin\phi) + \dot{\psi}^2(a - c)\sin\phi\cos\phi - c\dot{\theta}\dot{\psi}\sin\phi - \cos\phi + h\sin\phi, \tag{A.11}$$

The cyclic variables, $\dot{\psi}$ and $\dot{\theta}$, are eliminated using the conserved quantities, $H_z^{\mathcal{B}}$ and $H_z^{\mathcal{G}}$

$$(a + (\cos\phi - h\sin\phi)^2)\ddot{\phi} = \dot{\phi}^2(\sin\phi + h\cos\phi)(\cos\phi - h\sin\phi) + \frac{(H_z^{\mathcal{G}} - H_z^{\mathcal{B}}\cos\phi)(H_z^{\mathcal{G}}\cos\phi - H_z^{\mathcal{B}})}{a\sin^3(\phi)} - \cos\phi + h\sin\phi. \tag{A.12}$$

The system has been reduced to a non-linear, planar ODE with no requirement of small ϕ. As in the frictional case, we note that the singular dynamics occur only when $H_z^{\mathcal{G}} = H_z^{\mathcal{B}} = 0$. Therefore, we introduce $\epsilon^{1/2} = |H_z^{\mathcal{B}}|$ and $H_z^{\mathcal{G}} = \zeta H_z^{\mathcal{B}}$ and expand the trigonometric terms in small ϕ to give

$$\ddot{\phi} = \epsilon\left(\frac{\alpha_3}{\phi^3} + \frac{\alpha_2}{\phi^2} + \frac{\alpha_1}{\phi} + \alpha_0\right) + \frac{h\dot{\phi}^2 - 1}{a+1}, \tag{A.13}$$

the slipping equivalent of the governing equation, eq. (2.63). However, the matched asymptotic approach used in Section 2.5 may fail due to the presence of the $\dot{\phi}^2$ term. An alternative solution method might involve geometric singular perturbation theory.

A.3 Coefficients in the reduced equation of motion

The polynomial coefficients for eq. (2.60) are computed in Maple and consist of bivariate quadratics in B_0 and B_{-2}

$$\begin{aligned}
a_3 =& B_{-2}^2 a_p,\\
a_2 =& -2\,\frac{h\left(\left(-1/3+\left(-3/4\,h^2+ap\,cp\right)k^2+\left(-cp/2+1/4\right)k\right)B_{-2}+B_0\right)B_{-2}}{kcp},\\
a_1 =& 2\,\frac{\left(\left(\left(1/3+1/2\,h^2k^3ap-1/4\,k^2h^2+\left(-ap/3-1/4\right)k\right)B_{-2}+B_0\left(ap\,k-1\right)\right)cp-B_{-2}h^2k^2\left(h^2k-1\right)\right)B_{-2}}{kcp},\\
a_0 =& \frac{1}{2880\,kcp}\Bigg[\left(-125\,cp\,k^5+1440\,k^4\right){B_{-2}}^2h^5\\
&-120\,k^2B_{-2}\left(\left(34-\frac{32\,cp\,k^2}{3}\left(ap+\frac{11}{128}\right)+\left(\frac{293\,cp}{12}+36\right)k\right)B_{-2}+B_0\left(kcp-84\right)\right)h^3\\
&+\left(\left[-960+\left(-3200\,ap+135\right)cp\,k^3+\left(1280\,ap+5850\right)cp\,k^2+\left(-1032\,cp+720\right)k\right]{B_{-2}}^2\right.\\
&\left.-3840\left[-5/4+cp\left(ap+\frac{3}{32}\right)k^2+\left(-\frac{27\,cp}{16}+3/8\right)k\right]B_0B_{-2}-5760\,{B_0}^2\right)h\Bigg].
\end{aligned}$$

The log coefficients are

$$\begin{aligned}
a_{l2} =& \frac{hB^2\left(h^2k-1\right)}{cp},\\
a_{l1} =& -\left(h^2k-1\right)B^2\left(ap\,k-1\right),\\
a_{l0} =& 2\,\frac{h\left(h^2k-1\right)B}{cp}\left(\left(-\frac{5}{12}+\left(-3/4\,h^2+1/3\,ap\,cp\right)k^2+\left(-cp/2+1/4\right)k\right)B+A\right),\\
a_{ll} =& -\frac{hk\left(h^2k-1\right)^2B^2}{2cp}.
\end{aligned}$$

The coefficients for the governing equation, eq. (2.63), are given by substituting $B_{-2} = 1$ and $B_0 = \zeta$.

A.4 Hamiltonian system

The governing equation for the rocking can, eq. (2.63), may be written as a planar Hamiltonian system with generalised coordinate, ϕ, and generalised momentum, Φ

$$\frac{\mathrm{d}\Phi}{\mathrm{d}t} = -\frac{\partial \mathcal{H}}{\partial \phi} = \epsilon\left(\frac{a_3}{\phi^3} + \frac{a_{l2}\log\phi}{\phi^2} + \frac{a_2}{\phi^2} + \frac{a_{l1}\log\phi}{\phi} + \frac{a_1}{\phi} + a_{ll}(\log\phi)^2 + a_{l0}\log\phi + a_0\right) - 1 \tag{A.14}$$

$$\frac{\mathrm{d}\phi}{\mathrm{d}t} = \frac{\partial \mathcal{H}}{\partial \Phi} = \Phi \tag{A.15}$$

where $\mathcal{H}$ is the Hamiltonian given by integrating eqs. (A.14) and (A.15)

$$\mathcal{H}(\Phi,\phi) = \frac{\Phi^2}{2} + \phi - \epsilon\left(\ln^2(\phi)\left(\frac{a_{ll}}{2} + a_{ll}\phi\right) + \left(a_{l0} - 2a_{ll} - \frac{a_{l2}}{\phi}\right)\ln(\phi) + (a_0 - 2a_{ll} - a_{l0})\phi - \frac{a_2 - a_{l2}}{\phi} - \frac{a_3}{2\phi^2}\right) \tag{A.16}$$

The Hamiltonian surface $\mathcal{H}(\Phi,\phi)$ is shown in fig. A.1. We see an upwards sloping trough caused by the non-singular terms, capped by the singularity near $\phi = 0$. In general, closed contours of the Hamiltonian indicate periodic orbits and these can be seen in fig. A.2, with many orbits squeezed in close to the Φ axis. An equilibrium point exists in the centre of the phase portrait, corresponding to the steady motion S_{steady}, eq. (2.23). Note that the Hamiltonian is symmetric with respect to the ϕ axis. This indicates the presence of a symmetry law in eq. (2.63), and also in the full equations of motion eq. (2.11)

$$\Phi \to -\Phi \quad \text{and} \quad t \to -t \tag{A.17}$$

Orbits above the ϕ axis move to the right, while orbits beneath the ϕ axis are identical but move to the left. We therefore restrict our study to the upper half plane $\Phi > 0$. The period of one oscillation is given by

$$T = 2\int_{\phi_0}^{\phi_1} \frac{1}{\Phi}\mathrm{d}\phi, \tag{A.18}$$

where ϕ_0 and ϕ_1 are the intersections of the contour with the line $\Phi = 0$. These intersections can be found from solutions of the Hamiltonian at $\Phi = 0$ with a particular energy, E

$$E - \phi + \epsilon\left(\ln^2(\phi)\left(\frac{a_{ll}}{2} + a_{ll}\phi\right) + \left(a_{l0} - 2a_{ll} - \frac{a_{l2}}{\phi}\right)\ln(\phi) + (a_0 - 2a_{ll} - a_{l0})\phi - \frac{a_2 - a_{l2}}{\phi} - \frac{a_3}{2\phi^2}\right) = 0 \tag{A.19}$$

The presence of $\ln(\phi)$ terms results in a transcendental equation which in general do not have solutions in terms of elementary functions. From fig. A.1 we expect either two positive solutions, $\phi_0 < \phi_1$, a single positive solution corresponding to the equilibrium or no solutions depending on the value of E. The parametrisation of the solution surfaces by E gives the period

$$T = \sqrt{2}\int_{\phi_0}^{\phi_1} \frac{1}{\sqrt{E - \phi + \epsilon\left(\ln^2(\phi)\left(\frac{a_{ll}}{2} + a_{ll}\phi\right) + \left(a_{l0} - 2a_{ll} - \frac{a_{l2}}{\phi}\right)\ln(\phi) + (a_0 - 2a_{ll} - a_{l0})\phi - \frac{a_2 - a_{l2}}{\phi} - \frac{a_3}{2\phi^2}\right)}}\mathrm{d}\phi. \tag{A.20}$$

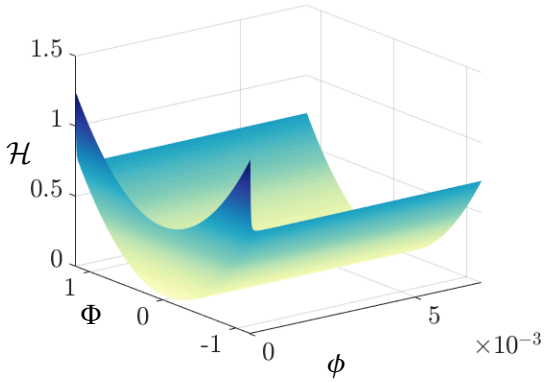

Figure A.1: The Hamiltonian surface, eq. (A.19), with ϵ determined by the initial conditions and parameters in eqs. (2.14) and (2.15) respectively. The sharp increase in $\mathcal{H}$ near $\phi = 0$ is due to the repulsive singularity.

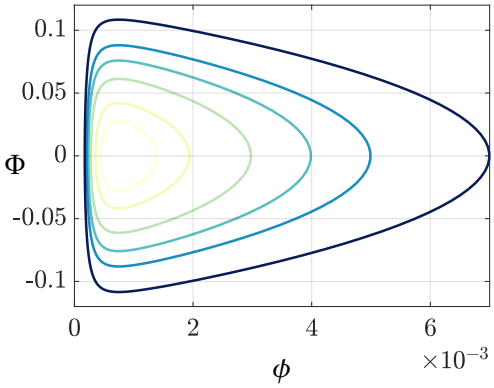

Figure A.2: Contour plot of the Hamiltonian eq. (A.19), for $E = 7.5 \times 10^{-4}, 1 \times 10^{-3}, 2 \times 10^{-3}, 3 \times 10^{-3}, 4 \times 10^{-3}, 5 \times 10^{-3}$. Solutions of eq. (2.63) follow the contours in a clockwise direction.

In the case of $\epsilon = 0$ we may compute the period T exactly

$$T|_{\epsilon=0} = \sqrt{2}\int_{\phi_0}^{\phi_1} \frac{1}{\sqrt{h-\phi}} \mathrm{d}\phi. \tag{A.21}$$

If $\epsilon = 0$ then the can falls flat, reaching $\phi_0 = 0$. Furthermore, if the can is released from rest at $\phi = \phi_1$, then ϕ_1 is the highest angle attained by the can and $\mathcal{H} = \phi_1$. The period for such motion is

$$T|_{\epsilon=0} = 2\sqrt{2\phi_1}. \tag{A.22}$$

which agrees with the calculation for $\ddot{\phi} = -1$ given by eq. (2.63) with $\epsilon = 0$. In unscaled time, the period is

$$T|_{\epsilon=0} = 2\sqrt{\frac{2\phi_1(A + mH^2 + mR^2)}{mgR}}. \tag{A.23}$$

As might be expected, taller cans with larger H take a longer time to fall. Although it is simpler to compute this leading order estimate of the oscillation period using eq. (2.63), the Hamiltonian method of this section suggests a method for computing the period with non-zero ϵ.

A.5 Coefficients in the outer problem

The coefficients in eq. (2.69) are

$$
\begin{aligned}
b_3 &= \frac{8a_3}{I^2},\\
b_{l2} &= \frac{4a_{l2}}{I},\\
b_2 &= \frac{4a_2}{I^2} + \frac{4a_{l2}\log(I/2)}{I},\\
b_{l1} &= 2a_{l1},\\
b_1 &= 2a_1 + 2a_{l1}\log(I/2),\\
b_{ll} &= a_{ll}I,\\
b_{l0} &= a_{l0}I + 2a_{ll}I\log(I/2),\\
b_0 &= a_0 I + a_{l0}I\log(I/2) + a_{ll}I\log^2(I/2).
\end{aligned}
$$

A.6 Integrals

The integrals for eq. (2.71). First the polynomial integrals

$$J_1 = \int\int \frac{1}{(1-T^2)}\mathrm{d}T\mathrm{d}T = T\,\mathrm{arctanh}(T) + \frac{1}{2}\ln(1-T^2) \tag{A.24}$$

$$J_2 = \int\int \frac{1}{(1-T^2)^2}\mathrm{d}T\mathrm{d}T = \frac{T}{2}\,\mathrm{arctanh}(T) \tag{A.25}$$

$$J_3 = \int\int \frac{1}{(1-T^2)^3}\mathrm{d}T\mathrm{d}T = \frac{T^2}{8T^2-8} + \frac{3T}{8}\,\mathrm{arctanh}\,T \tag{A.26}$$

and secondly the logarithmic integrals, computed in MATHEMATICA

$$
\begin{aligned}
J_{l2} = \int\int \frac{\log\left(1-T^2\right)}{\left(1-T^2\right)^2}\,\mathrm{d}T\,\mathrm{d}T = \frac{1}{8}\Big[&2(T+1)\mathrm{Li}_2\left(\frac{1-T}{2}\right) - 2(T-1)\mathrm{Li}_2\left(\frac{T+1}{2}\right) - T\log^2(1-T) + T\log^2(T+1)\\
&- 4\left(\log(8)\log(1-T) + \log(T+1) + \log(8-8T) - 3 + 2\log^2(2)\right) + 4\log(4)\log(1-T)\\
&+ 2\log(T+1)\log(1-T) + (T(\log(16)-4) - 2\log(4))\tanh^{-1}(T)\Big]
\end{aligned} \tag{A.27}
$$

$$
\begin{aligned}
J_{l1} = \int\int \frac{\log\left(1-T^2\right)}{1-T^2}\,\mathrm{d}T\,\mathrm{d}T = \frac{1}{4}\Big[&2(T-1)\mathrm{Li}_2\left(\frac{1-T}{2}\right) - 2(T+1)\mathrm{Li}_2\left(\frac{T+1}{2}\right) - 2(T-1)\log^2(1-T) + \log^2(1-T)\\
&+ (T+1)\log^2(T+1) + (2(T-1)\log(1-T) + \log(4))\log(1-T) - T\log(1-T)\log(4(1-T))\\
&+ (T+1)\log(4)\log(T+1) + 8 - 2\log(4)\Big]
\end{aligned} \tag{A.28}
$$

$$J_{l0} = \int\int \log\left(1-T^2\right)\mathrm{d}T\,\mathrm{d}T = \frac{1}{2}\left(-3T^2 + \left(T^2+1\right)\log\left(1-T^2\right) + 4T\tanh^{-1}(T)\right) \tag{A.29}$$

$$
\begin{aligned}
J_{ll} = \int\int \log^2\left(1-T^2\right)\mathrm{d}T\,\mathrm{d}T = \frac{1}{2}\Big[&4(T-1)\mathrm{Li}_2\left(\frac{1-T}{2}\right) - 4(T+1)\mathrm{Li}_2\left(\frac{T+1}{2}\right) + 14T^2\\
&+ \log(1-T)\left(-6T^2 + 2\left(T^2-1\right)\log(T+1) + 4(T-1)\log(1-T) - 2 + \log(16)\right)\\
&+ (T-3)(T-1)\log^2(1-T) - 2(T-1)\log^2(1-T) + (T+1)^2\log^2(T+1)\\
&- 4T(\log(2)-2)\log(1-T) - 2(T+1)(3T+1-\log(4))\log(T+1) + 16 - 8\log(2)\Big]
\end{aligned} \tag{A.30}
$$

Note the appearance of the dilogarithm Li_2.

APPENDIX B

APPENDIX B

In this appendix, we give the results of the base-plate material experiments in Section 3.2. In Table B.1, we show experimentally determined energy exponents for Euler's disk rolling on different base-plates. The energy is estimated using eq. (3.8) for which the state variables are calculated from the experimental data as described in Section 3.2.5. To determine the energy exponent, n, we fit the power law eq. (3.2) to the experimental energy. In Tables B.2 and B.3, we show the corresponding experimental results for the flipped Euler's disk and the brass disk respectively. The data is ordered by increasing n, rather than experimental repeat.

m. steel	s. steel	oak	pine	acrylic	Teflon	silicone	concave
0.3766	0.3053	0.5027	0.4619	0.4909	0.4264	0.6159	0.5676
0.4075	0.4024	0.5224	0.5032	0.5102	0.5232	0.6173	0.5714
0.4124	0.4232	0.5553	0.5329	0.5202	0.5325	0.6381	0.5813
0.4552	0.4257	0.5685	0.5509	0.5238	0.5528	0.6409	0.5839
0.4808	0.4333	0.5691	0.5714	0.5293	0.5760	0.6617	0.5990
0.4820	0.4481	0.5857	0.5796	0.5323	0.5852	0.6690	0.6032
0.4978	0.4510	0.6038	0.5820	0.5371	0.5963	0.7029	0.6445
0.4992	0.4590	0.6144	0.5916	0.5498	0.6059	0.7348	0.64571
0.5020	0.4668	0.6151	0.5999	0.5917	0.6333	0.7547	0.6467
0.5463	0.4882	0.6422	0.6061	0.6123	0.6347	0.7620	0.6486
0.5698	0.5023	0.7015	0.6303	0.6165	0.6472	0.7751	0.7016
0.5936	0.5239	0.7137	0.6314	0.6274	0.6581	0.8942	0.7133

Table B.1: Experimentally determined energy exponents for Euler's disk rolling on different base-plate materials.

m. steel	s. steel	oak	pine	acrylic	Teflon	silicone
0.4598	0.3638	0.5576	0.5788	0.5392	0.5479	0.6010
0.4792	0.3836	0.5763	0.5806	0.5563	0.5603	0.6178
0.5064	0.3991	0.5779	0.5980	0.5642	0.5662	0.6289
0.5255	0.4095	0.5931	0.6088	0.5655	0.5869	0.6317
0.5322	0.4129	0.5947	0.6169	0.5705	0.5979	0.6331
0.5471	0.4401	0.6033	0.6268	0.5874	0.6025	0.6612
0.5534	0.4421	0.6054	0.6343	0.5885	0.6037	0.6689
0.5578	0.4433	0.6393	0.6426	0.5933	0.6040	0.6774
0.5633	0.4675	0.6405	0.6543	0.6163	0.6052	0.6853
0.5666	0.4819	0.6527	0.6647	0.6271	0.6226	0.7142
0.5987	0.4924	0.6703	0.6705	0.6559	0.6258	0.7228
0.6445	0.5051	0.7190	0.6748	0.6638	0.6264	0.7263

Table B.2: Experimentally determined energy exponents for the flipped Euler's disk rolling on different base-plate materials.

m. steel	s. steel	oak	pine	acrylic	Teflon	silicone
0.4507	0.4189	0.4432	0.4777	0.4768	0.5763	0.5765
0.4516	0.4428	0.4489	0.5527	0.4901	0.5894	0.5896
0.5106	0.4450	0.4843	0.6112	0.5061	0.5925	0.6048
0.5181	0.4451	0.5122	0.6320	0.5444	0.5955	0.6256
0.5299	0.4545	0.5465	0.6331	0.5455	0.5964	0.6270
0.5311	0.4642	0.5663	0.6426	0.5529	0.5986	0.6423
0.5526	0.4808	0.5753	0.6637	0.5535	0.6145	0.6467
0.5637	0.4888	0.5809	0.6657	0.5836	0.6152	0.6662
0.5817	0.4982	0.5819	0.6673	0.6004	0.6163	0.6761
0.6019	0.4998	0.5902	0.6683	0.6061	0.6336	0.6809
0.6524	0.5098	0.6035	0.7097	0.6251	0.6400	0.6956
0.6544	0.5559	0.6077	0.7407	0.6515	0.6930	0.7365

Table B.3: Experimentally determined energy exponents for the brass disk rolling on different base-plate materials.

APPENDIX C

APPENDIX C

C.1 Additional functions in the equations of motion

Here we define the functions g_i and h_i used in derivation of the equations of motion eq. (4.25) and eq. (4.32). First, the functions used in the rolling equations, eq. (4.25), which describe the dissipation-free dynamics

$$g_\psi = ((kc_p - 2)\cos\phi - kh)\dot{\psi}\dot{\phi} + \frac{kc_p}{\sin\phi}\dot{\theta}\dot{\phi}, \tag{C.1}$$

$$g_\theta = (-kc_P\cos\phi + kh)\dot{\theta}\dot{\phi} + \left(-kc_p\cot\phi\cos\phi - ka_p\sin\phi + 2kh\cos\phi + \frac{2}{\sin\phi}\right)\dot{\psi}\dot{\phi}, \tag{C.2}$$

$$g_\phi = \frac{1}{a_p + 1}\left((a_p - c_p)\sin\phi\cos\phi - h\cos(2\phi))\dot{\psi}^2 - (cp\sin\phi + h\cos\phi)\dot{\theta}\dot{\psi}) - (\cos\phi - h\sin\phi)\right). \tag{C.3}$$

Next, the functions in the slipping equations, eq. (4.32)

$$h_\psi = \frac{c\dot{\theta}\dot{\phi} - (2a - c)\dot{\psi}\dot{\phi}\cos\phi)}{a\sin\phi}, \tag{C.4}$$

$$h_\theta = \frac{((ca - c^2)\cos^2\phi + ca)\dot{\psi}\dot{\phi} - c^2\dot{\theta}\dot{\phi}\cos\phi}{ac\sin\phi}, \tag{C.5}$$

$$h_\phi = \frac{(a - c)\cos\phi\sin\phi\dot{\psi}^2 - c\sin\phi\dot{\psi}\dot{\theta}}{a}, \tag{C.6}$$

$$f_\phi = \eta q_y - \mu\frac{\dot{x}}{\sqrt{\dot{x}^2 + \dot{y}^2}}(h\cos\phi + \sin\phi) - (\cos\phi - h\sin\phi), \tag{C.7}$$

where the h_i describe the slipping, dissipation-free dynamics and f_ϕ describes the contact forces on the disk when slipping.

BIBLIOGRAPHY

[1] *Da Tuoluo*.
https://da-tuoluo.com/wordpress/en/practice/chinese-spinning-tops/.
Online; accessed 9 September 2022.

[2] *Dreidel*.
https://simple.wikipedia.org/wiki/Dreidel#/media/File:Dreidel_001.jpg.
Online; accessed 9 September 2022.

[3] *'Euler's disk' spinning desk toy*.
http://toolsandtoys.net/eulers-disk-spinning-desk-toy/.
Online; accessed 15 September 2022.

[4] *Gasing pangkah*.
https://en.wikipedia.org/wiki/Gasing_pangkah#/media/File:Gasing.jpg.
Online; accessed 9 September 2022.

[5] *Rattleback*.
https://www.wikiwand.com/en/Rattleback.
Online; accessed 9 September 2022.

[6] D. ACHESON, *Elementary Fluid Dynamics*, Clarendon Press, Oxford, 1990.

[7] M. ANTALI AND G. STEPAN, *Sliding and crossing dynamics in extended Filippov systems*, SIAM Journal on Applied Dynamical Systems, 17 (2018), pp. 823–858.

[8] ——, *Nonsmooth analysis of three-dimensional slipping and rolling in the presence of dry friction*, Nonlinear Dynamics, 97 (2019), pp. 1799–1817.

[9] M. ANTALI AND P. VÁRKONYI, *The nonsmooth dynamics of combined slip and spin motion under dry friction*, Journal of Nonlinear Science, 32 (2022), pp. 1–43.

[10] P. APPELL, *Sur l'intégration des équations du mouvement d'un corps pesant de révolution roulant par une arête circulaire sur un plan horizontal; cas parficulier du cerceau*, Rendiconti del Circolo Matematico di Palermo, 14 (1900), pp. 1–6.

[11] T. BARANYAI AND P. VÁRKONYI, *Imperfections, impacts, and the singularity of Euler's disk*, Physical Review E, 96 (2017), p. 033005.

[12] M. BATISTA, *Integrability of the motion of a rolling disk of finite thickness on a rough plane*, International Journal of Non-Linear Mechanics, 41 (2006), pp. 850–859.

[13] ——, *The nearly horizontally rolling of a thick disk on a rough plane*, Regular and Chaotic Dynamics, 13 (2008), pp. 344–354.

[14] J. BENDIK, *The History of Euler's Disk ® (Spinning and Rolling Disk)*. http://www.eulersdisk.com/History_20b.pdf. Online; accessed 14 September 2022.

[15] L. BILDSTEN, *Dissipation for Euler's disk and a desktop demonstration of coalescing neutron stars*, arXiv:gr-qc/0102046, (2001).

[16] ——, *Viscous dissipation for Euler's disk*, Physical Review E, 66 (2002), p. 056309.

[17] A. BORISOV, A. KILIN, AND Y. KARAVAEV, *Retrograde motion of a rolling disk*, Physics-Uspekhi, 60 (2017), p. 931.

[18] A. BORISOV AND I. MAMAEV, *Strange attractors in rattleback dynamics*, Physics-Uspekhi, 46 (2003), p. 393.

[19] A. BORISOV, I. MAMAEV, AND Y. KARAVAEV, *On the loss of contact of the Euler disk*, Nonlinear Dynamics, 79 (2015), pp. 2287–2294.

[20] A. BORISOV, I. MAMAEV, AND A. KILIN, *Dynamics of rolling disk*, Regular and Chaotic Dynamics, 8 (2003), pp. 201–212.

[21] D. BREWE AND B. HAMROCK, *Simplified solution for elliptical-contact deformation between two elastic solids*, Journal of Lubrication Technology, 99 (1977), pp. 485–487.

[22] S. BURGER, M. EGGER, J. BACHMANN, M. VASSILIOU, AND B. STOJADINOVIC, *Behavior of inverted pendulum cylindrical structures that rock and wobble during earthquakes*, in Proceedings of the 16th World Conference on Earthquake Engineering (WCEE 2017), National Information Centre of Earthquake Engineering, Indian Institute of Technology Kanpur, 2017, p. 594.

[23] H. CAPS, S. DORBOLO, S. PONTE, H. CROISIER, AND N. VANDEWALLE, *Rolling and slipping motion of Euler's disk*, Physical Review E, 69 (2004), p. 056610.

[24] W. CASE AND S. JALAL, *The rattleback revisited*, American Journal of Physics, 82 (2014), pp. 654–658.

[25] S. CHAPLYGIN, *On a motion of a heavy body of revolution on a horizontal plane*, Proceedings of the Physical Sciences, Section of the Society of Amateurs of Natural Sciences, 9 (1897), pp. 10–16.

[26] N. CHEESMAN, S. HOGAN, AND K. KRISTIANSEN, *The geometry of the Painlevé paradox*, SIAM Journal on Applied Dynamical Systems, 21 (2022), pp. 1798–1831.

[27] N. CHEESMAN, K. KRISTIANSEN, AND S. J. HOGAN, *Regularization of isolated codimension-2 discontinuity sets*, SIAM Journal on Applied Dynamical Systems, 20 (2021), pp. 2630–2670.

[28] K. CHU, *Comments on 'The abrupt ending of a spinning disk'*, European Journal of Physics, 41 (2020), p. 038001.

[29] R. COHEN, *The tippe top revisited*, American Journal of Physics, 45 (1977), pp. 12–17.

[30] P. CONTENSOU, *Couplage entre frottement de glissement et frottement de pivotement dans la théorie de la toupie*, in Kreiselprobleme/Gyrodynamics, Springer, 1963, pp. 201–216.

[31] R. CROSS, *Effects of rolling friction on a spinning coin or disk*, European Journal of Physics, 39 (2018), p. 035005.

[32] ——, *The abrupt ending of a spinning disk*, European Journal of Physics, 40 (2019), p. 065002.

[33] R. CUSHMAN AND J. DUISTERMAAT, *Nearly flat falling motions of the rolling disk*, Regular and Chaotic dynamics, 11 (2006), pp. 31–60.

[34] DESIGNERDATA, *PTFE*.
https://designerdata.nl/materials/plastics/thermo-plastics/polytetrafluoroethylene-(teflon).
Online; Accessed 16 March 2022.

[35] J. DOORNIK, *Numerical evaluation of the Gauss hypergeometric function by power summations*, Mathematics of Computation, 84 (2015), pp. 1813–1833.

[36] K. EASWAR, F. ROUYER, AND N. MENON, *Speeding to a stop: the finite-time singularity of a spinning disk*, Physical Review E, 66 (2002), p. 045102.

[37] ENGINEERING TOOLBOX, *Poisson's Ratio*.
https://www.engineeringtoolbox.com/poissons-ratio-d_1224.html.
Online; Accessed 16 March 2022.

[38] ENGINEERING TOOLBOX, *Young's modulus, tensile strength and yield strength values for some materials*.
https://www.engineeringtoolbox.com/young-modulus-d_417.html.
Online; Accessed 16 March 2022.

[39] D. FEATONBY, *Dare we teach tops?*, Physics Education, 45 (2010), p. 409.

[40] A. FILIPPOV, *Differential equations with Discontinuous Right-hand Sides*, Mathematics and its Applications, Springer, 1988.

[41] FOREST PRODUCTS LABORATORY (US), *Wood handbook: wood as an engineering material*, no. 72, The Laboratory, 1987.

[42] F. GÉNOT AND B. BROGLIATO, *New results on Painlevé paradoxes*, European Journal of Mechanics-A/Solids, 18 (1999), pp. 653–677.

[43] H. GOLDSTEIN, C. POOLE, AND J. SAFKO, *Classical Mechanics*, Pearson, third ed., 2002.

[44] B. GOODWINE AND G. STÉPÁN, *Controlling unstable rolling phenomena*, Journal of Vibration and Control, 6 (2000), pp. 137–158.

[45] I. GORYACHEVA AND A. ZOBOVA, *Dynamics of rolling with a microslip for an elastic cylinder on an elastic half-space*, Doklady Physics, 63 (2018), pp. 263–265.

[46] ——, *Deceleration of a rigid cylinder sliding along a viscoelastic foundation*, Mechanics of Solids, 54 (2019), pp. 278–288.

[47] J. GREENWOOD, *Analysis of elliptical Hertzian contacts*, Tribology International, 30 (1997), pp. 235–237.

[48] B. J. HAMROCK AND D. BREWE, *Simplified solution for stresses and deformations*, Journal of Lubrication Technology, 105 (1983), pp. 171–177.

[49] E. HINCH, *Perturbation Methods*, Cambridge University Press, 1991.

[50] S. J. HOGAN, *The many steady state responses of a rigid block under harmonic forcing*, Earthquake Engineering & Structural Dynamics, 19 (1990), pp. 1057–1071.

[51] S. J. HOGAN AND K. KRISTIANSEN, *On the regularization of impact without collision: the Painlevé paradox and compliance*, Proceedings of the Royal Society A: Mathematical, Physical and Engineering Sciences, 473 (2017), p. 20160773.

[52] G. HOUSNER, *The behavior of inverted pendulum structures during earthquakes*, Bulletin of the Seismological Society of America, 53 (1963), pp. 403–417.

[53] S. HUNTER, *The rolling contact of a rigid cylinder with a viscoelastic half space*, Journal of Applied Mechanics, 28 (1961), pp. 611–617.

[54] A. IUORIO, N. POPOVIC, AND P. SZMOLYAN, *Singular perturbation analysis of a regularized MEMS model*, SIAM Journal on Applied Dynamical Systems, 18 (2019), pp. 661–708.

[55] A. IVANOV, *On detachment conditions in the problem on the motion of a rigid body on a rough plane*, Regular and Chaotic Dynamics, 13 (2008), pp. 355–368.

[56] A. IVANOV, *Rolling friction*, Doklady Physics, 64 (2019), pp. 129–133.

[57] D. JACKSON, J. HUDDY, A. BALDONI, AND W. BOYES, *The mysterious spinning cylinder—rigid-body motion that is full of surprises*, American Journal of Physics, 87 (2019), pp. 85–94.

[58] K. JOHNSON, *Contact Mechanics*, Cambridge University Press, 1987.

[59] I. JOLLIFFE, *Principal Component Analysis*, Springer, 2nd ed., 2002.

[60] P. KESSLER AND O. O'REILLY, *The ringing of Euler's disk*, Regular and Chaotic dynamics, 7 (2002), pp. 49–60.

[61] A. KOH AND G. MUSTAFA, *Free rocking of cylindrical structures*, Journal of Engineering Mechanics, 116 (1990), pp. 35–54.

[62] D. KORTEWEG, *Ueber eine ziemlich verbreitete unrichtige Behandlungsweise eines Problems der rollenden Bewegung, über die Theorie dieser Bewegung und insbesondere über kleine rollende Schwingungen um eine Gleichgewichtslage*, Nieuw archief voor wiskunde, 4 (1899), pp. 130–155.

[63] S. KOWALEVSKI, *Sur le problème de la rotation d'un corps solide autour d'un point fixe*, Acta mathematica, 12 (1889), pp. 177–232.

[64] C. KUEHN, *Multiple Time Scale Dynamics*, Springer, 2015.

[65] J.-L. LAGRANGE, *Mécanique analytique. Tome 2*, Courcier, 1811.

[66] A. LAZER AND S. SOLIMINI, *On periodic solutions of nonlinear differential equations with singularities*, Proceedings of the American Mathematical Society, 99 (1987), pp. 109–114.

[67] C. LE SAUX, R. LEINE, AND C. GLOCKER, *Dynamics of a rolling disk in the presence of dry friction*, Journal of Nonlinear Science, 15 (2005), pp. 27–61.

[68] R. LEINE, *Experimental and theoretical investigation of the energy dissipation of a rolling disk during its final stage of motion*, Archive of Applied Mechanics, 79 (2009), pp. 1063–1082.

[69] C. LIU, H. ZHANG, Z. ZHAO, AND B. BROGLIATO, *Impact–contact dynamics in a disc–ball system*, Proceedings of the Royal Society A: Mathematical, Physical and Engineering Sciences, 469 (2013), p. 20120741.

[70] D. MA AND C. LIU, *Dynamics of a spinning disk*, Journal of Applied Mechanics, 83 (2016), p. 061003.

[71] D. MA, C. LIU, Z. ZHAO, AND H. ZHANG, *Rolling friction and energy dissipation in a spinning disc*, Proceedings of the Royal Society A: Mathematical, Physical and Engineering Sciences, 470 (2014), p. 20140191.

[72] MATWEB, *Overview of materials for Silicone Rubber*.
https://tinyurl.com/mrzpt6sj.
Online; Accessed 14 September 2022.

[73] A. MCDONALD AND K. MCDONALD, *The rolling motion of a disk on a horizontal plane*, arXiv preprint physics/0008227, (2000).

[74] H. MOFFATT, *Euler's disk and its finite-time singularity*, Nature, 404 (2000), pp. 833–834.

[75] A. OR, *The dynamics of a tippe top*, SIAM Journal on Applied Mathematics, 54 (1994), pp. 597–609.

[76] O. O'REILLY, *The dynamics of rolling disks and sliding disks*, Nonlinear Dynamics, 10 (1996), pp. 287–305.

[77] H. PACEJKA AND E. BAKKER, *The magic formula tyre model*, Vehicle System Dynamics, 21 (1992), pp. 1–18.

[78] P. PAINLEVÉ, *Sur les loi du frottement de glissement*, Comptes Rendu des Séances de l'Academie des Sciences, 141 (1905), pp. 401–405.

[79] P. PARIS AND L. ZHANG, *A disk rolling on a horizontal surface without slip*, Mathematical and Computer Modelling, 36 (2002), pp. 855–860.

[80] D. PETRIE, J. HUNT, AND C. GRAY, *Does the Euler Disk slip during its motion?*, American Journal of Physics, 70 (2002), pp. 1025–1028.

[81] M. PRZYBYLSKA AND S. RAUCH-WOJCIECHOWSKI, *Dynamics of a rolling and sliding disk in a plane. Asymptotic solutions, stability and numerical simulations*, Regular and Chaotic Dynamics, 21 (2016), pp. 204–231.

[82] O. REYNOLDS, *VI. On rolling-friction*, Philosophical Transactions of the Royal Society of London, (1876), pp. 155–174.

[83] D. ROJAS AND P. TORRES, *Periodic bouncing solutions of the Lazer–Solimini equation with weak repulsive singularity*, Nonlinear Analysis: Real World Applications, 64 (2022), p. 103441.

[84] M. RUPERT, *Simultaneous Statistical Inference*, Springer, 1966.

[85] S. SAILER AND R. LEINE, *Singularly perturbed dynamics of the tippedisk*, Proceedings of the Royal Society A, 477 (2021), p. 20210536.

[86] M. SRINIVASAN, *Chaos in a soda can: Non-periodic rocking of upright cylinders with sensitive dependence on initial conditions*, Mechanics Research Communications, 36 (2009), pp. 722–727.

[87] M. SRINIVASAN AND A. RUINA, *Rocking and rolling: a can that appears to rock might actually roll*, Physical Review E, 78 (2008), p. 066609.

[88] A. STANISLAVSKY AND K. WERON, *Nonlinear oscillations in the rolling motion of Euler's disk*, Physica D: Nonlinear Phenomena, 156 (2001), pp. 247–259.

[89] I. STEFANOU, I. VARDOULAKIS, AND A. MAVRAGANIS, *Dynamic motion of a conical frustum over a rough horizontal plane*, International Journal of Non-Linear Mechanics, 46 (2011), pp. 114–124.

[90] D. TABOR, *The mechanism of rolling friction II. The elastic range*, Proceedings of the Royal Society of London. Series A. Mathematical and Physical Sciences, 229 (1955), pp. 198–220.

[91] D. TAKÁCS, G. OROSZ, AND G. STÉPÁN, *Delay effects in shimmy dynamics of wheels with stretched string-like tyres*, European Journal of Mechanics-A/Solids, 28 (2009), pp. 516–525.

[92] H. TAKANO, S. TAKATORI, AND T. ICHINO, *Continuous rolling motion of a disk on a vibrating plate*, Nonlinear Dynamics, 100 (2020), pp. 2205–2214.

[93] G. VAN DEN ENGH, P. NELSON, AND J. ROACH, *Numismatic gyrations*, Nature, 408 (2000), pp. 540–540.

[94] M. VASSILIOU, S. BURGER, M. EGGER, J. BACHMANN, M. BROCCARDO, AND B. STOJADINOVIC, *The three-dimensional behavior of inverted pendulum cylindrical structures during earthquakes*, Earthquake Engineering & Structural Dynamics, 46 (2017), pp. 2261–2280.

[95] A. VIERKANDT, *Über gleitende und rollende bewegung*, Monatshefte für Mathematik und Physik, 3 (1892), pp. 97–116.

[96] R. VILLANUEVA AND M. EPSTEIN, *Vibrations of Euler's disk*, Physical Review E, 71 (2005).

[97] M. WECHSELBERGER, *Geometric singular perturbation theory beyond the standard form*, Springer, 2020.

[98] V. ZAITSEV AND A. POLYANIN, *Handbook of Exact Solutions for Ordinary Differential Equations*, CRC press, 2002.